

COMPUTATIONAL STUDY OF REACTIVE MISCIBLE VISCOUS FINGERING IN POROUS MEDIUM

DOCTORAL THESIS

By

PRIYA VERMA

(2017MAZ0006)



**DEPARTMENT OF MATHEMATICS
INDIAN INSTITUTE OF TECHNOLOGY ROPAR
RUPNAGAR, PUNJAB 140001, INDIA**

DECEMBER, 2023

COMPUTATIONAL STUDY OF REACTIVE MISCIBLE VISCOUS FINGERING IN POROUS MEDIUM

*A Thesis Submitted
In Partial Fulfilment of the Requirements for the Degree of*

DOCTOR OF PHILOSOPHY

by

**PRIYA VERMA
(2017MAZ0006)**

Under the Guidance of

PROF. MANORANJAN MISHRA

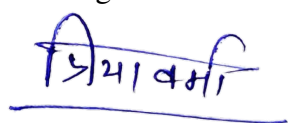


**Department of Mathematics
Indian Institute of Technology Ropar
December, 2023**

To my Parents.

DECLARATION OF ORIGINALITY

I hereby declare that the work which is being presented in the thesis entitled “**Computational study of reactive miscible viscous fingering in porous medium**” has been solely authored by me. It presents the result of my own independent investigation/research conducted during the time period from January 5, 2018, to December 8, 2023 under the supervision of Prof. Manoranjan Mishra, Professor, Department of Mathematics, Indian Institute of Technology Ropar. To the best of my knowledge, it is an original work, both in terms of research content and narrative, and has not been submitted or accepted elsewhere, in part or in full, for the award of any degree, diploma, fellowship, associateship, or similar title of any university or institution. Further, due credit has been attributed to the relevant state-of-the-art and collaborations (if any) with appropriate citations and acknowledgments, in line with established ethical norms and practices. I also declare that any idea/data/fact/source stated in my thesis has not been fabricated/ falsified/ misrepresented. All the principles of academic honesty and integrity have been followed. I fully understand that if the thesis is found to be unoriginal, fabricated, or plagiarized, the Institute reserves the right to withdraw the thesis from its archive and revoke the associated Degree conferred. Additionally, the Institute also reserves the right to appraise all concerned sections of society of the matter for their information and necessary action (if any). If accepted, I hereby consent for my thesis to be available online in the Institute’s Open Access repository, inter-library loan, and the title & abstract to be made available to outside organizations.



Signature

Name: Priya Verma

Entry Number: 2017MAZ0006

Program: Ph.D.

Department: Mathematics

Indian Institute of Technology Ropar

Rupnagar, Punjab 140001

Date: 08 December, 2023

CERTIFICATE

This is to certify that the thesis entitled “**Computational study of reactive miscible viscous fingering in porous medium**”, submitted by **Priya Verma** for the award of the degree of **Doctor of Philosophy** of Indian Institute of Technology Ropar, is a record of bonafide research work carried out under my guidance and supervision. To the best of my knowledge and belief, the work presented in this thesis is original and has not been submitted, either in part or full, for the award of any other degree, diploma, fellowship, associateship or similar title of any university or institution.

In my opinion, the thesis has reached the standard of fulfilling the requirements of the regulations relating to the Degree.



Signature of the Supervisor

Name: Prof. Manoranjan Mishra

Department: Mathematics

Indian Institute of Technology Ropar

Rupnagar, Punjab 140001

Date: 8 December, 2023

ACKNOWLEDGEMENT

Earning this PhD has been an incredibly transformative journey, and I credit my success to the invaluable support and guidance of numerous individuals. I am sincerely thankful for their assistance and would like to convey my deepest appreciation. Above all, I want to express my deepest gratitude to my Ph.D. advisor, Prof. Manoranjan Mishra. His unwavering faith and support, both mentally and academically, alongside his patience, inspiration, motivation, and most importantly, guidance, remained my driving force. I owe him an immense debt of gratitude for introducing me to the field of Fluid Mechanics and steering me toward achievements I had never imagined possible.

I extend my gratitude to my Doctoral Committee members: Dr. Subash Chandra Martha, Dr. Partha Sharathi Dutta, Dr. Arun Kumar, and Dr. Swati Patel for their unwavering guidance and support, which fueled my research efforts throughout my Ph.D. Additionally, I thank all the esteemed faculty members at the Department of Mathematics, IIT Ropar, for fostering a nurturing environment and creating unforgettable memories. Special appreciation goes to Mr. Neeraj Sharma, JLA, our office assistant, whose assistance in maintaining our systems, especially during the lockdown, ensured seamless remote connectivity. The collaboration and aid from the IT department were instrumental, and I am grateful for their support. I also express my gratitude to Ms. Jaspreet Kaur for her invaluable assistance in official matters. I am thankful for IIT Ropar Library's access to esteemed journals, enriching my academic pursuits. I thank the University Grants Commission (UGC), the Government of India, and IIT Ropar for their financial backing. Furthermore, I am appreciative of IIT Ropar's provision of travel grants, enabling me to attend conferences abroad and in India, fostering the exchange of new ideas, and facilitating connections for future research endeavors.

I wish to extend my heartfelt appreciation to Prof. Ching-Yao Chen from the National Yang-Ming Chiao-Tung University, Taiwan, for graciously hosting me in his laboratory. He ensured my utmost comfort during my stay while fostering an environment conducive to productive research through insightful discussions and group meetings. Prof. Chen's research funding enabled my participation in the IACM CFC conference held in Cannes, France, for which I am immensely grateful as he provided partial support for my attendance. Furthermore, I would like to recognize the invaluable support rendered by Prof. Yuichiro Nagatsu and Prof. Ryuta X. Suzuki from the Tokyo University of Agriculture and Technology, Japan, along with their students, Yuka, Kawri, and Harumi, during my visit in November 2022.

I extend my gratitude to my esteemed colleagues in the research group: Anoop Bhaiya, Vandita Di, Sada Nand Bhaiya, Surya, Santanu, Tarani, Priyanka, Ajay, Sahil, Vishal, and Lopa Ma'am, for engaging in discussions and delightful dinner outings. Each of them has not only been a valuable professional colleague but also a wonderful friend, contributing to many memorable moments we've shared. I am particularly thankful to Vandita Di, my senior, mentor and elder sister who has played a significant role in my learning journey about research and fluid dynamics. She has been a co-author in almost every paper of mine. Sada Nand Bhaiya, my senior and elder brother, has imparted invaluable academic and life lessons. Whenever I've faced challenges or need someone to share with, his comforting presence with a cup of tea and his words, '*chal chai pine chlte h,*' have been solace. Tarani and I began our academic journey in this institute under Prof. Mishra. We went through coursework together and presented our thesis proposal seminars, and though he left the Ph.D., he is now an assistant professor in his home state. I'm grateful that we are still in contact. My seniors, Anoop Bhaiya and Surya, also deserve my gratitude for their academic assistance whenever I need it. I also thank my super seniors, Satyajit Sir and Tapan Sir for their critical comments and valuable suggestions on my work. Moving to the current members of the FDRL lab—Priyanka, Ajay, Sahil, Vishal, Lopa Ma'am, and our two new members, Bikky and Mounesh—our discussions during tea breaks and dinner outings have been delightful. All these are comrades to me. Spending quality time with my lab mates has been instrumental in making my time at IIT Ropar unforgettable.

I consider myself incredibly fortunate to have formed strong friendships at IIT Ropar, and I'm grateful to each of them for making my time here unforgettable. I extend my heartfelt thanks to Vikash, my roommates Akriti and Sumitra, Taranjot, Abhijit, Neha, Shubhendu, Gopika, Himanshu, Bipasha, Arzoo, Sahil, Ankita, Aditi, Monika, Sonam, Niharika, Kalyani, Piyush Bhaiya, Gargi, and Nazim. They have not just been friends but have treated me like family, creating beautiful memories together. Sumitra, in particular, feels like a younger sister to me. I used to play basketball – yes, I play! I also run. Akriti, Priya, Taranjot, Ashitha, Shubham, Amit, Venki, Karan, and Rajat patiently taught me basketball and bore me on the court. During my visit to Taiwan, I formed lasting friendships with Avdhesh, Sanjay, Anshika, Manisha di, Chi-Chian, and Deepali, along with my roommates Henny, Yiting, and Uma. Their company in Taiwan made it feel like a home away from home. Completing this list seems impossible. But I can't stress enough how much harder this journey would've been without this wonderful family-like circle of friends. Words truly fail to convey my immense gratitude and affection for all of them. I'm also grateful to my old friends—Jyoti, Swati, Bharti, Samiksha, Neha, and Rajkiran. In particular, Swati has been a constant source of comfort, always there for lengthy conversations whenever I needed a listening ear during difficult times.

Most importantly, my profound gratitude goes to my family—Mumma, Papa, Bhanu, and Karan. Especially, Papa, for their unwavering faith and support in every decision I've made. I owe everything I am today to him. He was present for every interview, exam, and coaching class, patiently waiting outside classrooms and buildings. His dedication and sacrifices have been the driving force behind my success. My mother, my closest confidante, is an integral part of my day, and it feels incomplete without sharing moments with her. Bhanu and Karan have always been there for me as well. I also want to express my gratitude to Nanaji, Nani, Mamaji, Mamiji, and all Mosi and Buaji. My Nani couldn't see this thesis, but I know she would have been proud. I'm fortunate to have the best cousins: Nisha, Vinita, Gunjan, Barkha, Mahima, Dheeraj, Rohit, Hitesh, Kuldeep, Pranjul, Arti, Neha, Deepak Bhaiya, Harish, and Nikhil. This acknowledgment would be incomplete without mentioning my to-be husband. He is not just my labmate but also a friend who has been there for me since last year. He supported me during the most frustrating times of my Ph.D., taking care of me at his best. Thanks to him, I am going to have a loving mother-in-law and a wonderful sister-in-law.

In conclusion, I extend my thanks to the Almighty, God, for bestowing upon me countless blessings, knowledge, opportunities, as well as a wonderful circle of friends and family. These have collectively enabled me to complete my thesis. ***Om Namah Shivay!***

Abstract

A hydrodynamic instability called viscous fingering (VF) arises when a less viscous fluid displaces a more viscous one in a porous medium. This phenomenon is prevalent in diverse transport scenarios, including applications in the petroleum industry, aquifer contamination, and CO₂ sequestration. A chemical reaction may modify the viscosity of the fluids flowing in a porous medium and influence the VF. From macro to micro scales fields utilize VF induced by chemical reactions to enhance mixing. To comprehend chemo-hydrodynamic instability, we examine a reactive displacement involving a second-order chemical reaction, denoted as $A + B \rightarrow C$, assuming miscible, Newtonian, and neutrally buoyant fluids. These bio-molecular reactions serve as fundamental components for diverse complex reactions. Moreover, the viscosity profile depends on the viscosities of the reactants and products, determined by $R_b = \ln(\mu_B/\mu_A)$ and $R_c = \ln(\mu_C/\mu_A)$ where μ_i is the viscosity of fluid $i \in \{A, B, C\}$. When reactants and products exhibit viscosity contrasts, a nonlinear interaction arises between chemical reactions and hydrodynamics. This interaction is modeled using a coupled system of partial differential equations that encompasses Darcy's law and three convection-diffusion-reaction (CDR) equations.

We employ non-linear simulations (NLS) to investigate reactive VF in radial flow. Our study involves discussing a numerical technique that combines compact finite differences and a pseudo-spectral method. For stable displacements, we report a transient growth in total reaction rate at higher Damköhler numbers (Da) in radial flow, leading to more product formation, a phenomenon absent in rectilinear flow. Additionally, we observe an earlier onset of instability and enhanced fluid mixing with increasing viscosity contrast. It also depends on whether the product is high or less viscous than reactants for a constant R_b . Moreover, as the viscosity contrast increases, the mixing process reaches a saturation point, and we identify the existence of frozen fingers in this reactive fluid system at later stages. Further, we extend our analysis for infinitely fast reactions having iso-viscous reactants ($R_b = 0$) and establish a scaling relation for the onset time of instability depending on the Péclet number (Pe) and R_c . Further, we conduct the stability analysis using both the approaches, NLS, and linear stability analysis (LSA). Interestingly, the viscosity profile is not modified after the reaction when $R_c = R_b$. This scenario serves as an equivalent non-reactive case, allowing us to compare VF dynamics when the viscosity profile changes. We establish a phase plane (R_b, R_c) phase plane for a wide range of Da and Pe divided by critical viscosity contrast to induce instability. It states that if the equivalent non-reactive case, is stable, there exists a range of R_c that corresponds to stable for each R_b and vanishes at the critical value of R_b that triggers instability for the equivalent non-reactive cases. Otherwise, the flow remains unstable. The stable zone contracts for

larger values of Da and Pe , yet it never disappears, even with $Da \rightarrow \infty$. Intriguingly, a region near the line $R_c = R_b$ is identified where flow stability remains unaffected by reaction rate (Da).

To explore the influence of flow geometry on reactive VF, we investigate reactive displacements for rectilinear flow in a linear regime. The unsteady base state renders a stability matrix highly non-normal, and hence, the modal analysis like QSSA, may not predict the transient behavior accurately. Therefore, we opt for a non-modal linear stability analysis (NMA) using a propagator matrix approach to assess reactive displacements. As the viscosity contrast increases, an early onset occurs and more amplified perturbations when the reaction generates a less viscous product ($R_c < R_b$) than the equivalent non-reactive scenario. Conversely, there exist some reactive cases where onset is delayed if $R_c > R_b$ compared to the equivalent non-reactive case ($R_c = R_b$) for infinitely fast reactions, even with a steeper viscosity contrast. Further, we focus on the reactions having a non-monotonic viscosity profile featuring finite reaction rates with iso-viscous reactants ($R_b = 0$). For such instances, the unstable zone contracts, and a stable zone develops in the mixing zone. As a consequence of this stable zone, fingering patterns localize and develop either upstream or downstream of the flow, depending on whether the viscosity profile exhibits a maximum or minimum. When $R_c > 0$, certain reactions exhibit transient growth within the perturbation amplification curve, resulting in secondary instability. Here, we obtain a significant contrast in the early-stage VF dynamics across both flow geometries. For radial flow, we observe the transient growth in perturbation amplification but do not observe secondary instability for the similar non-monotonic viscosity profile having maxima. In rectilinear flow, the velocity consistently facilitates convection towards the interface throughout the process, contrasting with radial flow geometry where it diminishes over time at the interface.

The numerical technique employed for NMA in this thesis introduces a new perspective for comprehending time-dependent linear systems inherent in miscible reactive VF. The outcomes obtained align more closely with non-linear simulations than the conventional approach, QSSA. This research contributes a numerical and theoretical framework with potential applications for controlling and enhancing VF in various geophysical processes, including CO₂ sequestration, chemical flooding, and reactive pollutant displacement.

Keywords: Viscous fingering instability, porous media, chemo-hydrodynamic instability, radial flow, rectilinear flow, Darcy's law, convection-diffusion-reaction equations, pseudo-spectral method, frozen fingers, saturation in mixing phenomena, linear stability analysis, compact finite difference, non-normal matrix, non-modal analysis.

Contents

DECLARATION OF ORIGINALITY	vii
CERTIFICATE	vii
ACKNOWLEDGEMENT	ix
ABSTRACT	xv
CONTENTS	xvii
LIST OF FIGURES	xxi
LIST OF TABLES	xxix
1 Introduction	1
1.1 Introduction	1
1.1.1 Viscous fingering instability	2
1.1.2 Miscible displacement in porous media	3
1.1.3 Chemo-hydrodynamics instabilities	8
1.1.4 Convection-diffusion-reaction equations	9
1.1.5 Understanding of reactive miscible viscous fingering	9
1.1.6 VF dynamics due to altered viscosity profile	11
1.2 Motivation and objectives	13
1.3 Outline of thesis	14
2 Flow dynamics of a radial miscible $A + B \rightarrow C$ reaction front	19
2.1 Introduction	19
2.2 Mathematical formulation	20
2.2.1 Numerical scheme	22
2.3 Results and discussion	24
2.3.1 Chemical reaction characteristics	25
2.3.1.1 Total reaction rate	25
2.3.1.2 Total amount of product	27
2.3.1.3 Reaction rate and center of reaction front	29
2.3.2 Interaction of chemical reaction and VF dynamics	30
2.3.2.1 VF dynamics for $R_b > 0$	31
2.3.2.2 VF dynamics for $R_b < 0$	35

2.3.2.3	Effect of Da on VF dynamics	36
2.3.2.4	Effect of VF on R_{tot}	37
2.3.2.5	VF and total amount of product	38
2.3.2.6	VF affecting reaction front	38
2.3.3	Mixing dynamics	40
2.4	Conclusion	43
3	Linear stability analysis of radial reactive viscous fingering	45
3.1	Introduction	45
3.2	Mathematical formulation	47
3.3	Linear Stability analysis	49
3.3.1	Linearised perturbed equations	49
3.3.2	Initial value calculations	50
3.3.3	Transient energy growth	52
3.3.3.1	Effect of R_c	53
3.3.3.2	Effect of Da	58
3.4	Non-linear simulations	60
3.4.1	Effect of Da and Pe ($Da \rightarrow \infty$)	64
3.5	Conclusion	67
4	Radial viscous fingering induced by an infinitely fast reaction	69
4.1	Introduction	69
4.2	Mathematical formulation	70
4.3	Numerical scheme	72
4.3.1	Order of convergence	77
4.4	Results and discussion	79
4.4.1	Effect of different reactants on the VF dynamics	80
4.4.1.1	Varying the viscosity of the reactants	80
4.4.1.2	Effect of Péclet number	81
4.4.2	Unstable displacements	82
4.4.2.1	Onset of instability	82
4.4.2.2	Dependence of t_{on} on R_c and Pe	85
4.4.2.3	Finger length	87
4.5	Conclusion	90
5	Non-modal analysis of reactive flow for infinitely fast reactions	93
5.1	Introduction	93
5.2	Mathematical formulation	95
5.3	Linear stability analysis	97
5.3.1	Non-modal analysis	99

5.3.1.1	Self-similarity transformation	100
5.3.1.2	Propagator matrix approach	101
5.3.1.3	Transient energy growth	101
5.3.1.4	Convergence study and validation of numerical scheme	102
5.4	Result and discussion	104
5.4.1	VF dynamics when viscosity profile is monotonic $R_c(R_b - R_c/2) \geq 0$	105
5.4.2	VF dynamics when viscosity profile is non-monotonic $R_c(R_b - R_c/2) < 0$	107
5.4.2.1	Optimal amplification for $R_b > 0$	107
5.4.2.2	Optimal amplification for $R_b < 0$	110
5.4.3	Computing perturbation energy balance	112
5.4.4	Comparison with QSSA	114
5.5	Conclusion	114
6	Non-modal analysis of reaction-induced viscous fingering	117
6.1	General introduction	117
6.2	Mathematical formulation	118
6.3	Linear stability analysis	120
6.3.1	QSSA	122
6.3.2	Non-modal analysis	123
6.3.2.1	Validation of numerical method	125
6.4	Result and discussion	125
6.4.1	Effect of R_c	126
6.4.2	Effect of Da	129
6.4.3	Effect of geometry	131
6.5	Conclusion	131
7	Summary and future work	133
7.1	Summary of the thesis	133
7.2	Future work	135
	APPENDIX	136
A	Grid independence and effect of σ_1	137
B	Why $h < 0.5$ when $a = 0$?	139
B.1	To show $a + b + 2c = 1$	139
B.2	Why $h < 0.5$ when $a = 0$?	140
B.3	Different choices of H_1, H_2	141
C	Pseudo-code of the numerical method	143

D	Pressure and velocity component	145
E	Non-normality of the stability matrix	147
	REFERENCES	148

List of Figures

1.1	(a) Rayleigh-Taylor instability [3], (b) Viscous fingering instability [75] and (c) Kelvin-helmholtz instability [32]. The images are taken from the article, Banerjee [3], Nand et al. [75], Govindarajan and Sahu [32], respectively.	1
1.2	A Hele-Shaw cell showing the displacement of high viscous fluid than less viscous fluid used in experiments [77].	3
1.3	Schematic of the miscible displacement in two-dimensional porous media for (a) rectilinear flow and (b) radial flow. The images are taken from Hota and Mishra [37] and Sharma et al. [92].	4
1.4	The illustration of Viscous fingering during (a) Enhanced CO ₂ Storage and (b) gas EOR showing a radial and rectilinear flow. The images are taken from Burrows et al. [14] and Bello et al. [4].	4
1.5	Vector example of transient growth [86]. Starting on the left, the vector \mathbf{f} is defined as the difference between the nearly collinear vectors ϕ_1 and ϕ_2	7
1.6	A comparison of Spectral abscissa (circles) and numerical abscissa (squares) for $R = 3$, at different times (a) $t = 10^{-8}$, (b) $t = 10^{-5}$, (c) $t = 1$, and (d) $t = 10$ to illustrate the presence of non-normality in the stability matrix at early times. The image is taken from Hota et al. [39].	7
1.7	Reaction-induced instability. (a) Kelvin -Helmholtz instability [63] and (b) Viscous fingering instability [83].	9
1.8	(R_b, R_c) Phase plane. The inset figures are viscosity depending on the value of (R_b, R_c) , i.e. $\ln(\mu) = R_b b + R_c c$. This figure is a reproduction of figure 3 from Hejazi et al. [35].	12
2.1	Schematic of $A + B \rightarrow C$ chemical reaction in a radial source flow. The region inside the inner circle and outside the outer circle is occupied by reactants A and B , respectively. The product C is generated in the annulus region where the reactants come in contact. We denote that region inside the annulus as the reaction front.	21
2.2	Total reaction rate for $R_b = R_c = 0$, $Pe = 3000$ and various Da	26
2.3	Contours of the reaction rate $R(x, y, t) = Da a(x, y, t)b(x, y, t)$ for (a) $Da = 100$ and (b) $Da = 15$ at different times.	26

2.4	(a) Total amount of product c_{tot} for stable displacement and various Da . Inset: Log-log plot of the same at later times. Here dotted lines are fitted lines. (b) Log-log plot of c_{tot} at early times. The solid curves are fitted and markers represent the original data. All the curves follow the power law relation $c_{tot} \propto t^{f(Da)}$. Inset: Da vs $f(Da)$	28
2.5	Temporal evolution of average reaction rate for $Da = 15, 60, 100$ and stable displacement. Inset: The first moment of the average reaction rate coincides with the center of front at all times for stable displacement. Here, $Da = 100$. Here, solid, dashed and dotted lines denotes the averaged reaction rate at time $t = 0.1, 0.55, 1$, respectively.	29
2.6	Log-viscosity profile for $Da = 100, Pe = 3000$, (a) $R_b = 1$ and (b) $R_b = -1$ and various R_c . No product is generated for $Da = 0$, and hence the value of R_c is insignificant when $Da = 0$. Also, the value of Da is irrelevant when $R_b = R_c$ and thus the viscosity profile is the same as that of the non-reactive case.	30
2.7	Density plots of the reaction rate for $Pe = 3000, Da = 100$, (a) $R_b = 1$ and (b) $R_b = -1$ and various R_c at $t = 1$. The R_c values in each row are chosen in order to have constant $ R_b - R_c $ value. For instance, $R_c = -3, 5$ correspond to $ R_b - R_c = 4$. Similarly, $R_c = 0, 2$ result in $ R_b - R_c = 1$, while $ R_b - R_c = 0$ for $R_c = 1$	30
2.8	Product concentration profile for $Pe = 3000, Da = 100, R_b = 1$ and various R_c at different times.	32
2.9	Product concentration profile for $Pe = 3000, Da = 100, R_b = 1$ and (a) $R_c = 5$ and (b) $R_c = -3$. It can be observed that no new fingers are generated after $t = 0.1$ for both the parameters $R_c = 5, -3$. Also, the developed fingers experience the shielding and merging effect as the number of fingers decreases and some of the fingers are merged after time $t = 0.2$ for $R_c = -3$	34
2.10	Product concentration profile for $Pe = 3000, Da = 100, R_b = -1$ and various (a) $R_c > 0$ and (b) $R_c < 0$ at time $t = 1$	35
2.11	Product concentration profile for $Pe = 3000, Da = 15$, (a) $R_b = 1$, (b) $R_b = -1$ and various R_c at final time $t = 1$	36
2.12	Total reaction rate for $Da = 100, Pe = 3000$, (a) $R_b = 1$ and (b) $R_b = -1$ and various R_c . Black dotted curve is for $R_b = R_c = 0$. Here, solid lines are plotted when $R_b - R_c < 0$ that is for $R_c = 5, 3, 2; R_b = 1$ ($R_c = 6, 4; R_b = -1$) and while dashed lines are plotted for corresponding $R_b - R_c > 0$ that is for $R_c = -3, -1, 0; R_b = 1$ ($R_c = -4, -6; R_b = -1$).	37
2.13	Total amount of product for $Da = 100, Pe = 3000$, (a) $R_b = 1$ and (b) $R_b = -1$ and various R_c	38

2.14	Averaged reaction rate profile for $Da = 100$, (a) $R_b = 1$, (b) $R_b = -1$ and various R_c at time $t = 0.95$	39
2.15	Temporal evolution of center of mass of averaged reaction rate $\langle R \rangle(r, t)$ for $R_b = 1$, various R_c and $Da = 15$. Inset: Relative difference, Δm_R in first moment of $R_b \neq 0$, $R_c \neq 0$ and stable displacement $R_b = R_c = 0$	39
2.16	Temporal evolution of center of mass of averaged reaction rate $\langle R \rangle(r, t)$ for (a) $R_b = 1$, and (b) $R_b = -1$, various R_c and $Da = 100$. Inset: Relative difference, Δm_R in first moment of $R_b \neq 0$, $R_c \neq 0$ and stable displacement $R_b = R_c = 0$	40
2.17	Degree of mixing for $Da = 100$, (a) $R_b = 1$ and (b) $R_b = -1$ and various R_c . Here the onset of instability can be noted when the degree of mixing exceeds zero <i>i.e.</i> $\chi > 0$ as this quantification is a direct comparison of mixing between stable to unstable displacement.	41
2.18	Log-log plot of interfacial length for (a) $R_c = -3, 5$, $R_b = 1$, (b) $R_c = 6$, $R_b = -1$ and $R_b = R_c = 0$. Inset: interfacial length for $R_c = 5, -3$. Blue-dashed line for $R_c = -3$ and Red solid is for $R_c = 5$	43
3.1	Schematic of $A + B \rightarrow C$ chemical reaction in a radial source flow. The green-colored shaded region bounded by dashed lines, is where both the reactants come into	47
3.2	Base state profile of (a) Reactant A , (b) Reactant B , (c) product C and (d) Dye concentrations for $Da = 100$, $Pe = 3000$ at final time $t = 1$	50
3.3	(a) Viscosity profile for $Da = 100$, $R_b = 0.5$ and various R_c . (b) Log energy amplification with time for $Da = 100$, $R_b = 0.5$ and various R_c showing unstable displacement. Inset: $\ln(G(t))$ of $R_b = 0.5, 0.3$, $Da = 0$	54
3.4	(a) Averaged reaction rate profile, $\langle R \rangle(r, t) = \frac{1}{2\pi} \int_{r_0}^R R(r, \theta, t) d\theta$ and $R = DaA_0B_0$ for base state for $Da = 100$. Density plot for perturbed concentration of C, c' for $Da = 100$, $R_b = 0.5$, (b) $R_c = -0.5$, (c) $R_c = 0.5$ and (d) $R_c = 1.5$ at final time $t = 1$ in polar coordinates. Here the black-dashed line denotes the position where the reaction rate is maximum as shown in (a).	55
3.5	Density plot for perturbed concentration (a) a' , (b) b' and (c) z' for $Da = 100$, $R_b = 0.5$ and $R_c = 0.5$ at final time $t = 1$ in polar coordinates.	56
3.6	(a) Log energy amplification and (b) growth rate with time for $Da = 100$, $R_b = 0.3$ and various R_c showing unstable displacement. Inset: Growth rate for $R_c = 1.1, -0.5$ showing an unstable and stable displacement respectively despite the same viscosity contrast $ R_b - R_c $	57

3.7	Log energy amplification with time for $Da = 10$, (a) $R_c = 0.5$, (b) $R_c = 0.3$ and various R_c showing unstable displacement.	59
3.8	Log energy amplification with time for $R_b = R_c = 0.5, 0.3$ and various Da . Here all the curves for different Da and fixed viscosity contrast, are merged.	59
3.9	Dye concentration profile for $(Da, Pe) = (100, 3000)$, (a) $R_b = 0.3$ and (b) $R_b = 1$ and various R_c at final time $t = 1$	61
3.10	The (R_b, R_c) phase plane for $Pe = 3000$, various Da along with $Da \rightarrow \infty$. Dye concentration profile for $R_b = 1$, (i) $R_c = -3$, (ii) $R_c = 1$, (iii) $R_c = 5$ showing unstable displacement and (iv) $R_b = R_c = 0$ showing stable displacement in polar coordinates. The viscosity profile is non-monotonic for $R_c = -3$, and 5 with the decreased and increased product viscosity that leads to the localized fingering pattern in the upstream mixing and downstream mixing zone, respectively. While the viscosity profile remains monotonic for $R_b = R_c = 1$ and the resultant fingering patterns are not localized unlike the cases $R_b = 5, -3$	62
3.11	(a) Phase plane between the viscosity ratio at upstream mixing and downstream mixing zone, $R_c/2$ and $R_b - R_c/2$ for $Pe = 3000$ and various Da . (b) (R_b, R_c) phase plane for $Pe = 3000, 1000$ for $Da \rightarrow \infty$. Here below the curve is a stable region, and above the curve is an unstable region. Here the dashed line corresponds to the non-reactive case $Da = 0$ for $Pe = 3000$ (blue) and $Pe = 1000$ (red).	65
4.1	(a) A schematic of the problem at $t = 0$ showing reactant A contained in a circle of radius r_0 . The region outside the circle is occupied by reactant B . (b) The same schematic at $t > 0$ depicts the generation of the product C in the yellow-colored annulus region where the reactants come in contact. Here $r > r_0$	72
4.2	Error in product concentration E_N^C versus dx for $Pe = 2000$, $R_c = 0$. The dashed and dotted lines represent the reference lines with slope dx and $dx^{1.5}$, respectively.	78
4.3	Density plots of product C concentration at final time $t = 1$ for $Pe = 3000$ and (a) $R_c > 0$ (in first row) (b) $R_c < 0$ (in second row). <i>Flower</i> like instability for $R_c \geq 2$ and <i>crown</i> like instability for $R_c \leq -2$ is evident.	80
4.4	Density plots of product C concentration for various Pe and (a) $R_c = 5$ (in first row), (b) $R_c = -5$ (in second row) at final time $t = 1$	81
4.5	Temporal evolution of concentration of product for (a) $R_c = 4$ (in first row) and (b) $R_c = -4$ (in second row) for $Pe = 1000$. The instability appears at $t \approx 0.2$ for $R_c = 4$ while at $t \approx 0.3$ for $R_c = -4$	82

4.6	(a) Temporal evolution of the interfacial length for various R_c and $Pe = 3000$. Clearly, the onset of instability is early for $R_c > 0$. Inset: δI versus t for $ R_c = 2$ showing the delayed onset for $R_c = -2$. (b) The onset time versus $ R_c $ showing a delayed onset for $R_c < 0$	83
4.7	(a) Onset time t_{on} versus R_c for $Pe = 3000, 1000, 500$ showing a delayed onset for smaller Pe . (b) Plot for R_c versus Pe for a given time t	84
4.8	Log-log plot of R_c versus Pe at various time t . These curves can be well fitted using the power law $R_c^- = -160Pe^{-0.58}$ for $R_c < 0$ in (a) and $R_c^+ = 260Pe^{-0.64}$ for $R_c > 0$ in (b).	86
4.9	Onset time curves for various Pe , merged into a single curve for (a) $R_c < 0$ and (b) $R_c > 0$. 87	
4.10	Density plots of product concentration in the (r, θ) coordinates for $Pe = 1000$ and (a) $R_c = 4$, (b) $R_c = -4$, (c) $R_c = 5.5$ and (d) $R_c = -5.5$ at final time $t = 1$. For $R_c < 0$, the vertical axis is reversed for a better comparison of the finger length.	88
4.11	(a) Temporal evolution of L_- and L_+ for $Pe = 1000$ and various R_c . (b) Length of inward and outward fingers for $R_c = 5, -5$ and $Pe = 2000, 700$. Here solid lines are for $R_c = 5$ and dashed lines are for $R_c = -5$. Clearly, transition in VF dynamics also occurs for a given viscosity ratio and varying Pe	88
5.1	Schematic of the two-dimensional rectilinear reactive flow $A + B \rightarrow C$. The dashed lines illustrate the initial position of the interface and \tilde{U}_0 is the velocity at which the reactant A has been injected. Here, brown and black colored regions are occupied with reactants A and B . The reaction zone is occupied by all three fluids.	95
5.2	Optimal amplification for $R_b = 2, R_c = -2, k = 0.2$ and various dx . Here the markers denote the onset time. The onset time does not alter by taking $dx = 0.4$ in comparison to $dx = 0.2$. Inset: absolute error versus dx	103
5.3	(a) Viscosity profile (b) optimal amplification for $R_b = 3; Da = 0$ and $R_b = R_c = 3; Da \rightarrow \infty$	104
5.4	(a) The $R_b - R_c$ phase plane. Here in the colored region bounded between the lines $R_c = 0$ and $R_c = 2R_b$, the viscosity profile remains monotonic as shown in the Inset figure. Inset: Log-viscosity profile for $R_b = 2$ and $R_c = 4, 2, 0$. (b) Optimal amplification for $R_b = 2, R_c = 0, 2, 4$. Inset: Growth rate for $R_c = 4, 2$ at the later time showing that the growth of the perturbations is more for $R_c = 4$ than $R_c = 2$	106

5.5	(a) z concentration profile for $R_b = 2$ and $R_c = 4, 2, 0$. (b) Mixing length for $R_b = 2$ and various $R_c = 0$ with the stable displacement $R_b = R_c = 0$. This figure is a reproduction of figures 6,7 and 9(a) from [69].	106
5.6	(a) The (R_b, R_c) phase plane for $R_b > 0$. Here in the uncolored region bounded between the lines $R_c = 0$ and $R_c = 2R_b$, the viscosity profile remains monotonic. Inset: Log-viscosity profile for $R_b = 2$, (i) $R_c = -2$, (ii) $R_c = 6$. (b) Optimal amplification for $R_b = 2$, $R_c = 6, -2, 2$. Here the squared marker denotes the onset time. Inset: Growth rate for $R_c = 6, 2$	107
5.7	Perturbation contour plot for $R_b = 2$, $k = 0.2$ and $R_c = 2$, of (a) A and B and (b) C . Here the time integration intervals are (i) $= [0.001, 0.1]$, (ii) $= [0.001, 5]$ and (iii) $= [0.001, 30]$. In (a) the solid lines show the reactant A perturbation contour and dashed lines present reactant B perturbation contours.	108
5.8	Perturbation contour plot for $R_b = 2$, (a) $R_c = 2$, (b) $R_c = 6$ and (c) $R_c = -2$, showing the evolution of the perturbations of product, $c = V \cos(ky)$ and $k = 0.2$. Here the time integration intervals, $[t_p, t]$ are (i) $[0.001, 0.1]$, (ii) $[0.001, 5]$ and (iii) $[0.001, 30]$. The perturbation contours are shown to span from their minimum to maximum values in five equal increments. (d) Onset time <i>versus</i> R_c for various R_b	109
5.9	(a) The (R_b, R_c) phase plane for $R_b < 0$. Here the colored regions depict the non-monotonic viscosity profile. Inset: log-viscosity profile for $R_b = -1$ and (i) $R_c = 6$, (ii) $R_c = -1$, (iii) $R_c = 4$. (b) Optimal amplification for $R_b = -1$ and $R_c = 4, -6$	111
5.10	Perturbation contour plot for $R_b = -1$, $Da \rightarrow \infty$ and (a) $R_c = -6$, $k = 0.15$ and (b) $R_c = 4$, $k = 0.1$. Here the time integration intervals $[t_p, t]$ (i) $= [0.001, 30]$, (ii) $= [0.001, 50]$ and (iii) $= [0.001, 80]$	111
5.11	Energy balance for reactive fluids, $Da \rightarrow \infty$, $k = 0.2$, $R_b = 2$ obtained in (ξ, t) domain for (a) $R_c = 0$, (b) $R_c = 2$ and (c) $R_c = 4$ at different times.	112
6.1	Schematic of the flow of a reactive front $A + B \rightarrow C$	119
6.2	Base state concentration profile for A (blue lines), B (red lines) and C (green lines) at time $t = 1, 5$ and 10 represented by dotted, dashed and solid lines, respectively. Here, S_b is the dummy variable for base state concentrations.	121
6.3	Log of optimal amplification, $\ln(G(t))$ for $R_b = 3$, $Da = 0$ in the reactive case. Here, the (\times) curve shows the $\ln(G(t))$ for the non-reactive case.	126
6.4	Logarithm of optimal amplification, $\ln(G(t))$ for $R_b = 0$, $Da = 1$ and (a) $R_c > 0$ and (b) $R_c < 0$. Here the diamond dots denote the onset time of instability.	127

6.5	Growth rate, σ for $R_b = 0$, $Da = 1$ and $R_c > 0$. Here the squared dots denote the onset time of instability.	128
6.6	Viscosity profile for $R_c = 5$ and various Da at different times (a) $t = 5$, (b) $t = 10$ and $t = 20$ depicting an increased viscosity contrast with time.	129
6.7	Logarithm of optimal amplification, $\ln(G(t))$ for $R_b = 0$, (a) $R_c = 5$ and (b) $R_c = -5$ and various Da . Here the squared dots denote the onset time of instability. Inset: $\ln(G(t))$ curve for $Da = 0.1$ at later times showing onset time.	130
6.8	(a) Base viscosity profile for $R_c = 5$, $Da \rightarrow \infty$ at different times. Clearly, The viscosity gradient for infinitely fast reactions decreases with time. (b) Logarithm of optimal amplification, $\ln(G(t))$ for various R_c and $Da \rightarrow \infty$. Here the squared dots denote the onset time of instability.	130
A.1	Temporal evolution of concentration for $R_c = -3.5$, $Pe = 3000$ for (a) $N = 512$ (in first row) and (b) $N = 1024$ (in second row) at time $t = 0.1, 0.4, 0.7, 1$ (left to right).	137
A.2	Interfacial length for $Pe = 3000$, $R_c = -3.5$ for various grid points.	138
A.3	(a) Product concentration profile at time $t = 1$ and (b) interfacial length for $Pe = 3000$, $R_c = -2.5$, $r_0 = 0.075$ and various σ . Evidently, both concentration plot and interfacial length are identical for $\sigma \leq r_0$	138
B.1	Averaged concentration profile, $\langle a \rangle$, $\langle b \rangle$, $\langle c \rangle$ and $\langle a + b + 2c \rangle$ represented by blue, red, green and black lines, respectively, at different times. Here these curves are plotted at time $t = 1, 5$ and 10 represented by dotted, dashed, and solid lines, respectively. Here, s is the dummy variable for concentrations.	139
B.2	Temporal evolution of the angular averaged concentration plots of A , B , C , for $Pe = 3000$ and $Da \rightarrow \infty$	140
D.1	(a) Potential component of velocity. Here only one plot is shown as it does not depend on time, Pe and R_c . Temporal evolution of (b) rotational component of velocity \mathbf{u}_{rot} and (c) total velocity \mathbf{u} for $R_c = -3.5$, $Pe = 3000$. (d) Temporal evolution of total velocity for $R_c = -5$, $Pe = 2000$	146
E.1	Condition number of the stability matrix \mathcal{L} in equation (6.5) in (x, t) domain for the viscosity profile, $R_b = 2$, $R_c = -2$. (b) Condition number for the stability matrix in (x, t) and (ξ, t) domain corresponds to QSSA and SS-QSSA for $R_b = 2$, $R_c = -2$ and $k = 0.2$. For (ξ, t) domain, the stability matrix is from the equation (6.7).	147

E.2	The singular vectors and eigen functions obtained from (a) NMA and (b) QSSA, respectively, for the viscosity profile $R_b = 2$, $R_c = -2$, $k = 0.2$ for (i) ϕ_z , (ii) ϕ_a , (iii) ϕ_b and (iv) ϕ_c . Here, in figure (a), the singular vectors are plotted at $t = 10^{-3}$ (dashed lines) and $t = 10$ (solid lines).	147
-----	---	-----

List of Tables

3.1	Table showing the parameters used in the LSA.	51
4.1	Error and order for various N . Used parameters are $Pe = 2000$, $R_c = 0$. E_N^C, E_N^A and E_N^B respectively denote the error in the numerical solution of product concentration, reactant A concentration and reactant B concentration.	78
5.1	The parameters and corresponding values used in the numerical study.	103

Chapter 1

Introduction

1.1 Introduction

Hydrodynamic instabilities arise at the interface between two fluids when there exists a gradient in physical properties, for instance, density, viscosity, or surface tension, and emerge in the form of waves, vortices, or other complex flow patterns. Depending on the specific flow conditions, various hydrodynamic instabilities may be observed. For instance, the Saffman-Taylor instability is driven by viscosity contrast [102], the Kelvin-Helmholtz instability occurs in shearing flows [84], and a density gradient drives the Rayleigh-Taylor instability [56] as shown in figure 1.1. Several experimental and theoretical research has been conducted to gain insight into these instabilities. While researchers employ convection-diffusion-reaction equations to investigate such pattern-forming instabilities and spatiotemporal structures. Nevertheless, the interaction between chemical reactions and hydrodynamics has received less attention in comparison to non-reactive displacements. These phenomena are referred to as chemohydrodynamic instability.

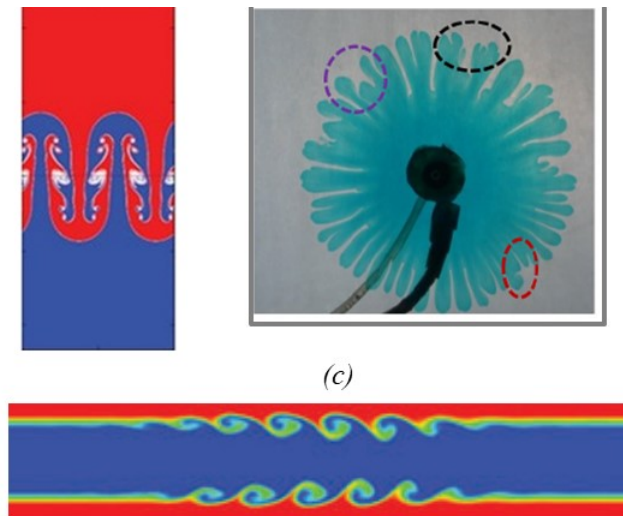


FIGURE 1.1: (a) Rayleigh-Taylor instability [3], (b) Viscous fingering instability [75] and (c) Kelvin-helmholtz instability [32]. The images are taken from the article, Banerjee [3], Nand et al. [75], Govindarajan and Sahu [32], respectively.

1.1.1 Viscous fingering instability

When a less viscous fluid displaces a more viscous one, it penetrates the displaced fluid into the shape of fingers. This phenomenon is known as viscous fingering (VF) instability. It is a fundamental fluid mechanics phenomenon with significant real-world applications such as oil recovery [102], chromatography separation [81], spreading of pollution zones in aquifers [55, 117], medicines [7], diffusion-limited aggregation [119] to name a few. The term ‘viscous fingering’ was introduced by engineers who were primarily concerned with its application in secondary oil recovery from porous rocks [26]. In contrast, physicists recognize VF as a morphological archetype that leads to the formation of interfacial patterns [15, 41, 50]. Moreover, mathematicians have shown interest in this problem. It is often referred to as the Hele-Shaw problem due to its relatively simple and occasionally solvable nature as a free-boundary problem [104, 105]. Hill [36] has carried out the first experimental research and documented the instability with miscible fluids in a porous medium. They have considered the displacements of sugar liquors by water from the columns of granular media and explained the resulting instability. Since the publication of this fundamental study, numerous theoretical, computational, and experimental studies have been conducted to understand the process underlying VF instability better. Homsy [102] provides an excellent evaluation of VF.

The instability improves fluid mixing, which can be beneficial or negative depending on the application. For instance, it is helpful in a variety of applications, such as the remediation of contaminated aquifers [76, 107] and the sequestration of CO₂ [42]. Furthermore, mixing, separation, and reaction control are some of the applications for microfluidic devices that make use of VF instability [44, 45, 97, 112]. Microfluidic devices, which can be used to mix fluids and transport particles, can produce intricate flow patterns using VF instability. Further, it controls the enhanced mixing of CO₂ plumes in porous matrix [6, 61]. Overall, VF can be advantageous because it can improve the efficiency of fluid transport by generating intricate flow patterns that distribute fluids across porous media. On the contrary, the formation of fingers might have negative impacts in situations where the purpose is to spread a fluid evenly through a porous media or where they can cause clogging, leakage, or other undesirable outcomes. VF can lead to an early breakthrough of the invading fluid (typically water or brine), reducing the efficiency of oil recovery and, in some cases, rendering it economically unviable [48]. Thus, it holds significant importance to control the instability since even a slight suppression or reduction of viscous fingering, by just a small percentage, can yield substantial economic benefits by lowering recovery costs.

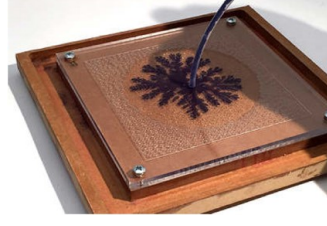


FIGURE 1.2: A Hele-Shaw cell showing the displacement of high viscous fluid than less viscous fluid used in experiments [77].

1.1.2 Miscible displacement in porous media

Miscibility refers to the ability of fluids to mix and result in a uniform solution. Examples of well-known miscible liquid combinations include water-ethanol, water-glycerol, and water-sugar syrup. In miscible fluids, the occurrence of VF is influenced by several factors, including the contrast in viscosity between underlying fluids, injection velocity, and rate of dispersion. The relative movement between the fluids becomes more pronounced as the injection velocity increases, thereby intensifying the instability. Conversely, the diffusive mixing of one fluid into the other diminishes the viscosity contrast between the underlying fluids, hence reducing the tendency for fingering instability. Consequently, the dynamics of miscible VF are determined by the interplay between the forces due to convection and diffusion.

To simulate the displacement of two miscible fluids, we adopt certain assumptions that the fluids exhibit Newtonian behavior, are non-reactive, and possess neutral buoyancy. We also assume the presence of a uniform, homogeneous porous medium with isotropic dispersion characteristics. Further, we assume the flow is incompressible. In the context of incompressible flow within miscible multiphase fluids, the assumption of incompressibility implies that the overall density of the fluid mixture remains constant as it flows, regardless of the presence of multiple phases. This assumption simplifies the mathematical modeling of fluid flow, allowing for the use of conservation of mass equations, the continuity equation. This combination of characteristics can be found in various natural and engineering systems. For instance, in Oil-Water Systems, Polymer Solutions, and Groundwater Contamination. The modeling of miscible viscous fingering involves a coupled system of equations, which combines Darcy's law with a convection-diffusion equation. The mathematical formulation incorporates the principles of momentum conservation and volume-averaged mass balance for solute concentration, denoted as \tilde{c} . The resulting equations are as follows:

$$\tilde{\nabla} \cdot \tilde{\mathbf{u}} = 0, \quad (1.1a)$$

$$\tilde{\nabla} \tilde{p} = -\frac{\tilde{\mu}}{\tilde{\kappa}} \tilde{\mathbf{u}}, \quad (1.1b)$$

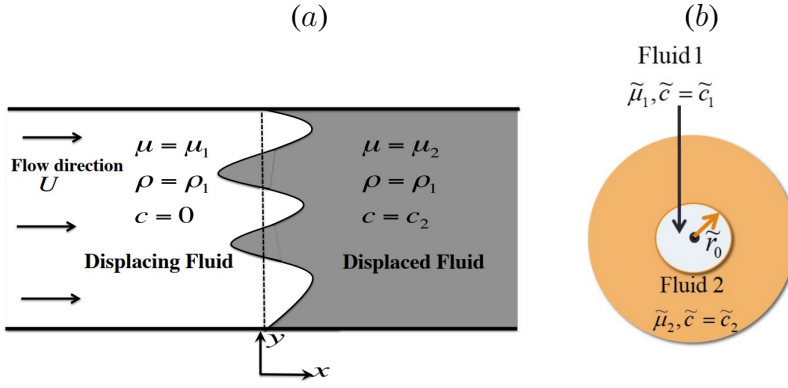


FIGURE 1.3: Schematic of the miscible displacement in two-dimensional porous media for (a) rectilinear flow and (b) radial flow. The images are taken from Hota and Mishra [37] and Sharma et al. [92].

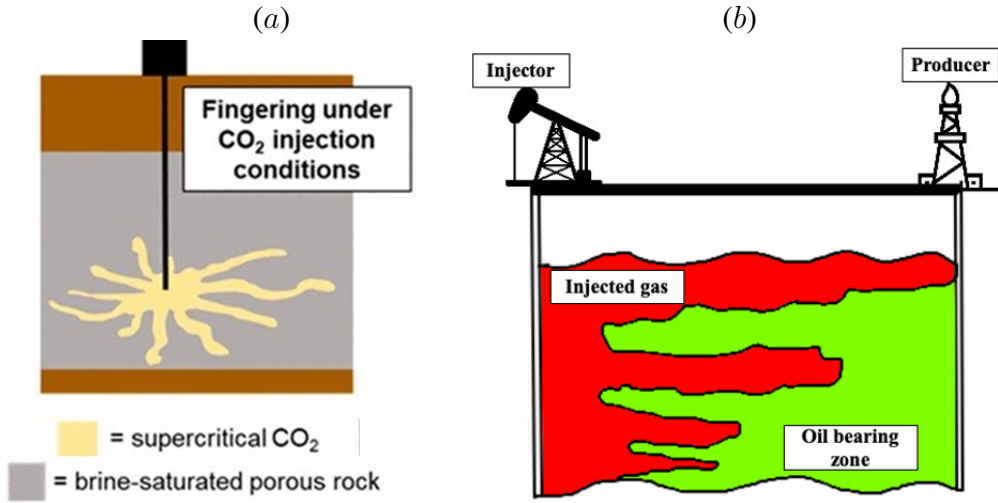


FIGURE 1.4: The illustration of Viscous fingering during (a) Enhanced CO₂ Storage and (b) gas EOR showing a radial and rectilinear flow. The images are taken from Burrows et al. [14] and Bello et al. [4].

$$\frac{\partial \tilde{c}}{\partial \tilde{t}} + \tilde{\mathbf{u}} \cdot \tilde{\nabla} \tilde{c} = \tilde{D} \tilde{\nabla}^2 \tilde{c}. \quad (1.1c)$$

$$\tilde{\mu} = \tilde{\mu}_0 e^{R\tilde{c}/\tilde{c}_0}, \quad R = \ln \left(\frac{\tilde{\mu}_1}{\tilde{\mu}_0} \right). \quad (1.1d)$$

Here, $\tilde{\mathbf{u}} = (\tilde{u}, \tilde{v})$ represents the velocity, \tilde{p} denotes pressure, $\tilde{\kappa}$ stands for the permeability of the porous medium, and \tilde{D} signifies the diffusion coefficient of the solute. Further, $\tilde{\mu}_1$ and $\tilde{\mu}_0$ are the viscosity of displaced and displacing fluid, respectively. All the quantities in the tilde are the dimensional quantities.

In recent years, significant advancements have enriched the field of miscible viscous fingering research [102]. These contributions encompass a wide range of experimental work, developing novel mathematical tools, and formulating numerical techniques to enhance our comprehension of this intriguing

phenomenon. To investigate VF, two distinct flow domain geometries are considered: radial and rectilinear. The velocity profile is uniform for rectilinear displacement while it decreases with radial distance for radial flow. This fundamental difference in the velocity profile for the flow geometries affects the overall flow dynamics. For rectilinear displacements, Tan and Homsy [103] introduced a numerical methodology to conduct non-linear simulations (NLS) and gain insights into the intricacies of non-linear behavior. The numerical approach employs a Fourier spectral method with periodic boundary conditions. In parallel, Chen et al. [17] have performed numerical experiments to understand VF within radial flow configuration. They employ a hybrid scheme hybridized by the pseudospectral method and compact finite difference.

For miscible displacements, the base flow profile includes the advection-diffusion equation, which admits a time-dependent solution. Owing to the unsteady base state profile, the system of linearized perturbed equations becomes non-autonomous. Tan and Homsy [101] have performed a linear stability analysis (LSA) using a quasi-steady-state approach (QSSA) and Initial value problem (IVP) analysis. They observed that QSSA fails to capture the flow dynamics in the initial stages and concluded that an IVP must be approached numerically with random initial conditions at early times. The QSSA approach reduces the initial value problem into an autonomous system by freezing the base state at a specific time and applying modal analysis. In contrast, the IVP approach provides a comprehensive solution to the non-autonomous linearized problem for representative initial conditions. It is reported that QSSA demonstrates poor agreement with both IVP and nonlinear simulations. While the IVP approach offers superior predictions of early-time behavior compared to QSSA, it is not without its challenges. However, selecting random initial conditions does not guarantee optimal perturbation growth, and determining perturbation growth from IVP analysis remains a contentious issue. Furthermore, these random initial conditions are intended to be localized within the diffusive layer. However, it perturbs the entire computational domain. In an effort to address the limitations of LSA as carried out by Tan and Homsy [101], Ben et al. [5] performed a spectral analysis method without QSSA within a self-similar coordinate system. The base state remains steady in self-similar coordinates. Kim and Choi [52] adopted an eigenanalysis approach in a self-similar coordinate system to eliminate the transient nature of the base state for a non-monotonic viscosity profile. Although the linearized operator retains its time-dependent character. Subsequently, acknowledging the non-autonomous nature of the linear stability matrix, Hota et al. [39] adopted a non-modal analysis based on a propagator matrix approach within a self-similar domain. This innovative approach enables a more precise exploration of time-evolving modes and their spatial characteristics compared to the QSSA or other eigenanalysis methods.

On the contrary, for radial displacement, the perturbations exhibit algebraic behavior with time, unlike the exponential growth in the rectilinear displacement [102]. It imposes that the onset of instability in

radial displacement requires a minimum viscosity ratio between the involved fluids. This characteristic distinguishes radial flow from rectilinear flow in terms of stability. Recently, Sharma et al. [93] comprehended the VF for radial flow and explained the transition in the flow stability numerically and empirically. They present a phase plane between Péclet number (Pe) and viscosity ratio (R) classified into stable and unstable zones. Here, Pe shows the ratio of transport due to the advection and due to the diffusion [102]. Further, they introduce the initial radius of the circular region occupied by the displacing fluid, r_0 , a control parameter in their study. For decreasing r_0 , the stable region in the phase plane between Pe and R is contracted but never vanishes. It persists even when the point source is considered [8, 102, 115].

Non-normality of stability matrix:

In order to perform LSA, the approaches can be classified into two groups: modal analysis and non-modal analysis. When we perform modal analysis, the perturbations are assumed to be exponential with time, and hence the initial value problem associated with linearised perturbed equations, reduces into an eigenvalue problem, for instance, QSSA. The flow stability is determined by the least stable eigenmode. However, there are several instances where this approach describes the fate of perturbation only at asymptotic times ($t \rightarrow \infty$). Thus, it fails to capture the short-term behavior of perturbations such as wall-bounded shear flows [88], falling liquid curtains [87], to cite a few. To determine the true fate of infinitesimal perturbations, it is important to analyze the norm of stability matrix exponential containing comprehensive dynamical information without imposing restrictive assumptions. Additionally, one must identify the optimal initial condition that leads to the maximum amplification of its kinetic energy. The optimal amplification, denoted as $G(t)$, of initial energy over a specified time interval for a stability matrix, named \mathbf{A} , can be formulated as [37, 39, 85, 86]:

$$G(t) = \max_{\mathbf{q}_0} \frac{\|\mathbf{q}(t)\|}{\|\mathbf{q}_0\|} = \max_{\mathbf{q}_0} \frac{\|\mathbf{B} \exp(t\mathbf{A}) \mathbf{C} \mathbf{q}_0\|}{\|\mathbf{q}_0\|} = \|\mathbf{B} \exp(t\mathbf{A}) \mathbf{C}\| \quad (1.2)$$

where \mathbf{q}_0 and \mathbf{q} are the set of initial conditions and the corresponding temporal evolution.

Using the eigenvalue decomposition of Φ *i.e.* $\mathbf{A} = \mathbf{V} \mathbf{\Lambda} \mathbf{V}^{-1}$, the optimal amplification can be determined as $G(t) = \|\mathbf{V} \exp(t\mathbf{\Lambda}) \mathbf{V}^{-1}\|$. However, this is only true when \mathbf{V} is a unitary matrix, the least stable eigenvalue (or real part of the largest eigenvalue of \mathbf{A} , $g(t)$), can accurately describe the norm of the matrix exponential for all time. Hence, if the stability matrix contains non-orthogonal eigenvectors, the temporal evolution of $G(t)$ significantly differs from that of $g(t)$. We describe such a matrix as non-normal if it contains a set of non-orthogonal eigenvectors. We can illustrate the influence of non-normality by a simple geometric example as explained by Schmid [86]. Consider an initial condition \mathbf{f} of unit length,

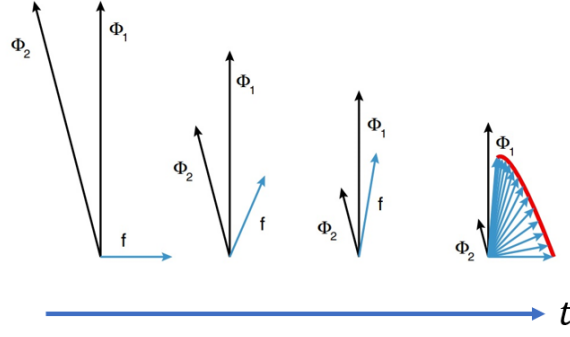


FIGURE 1.5: Vector example of transient growth [86]. Starting on the left, the vector \mathbf{f} is defined as the difference between the nearly collinear vectors ϕ_1 and ϕ_2 .

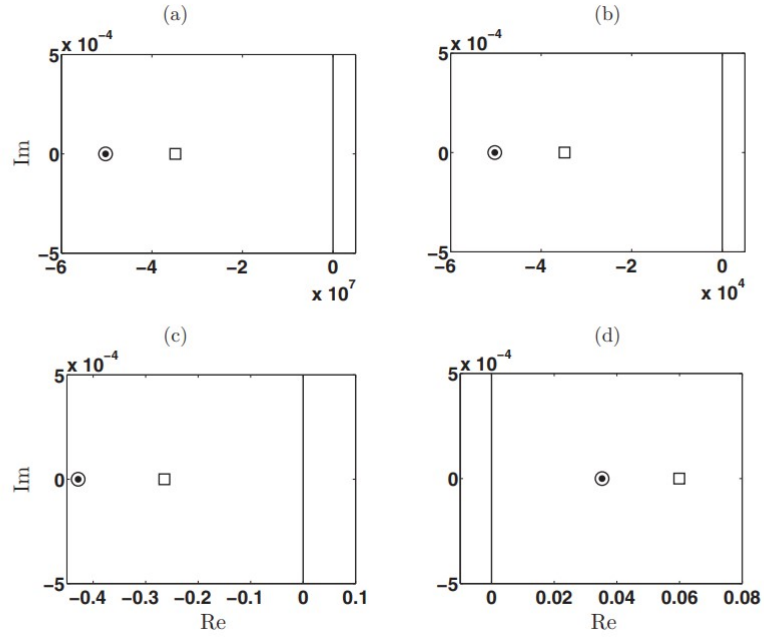


FIGURE 1.6: A comparison of Spectral abscissa (circles) and numerical abscissa (squares) for $R = 3$, at different times (a) $t = 10^{-8}$, (b) $t = 10^{-5}$, (c) $t = 1$, and (d) $t = 10$ to illustrate the presence of non-normality in the stability matrix at early times. The image is taken from Hota et al. [39].

depicted in figure 1.5. Here, ϕ_1 and ϕ_2 represent non-orthogonal eigenvectors. Initially, \mathbf{f} aligns with ϕ_1 as it is the dominant eigenvector. However, it undergoes substantial early-time growth before eventually decaying. Consequently, the combination of these vectors can demonstrate perturbation growth during the initial stages. Now, if ϕ_1 and ϕ_2 were orthogonal, the perturbations would align and decay consistently with ϕ_1 . Therefore, one can infer that the non-orthogonality of eigenvectors significantly influences the short-term amplification of $|\mathbf{f}|$, leading to misrepresentation of flow dynamics while conducting modal analysis. Hence, they only describe the asymptotic fate of \mathbf{f} but may fail to capture its transient behavior.

We can examine the non-normality in several ways, for instance, by computing condition numbers and

comparing spectral abscissa to numerical abscissa. In conducting LSA for equation (1.1), where we perturb the base state and linearize it, we observe that the resulting stability matrix exhibits significant non-normality as shown in 1.6. As a consequence, the modal analysis approaches, for instance, QSSA, lack in predicting the early time dynamics such as diffusion. In our study, we perform LSA for a reactive displacement. It can be examined that non-normality persists in the associated stability matrix. Consequently, we opt for non-modal analysis in our study to gain a more comprehensive understanding of the system's behavior.

1.1.3 Chemo-hydrodynamics instabilities

Chemical reactions have the potential to interact with hydrodynamic flows, giving rise to chemo-hydrodynamic instabilities. Within reactive flows, the resultant products of these chemical reactions can bring about changes in the physical characteristics of the fluids involved, such as viscosity and density. This leads to a complex and nonlinear feedback loop that interconnects the chemical reactions with the corresponding processes of diffusion and convection [22, 51, 63, 111, 116]. Such instabilities play a pivotal role in a multitude of industrial and environmental scenarios, encompassing groundwater flow [24], enhanced oil recovery [47, 68], chromatography separation [16, 91], and CO₂ sequestration [12, 42, 58]. Further, the instability can either be solely induced by the chemical reaction itself or can influence the dynamics of pre-existing fingering patterns. Consequently, gaining a comprehensive understanding of reactive flows is of paramount importance. In most of the numerical investigations, the reactive fluids are assumed to form a product through a second-order irreversible chemical reaction, $A + B \rightarrow C$ [34, 35, 69, 90, 94]. Such types of bimolecular chemical reactions serve as a foundational building block for a wide range of complex chemical processes. Therefore, a firm grasp of this fundamental reaction can offer valuable insights into understanding more complex chemical reactions.

The dynamics of reactive displacement can be harnessed for optimizing mixing, as the chemical reaction may finely tune the location and magnitude of instability. Experimental [70, 71, 72, 83] and theoretical [34, 35, 69, 90] investigations into reactive VF have revealed that the presence of reactive fluids intensifies VF dynamics when compared to non-reactive displacements. At first, Podgorski et al. [78] experimentally showcase chemically induced instability, wherein the reaction results in the formation of a more viscous and elastic micellar product upon contact between two reactants with equal viscosity. Notably, Nagatsu et al. [71] conducted experiments involving instantaneous neutralization reactions, revealing the emergence of shielding effects when the reaction produces a less viscous product than reactants. Conversely, the generation of a high viscous product suppresses the shielding effect. Further, Nagatsu

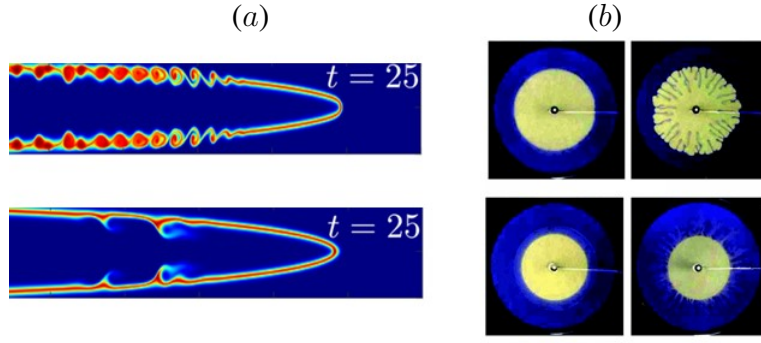


FIGURE 1.7: Reaction-induced instability. (a) Kelvin-Helmholtz instability [63] and (b) Viscous fingering instability [83].

et al. [70] reported experimental findings involving moderately fast reactions, showcasing a diverse array of complex fingering patterns depending on reaction rate.

1.1.4 Convection-diffusion-reaction equations

The reactive transport can be modeled by a convection-diffusion-reaction (CDR) system of equations:

$$\frac{\partial \tilde{\alpha}}{\partial t} + \tilde{\mathbf{u}} \cdot \tilde{\nabla} \tilde{\alpha} = \tilde{D}_\alpha \tilde{\nabla}^2 \tilde{\alpha} \pm f(\tilde{\alpha}) \quad (1.3)$$

In these equations, the variable $\tilde{\alpha}$ represents concentrations of fluid species participating in the chemical reaction, and $\tilde{\mathbf{u}}$ characterizes the velocity field. In these equations, the terms, $\tilde{\mathbf{u}} \cdot \tilde{\nabla} \tilde{\alpha}$, $\tilde{D}_\alpha \tilde{\nabla}^2 \tilde{\alpha}$ and $\pm f(\tilde{\alpha})$ correspond to convection, diffusion and reaction. Here, the reaction depends on the specific nature of the chemical reaction under consideration. To illustrate, in the context of a second-order chemical reaction, such as $A + B \rightarrow C$, the reaction term is proportional to $\tilde{a}\tilde{b}$ within the equation corresponding to the concentrations of reactants, where \tilde{a} and \tilde{b} represent the concentrations of reactants A and B [2]. While for the product concentration profile, the reaction term is proportional to $\tilde{a}\tilde{b}$. In the absence of convection, the equation will be converted into reaction-diffusion equations. For non-reactive situations, the equations are converted into convection-diffusion equations.

1.1.5 Understanding of reactive miscible viscous fingering

To investigate reactive VF, numerous experimental investigations have been conducted within radial flow geometry. In contrast, the theoretical and numerical aspects of the literature predominantly focus on rectilinear flow geometry. In 2009, Gérard and De Wit [31] modeled reactive miscible displacement in

rectilinear flow specifically for types of reactions involving iso-viscous reactants.

$$\tilde{\nabla} \cdot \tilde{\mathbf{u}} = 0, \quad (1.4a)$$

$$\tilde{\nabla} \tilde{p} = -\frac{\tilde{\mu}}{\kappa} \tilde{\mathbf{u}}, \quad (1.4b)$$

$$\frac{\partial \tilde{a}}{\partial \tilde{t}} + \tilde{\mathbf{u}} \cdot \tilde{\nabla} \tilde{a} = \tilde{D}_A \tilde{\nabla}^2 \tilde{a} - \tilde{k} \tilde{a} \tilde{b}, \quad (1.4c)$$

$$\frac{\partial \tilde{b}}{\partial \tilde{t}} + \tilde{\mathbf{u}} \cdot \tilde{\nabla} \tilde{b} = \tilde{D}_B \tilde{\nabla}^2 \tilde{b} - \tilde{k} \tilde{a} \tilde{b}, \quad (1.4d)$$

$$\frac{\partial \tilde{c}}{\partial \tilde{t}} + \tilde{\mathbf{u}} \cdot \tilde{\nabla} \tilde{c} = \tilde{D}_C \tilde{\nabla}^2 \tilde{c} + \tilde{k} \tilde{a} \tilde{b}, \quad (1.4e)$$

$$\tilde{\mu} = \tilde{\mu}_0 e^{(R_c \tilde{c})/\tilde{a}_0}, \quad R_c = \ln \left(\frac{\tilde{\mu}(\tilde{c} = \tilde{a}_0)}{\tilde{\mu}_0} \right). \quad (1.4f)$$

Here, the velocity vector, pressure, and viscosity are denoted by $\tilde{\mathbf{u}} = (\tilde{u}, \tilde{v})$, \tilde{p} , and $\tilde{\mu}$, respectively. Furthermore, the concentrations of the involved fluids, namely A , B , and C , are represented as \tilde{a} , \tilde{b} , and \tilde{c} , respectively and $\tilde{D}_{A,B,C}$ is the diffusion coefficient of fluid A , B , C . Equation (1.4a) corresponds to the continuity equation for mass conservation, equation (1.4b) reflects Darcy's law for momentum conservation, and equations (1.4c)-(1.4e) encompass the reaction-diffusion-convection (RDC) equations governing the averaged mass volume conservation for fluids A , B , and C . In the last equation (1.4f), the viscosity is considered to be dependent on product concentration, and $(\tilde{a}_0, \tilde{\mu}_0)$ are the initial concentration and viscosity of reactants. While conducting non-linear simulations and linear stability analysis, the equations undergo non-dimensionalization. This process introduces two additional non-dimensional parameters, namely the Péclet number (Pe) and the Damköhler number (Da). The definitions of these parameters depend on the specific flow configurations being considered. Here, Da represents the reaction rate. For rectilinear flow, the flow described by the equations (1.4) is numerically solved using a pseudospectral method that incorporates the effects of chemical reactions. They consider the reactive cases when a reaction generates a high viscous product and induces instability upstream of the flow. Later, Hejazi et al. [35] conducted an LSA on a reactive system and employed the quasi-steady state approximation (QSSA) approach. They considered the viscosity profile, accounting for its dependence on both reactants and product concentrations, as expressed by $\tilde{\mu} = \tilde{\mu}_0 e^{(R_c \tilde{c} + R_b \tilde{b})/\tilde{a}_0}$ and presented the stability zones with contour plots of the maximum instantaneous growth rate for various reactions at different times. Here R_b is the log-mobility ratio between reactants as $R_b = \ln(\tilde{\mu}_B/\tilde{\mu}_A)$. Further, Nagatsu and De Wit [69] and Hejazi and Azaiez [34] offered numerical insights into how chemical reactions affect VF while taking into account the same viscosity profile. Using the pseudospectral method, they conduct numerical simulations for reactive flow involving infinitely fast and moderately fast reactions.

Their findings revealed that when the non-reactive situation is unstable, *i.e.* $R_b > 0$, the chemical reaction can have a destabilizing effect on the system when the viscosity of the products differs from that of the reactants, *i.e.* $R_c \neq R_b$. As $|R_c - R_b|$ increases, the onset of VF occurs earlier. Conversely, when $R_b < 0$, the chemical reaction can induce instability if it results in a non-monotonic viscosity profile. Importantly, when $R_b \leq 0$, chemical reactions are able to disrupt the symmetries of convective instabilities and confine fluid motion to localized regions.

Despite the majority of experimental studies being conducted in radial flow geometry, there need to be more numerical and theoretical investigations focusing on this particular flow configuration. This research gap was recently addressed by Sharma et al. [94], who examined reactive flow within radial geometries. They specifically explored scenarios where reactants had iso-viscous properties, and the resulting product exhibited variations in viscosity compared to the reactants. However, it is reported that there exists a critical viscosity contrast to trigger the instability for reactive displacement in radial flow geometry due to spatially decreased velocity profile, unlike in the rectilinear flow domain. Notably, it was observed that the onset of instability occurs earlier when a chemical reaction produces a highly viscous fluid. In conclusion, De Wit [22] has provided a comprehensive account of the chemical reactions influencing these instabilities, with a particular focus on how chemical reactions alter the viscosity of the system and modify the flow dynamics.

1.1.6 VF dynamics due to altered viscosity profile

We non-dimensionalize the concentration of A , B and C , and viscosity, using the initial concentration and viscosity of A , $(\tilde{a}_0, \tilde{\mu}_0)$. The non-dimensionalized concentrations of A , B and C are (a, b, c) respectively and viscosity is μ . In the absence of a chemical reaction *i.e.* $Da = 0$, the viscosity is a monotonic function of space. The system is hydrodynamically unstable for the non-reactive fluids for $R_b > 0$ while a stable displacement is observed for $R_b < 0$. The generation of the product due to a chemical reaction modifies the viscosity profile, thereby affecting the VF dynamics. A (R_b, R_c) phase plane is presented in figure 1.8 showing various types of viscosity profiles depending on the various values of R_b and R_c . When product viscosity is the same as reactant B *i.e.* $R_b = R_c$, the viscosity profile becomes $\mu = e^{R_b(b+c)}$. Here $(b + c)$ follows the convection-diffusion as followed by reactant B when $Da = 0$ and hence the consumed amount of the reactant B in the reaction is equated by the product C in the expression $(b + c)$. Consequently, the system retains its inherent monotonic viscosity profile for $R_c = R_b$ demonstrated by the system if fluids A and B are considered to be non-reactive. We use this information to compare the VF dynamics for $R_c \neq R_b$ to this case $R_b = R_c$. Further, due to the presence of three miscible fluids A , B , and C , two mixing zones appear when C produces. These are identified as the upstream mixing

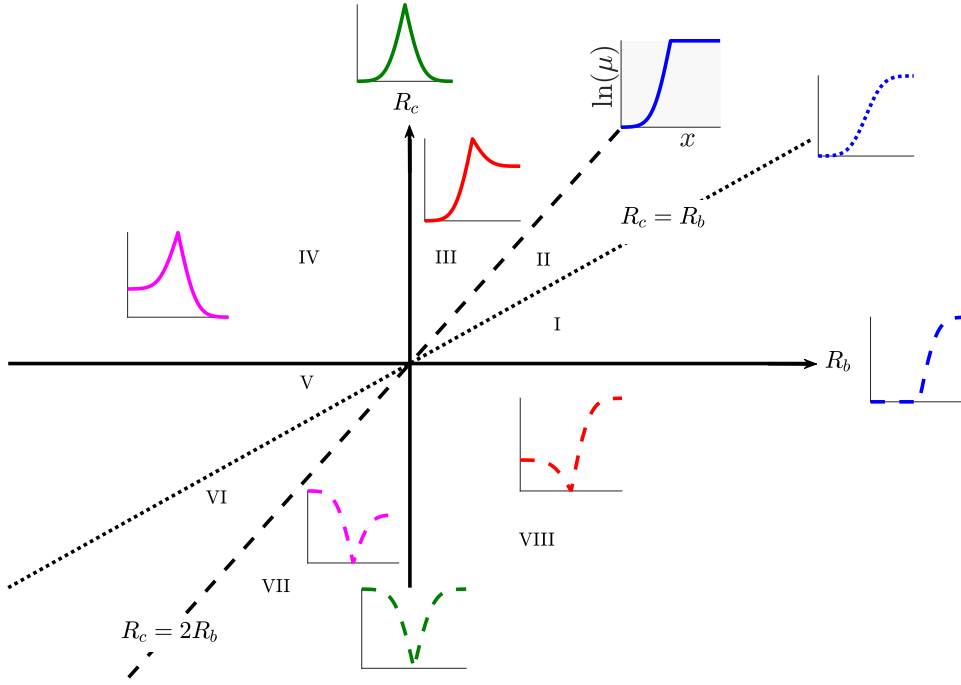


FIGURE 1.8: (R_b, R_c) Phase plane. The inset figures are viscosity depending on the value of (R_b, R_c) , i.e. $\ln(\mu) = R_b b + R_c c$. This figure is a reproduction of figure 3 from Hejazi et al. [35].

zone, primarily occupied by fluids A and C , and the downstream mixing zone, mostly occupied by fluids B and C . The viscosity profile can be distinguished at these two zones for $R_b \neq R_c$. The viscosity profile at these two zones decides the fate of the stability of the system. Since it is assumed that all fluids have the same diffusion coefficient, and the initial concentration of both reactants is identical. Under this assumption, $(a + b + 2c)$ follows the convection-diffusion equation with the initial condition as $(a + b + 2c)(x, t = 0) = 1$ and attains only one solution as $(a + b + 2c) = 1$ [35, 69]. (See appendix B.) To analyze the viscosity distribution along the direction of the flow, we take the gradient of the viscosity profile along x -direction using the relation $a + b + 2c = 1$ as referenced in [35] as:

$$\frac{\partial \mu}{\partial x} = \mu \left[\frac{R_c}{2} \left(-\frac{\partial a}{\partial x} \right) + \left(R_b - \frac{R_c}{2} \right) \frac{\partial b}{\partial x} \right]. \quad (1.5)$$

Both $-\partial a / \partial x$ and $\partial b / \partial x$ are positive in x -direction, and the viscosity profile solely depends on the sign of R_c and $R_b - R_c/2$. The viscosity profile can be categorized mainly into two parts, monotonic or non-monotonic viscosity profile, depending on the value of R_c and $R_b - R_c/2$.

The viscosity profile remains monotonic when $R_c(R_b - R_c/2) > 0$. In the (R_b, R_c) parameter plane (figure 1.8), the region $R_c(R_b - R_c/2) > 0$ comprises two sub-regions and their confined boundary can be defined as below. First, when the product is high viscous, then reactant B i.e. $R_c \geq R_b$, but

$R_c \leq 2R_b$ (region II), the viscosity profile becomes steeper at the upstream mixing zone. The confined boundaries for this region are $R_c = R_b$ and $R_c = 2R_b$. The viscosity profile remains unaffected by the reaction for $R_b = R_c$. While, for $R_c = 2R_b$, the downstream mixing zone stabilizes neutrally, so instability is more prone to appear at the upstream mixing zone. Secondly, when the product is more viscous than reactant A , $R_c \geq 0$ but $R_c \leq R_b$ (region I), the steeper viscosity contrast shifts towards the downstream mixing zone. Here, instability is more likely to occur in the downstream mixing zone. These two regions are separated by the line $R_b = R_c$ in (R_b, R_c) phase plane. In the case of $R_b < 0$, both the regions are re-defined as $R_c \leq 0$ and $2R_b \leq R_c$ (region V and VI) shows a decreasing viscosity profile, that is, the only unconditionally stable region presents in (R_b, R_c) parameter plane. The viscosity profile becomes non-monotonic with an extremum when $R_c(R_b - R_c/2) < 0$ and one of the zones will be destabilized. When $R_c > 0$ and $R_c > 2R_b$, the viscosity profile attains a maximum, and instability is expected to appear at the upstream mixing zone. On the other hand, when $R_c < 0$ and $R_c < 2R_b$, an unfavorable viscosity gradient occurs at the downstream mixing zone with a local minimum. Our investigation comprehensively explores these cases across both radial and rectilinear flow geometries.

1.2 Motivation and objectives

Motivated by the extensive applications of reactive viscous fingering, we aim to gain insight into the interaction of a reactive miscible interface with a chemical reaction $A + B \rightarrow C$ and VF. Within this context, the thesis sets out to achieve the following objectives:

- *To understand the non-linear interaction between a chemical reaction and hydrodynamics in a porous medium.* We conduct the stability analysis of the reactive system concerning VF in both flow geometries, radial and rectilinear. We examine the influence of flow configuration on stability.
- *To examine the reaction-diffusion-convection equations system in the absence/presence of VF.* We explore how VF can improve mixing and enhance reaction efficiency.
- *Develop an advanced numerical method* for conducting LSA to understand the transient behavior of reactive flow for a rectilinear flow geometry. We address the limitations of the existing theoretical approach and develop the numerical scheme to overcome all the shortcomings in QSSA.
- *Create a numerical approach* for comprehending the dynamics of reactive flows in linear regime with reactions occurring at an infinitely fast rate. For $Da \rightarrow \infty$, we reconstruct the system of governing equations and, hence, the linearized perturbed equations.

1.3 Outline of thesis

The pursuit of the aforementioned goals is organized and elucidated across the following six chapters. The initial chapter encompasses a comprehensive literature review coupled with an exploration of relevant terminologies. Chapters two and three focus on exploring the flow and reaction properties, followed by a stability analysis specific to radial flow. The analysis employs both NLS and LSA methodologies. In chapter four, we investigate the reactive displacements with infinitely fast reactions for radial flow by performing NLS. The final two chapters are dedicated to exploring the impact of chemical reactions on viscous fingering dynamics during rectilinear displacement through linear stability analysis.

Chapter 1 offers a comprehensive overview of viscous fingering instability, in particular, miscible VF. It encompasses an extensive exploration of existing literature, including theoretical, experimental, and numerical studies related to miscible VF. Moreover, it gains insight into the profound influence of chemical reactions on VF instability and the resulting modifications to the viscosity profile. The chapter briefly reviews pertinent literature concerning the properties of chemical reactions, particularly within the framework of a system governed by CDR equations.

Chapter 2 is divided into two main sections. In the first part, we examine the reaction-advection-diffusion equations for radial flow and investigate the influence of radial geometry on the reaction properties of the chemical reaction, $A + B \rightarrow C$. We compute several properties such as total reaction rate, first moment of reaction rate, and the total amount of product and derive them as a function of Damköhler number (Da) for stable displacement. It is observed that the reaction rate exhibits a non-monotonic behavior over time, influenced by Da . We discuss different temporal scaling relationships for the total product yield. Further, we investigate whether the reaction properties are impacted by the presence of VF for radial flow. We consider the viscosity profile as viscosity depends on reactants and product concentrations exponentially. We model the flow with reaction-convection-diffusion equations coupled with Darcy's law. We conduct a thorough numerical study using a numerical method hybridized by pseudospectral and compact finite difference methods. When the viscosity of the product differs from that of the reactant, B , *i.e.* $R_c \neq R_b$, the chemical reaction modifies the viscosity profile, and hence the VF dynamics. When $R_b > 0$, the flow becomes more unstable in the presence of a chemical reaction when $R_c \neq R_b$. On the contrary, when $R_b < 0$, the flow is stable in the absence of a chemical reaction, the chemical reaction may destabilize the flow. We observe various fingering patterns depending on the value of the governing parameters, R_b , R_c , and Da . Further, we seek to comprehend the effects of VF on reaction characteristics such as reaction rate and total product yield for a wide range of R_c and Da . As the viscosity contrast ($|R_b - R_c|$) increases, the displacement becomes more unstable, resulting in the total reaction rate enhanced

and more amount of product generated. Moreover, we measure the deformation at the interface with the help of interfacial length. It is observed that the onset of instability and degree of fluid mixing depend on the sign of $R_c - R_b$. When $R_b - R_c < 0$, we observe a higher degree of mixing, indicating the role of fingering instability in enhancing fluid mixing than the corresponding case, $R_b - R_c > 0$. Additionally, we identify the presence of diffusion-dominated zones at later times in the case of reactive VF. For higher viscosity ratios, the fingering pattern does not evolve with time and follows a diffusive regime in later stages. We refer to these fingers as frozen fingers. One part of this chapter is published in the *Physics of Fluids* journal.

Chapter 3 provides a comprehensive stability analysis for the reactive displacement, $A + B \rightarrow C$ within radial flow. By performing NLS and LSA, we gain insights into how the altered viscosity profile affects the stability of the system. We demonstrate that the flow becomes more unstable following product generation (after chemical reaction) when the reactants exhibit an unfavorable viscosity contrast triggering instability (R_b), and the product has a viscosity contrast to the reactants. Conversely, when the equivalent non-reactive case is stable, we identify a range of R_c values for which the corresponding reactive displacement is stable. The range of R_c that corresponds to stable displacement, decreases as R_b increases and vanishes at the critical value of R_b triggering instability for non-reactive situations. Further, we investigate how Da influences the critical values of (R_b, R_c) for instability. As Da increases, the flow becomes more unstable for reactive cases if the corresponding non-reactive situation is already unstable. Conversely, if the non-reactive flow counterparts ($Da = 0$) are stable, the stable range of R_c decreases with increasing Da . Further, we validate these results predicted by LSA through NLS and establish a phase plane based on the log-mobility ratios (R_b, R_c) divided by the critical viscosity ratios to trigger instability. Interestingly, we obtain a region in the (R_b, R_c) phase plane in the neighborhood of $R_c = R_b$ line, for which the stability is not modified after the reaction. This phase plane provides a classification of reactive flows, specifically those involving the chemical reaction $A + B \rightarrow C$, based on their viscosity profiles.

Chapter 4 focuses on the investigation of the non-linear interactions between infinitely fast reactions and VF dynamics. Further, we consider the reactants to be iso-viscous and the instability is induced by the reactions if they generate a product having viscosity contrast *i.e.* ($R_b = 0, R_c \neq 0$). Such types of reactions generate a non-monotonic viscosity profile if $R_c \neq 0$. We analyze how this non-monotonicity in the viscosity profile affects the flow dynamics, as it introduces a combined effect of stable and unstable zones. We determine the onset time for various values of R_c and Péclet number (Pe). Using this information, we establish a phase plane between R_c and Pe at a specific time and derive a power law relationship. Additionally, we determine the critical viscosity ratio, R_c required to trigger instability for a

given Pe and fit a power law relationship between the critical viscosity ratio and Pe . These power laws can assist in selecting the appropriate type of chemical reaction to modify viscosity while maintaining a stable or unstable flow, depending on the specific application. Furthermore, we investigate the VF dynamics after the onset of instability, particularly focusing on finger length. For cases with lower viscosity ratios, we observe longer fingers develop when $R_c > 0$ compared to corresponding cases with $R_c < 0$. However, for higher viscosity ratios, the trend is reversed. This chapter is published in the *Journal of Fluid Mechanics*.

In **Chapter 5**, we aim to gain insights into the stability of reactive flow when subjected to VF instability during rectilinear displacement in a linear regime. To accomplish this, we employ a non-modal linear stability analysis (NMA) for a reactive system $A + B \rightarrow C$ with a propagator matrix approach and discuss the limitations of the previously employed approach for LSA, QSSA method. We explore the reactive displacement with the reactions having viscosity mismatched reactants, *i.e.* $R_b \neq 0$. Further, we constrain our analysis in this chapter to infinitely fast reactions only. In the context of such rapid reactions, the mathematical modeling incorporates a scalar parameter, denoted as $z = a + c = 1 - b - c$, which follows the convection-diffusion equation. Furthermore, we derive explicit expressions for fluid concentrations as functions of this parameter z , represented as $(a, b, c) = (f_1, f_2, f_3)(z)$. This modeling approach suggests the existence of a steady base state for the reactive flow and an analytic solution is attainable for base state equations. As the viscosity contrast increases, an early onset occurs and more amplified perturbations when the reaction generates a less viscous product ($R_b < R_b$) than the equivalent non-reactive scenario ($R_c = R_b$). Conversely, when $R_c > R_b$, there exist some reactive cases where onset is delayed compared to the equivalent non-reactive case ($R_c = R_b$), even with a steeper viscosity contrast. However, after onset time, we observe an accelerated growth rate of perturbations, indicating a more unstable displacement than the scenario where $R_c = R_b$. Furthermore, our findings reveal that the onset time delays most when $R_c = 2R_b$ for a given R_b . We also present a comparative analysis between NMA and QSSA, demonstrating that NMA consistently aligns more with the results of nonlinear simulations than QSSA.

Chapter 6 builds upon the discussion initiated in **Chapter 5**. We perform LSA for the type of reactions having iso-viscous reactants and the product has viscosity contrast. We employ a non-modal LSA for a reactive system $A + B \rightarrow C$ with a propagator matrix approach. By examining optimal amplification and growth rate, we focus on the transient behavior of eigenmodes in response to the most unstable initial perturbations. We illustrate that an increase in the viscosity contrast, $|R_c|$, resulting from a chemical reaction, leads to a more unstable system. Further, we observe a weak transient instability for some values of $R_c > 0$ that delays the onset time of instability. We refer to this phenomenon as secondary

instability. We also determined how the flow stability is affected by Da . We found an early onset for increasing Da showing a more unstable displacement. Further, an early onset is obtained for the reactive displacements generating a high viscous product rather than a less viscous product for a given viscosity contrast and each Da including the case when $Da \rightarrow \infty$. These findings diverge from those obtained through the QSSA approach but align well with results derived from NLS. Further, we compare the effect of geometry, we both observe the transient growth for the reactive case with a non-monotonic viscosity profile with maximum. However, we do not observe the secondary instability for radial flow.

Chapter 2

Flow dynamics of a radial miscible $A + B \rightarrow C$ types of reaction front in a porous medium

2.1 Introduction

Chemical reactions are important in a variety of fields *viz.*, petrochemical industry, water decontamination [30], metabolic activity of bio-films [96] and medical industry, to name a few. In most of the numerical studies, the reactive fluids are assumed to generate a product undergoing an irreversible chemical reaction of second order [34, 69, 35, 94, 90]. Employing a chemical reaction of second order means that the reaction rate depends on the concentration of both the reactants *i.e.* reaction rate is proportional to ab where a and b is the concentration of reactant A and B . It means if we increase both of the reactant's concentrations by n times, the reaction rate will be increased by n^2 [2]. A bi-molecular chemical reaction $A + B \rightarrow C$, is a building block for various complex reactions. Hence, knowledge about this basic reaction might help comprehend other chemical reactions. Understanding various characteristics of the chemical reaction is necessary to gain insights into the yield and the outcome of the chemical reaction.

During reactive displacements, the generated product may modify the viscosity profile, resulting in a hydrodynamic instability, termed viscous fingering [22]. The instability occurs when a less viscous fluid displaces a more viscous one in a porous medium resulting in intricate fingering patterns [101]. It controls the efficiency of several applications including soil contamination in groundwater flow [24, 57, 9, 99, 21], enhanced oil recovery [47, 68], chromatography separation [16, 91] and CO₂ sequestration [42, 12, 58]. One advantage of the fingering instability is in mixing when fluids are miscible [44]. An enhanced mixing due to increased fluid-fluid interactions is anticipated in the presence of VF. Further, a reactive displacement can be used as an optimization of mixing due to VF instability as the reaction may tune the location and amplitude of instability. In this chapter¹, we discuss the flow dynamics when reactants have some viscosity contrast for a range of reaction rates. We consider the displacing reactant A

¹The part of this chapter is published in the *Phys. Fluids* [114].

having less viscosity than the displaced reactant B and then investigate how the reaction can modulate the product formation with such a hydro-dynamical unstable interface for radial flow. We ask how the non-monotonicity in the viscosity profile introduced by the reaction affects the fingering instability and how the instability alters the reaction characteristics like the total amount of product, etc.? In this way, we explore how the hydrodynamics affect the reaction kinematics. Further, we explore if the VF dynamics like onset of instability, mixing, etc observed for similar non-monotonic profiles and whether chemical reactions have more or less viscous product than reactants. For radial displacement, the forces due to convection and diffusion are known to compete. The effect of these forces on reactive VF in terms of total reaction rate and degree of mixing is discussed.

This chapter is organized as follows. We describe the mathematical formulations followed by the numerical method in §2.2. We discuss the effect of VF dynamics and various characteristics of the chemical reaction in the presence and absence of the instability in §2.3. At last, we summarise all the results in conclusion §2.4.

2.2 Mathematical formulation

We investigate the transport of the reactive fluids in a homogeneous and isotropic two-dimensional porous medium. We regard the reactants as fluid A and B which are Newtonian, neutrally buoyant, allowing us to ignore the effect of gravity and undergo a second-order, irreversible chemical reaction $A + B \rightarrow C$. Further, the considered flow is incompressible and density remains constant. In order to understand the reactive flow in the porous medium, the governing equations include Darcy's law coupled with the convection-diffusion-reaction equations one for each reactant and product. The non-dimensional set of governing equations is [35, 94]:

$$\nabla \cdot \mathbf{u} = 0, \quad (2.1a)$$

$$\nabla p = -\mu \mathbf{u}, \quad (2.1b)$$

$$\frac{\partial a}{\partial t} + \mathbf{u} \cdot \nabla a = \frac{1}{Pe} \nabla^2 a - Da \, ab, \quad (2.1c)$$

$$\frac{\partial b}{\partial t} + \mathbf{u} \cdot \nabla b = \frac{1}{Pe} \nabla^2 b - Da \, ab, \quad (2.1d)$$

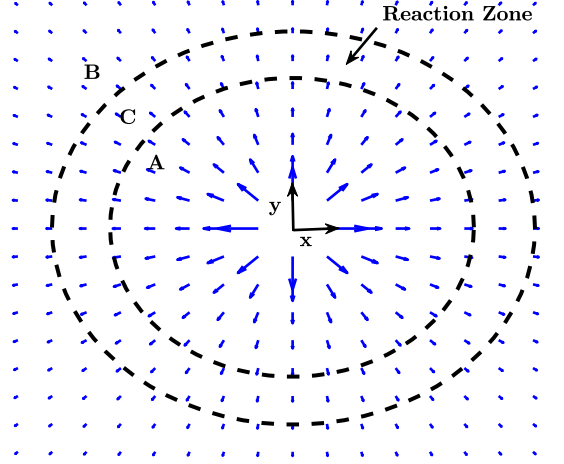


FIGURE 2.1: Schematic of $A + B \rightarrow C$ chemical reaction in a radial source flow. The region inside the inner circle and outside the outer circle is occupied by reactants A and B , respectively. The product C is generated in the annulus region where the reactants come in contact. We denote that region inside the annulus as the reaction front.

$$\frac{\partial c}{\partial t} + \mathbf{u} \cdot \nabla c = \frac{1}{Pe} \nabla^2 c + Da ab. \quad (2.1e)$$

To render the equations non-dimensional, we characterize the time by \tilde{t}_f , the final time up to which we inject fluid A . It is important to note that \tilde{t}_f represents the duration up to which we want to conduct the study. However, determining an appropriate characteristic length scale has been a challenge. For the non-dimensionalization of the spatial vector, $\tilde{\mathbf{x}}$, we can either utilize the permeability $\tilde{\kappa}$, which has units of length^2 , or a function of $\tilde{Q}\tilde{t}_f$ with the same units. Here, \tilde{Q} is volumetric flow rate per unit depth. Previous works by Tan and Homsy [102] utilized $\sqrt{\tilde{\kappa}}$ as a length scale due to the absence of an explicit length scale. In contrast, in our study, we are provided with both \tilde{Q} and \tilde{t}_f , allowing us to define the length scale as $\sqrt{\tilde{Q}\tilde{t}_f}$ [94]. This choice not only addresses the absence of an explicit length scale but also offers practical advantages. Furthermore, it enables us to confine our temporal domain, given that the fingering pattern develops in the diffusive regime in later stages, contingent upon the Péclet number (Pe) [18, 114]. Further, we non-dimensionalize Darcy velocity \mathbf{u} , viscosity μ , pressure p and fluid concentrations (a, b, c) by $\sqrt{\tilde{Q}/\tilde{t}_f}$, $\tilde{\mu}_A$, $\tilde{Q}\tilde{\mu}_A/\tilde{\kappa}$ and \tilde{a}_0 , respectively. The term $R = Da ab$ is a reaction term that works as a source for product concentration and a sink for reactant concentrations.

In addition, we consider the chemical reaction to take place in isothermal conditions. Further,

there exist experimental pieces of evidence with unstable displacement [72, 73, 71, 83] where the viscosity changes with a variation in the concentration of chemical species and the heat release is negligible [72]. The experimental work of Taitelbaum et al. [100], Koo et al. [54] involves stable displacement with no heat release due to reaction. Thus, we do not require an energy equation and the use of a system of convection-diffusion-reaction equation is sufficient to complete the mass balance of chemical species.

In our study, the viscosity is a function of the concentration of the reactants as well as the product. The viscosity-concentration relation is taken as the well-known Arrhenius relation used in various theoretical and numerical studies concerning VF [35, 34, 31, 94]:

$$\mu = \exp(R_b b + R_c c), \quad (2.2)$$

where $R_b = \ln(\mu_B/\mu_A)$ and $R_c = \ln(\mu_C/\mu_A)$ are the log-mobility ratios. The viscosity of the reactant B and the product C are denoted as μ_B and μ_C . In addition to R_b , R_c , we encounter another two non-dimensional parameters Damköhler number (Da) and the Péclet number (Pe). The pace of the chemical reaction is decided by Da which is the ratio of the convective time scale to the reactive time scale, while Pe being the ratio of convective transfer to diffusive transport, helps study the effect of diffusion in the system. The fluid A displaces fluid B radially. We consider a finite source, that is, a circular region of radius r_0 near the source is initially filled with fluid A which is surrounded by fluid B contained outside the circle of radius r_0 . The fluid A is continuously injected up to time \tilde{t}_f . The initial distribution of fluids A , B and C is:

$$(a, b, c)(\mathbf{x}, t = 0) = \begin{cases} (1, 0, 0) & 0 < |\mathbf{x}| < r_0, \\ (0, 1, 0), & \text{Otherwise} \end{cases}. \quad (2.3)$$

The reactants generate the product as soon as they come in contact so that in the absence of any viscosity contrast, the product is contained in an annulus between the reactants as shown in figure 2.1.

2.2.1 Numerical scheme

Owing to the coupling of the governing equations, we sought a numerical solution to the governing equations. A hybrid of compact finite difference and pseudo-spectral method is used

to obtain the numerical solution. We consider the computational domain as a square of side L with the origin at the center. The fluid A is injected from the center with the potential velocity, a characteristic of the radial flow, given as:

$$\mathbf{u}_{pot} = \frac{\mathbf{x}}{2\pi|\mathbf{x}|^2}. \quad (2.4)$$

Further, due to a change in the viscosity owing to the chemical reaction, the velocity is modified at the interface. To capture this, we introduce an additional rotational component in the velocity profile denoted as \mathbf{u}_{rot} so that total velocity becomes $\mathbf{u} = \mathbf{u}_{pot} + \mathbf{u}_{rot}$.

Although \mathbf{u}_{pot} is known at all times, it has a singularity at the origin which must be resolved before using any numerical method. We resolve the singularity by introducing a Gaussian source of core size σ_1 [94, 17] so that the potential component of velocity becomes

$$\mathbf{u}_{pot} = \frac{1 - \exp(-|\mathbf{x}|^2/\sigma_1^2)}{2\pi|\mathbf{x}|^2} \mathbf{x}, \quad (2.5)$$

here $\sigma_1 \leq r_0$ so that the exponential modification does not affect the VF dynamics [113]. On the contrary, \mathbf{u}_{rot} is smooth and must be computed at each time to obtain total velocity \mathbf{u} . We compute the rotational velocity with the help of the stream function as:

$$\mathbf{u}_{rot} = \left(\frac{\partial \psi}{\partial y}, -\frac{\partial \psi}{\partial x} \right). \quad (2.6)$$

Further, we take the curl of equation (2.1b) to obtain the stream function-vorticity formulation,

$$\nabla^2 \psi = -\omega, \quad \omega = R_c \left(v \frac{\partial c}{\partial x} - u \frac{\partial c}{\partial y} \right) + R_b \left(v \frac{\partial b}{\partial x} - u \frac{\partial b}{\partial y} \right). \quad (2.7)$$

The Poisson equation (2.7) is solved by the pseudo-spectral method, where the partial derivatives in the x direction are discretized by the Fourier sine expansion method. And the partial derivative in the y direction by the compact finite difference method of sixth order. We solve the convection-diffusion-reaction equation using the method of lines wherein the initial value problems are solved using the Runge Kutta method of third order with adaptive time steps satisfying Courant–Friedrichs–Lewy (CFL) condition as discussed by Sharma et al. [94].

In the initial condition for the concentration of the reactants, we observe a discontinuity as shown in equation (2.3). To avoid this, we consider the initial condition for a and b which is a

solution of a convection-diffusion equation in the absence of any viscosity contrast as follows:

$$\frac{\partial a_1}{\partial t_1} + \mathbf{u} \cdot \nabla a_1 = \frac{1}{Pe} \nabla^2 a_1, \quad |\mathbf{u}| = \frac{1}{r} \quad (2.8)$$

where $r = |\mathbf{x}|$. The equation (2.8) attains a solution as referenced in Tan and Homsy [102]:

$$a_1 = \frac{\int_0^{\eta_1} \exp\left(-\frac{s^2}{2}\right) s^{Pe-1} ds}{\int_0^\infty \exp\left(-\frac{s^2}{2}\right) s^{Pe-1} ds} \quad (2.9)$$

where $\eta_1 = r(Pe/2t_1)^{1/2}$ is the self-similarity variable. We consider for $a(\mathbf{x}, t = 0) = a_0 = a_1(t_1 = r_0^2/2)$ and $b(\mathbf{x}, t = 0) = 1 - a_0$. Here, Pe is chosen in such a way that it maintains a stable displacement. We add a small perturbation, $0.01 \sin(2\pi N)$ at the points at which $|\mathbf{x}| = r_0$. Here N is the set of random numbers between 0 and 1, and we keep the same set of numbers for all the simulations to confirm the same initial condition. We discuss the order of convergence for the numerical method in chapter 4, section 4.3.1 and convergence study for spatial discretization in appendix A.

2.3 Results and discussion

Chemical reaction results in the generation of the product and the spatially localized region where the product C is non-zero is termed as the reaction zone [22] and is shown in figure 2.1. We refer to a displacement with no viscosity contrast between the reactants and the product, as the stable displacement. Mathematically, a stable displacement is represented as $R_b = R_c = 0$. It indicates no viscosity contrast in the system and Darcy's law becomes decoupled from the reaction-diffusion-convection equations. As a result, the velocity profile remains unperturbed by the fluid concentrations. Hence, the reaction front features only advection-diffusion-reaction equations and does not exhibit instability. On the other hand, an unstable displacement is observed when a less viscous fluid displaces a more viscous one. Various characteristics like the total yield of the product, location of the maximum of product or front position, width of the reaction front, etc. have been of interest to many researchers. Various studies [29, 10, 110] have focused on obtaining various scalings for these characteristics for both radial and rectilinear geometry but by considering stable displacement only. Also, the effect of the rate of chemical

reaction has not been taken into consideration. In this work, we discuss various characteristics for stable displacement for various chemical reactions by varying Da and then see how VF affects these results by considering unstable displacements. An insight into mixing due to the interaction between chemical reaction and instability is gained.

2.3.1 Chemical reaction characteristics

In this section, we consider a stable displacement, that is the reactant A radially displaces reactant B and generates product C on contact. We obtain insights into various characteristics of a second-order chemical reaction $A + B \rightarrow C$. For convenience, we convert the data from Cartesian coordinates (x, y) to polar coordinates (r, θ) as done in Sharma et al. [94].

2.3.1.1 Total reaction rate

The quantity $R(r, \theta, t) = Da a(r, \theta, t)b(r, \theta, t)$ is the reaction rate and is evidently non-zero only when the concentration of both the reactants is non-zero or where both the reactants A and B co-exist. It tells about the generation of the product and is also called the production rate [29]. The total reaction rate, thus, gives information about the consumption of the reactants or the generation of the product with time. We calculate the total reaction rate as [31]

$$R_{tot}(t) = \int_0^{2\pi} \int_{r_0}^L R(r, \theta, t) r dr d\theta. \quad (2.10)$$

At $t = 0$, we initiate a step-like initial condition for the reactants, and initially, no mixing zone exists. However, in the reaction-diffusion-convection system, right after $t = 0$, the reactants diffuse throughout the domain, resulting in the formation of a mixing zone. As a result, the maximum amount of reactants is present in the mixing zone, and thus, R_{tot} is expected to be maximum near $t = 0$. However, it is found that R_{tot} depends on Da as shown in figure 2.2. For sufficiently high Da , R_{tot} is found to be a non-monotonic function of time. It is evident that R_{tot} attains a maximum near the start of the experiment, followed by a minimum and then increases attaining saturation with time. However, the value of the maximum decreases initially with a decrease in Da . This may be attributed to slower consumption of the reactants or equivalently lesser generation of the product for a smaller Da . Interestingly, for $Da = 60$, the maximum is obtained at $t > 0$ despite the fact that the concentration of the reactants is the maximum at $t = 0$.

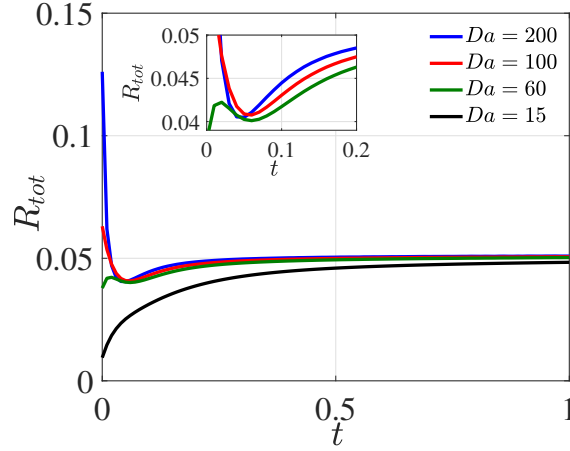


FIGURE 2.2: Total reaction rate for $R_b = R_c = 0$, $Pe = 3000$ and various Da .

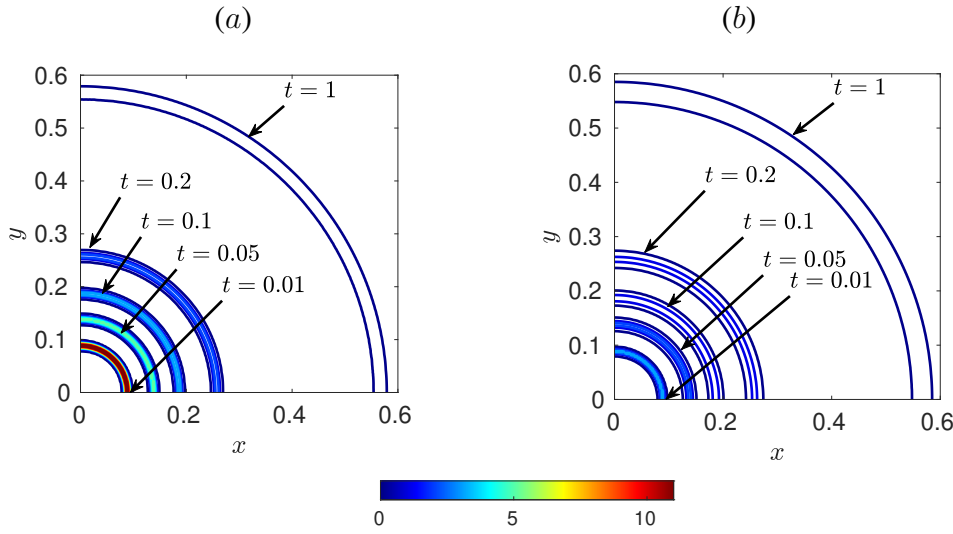


FIGURE 2.3: Contours of the reaction rate $R(x, y, t) = Da a(x, y, t)b(x, y, t)$ for (a) $Da = 100$ and (b) $Da = 15$ at different times.

On the contrary, no maximum is obtained for $Da = 15$ and $R_{tot}(t)$ is a monotonic function of time. This may be a consequence of a slower rate of reaction for these values of Da , resulting in slow consumption of the reactants.

We plot the contours of the reaction rate $R(x, y, t) = Da a(x, y, t)b(x, y, t)$ in figure 2.3 for two values of Da . It is mentioned that we opt to plot $R(x, y, t)$ in order to visualize the radial flow. It is clear that independent of Da , $R(x, y, t)$ is the maximum at initial time and decreases with time due to the consumption of the reactants. With the help of colorbar in figure 2.3, it is easy to compare the reaction rate at the initial time for different Da . Evidently, the reaction rate is much higher initially for higher Da . In other words, the initial reaction rate increases with an increase

in Da . Thus, for a smaller Da , reactants are consumed gradually, and hence $R_{tot}(t)$ increases monotonically. However, with an increase in Da , most of the reactants are consumed at the initial time resulting in a maximum in $R_{tot}(t)$ at the initial time (for $Da \geq 100$) and at some $t > 0$ for intermediate Da like $Da = 60$. Ultimately, with the passage of time, all reactants are consumed resulting in equilibrium, and species are advected radially. However, in the case of stable displacement, we observe a potential flow, which results in a decrease in the force caused by the radial spreading of a front as it moves away from the source. Ultimately, the diffusion dominates, and saturation in $R_{tot}(t)$ is obtained independent of Da .

The minimum $R_{tot}(t)$ for higher Da is reported for radial displacement for the first time in this work. In the case of radial displacement, we need to consider both the forces due to diffusion and radial spreading affecting the reaction characteristics. The initial decrease is caused by diffusion while the increase after the minimum in R_{tot} can be attributed to advection due to potential velocity.

2.3.1.2 Total amount of product

The total yield of the product is the most important characteristic of the chemical reaction. As such, many studies have been conducted to understand the effect of the geometry and other parameters on the total amount of product. Recently, Brau & De Witt [10] compared the yield of the product in both rectilinear and radial geometry in the absence of any instability. It is found that under given conditions, the radial flow generates more product per unit area of contact than the rectilinear displacement. For a stable rectilinear displacement, the yield of the product increases as $t^{1/2}$ that is proportional to the diffusive growth of the reaction zone [34, 10, 110]. In rectilinear flow, a stable displacement exhibits a reaction-diffusion system within the reaction front. While the reaction front is characterized by an advection-diffusion-reaction system in case of radial flow [10]. Further, Comolli et al. [19] compared the yield of the product during early and long time. It is reported that the yield of the product grows with time as $\propto t^2$ at early time [19] and $\propto t$ at a long time [11, 10]. The yield of the product for varying Da is not studied in the majority of the literature until recently Sharma et al. [92]. has reported the dependence of the total amount of product on Da . However, the variation of total yield in different time regimes for different Da is not reported. We gain insight into the same by calculating the total

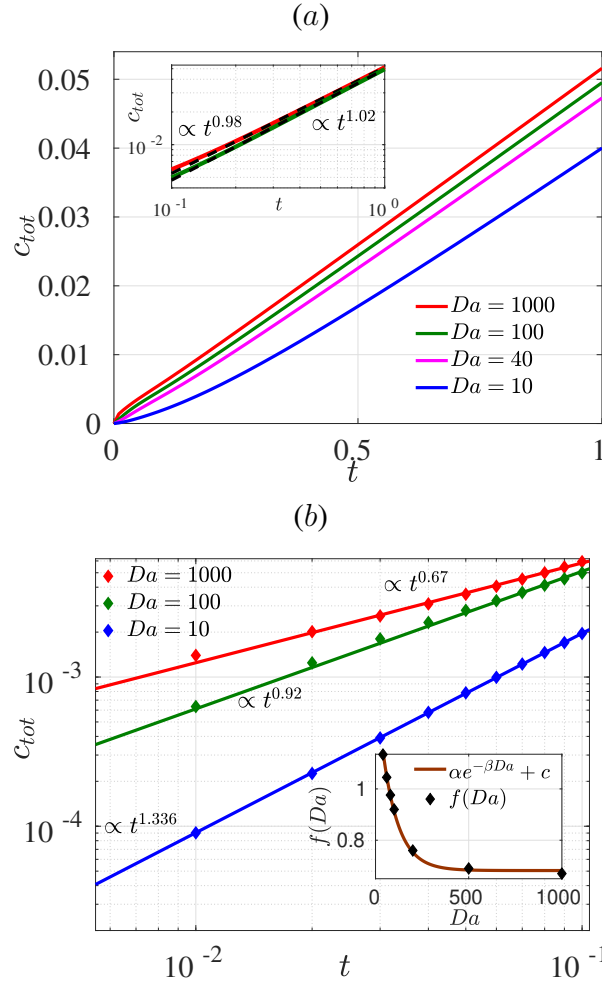


FIGURE 2.4: (a) Total amount of product c_{tot} for stable displacement and various Da . Inset: Log-log plot of the same at later times. Here dotted lines are fitted lines. (b) Log-log plot of c_{tot} at early times. The solid curves are fitted and markers represent the original data. All the curves follow the power law relation $c_{tot} \propto t^{f(Da)}$. Inset: Da vs $f(Da)$.

amount of the product as

$$c_{tot}(t) = \int_0^{2\pi} \int_{r_0}^L c(r, \theta, t) r dr d\theta. \quad (2.11)$$

For a stable displacement, c_{tot} is plotted as a function of time in figure 2.4(a). It is found that at early times, $c_{tot} \propto t^{f(Da)}$ (see figure 2.4(b)), where $f(Da) = \alpha e^{-Da\beta} + \alpha_0$ is a fitted exponential function. Here $\alpha e^{-Da\beta}$ is a decreasing function of Da and the added coefficient α_0 shows that the exponent $f(Da)$ does not vanish for large values of Da . If we consider the product formation at later times, the temporal evolution of product yield follows a different trend as $\propto t^b$, where $b \sim 1$ for $Da \geq 100$ as shown in figure 2.4(a), while $b > 1$ for smaller Da which is in agreement with the base state analysis of Sharma et al. [92].

2.3.1.3 Reaction rate and center of reaction front

We calculate the average of the reaction rate along θ direction as

$$\langle R \rangle(r, t) = \frac{1}{2\pi} \int_0^{2\pi} R(r, \theta, t) d\theta, \quad (2.12)$$

and plot the same in figure 2.5. For a stable displacement, the averaged reaction rate follows

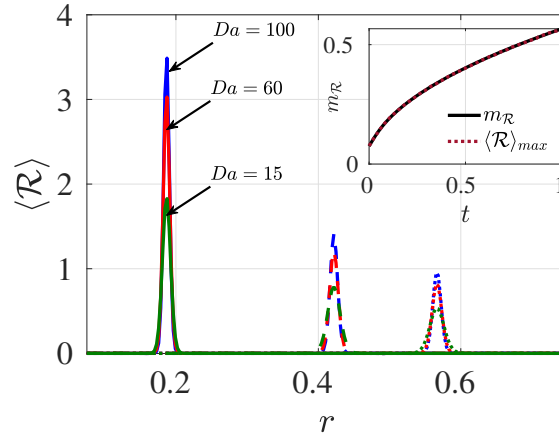


FIGURE 2.5: Temporal evolution of average reaction rate for $Da = 15, 60, 100$ and stable displacement. Inset: The first moment of the average reaction rate coincides with the center of front at all times for stable displacement. Here, $Da = 100$. Here, solid, dashed and dotted lines denotes the averaged reaction rate at time $t = 0.1, 0.55, 1$, respectively.

a bell-shaped profile with the width increasing with time owing to the diffusion of the species. Further, the maximum value of $\langle R \rangle(r, t)$ decreases with time due to the consumption of the reactants. It is evident in figure 2.5 that the width, as well as the maximum of $\langle R \rangle(r, t)$, depends on Da with the maximum being more for the larger Da .

At any time, the spatial position where the averaged reaction rate is the maximum is termed as the center of the front. The center of front is calculated mathematically by taking maximum of the averaged reaction rate which is denoted as $\langle R \rangle_{max}(r, t)$. Further, the average reaction rate profile is symmetrical along the center of the front for stable displacement. Further, it is known that for symmetric distribution of concentration profile, the center of the front coincides with the first moment m_R , of $\langle R \rangle(r, t)$ as in the inset of figure 2.5. The m_R is computed as

$$m_R = \frac{\int_{r_0}^L r \langle R \rangle(r, t) dr}{\int_{r_0}^L \langle R \rangle(r, t) dr}. \quad (2.13)$$

2.3.2 Interaction of chemical reaction and VF dynamics

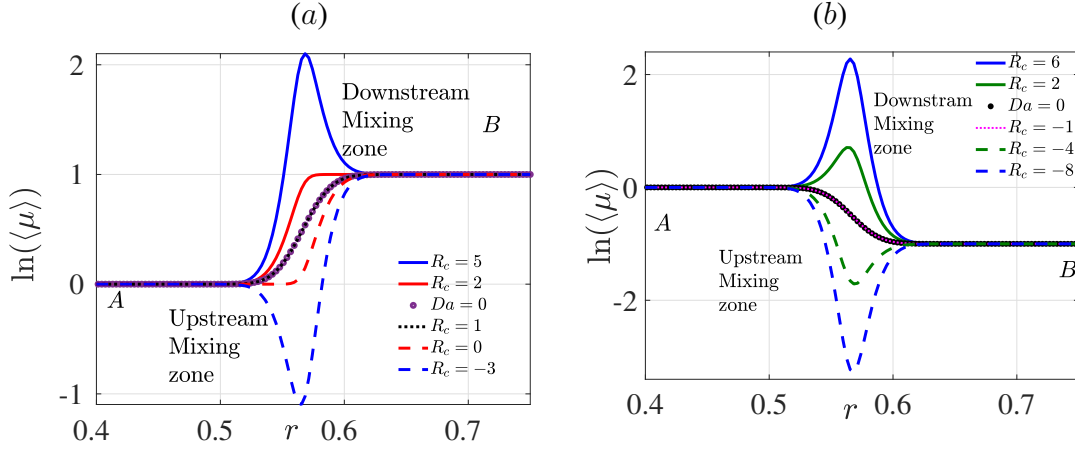


FIGURE 2.6: Log-viscosity profile for $Da = 100$, $Pe = 3000$, (a) $R_b = 1$ and (b) $R_b = -1$ and various R_c . No product is generated for $Da = 0$, and hence the value of R_c is insignificant when $Da = 0$. Also, the value of Da is irrelevant when $R_b = R_c$ and thus the viscosity profile is the same as that of the non-reactive case.

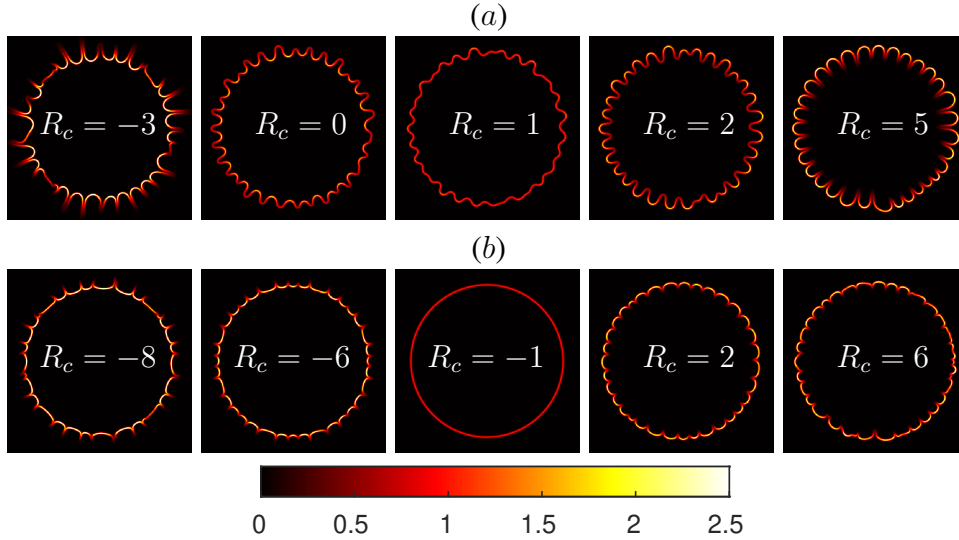


FIGURE 2.7: Density plots of the reaction rate for $Pe = 3000$, $Da = 100$, (a) $R_b = 1$ and (b) $R_b = -1$ and various R_c at $t = 1$. The R_c values in each row are chosen in order to have constant $|R_b - R_c|$ value. For instance, $R_c = -3, 5$ correspond to $|R_b - R_c| = 4$. Similarly, $R_c = 0, 2$ result in $|R_b - R_c| = 1$, while $|R_b - R_c| = 0$ for $R_c = 1$.

For $Da = 0$, the governing equations represent the dynamics of non-reactive fluids. In order to understand the effect of VF on chemical reactions and vice versa, we must be able to compare the dynamics for the same $Da \neq 0$. To tackle this problem, we compute the averaged viscosity as $\langle \mu \rangle(r, t) = \frac{1}{2\pi} \int_0^{2\pi} \mu(r, \theta, t) d\theta$, where $\mu(r, \theta, t)$ is the viscosity at time t converted to polar coordinates [94] and plot its natural logarithm versus distance from the origin in figure 2.6. In

the absence of a chemical reaction *i.e.* $Da = 0$, the viscosity is a monotonic function of space as shown by the averaged viscosity profiles for $R_b = 1, -1$ in figure 2.6.

Evidently, viscosity is an increasing function of space for $R_b > 0$ and $Da = 0$. Thus, for the non-reactive fluids, the system is hydrodynamically unstable (stable) for $R_b > 0$ ($R_b < 0$). The generation of the product due to a chemical reaction may modify the viscosity profile depending upon the viscosity of the newly formed product which is measured in terms of the non-dimensional parameter R_c . Clearly, the viscosity profile changes with a change in R_c in figure 2.6 and it either gets steeper or becomes non-monotonic exhibiting a maximum or minimum according to the product is more or less viscous than the reactants. However, the viscosity profile notably remains the same as that of the non-reactive case for $R_b = R_c$ [69]. Further, it can be observed that for a fixed R_b , the viscosity profiles for two values of R_c corresponding to the same $|R_b - R_c|$ are mirror images about the line $\ln(\langle\mu\rangle) = R_b/2$. Consequently, we discuss how the VF dynamics and its effect on chemical reactions are different for these values of R_b and R_c for various Da . Also, we investigate if the spatially varying velocity of the radial geometry affects the reaction properties and whether reaction properties differ from that of the rectilinear flow with uniform velocity.

We plot the reaction rate $R(x, y, t)$ in figure 2.7 for various parameters shown in figure 2.6. As clear from the definition of the reaction rate, it is non-zero where both the reactants are non-zero. It is evident in figure 2.7 that the reaction rate is non-zero in the finger-like patterns. This is due to the unstable displacement corresponding to $R_b \neq 0$ resulting in VF instability. The VF dynamics for the radial displacement for a wide range of (R_b, R_c) , $R_b \neq 0$ covering all the predicted viscosity profiles for $Da = 100$ and $Pe = 3000$ are discussed in the next subsections §2.3.2.1 and §2.3.2.2.

2.3.2.1 VF dynamics for $R_b > 0$

For a fixed $R_b > 0$, we choose R_c in order to explore the reactive case with monotonic as well as non-monotonic viscosity profiles and compare it with the corresponding non-reactive case. The sign of $R_c(R_b - R_c/2)$ decides the monotonicity of the viscosity profile [35]. We first discuss the cases when the viscosity profile remains monotonic even after the reaction. This happens when $R_c(R_b - R_c/2) \geq 0$ [35]. In figure 2.8, the product concentration profiles are presented for $R_b = 1$ and various R_c . The system is unstable for both non-reactive situations

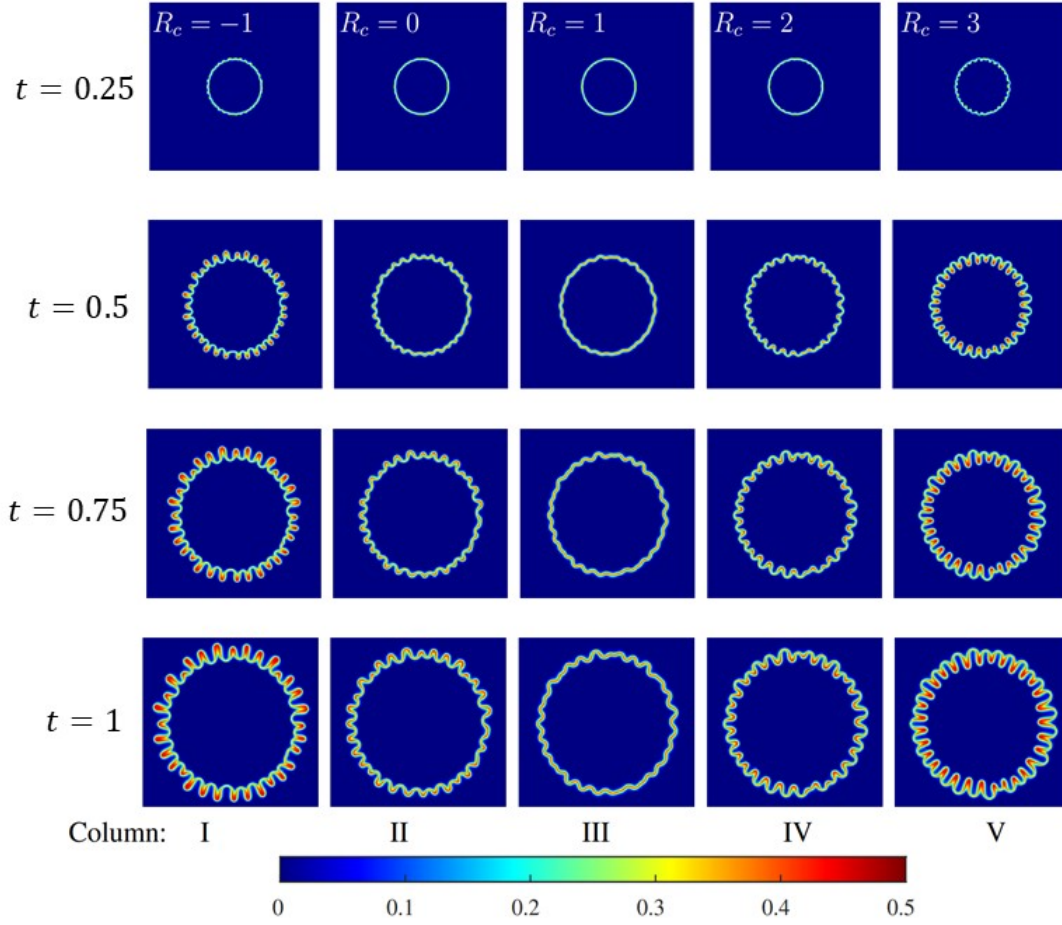


FIGURE 2.8: Product concentration profile for $Pe = 3000$, $Da = 100$, $R_b = 1$ and various R_c at different times.

and reactive situations when $R_b = R_c = 1$ as slight deformation is observed for $R_c = 1$ at any time. Clearly, $R_c(R_b - R_c/2) = 0$ for $R_b = 1$, $R_c = 0, 2$ and thus the viscosity is a monotonic increasing function of space for which $|R_b - R_c|$ is a constant. However, the fingering dynamics are different for the two values of R_c as shown in columns II and IV of figure 2.8 and is attributed to the steepness of the viscosity profile at downstream and upstream mixing zone, respectively (See figure 2.6). Notably, the product is more concentrated in the direction of flow for $R_c = 0$, and towards the origin for $R_c = 2$. We refer to fingers so obtained for $R_c = 0, 2$ as outward and inward fingers, respectively.

In general, when the product is more viscous than reactant B i.e. $R_c > R_b$ but $R_c \leq 2R_b$, the viscosity profile becomes steeper at the upstream mixing zone, resulting in inward fingers. On the other hand, when the product is less viscous than reactant B , but could have a higher viscosity than A , i.e. $0 \leq R_c < R_b$, a steeper viscosity contrast occurs at the downstream mixing

zone. In this case, the instability favors more in the downstream mixing zone, while the upstream mixing zone stabilizes viscously resulting in outward fingers. Thus, the sign of $R_b - R_c$ helps to classify the fingers as inward or outward fingers. Further, some little bumps at the upstream mixing zone are visible in the first row of figure 2.8 for $R_c = 2$ at time $t = 0.15$ while at the same time, the flow is stable for $R_c = 1, 0$. Thus, the onset time, when the interface starts to deform, occurs early for $R_c = 2$ than $R_c = 1, 0$ despite the similar monotonic viscosity contrast. Stronger convection at the steeper upstream mixing zone results in early onset for $R_c = 2$.

The non-monotonic viscosity profile is of particular interest as it introduces conflicting stability behavior due to the two zones where one is viscously stable and the other is predicted to be unstable. The viscosity profile becomes non-monotonic with an extremum when $R_c(R_b - R_c/2) < 0$. When the reaction produces a high viscous product than both of the reactants, *i.e.* $R_c > 0$ & $R_c > 2R_b$ so that $R_b - R_c < 0$, the viscosity profile attains a maximum. It shifts the fingering instability only at the unstable zone, the upstream mixing zone, while the stable downstream mixing zone resists the growth of fingering instability. The resultant fingering patterns grow more upstream to the flow resulting in inward fingers as shown in figure 2.8 (column V) for $R_c = 3$. On the other hand, when the product is less viscous than reactant A, *i.e.* $R_c < 0$ and thus $R_b - R_c > 0$, an unfavorable viscosity gradient occurs at the downstream mixing zone with local minimum as in figure 2.6(a) for $R_c = -1$. The instability develops predominantly in the downstream mixing zone, and the upstream mixing zone acts as a barrier, which hinders the growth of fingers and outward fingers are obtained as shown in figure 2.8 (column I) for $R_c = -1$.

If we increase the viscosity gradient further, the system gets more unstable and the onset of instability occurs early. To illustrate how this non-monotonic viscosity distribution affects the fingering pattern, we choose another suitable pair of (R_b, R_c) for increased viscosity ratio. In figure 2.9, we show the temporal evolution of the product concentration profile for $R_b = 1$ and $R_c = 5, -3$. For $R_c = -3$, fingers grow up to boundary in time $t = 0.97$, hence concentration plots are shown only up to time $t = 0.97$. If we see the concentration profile for $R_c = 5$, it can be observed that more fingers are generated in the upstream mixing zone in comparison to $R_c = 3$. Also, we observe the total number of fingers generated at the initial time, and at a later time, they grow only upstream to the flow with time. No new fingers generate after $t = 0.25$ as we can see the temporal evolution of $R_c = 3$ and 5 in figure 2.8(fifth column) and 2.9(a). When

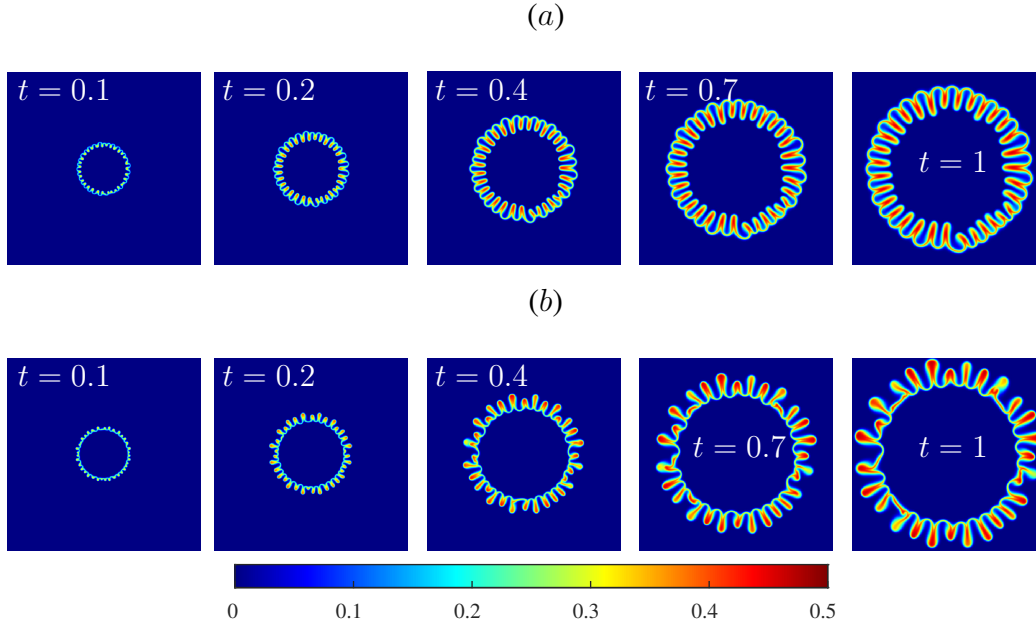


FIGURE 2.9: Product concentration profile for $Pe = 3000$, $Da = 100$, $R_b = 1$ and (a) $R_c = 5$ and (b) $R_c = -3$. It can be observed that no new fingers are generated after $t = 0.1$ for both the parameters $R_c = 5, -3$. Also, the developed fingers experience the shielding and merging effect as the number of fingers decreases and some of the fingers are merged after time $t = 0.2$ for $R_c = -3$.

we decrease the product viscosity from $R_c = -1$ to $R_c = -3$, we see a significant difference in the development of fingers. If we count the number of fingers, it can be observed that the number of fingers increases with time for $R_c = -1$. While for $R_c = -3$, it can be observed that some fingers are not growing with time as compared to neighboring fingers at time $t = 0.4$ showing shielding of fingers for $R_c = -3$. At a later time, it can be the shielded fingers merged with the neighboring fingers at time $t = 0.97$. Evidently, outward fingers exhibit a shielding effect for higher viscosity ratios such as $R_c = -3$.

Another comparison can be made for the same unfavorable viscosity jump. The viscosity gradient is shown by $|R_b - R_c| = |\ln(\mu_B/\mu_C)|$ and $|R_c| = |\ln(\mu_C/\mu_A)|$ at downstream or upstream mixing zone, respectively. When the product is less viscous, the shielding effect is observed and fewer fingers are generated for a higher viscosity gradient, $|R_b - R_c|$. Also, fingers are thinner when the product is highly viscous for $|R_b - R_c| = 4$, $R_b = 1$ than a less viscous product. These results are in good agreement with the existing experimental results [71] and theoretical [35], and numerical results [69] qualitatively that are obtained for the rectilinear case.

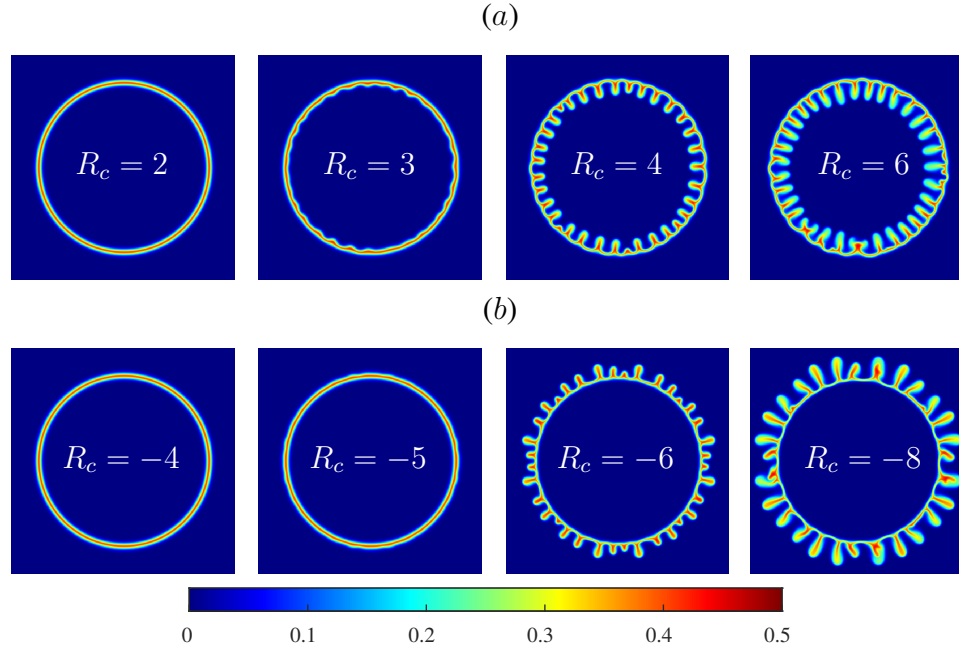


FIGURE 2.10: Product concentration profile for $Pe = 3000$, $Da = 100$, $R_b = -1$ and various (a) $R_c > 0$ and (b) $R_c < 0$ at time $t = 1$.

2.3.2.2 VF dynamics for $R_b < 0$

The non-reactive system is always stable for $R_b < 0$ as high viscous fluid A displaces a less viscous fluid B . However, for $R_b < 0$, independent of Da , R_c the system remains stable for monotonic viscosity profile obtained when $R_c(R_b - R_c/2) \geq 0$. When the product viscosity differs from that of the reactants such as $R_c(R_b - R_c/2) < 0$, the chemical reaction introduces non-monotonicity in the viscosity profile, and the instability is expected either at the downstream or upstream mixing zone. For $R_c = 2, -4$, the viscosity profile is a non-monotonic function of space in figure 2.6(b) for $R_b = -1$. However, the flow is stable as shown in figure 2.10 despite the displacement of a more viscous fluid by a less viscous one at the downstream mixing zone for $R_c = -4$ and the upstream mixing zone for $R_c = 2$. This is due to the radial displacement of the fluids and is not reported in the existing studies involving rectilinear displacement of the fluids. Thus for $R_b < 0$, a minimum viscosity gradient is required in order to induce the instability and observe the effect of chemical reaction on VF, similar to that for $R_b = 0$ [94]. The VF dynamics for the R_c values subject to $|R_b - R_c|$ is the same for $R_b = -1$ are compared in figure 2.10. It can be noticed that there are minor bumps at the upstream mixing zone for $R_c = 3$, but the flow is stable for $R_c = -5$ while the viscosity gradient, $|R_b - R_c|$ is identical in both cases. This is another consequence of radial flow is that the critical viscosity gradient

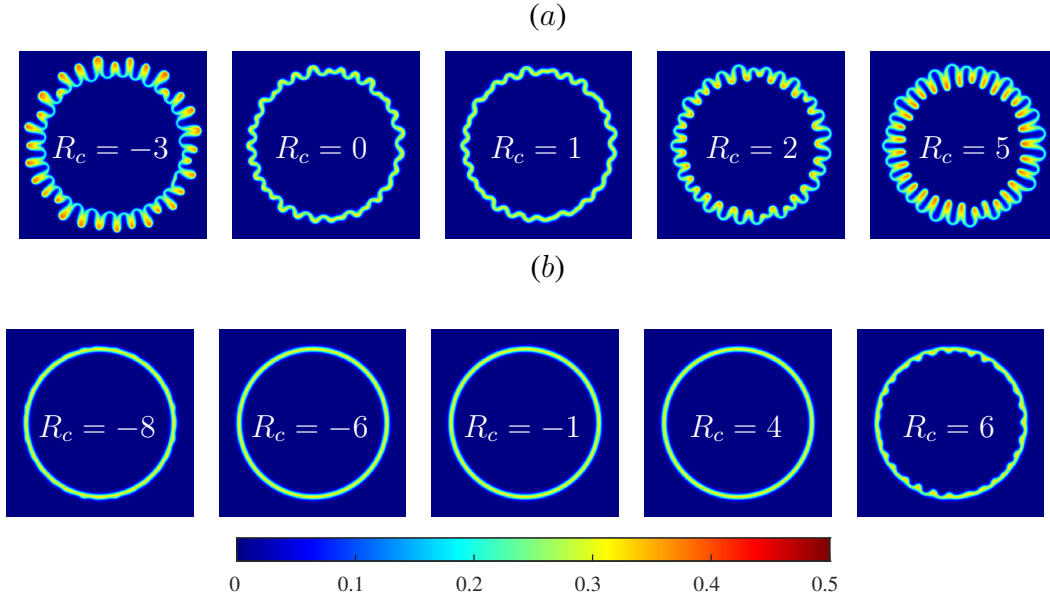


FIGURE 2.11: Product concentration profile for $Pe = 3000$, $Da = 15$, (a) $R_b = 1$, (b) $R_b = -1$ and various R_c at final time $t = 1$.

$|R_b - R_c|$ is more when the reaction produces a less viscous product.

If we further increase the viscosity ratio, fingers elongate more. In the symmetric conditions, with the same viscosity jump $|R_b - R_c|$, more fingers are generated when the instability appears at the upstream mixing zone. Also, the number of fingers increases if we increase the viscosity ratio from $R_c = 4$ to $R_c = 6$. In contrast, the tip of the outward fingers gets wider when they grow downstream to the flow, and fewer fingers develop for $R_c = -8$ than $R_c = -6$.

2.3.2.3 Effect of Da on VF dynamics

If we keep the viscosity ratio the same and vary Da , the VF dynamics are qualitatively the same, but the intensity of the fingering pattern changes as shown in figure 2.11. For higher Da such as $Da = 100$, the reaction time reduces, and a sufficient amount of product is formed in a short time that favors the rigorous fingering instability. However, when the reactants have the viscosity contrast itself, which is sufficient to induce instability in the corresponding non-reactive situation, the reaction affects the intensity of the fingering pattern and onset time for varying Da only. Otherwise, if a system is stable for $Da = 0$, there exists a critical R_c to trigger the instability for a given Da and R_b . In particular, the $R_b = 0$ case is already discussed in Sharma et al. [94]. Evidently, both the parameter Da and R_c are introduced by the reaction and thus, the chemical reaction plays a vital role in the development of fingering dynamics.

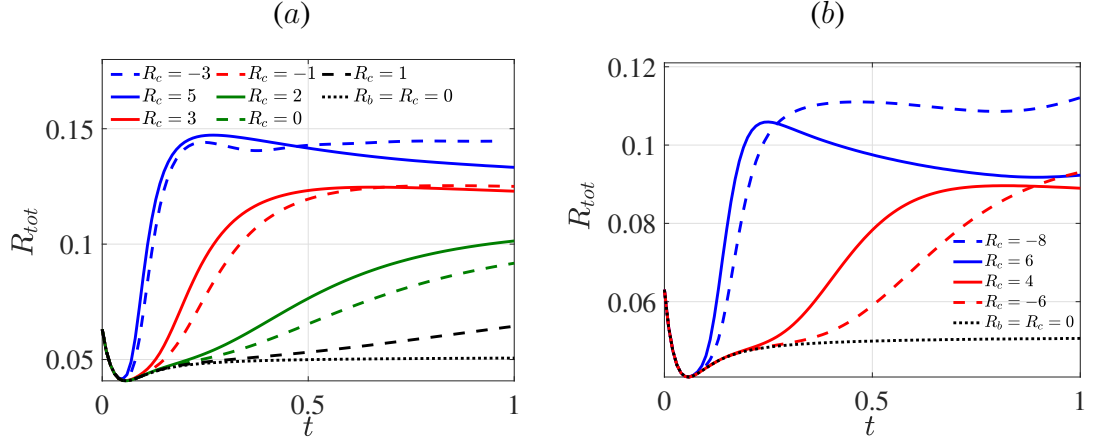
2.3.2.4 Effect of VF on R_{tot} 

FIGURE 2.12: Total reaction rate for $Da = 100$, $Pe = 3000$, (a) $R_b = 1$ and (b) $R_b = -1$ and various R_c . Black dotted curve is for $R_b = R_c = 0$. Here, solid lines are plotted when $R_b - R_c < 0$ that is for $R_c = 5, 3, 2$; $R_b = 1$ ($R_c = 6, 4$; $R_b = -1$) and while dashed lines are plotted for corresponding $R_b - R_c > 0$ that is for $R_c = -3, -1, 0$; $R_b = 1$ ($R_c = -4, -6$; $R_b = -1$).

For the displacement involving reactants having viscosity contrast and/or generating a product having a different viscosity than the reactants, instability may set in. We are interested in exploring how this instability affects R_{tot} . In figure 2.12, R_{tot} for various R_c and $R_b = 1, -1$ is plotted as a function of time for $Da = 100$. The curve for $R_b = R_c = 0$ corresponds to the stable displacement. Evidently, R_{tot} is more for unstable displacement than the stable displacement. Further, the effect of the forces due to convection and diffusion is clearly evident with R_{tot} attaining a local maximum at $t = 0$, then decreasing due to diffusion and ultimately increasing after minimum due to convection. The convection here is due to two factors: the potential velocity and the instability. Therefore, the increase in R_{tot} is more in the convective regime when instability sets in, bringing more reactants in contact. This is further evident from increased mixing for unstable displacement discussed in the next sections §2.3.3. Ultimately diffusion dominates and saturation is attained by R_{tot} depending upon the value of R_c . Up to some initial time, R_{tot} is independent of R_c . The instability starts to emerge at this time and it is termed as the onset time of instability. However, the time when the minimum is obtained and the time after which saturation is obtained depends upon R_c for a fixed R_b and Da . Both these times are early for a larger $|R_b - R_c|$ owing to a stronger instability. If we compare R_{tot} for same $|R_b - R_c|$ value, the total reaction rate is more for $R_b - R_c < 0$. Further, R_{tot} reverses the trend and becomes less for $R_b - R_c < 0$ at later times. This is due to the onset time of instability discussed in detail in next section §2.3.3.

2.3.2.5 VF and total amount of product

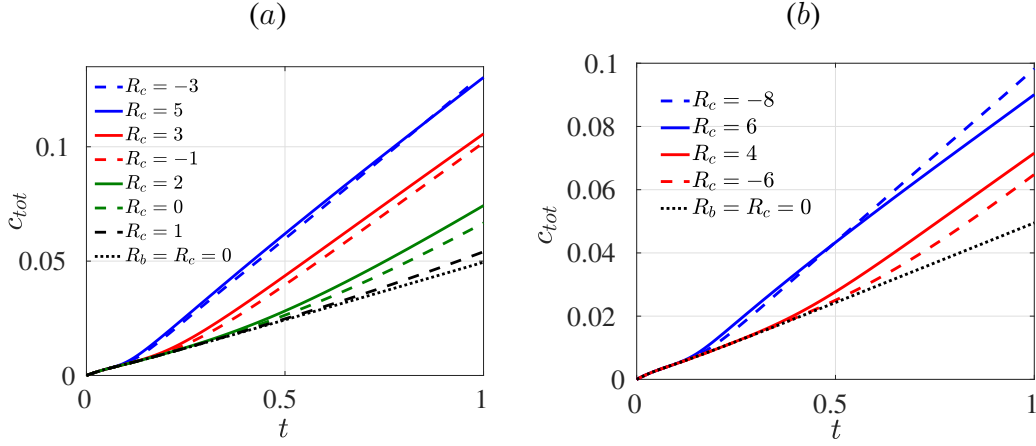


FIGURE 2.13: Total amount of product for $Da = 100$, $Pe = 3000$, (a) $R_b = 1$ and (b) $R_b = -1$ and various R_c .

Now we compare the total amount of product for stable and unstable displacement. The instability for $R_b \neq 0$, $R_c \neq 0$ results in an increased c_{tot} as shown in figure 2.13. The c_{tot} curve for stable displacement and other R_c values coincide up to the onset time of instability, after which the total amount of product increases with time for unstable displacements showing that the VF instability increases the yield of the reaction. Further, c_{tot} depends on R_c and sign of $R_b - R_c$ for a fixed R_b . A larger $|R_b - R_c|$ results in a more rigorous instability and hence larger c_{tot} . For the same value of $|R_b - R_c|$, the dependence of c_{tot} on the sign of $R_b - R_c$ follows a similar trend as that of R_{tot} . More c_{tot} is obtained for $R_b - R_c < 0$, until the onset of instability becomes independent of the sign of $R_b - R_c$ [94]. This is in contrast with the results obtained for rectilinear displacement [69] where the product is generated more when $R_b - R_c > 0$ than that of $R_b - R_c < 0$. Thus, the total amount of product is influenced by the viscous fingering as well as the kind of displacement considered.

2.3.2.6 VF affecting reaction front

As soon as we consider a viscosity contrast between the reactants and the reaction generates a less or more viscous product than the reactants, $\langle R \rangle(r, t)$ deviates from the bell-shaped profile and exhibits a left or right tail depending upon the sign of $R_b - R_c$ as shown in figure 2.14. For $R_b - R_c > 0$, the reaction rate is more towards the origin as evident in the density plots of the reaction rate. Hence, $\langle R \rangle(r, t)$ shifts towards the left of the bell-shaped stable profile. Due to a similar reason, $\langle R \rangle(r, t)$ is shifted towards the right of the bell-shaped stable curve for

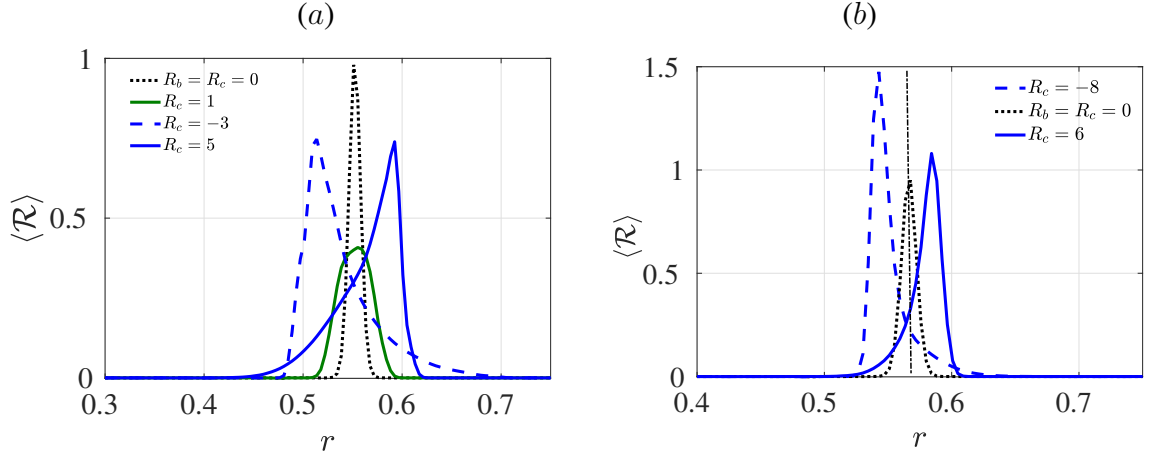


FIGURE 2.14: Averaged reaction rate profile for $Da = 100$, (a) $R_b = 1$, (b) $R_b = -1$ and various R_c at time $t = 0.95$.

$R_b - R_c < 0$ as shown in figure 2.14. Consequently, for $R_b \neq 0, R_c \neq 0$, the first moment of average reaction rate, m_R shifts above or below the first moment for $R_b = R_c = 0$ denoted as m_{R_0} . We plot m_R for $R_b = 1$, $Da = 15$ and various R_c in figure 2.15.

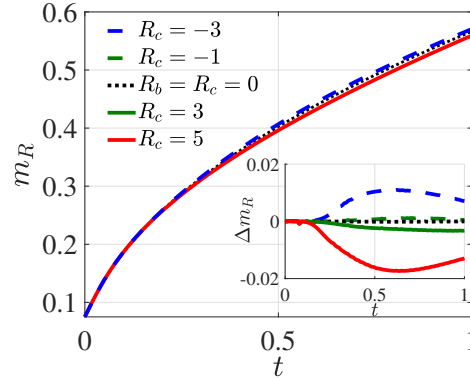


FIGURE 2.15: Temporal evolution of center of mass of averaged reaction rate $\langle R \rangle(r, t)$ for $R_b = 1$, various R_c and $Da = 15$. Inset: Relative difference, Δm_R in first moment of $R_b \neq 0, R_c \neq 0$ and stable displacement $R_b = R_c = 0$.

It is found that the relation between m_{R_0} and m_R depends on Da . In figure 2.15, the first moments are plotted for $Da = 15$ and evidently at all time, m_R lies above (below) m_{R_0} for $R_b - R_c > 0$ (< 0). Thus, the fingering results in the shifting of the reaction front. However, with an increase in Da , a shift in the trend of m_R is observed. For instance, for $Da = 100$, we observe the shifting of the reaction front. For smaller $|R_b - R_c|$, the reaction front shifts in the direction opposite to the fingering (inward or outward) and consequently m_R lies below (above) m_{R_0} for $R_b - R_c > 0$ (< 0) as shown in figure 2.16. Interestingly, the location of m_R depends

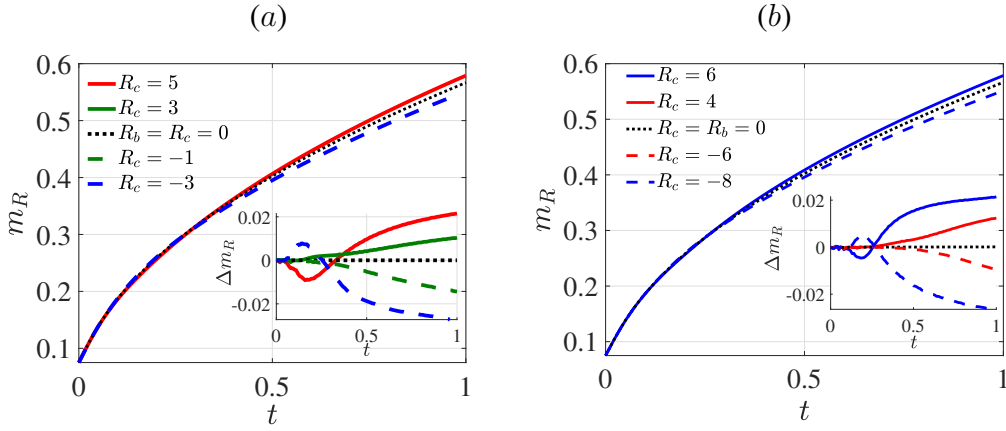


FIGURE 2.16: Temporal evolution of center of mass of averaged reaction rate $\langle R \rangle(r, t)$ for (a) $R_b = 1$, and (b) $R_b = -1$, various R_c and $Da = 100$. Inset: Relative difference, Δm_R in first moment of $R_b \neq 0, R_c \neq 0$ and stable displacement $R_b = R_c = 0$.

on R_c as well. For sufficiently high R_c such that the onset time of instability is independent of the sign of $R_b - R_c$, m_R initially moves in the direction of fingering but then experiences a transition into the opposite direction.

The first moment of the averaged reaction rate tends to move in the direction where more reactants are available. For a smaller Da , the reactants are consumed slowly and thus m_R moves in the direction of the fingers. On the other hand, for larger Da , the reactants are consumed at a faster rate thus less reactants are available in the direction of the fingers. Thus m_R tends to shift in the opposite direction where the concentration of the reactants is more. The transition in the direction of m_R for high R_c can be explained to be a result of convection. The early onset for such high R_c , tends to shift m_R in the direction of fingering but after some time, with the consumption of reactants, m_R reverses direction.

2.3.3 Mixing dynamics

With an aim to analyze how chemical reaction affects the mixing of the species, we compare the mixing of unstable to stable displacement using the degree of mixing of the product concentration [62, 44]

$$\chi_c(t) = \frac{\sigma_c^2(t)}{\sigma_{c,*}^2(t)} - 1, \quad (2.14)$$

where the variance σ_c^2 of the averaged concentration profile of product, is computed as

$$\sigma_c^2(t) = \frac{\int_{r_0}^L (r - m_c)^2 \langle c \rangle(r, t) dr}{\int_{r_0}^L \langle c \rangle(r, t) dr}. \quad (2.15)$$

Further, $\sigma_{c,*}^2(t)$ is the variance corresponding to stable displacement $R_b = R_c = 0$. Evidently, $\chi_c = 0$ for the case $R_b = R_c = 0$ in figure 2.17. Zero value of χ_c is a consequence of the normalization used in equation (2.14) and implies mixing attributed to diffusion in the absence of instability. At early time, all the degree of mixing curves for $R_b \neq 0$, $R_c \neq 0$ coincide with $R_b = R_c = 0$ curve and have value zero. It indicates the presence of an initial diffusion-dominated regime, independent of the value of R_b , R_c . But with time, χ_c becomes positive indicating an increase in the mixing due to instability. Evidently, figure 2.17 illustrates that the system is destabilized more and mixing in the reaction zone is more enhanced when the product has viscosity contrast with reactants ($R_b \neq R_c$).

Further, mixing enhances with increasing viscosity ratio and depends on the sign of $R_b - R_c$.

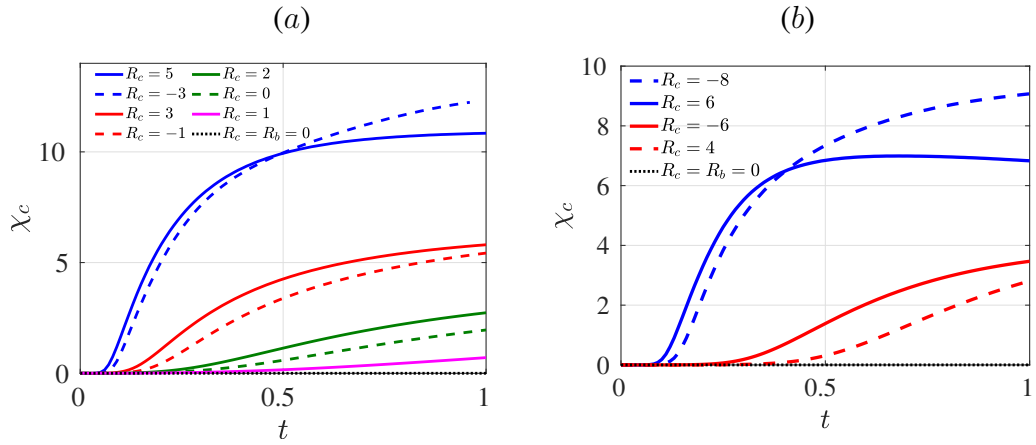


FIGURE 2.17: Degree of mixing for $Da = 100$, (a) $R_b = 1$ and (b) $R_b = -1$ and various R_c . Here the onset of instability can be noted when the degree of mixing exceeds zero *i.e.* $\chi > 0$ as this quantification is a direct comparison of mixing between stable to unstable displacement.

We compare the mixing in the reaction zone for the same viscosity jump or same $|R_b - R_c|$ value in figure 2.17. It can be noticed that the degree of mixing is more when $R_b - R_c < 0$ than that for $R_b - R_c > 0$ and a transition is evident with an increase in $|R_b - R_c|$. This is a consequence of the origin of the instability at one of the two mixing zones (downstream or upstream) and the radial displacement being considered. The potential velocity for the radial displacement is inversely proportional to the distance from the source. As a result, convection is stronger at the upstream mixing zone and hence the instability originates early at the upstream mixing zone.

The onset time of instability (t_{on}) can be defined as the minimum time when $\chi_c(t)$ becomes positive. It can be verified from figure 2.17 that the onset time is early for $R_b - R_c < 0$ when instability appears at the upstream mixing zone. This early onset of instability results in more degree of mixing for $R_b - R_c < 0$. The early onset for $R_b - R_c < 0$ is in contrast with the results with rectilinear displacement [69, 35] wherein the velocity is uniform for the undisturbed flow. If we keep increasing the viscosity ratio further ($|R_b - R_c| \geq 4$, $R_b = 1$ and $|R_b - R_c| \geq 7$, $R_b = -1$) in figure 2.17, the trend changes. For higher viscosity ratio, the onset occurs early and simultaneously; and the degree of mixing enhances more for $R_b - R_c > 0$ than $R_b - R_c < 0$ at later times. This is because the outward fingers for $R_b - R_c > 0$ grow in the direction of flow. Thus, whenever the onset of instability is the same for $|R_b - R_c|$, mixing will be more for $R_b - R_c > 0$ at later times.

An important observation to be made in figure 2.17 is that, in particular, χ_c is zero initially, becomes positive and is found to have obtained a saturation at later time for higher viscosity ratio. Initially, χ_c is zero as diffusion dominates before the origin of instability. With the passage of time, forces due to convection become stronger resulting in instability and more mixing. With a further increase in time, convection decreases due to a decrease in potential velocity with distance. No new fingers appear and the already existing fingers diffuse among themselves causing a decrease in mixing. At later times, saturation in χ_c confirms the dominance of diffusion at later times. Thus, the VF flow dynamics can be classified into three regimes: initial diffusion-dominated regime, intermediate convection-dominated regime, and the final diffusion-dominated regime. Chui et al. [18] experimentally reported a transition from convection-dominated to diffusion-dominated regime during radial VF with non-reactive fluids. To further strengthen the existence of three zones dominated by different forces, we calculate the interfacial length as $I(t) = \int_0^{2\pi} \int_{r_0}^L |\nabla c| r dr d\theta$. For $R_b = R_c = 0$, stable displacement without any instability is observed. Consequently, diffusion is the only force in action for $R_b = R_c = 0$ and thus $I(t) \propto t^{1/2}$ for $R_b = R_c = 0$ in figure 2.18. The instability originates as soon as $I(t)$ deviates from $R_b = R_c = 0$ curve and minimum such time is the onset time of instability t_{on} . For some $t > t_{on}$, $I(t) \propto t$ indicates a convection-dominated regime. Finally, $I(t)$ again becomes $\propto t^{1/2}$ due to dominance of diffusion. The onset time and the duration of each regime depend upon the value of $R_b - R_c$. In figure 2.18, the interfacial length for $R_b \neq 0, R_c \neq 0$ merges with $R_b = R_c = 0$ before onset time. When instability appears, $I(t)$ grows at a faster rate and scales

$\propto t$, but at a later time, again it scales $\propto t^{0.5}$. The transition in the scaling of interfacial length $I \propto t$ to $I \propto t^{0.5}$ implies the shutdown of instability as no new fingers are generated at later times. In the last regime, the instability does not generate new fingers and the existing fingers grow only as the injection of reactant A is still going on. Such fingers are termed as frozen fingers [8] and are reported for reactive fluids for the first time in this work.

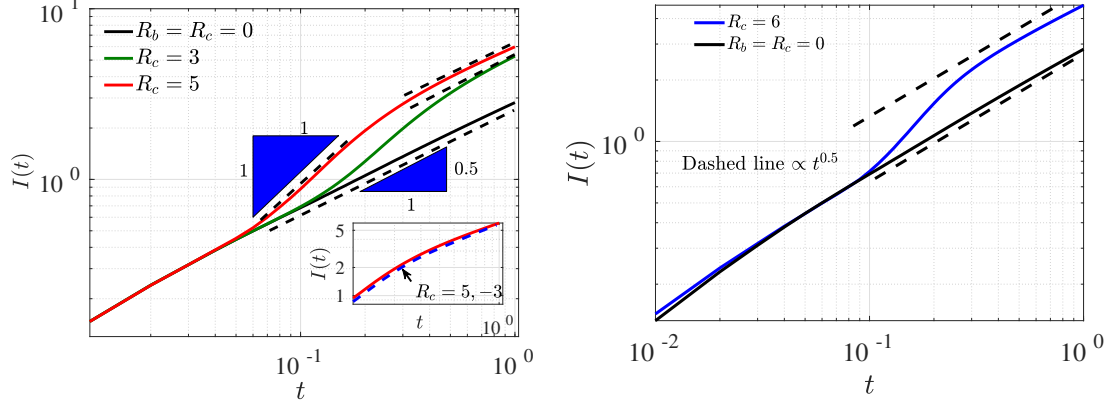


FIGURE 2.18: Log-log plot of interfacial length for (a) $R_c = -3, 5$, $R_b = 1$, (b) $R_c = 6$, $R_b = -1$ and $R_b = R_c = 0$. Inset: interfacial length for $R_c = 5, -3$. Blue-dashed line for $R_c = -3$ and Red solid is for $R_c = 5$.

2.4 Conclusion

A non-linear study is performed to understand a bi-molecular chemical reaction $A + B \rightarrow C$ generating a product having same or different viscosity than the reactants. The viscosity difference between the reactants and/or the products results in VF instability if a less viscous fluid displaces a more viscous one. A detailed analysis is performed to understand (a) various characteristics of the reaction and how VF affects them; and (b) the effect of the chemical reaction and VF on fluid mixing. First, we gain insight into various characteristics of the chemical reaction by considering $R_b = R_c = 0$ so that displacement is viscously stable. The total reaction rate and the total amount of product are found to be dependent on Da . For small Da , $R_{tot}(t)$ is an increasing function of time but with an increase in Da , R_{tot} becomes non-monotonic attaining a maximum value at $t = 0$ for large Da and at some $t > 0$ for intermediate values of Da . The non-monotonic nature is attributed to a different rate of consumption of reactants for different Da and the extrema are a result of the competition between the forces due

to convection and diffusion in radial displacements. The generated amount of product is found to follow a Da dependent power law, different in early and late time regimes.

For a fixed R_b , the viscosity profiles for the two values of $|R_b - R_c|$ are mirror images of each other. We compare the VF dynamics for such values. It is found that depending upon the sign of $R_b - R_c$, the product is more concentrated either towards the source or away from the source. For $R_b - R_c < 0$, inward fingers are obtained as the upstream mixing zone supports the instability and the downstream mixing zone acts as a barrier for the same. Enhanced mixing with chemical reaction is captured in terms of the degree of mixing. Chemical reaction as well as the forces due to convection and diffusion are found to contribute to increased mixing. For a fixed R_b , the degree of mixing ($\chi_c(t)$) is more for $R_b - R_c < 0$ and is a consequence of the radial displacement being considered which results in weaker convection at the downstream mixing zone. Thus, the onset of instability is early for $R_b - R_c < 0$ and hence mixing is more for such values of R_c . It is in contrast to results obtained for rectilinear displacement that corresponds to uniform flow [69, 67]. The degree of mixing is zero initially, increases and is finally found to attain a saturation with time. This indicates that initially, diffusion dominates followed by convection taking over with the onset of instability and ultimately diffusion again comes into the picture. Different time regimes dominated by convection or diffusion are established by calculating interfacial length. The duration of different time regimes depends on various parameters considered in the problem. The division of total time into three regimes with convection-dominated regime sandwiched between diffusion-dominated regime is reported for the first time for reactive fluids.

Further, to explore how hydrodynamic instability affects the reaction kinematics, we calculate several reaction characteristics for various values of R_b , R_c and compare the dynamics for mirror image viscosity profile corresponding to constant values of $|R_b - R_c|$. For unstable displacement, m_R shifts in the downstream or the upstream mixing zone depending upon the nature of fingers. For sufficiently high R_c , an initial transition in m_R is observed. For $R_b \neq 0$, $R_c \neq 0$, R_{tot} follows a similar trend as that for stable displacement, being a non-monotonic function of time for higher Da . However, the convection-dominated regime after the occurrence of minimum is larger for larger R_c because of higher instability. Further, mixing is enhanced with VF and thus, c_{tot} is also increased for $R_b \neq R_c \neq 0$, following a similar trend as the degree of mixing for $|R_b - R_c|$. It is concluded that the kind of displacement as well as VF affects reaction characteristics and a chemical reaction results in enhanced mixing.

Chapter 3

Linear stability analysis of reactive miscible viscous fingering for radial displacement

3.1 Introduction

By modifying the viscosity profile, chemical reactions can modify and even trigger viscous fingering (VF) instability in a porous medium. We consider a second-order chemical reaction, $A + B \rightarrow C$ and the viscosity profile to be dependent on reactants and product concentrations. The viscosity profile is modified if the reaction generates a product having viscosity contrast with reactants, resulting in instability. For rectilinear displacement, the VF dynamics affected by the chemical reaction are well understood both theoretically [35] and numerically [31, 34]. In this chapter¹, we discuss how can a chemical reaction affect the stability of the flow for radial displacement.

For radial flow, there exists a minimum viscosity contrast to trigger the instability in non-reactive displacements where both the flow are non-reactive in nature [93, 102], the same holds for the reactive displacement [94]. It is reported that when reactants are iso-viscous, instability is induced when the product and reactants have sufficient viscosity contrast. This has been observed both through numerical investigations through non-linear simulations [94, 113] and linear stability analysis [92]. However, they do not consider the reactive displacements with viscosity mismatched reactants. The critical viscosity contrast reduces when we increase the reaction rate. Further, Kim et al. [53] have performed a linear stability analysis (LSA) for radial flow utilizing spectral analysis restricted to the asymptotic limit of $Da \rightarrow \infty$, $Pe \rightarrow \infty$. Here Da , Pe and t represent the reaction rate, Péclet number and time respectively. They obtained critical viscosity ratios that trigger instability and establish a power law trend between Pe and the critical viscosity ratios. Further, they show that the LSA results are supported by non-linear simulations. To the best of our knowledge, no theoretical analysis of the radial reactive displacement, when reactants have some viscosity contrast for a finite range of Pe and

¹This chapter is under revision in the *J. Fluid Mech.* and the revised manuscript is submitted.

Da , has been documented in the literature. However, the prevalent focus in most experimental studies exploring reactive viscous fingering caused by reactants with mismatched viscosities [72, 71, 70, 83]. In addition, instabilities often occur even in the absence of a reaction, leading to an analysis of how chemical reactions impact viscous fingering [35, 114, 22]. Moreover, it is observed that when the reactants have an unfavorable viscosity contrast, the reaction can promote or stabilize viscous fingering for rectilinear flow, indicating that the chemical control of local fingering dynamics can be precisely tuned by selecting the appropriate chemical species with a particular difference in concentrations. [35, 22]. However, for radial flow, the literature lacks the numerical investigation of reactive displacement with viscosity mismatched reactants. Thus, it would be intriguing to investigate how the reaction rate influences the transition in stability for radial flow when the reactants have viscosity contrast.

In this chapter, we fill the above-mentioned literature gap and present a thorough examination that considers the effects of viscosity mismatch between the reactants and product for a range of Da and Pe by performing non-linear simulations (NLS) and linear stability analysis (LSA). In this work, we introduce an LSA to understand the dynamics of the reactive displacements in transient time. However, we encounter an unsteady base state as a solution of advection-diffusion-reaction equations [11]. The time-dependent nature of this base state renders the stability matrix non-orthogonal. However, it has been observed that if the stability matrix is not orthogonal, the early-time dynamics may not be captured [109, 86, 38]. Thus, we opt for non-modal analysis. For optimal initial conditions, we give initial perturbation around the interface instead of the entire r domain, as it is known as the fastest-growing perturbation [5, 40]. Later, we validate all LSA predictions through non-linear simulations. Both LSA and NLS predict the critical parameters for instability decay with Péclet number and reaction rate. Our research is novel in that we explore the stability of reactive displacement based on the viscosity profile for radial flow. We determine whether the modifications resulting from a chemical reaction impact the flow stability compared to the equivalent non-reactive situation. We determine a phase plane between the viscosity ratios between the reactants and product and reactants, divided by critical viscosity ratios for instability and find that the reactions can affect system stability up to a certain extent. For instance, there exists a stable region in the phase plane for even $Da \rightarrow \infty$.

The organization of the chapter is as follows. In §3.2, we provide the mathematical formulation. We present the base state equations and solve them numerically. In §3.3, we derive the linearised

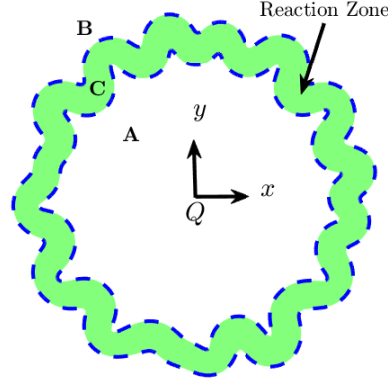


FIGURE 3.1: Schematic of $A + B \rightarrow C$ chemical reaction in a radial source flow. The green-colored shaded region bounded by dashed lines, is where both the reactants come into contact and product C is generated. We denote this region as reaction zone. The outside and inside region of the reaction zone is occupied by reactant B and A respectively.

perturbed equations and perform LSA. At last, we perform NLS and compare LSA results with NLS results in §3.4 and address the applications of the work in §3.5.

3.2 Mathematical formulation

A miscible displacement is considered in a homogeneous and isotropic porous medium where one fluid, let A , is injected from the source with flow rate Q per unit depth, displacing the other fluid, let B , radially. Both fluids are Newtonian, neutrally buoyant, and reactive. A second-order irreversible chemical reaction $A + B \rightarrow C$ occurs in the system whenever both fluids come into contact. The system of flow equations consists of the continuity equation for incompressible flow and Darcy's law, describing mass conservation and momentum conservation. Further, we couple the flow equations with reaction-convection-diffusion equations that interpret the transport of fluid species. In experiments, the dye concentration is added in displacing fluid initially. The dye is non-reactive in nature with the other fluids and has no impact on the viscosity profile. Further, we consider a convection-diffusion equation describing the transport of dye concentration, z . The equations can be represented in non-dimensionalized form as follows [35, 94]:

$$\nabla \cdot \mathbf{u} = 0, \quad (3.1a)$$

$$\nabla p = -\mu \mathbf{u}, \quad (3.1b)$$

$$\frac{\partial a}{\partial t} + \mathbf{u} \cdot \nabla a = \frac{1}{Pe} \nabla^2 a - Da ab, \quad (3.1c)$$

$$\frac{\partial b}{\partial t} + \mathbf{u} \cdot \nabla b = \frac{1}{Pe} \nabla^2 b - Da ab, \quad (3.1d)$$

$$\frac{\partial c}{\partial t} + \mathbf{u} \cdot \nabla c = \frac{1}{Pe} \nabla^2 c + Da ab, \quad (3.1e)$$

$$\frac{\partial z}{\partial t} + \mathbf{u} \cdot \nabla z = \frac{1}{Pe} \nabla^2 z. \quad (3.1f)$$

These equations are non-dimensionalised as in chapter 2. The viscosity profile depends on product and reactant concentrations exponentially as follows [35]:

$$\mu = \exp(R_b b + R_c c). \quad (3.2)$$

For every combination of (R_b, R_c) values, we have a specific reaction type, characterizing the viscosity contrast between reactants; and product and reactant, A is defined by $R_b = \ln(\mu_B/\mu_A)$ and $R_c = \ln(\mu_C/\mu_A)$ respectively. The initial conditions associated with equation (3.1) are:

$$(a, b, c, z)(\mathbf{x}, t = 0) = \begin{cases} (1, 0, 0, 1), & 0 < |\mathbf{x}| < r_0 \\ (0, 1, 0, 0), & \text{Otherwise} \end{cases}, \quad (3.3a)$$

$$\mathbf{u}(\mathbf{x}, t = 0) = \frac{\mathbf{x}}{2\pi|\mathbf{x}|^2}. \quad (3.3b)$$

where $\mathbf{x} = (x, y)$ and r_0 is the initial radius of the circular region filled with fluid A . Here we encounter four nondimensionalised parameters R_b, R_c , Damköhler number Da and Péclet number Pe . All the fluids are assumed to have the same diffusion coefficient, \tilde{D} , and $Pe = \tilde{Q}/\tilde{D}$, which shows a comparison of fluid transport due to convection and diffusion. While Da is obtained as a ratio of convective time scale and reactive time scale *i.e.* $Da = \frac{\tilde{t}_f}{(1/\tilde{k}\tilde{a}_0)}$. Here \tilde{k} is the reaction rate constant.

3.3 Linear Stability analysis

3.3.1 Linearised perturbed equations

In order to carry out a stability analysis, we need to formulate linearised perturbed equations for perturbed fluid concentrations and perturbed velocity around base state flow. We define (A_0, B_0, C_0, Z_0) , base state concentrations of A , B , C , and dye as the solution of equations (3.1c)-(3.1f) in the absence of any viscosity contrast *i.e.* $R_b = R_c = 0$ [92] as shown in figure 3.2. The base state solution is axisymmetric and it is just a function of radius, r only, hence, not a function of θ . However, the analytical base state solution can not be attained analytically [11]. Even, for the equation (3.1f) provided initial condition in the equation (3.3) an analytical solution is unattainable [93]. Thus, we compute the base state concentrations numerically using the method of lines, discussed in the next subsection §3.3.2. For stable displacement, the initial velocity provided by the source does not get perturbed and remains the same as in equation (3.3b) and it is considered as the base state velocity, \mathbf{u}_0 . Then, we perturb the base state profile as follows:

$$(a, b, c, z, \mathbf{u}) = (A_0, B_0, C_0, Z_0, \mathbf{u}_0) + (a', b', c', z', \mathbf{u}'). \quad (3.4)$$

For the ease of calculations, we redefine the governing equation in stream function-vorticity formulations. We define stream function as $\psi = \psi_0 + \psi'$, ψ_0 is base state stream function and ψ' is the perturbed component of stream function that is defined as $\mathbf{u}' = \left(-\frac{\partial \psi'}{\partial y}, \frac{\partial \psi'}{\partial x}\right)$. Thus, the linearized perturbed system of equations can be written in stream function-vorticity formulation as in Sharma et al. [92]:

$$\nabla^2 \psi' = -\omega, \quad (3.5a)$$

$$\omega = R_c (\mathbf{u}_0 \times \nabla c' + \mathbf{u}' \times \nabla C_0) \cdot \hat{\mathbf{k}} + R_b (\mathbf{u}_0 \times \nabla b' + \mathbf{u}' \times \nabla B_0) \cdot \hat{\mathbf{k}}, \quad (3.5b)$$

$$\frac{\partial a'}{\partial t} + \mathbf{u}_0 \cdot \nabla a' + \mathbf{u}' \cdot \nabla A_0 = \frac{1}{Pe} \nabla^2 a' - Da (B_0 a' + A_0 b'), \quad (3.5c)$$

$$\frac{\partial b'}{\partial t} + \mathbf{u}_0 \cdot \nabla b' + \mathbf{u}' \cdot \nabla B_0 = \frac{1}{Pe} \nabla^2 b' - Da (B_0 a' + A_0 b'), \quad (3.5d)$$

$$\frac{\partial c'}{\partial t} + \mathbf{u}_0 \cdot \nabla c' + \mathbf{u}' \cdot \nabla C_0 = \frac{1}{Pe} \nabla^2 c' + Da (B_0 a' + A_0 b'), \quad (3.5e)$$

$$\frac{\partial z'}{\partial t} + \mathbf{u}_0 \cdot \nabla z' + \mathbf{u}' \cdot \nabla Z_0 = \frac{1}{Pe} \nabla^2 z'. \quad (3.5f)$$

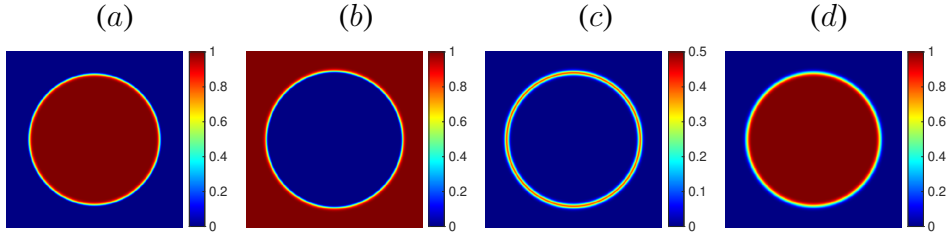


FIGURE 3.2: Base state profile of (a) Reactant A, (b) Reactant B, (c) product C and (d) Dye concentrations for $Da = 100$, $Pe = 3000$ at final time $t = 1$.

Here ω is \hat{k} component of vorticity. At boundary, we apply far-field boundary condition for all the perturbed quantity, *i.e.* $\psi' = 0$,

$$\begin{aligned} \frac{\partial}{\partial x}(a', b', c', z') &= \mathbf{0} \quad \text{at } x = \pm L/2, \\ \frac{\partial}{\partial y}(a', b', c', z') &= \mathbf{0} \quad \text{at } y = \pm L/2. \end{aligned} \quad (3.5g)$$

Here, $\Omega = [-L/2, L/2] \times [-L/2, L/2]$ is our computational domain.

3.3.2 Initial value calculations

Since radial flows exhibit an algebraic growth rate of perturbations rather than exponential, modal analysis cannot be applied. Therefore, we have employed non-modal analysis, solving initial value calculations for numerical LSA. This LSA serves as an efficient method to explore time-dependent linear systems in miscible VF [101, 92, 40, 80]. We solve the system of equations with the method of lines. We use the third-order Runge-Kutta method to solve the initial value problem, both base state and linearised perturbed equations (3.5c)-(3.5f), resulting from the discretization of spatial derivatives. Further, a highly efficient pseudo-spectral method hybridized by compact finite difference method of sixth order is used to solve the Poisson equation in (3.5a). In our study, we do not incorporate wavelength selection. While our LSA method does allow for wavelength selection [40]. Further, we perturb the base state around the interface only as it has been recognized with the highest perturbation growth [5]. We perturb the base state using a consistent set of random initial conditions around the interface as follows:

$$(a', b', c', z')(\mathbf{x}, t = 0) = 10^{-3} \begin{cases} (\sin(2\pi m_1), \sin(2\pi m_2), 0, \sin(2\pi m_1)), & |\mathbf{x}| = r_0, \\ (0, 0, 0, 0), & \text{Otherwise} \end{cases} \quad (3.6)$$

Parameters	dt	$n_x = n_y$	L	r_0	Pe
Value	10^{-4}	1025	1.5	0.075	3000

TABLE 3.1: Table showing the parameters used in the LSA.

Here, m_1 and m_2 are random functions generating numbers between 0 and 1 which is to be consistent across all parameters. The remaining parameters used in LSA are mentioned in table 3.1. The numerical method is explained in detail in Sharma et al. [92] and the references therein.

Since the base state is unsteady, we seek to analyze the temporal evolution of perturbations in the comparison of the base state [95, 39]. To do the same, we utilize the energy method approach and determine normalized energy function with respect to the base state profile for both the perturbed concentration, α' and \mathbf{u}' .

$$E(t) = \frac{\int_{\Omega} \alpha'^2 + \mathbf{u}'^2 d\Omega}{\int_{\Omega} \alpha_0^2 + \mathbf{u}_0^2 d\Omega}, \quad (3.7)$$

here, α' is the dummy variable for perturbed concentrations and $\alpha' \in \{a', b', c', z'\}$.

Further, we compute energy amplification, $G(t)$ by normalizing energy $E(t)$ with $E(t = 0)$ as [65]:

$$G(t) = \frac{E(t)}{E(t = 0)}. \quad (3.8)$$

Since we perturb the concentrations of the reactants initially, we use either a' or b' in energy calculation in equation (3.7). In addition, it is reported that the temporal evolution of $\ln(G(t))$ is same whether we choose a' or b' for computing $G(t)$ [92]. We use a' and A_0 for the further computation of energy amplification. For unstable displacement, when perturbations amplify with time, $\ln(G(t))$ increases with time. While a monotonically decreasing profile of $\ln(G(t))$ is obtained for stable displacements. The transition in stability from stable to unstable displacement is depicted by a minimum in the $\ln(G(t))$ curve. We denote that time as the onset time when perturbations start to grow [39].

It is noteworthy that the time domain is confined to $t = 1$, representing the duration over which our investigation is conducted. Hence, we analyze the stability of reactive displacement in

transient time regimes only, not for asymptotic times. It has been observed that there exists a diffusive regime at later times for radial flows [18, 114]. For non-reactive fluids, experimental observations indicate that the interface growth decelerates, scaling as $\sim t^{1/2}$ at later times, showing the existence of a diffusive regime as anticipated in a stable displacements [18]. It indicates the shutdown of overall flow instability. This phenomenon is reported as frozen fingers. Moreover, Verma et al. [114] has reported the existence of frozen fingers for reactive fluids. Hence, the asymptotic analysis for reactive VF for radial flow is not required.

3.3.3 Transient energy growth

The system of equations (3.1) describes the reactive and non-reactive flow both depending on the value of Da . For $Da = 0$, the system represents a non-reactive flow where all the fluids are non-reactive in nature and follow the convection-diffusion equation. The viscosity profile is monotonic and is given by $\mu = \exp(R_b b)$ due to no product formation *i.e.* $c = 0$. Further, the monotonic viscosity profile may be modified in the presence of a chemical reaction, $Da \neq 0$. In the present study, we aim to compare the reactive and non-reactive flow when the viscosity contrast between displacing fluid A and displaced fluid B , R_b is same. Further, for non-reactive fluids, it is reported there exists a critical viscosity contrast for instability for radial displacement [93]. Hence, we divide the reactive flow into two categories depending on whether the corresponding non-reactive flow, is stable or unstable. First, we consider the reactive flow when the corresponding non-reactive flow *i.e.* $(R_b, Da = 0)$, is stable and examine if the chemical reaction affects the flow stability.

In the second category, we consider those types of reactions for which reactants have already an unfavorable viscosity contrast for instability. We examine how stability behavior, such as the growth rate of perturbations and onset of instability, is affected by product formation. In order to evaluate the variation between reactive and non-reactive displacement, we must first review the stability of the non-reactive system before analyzing the reactive displacement. We observe a stability transition in the non-reactive system with two distinct values of R_b ($R_b = 0.5, 0.3$) representing unstable and stable displacements, respectively. Further, we examine the reactive situation associated with these two values of R_b .

To capture the transition of stability for increasing viscosity contrast, we analyze the energy

amplification in the course of time for a non-reactive situation and various values of R_b . It can be verified that the flow is unstable for $R_b = 0.5$, $Da = 0$, the $\ln(G(t))$ increases with time after obtaining a minimum as shown in the inset of figure 3.3(b). In the case of unstable displacement, the initial decrements in energy show that the initial diffusion in the system and instability take some time to manifest. The minimum denotes the onset time of instability when instability appears. From the onset time, the convection starts to dominate the flow dynamics and the perturbation growth begins. On the contrary, if we decrease the viscosity ratio between reactants to $R_b = 0.3$, the flow remains stable for the entire time domain as shown in the inset of figure 3.3(b) in spite of an unfavorable viscosity contrast. Thus, we have obtained two values of R_b showing that an increase in viscosity contrast leads to the transition in stability for the non-reactive situation. Now we analyze how the stability of the monotonic viscosity profile is influenced by varying R_c .

3.3.3.1 Effect of R_c

When we consider the non-reactive flow, we have to deal only with a perturbed concentration that follows a linearised perturbed equation corresponding to one convection-diffusion equation. While in the reactive case, we have to handle three perturbed concentrations that follow equations (3.5c)-(3.5e) and the complexity of the system analysis escalates. Therefore, it is absurd to compare the evolution of perturbed reactive or non-reactive concentrations directly. Additionally, we want to compare VF dynamics as a result of the modified viscosity profile, hence we find a value of R_c for which the corresponding viscosity profile is not modified in the presence or absence of the reaction.

When the product viscosity differs from that of the displacing fluid reactant B , *i.e.* $R_c \neq R_b$, the viscosity profile becomes either non-monotonic or remains monotonic but with steeper viscosity contrast as shown in figure 3.3(a) for $Da = 100$, $R_b = 0.5$ and various R_c . Due to the presence of all three fluids, Hejazi et al. [35] has identified two mixed zones: upstream and downstream mixing zone. The region occupied by the reactant A and product C is defined as the upstream mixing zone, while the region inhabited by B and C is termed as downstream mixing zone. The significance of defining these regions is that different viscosity contrast occurs in these two zones when $R_b \neq R_c$ and play an individual role in determining the overall stability of the system. The viscosity contrast at the upstream mixing zone is decided by the factor $R_c/2$

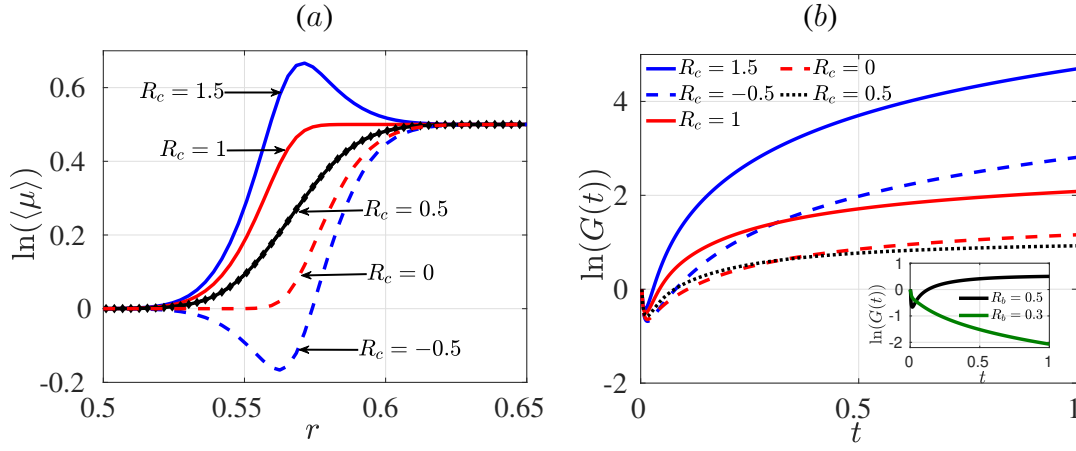


FIGURE 3.3: (a) Viscosity profile for $Da = 100$, $R_b = 0.5$ and various R_c . (b) Log energy amplification with time for $Da = 100$, $R_b = 0.5$ and various R_c showing unstable displacement. Inset: $\ln(G(t))$ of $R_b = 0.5, 0.3$, $Da = 0$.

while $R_b - R_c/2$ determines the viscosity ratio at the downstream mixing zone [35, 114]. For $R_b = R_c = 0.5$, it is evident that $R_c/2 = R_b - R_c/2$, that is, the viscosity in both zones is the same. Thus, the viscosity contrast for $R_c = 0.5$ is monotonic, similar to that of $R_b = 0.5$ as shown in figure 3.3(a). Thus, when a chemical reaction alters the viscosity profile, this specific case of $R_c = 0.5$ can be used as a reference viscosity profile. For instance, if we compare the viscosity profile in figure 3.3(a), it is evident that the viscosity profile remains monotonic for $R_c = 0, 1$ but the reaction results in a non-monotonic viscosity profile for $R_c = 1.5, -0.5$. Even for the monotonic case, if we compare the profiles for $R_c = 0, 0.5, 1$, we can see that the viscosity profile at the upstream mixing zone is steepened for $R_c = 1$, while it is steepened at the downstream mixing zone for $R_c = 0$. We analyze how this affects the onset of instability.

We have plotted the log energy amplification curve for various R_c with $R_b = 0.5$ in figure 3.3(b). For $R_c = 1$, the viscosity profile steepens at the upstream mixing zone particularly and becomes flat at the downstream mixing zone where $R_b - R_c/2 = 0$. Due to this, the onset occurs early and the system exhibits more energy amplification for $R_c = 1$ than $R_c = 0.5$ despite the same endpoint viscosity contrast. Now we analyze the energy amplification for $R_c = 0$, where unfavorable viscosity contrast is shifted at the downstream mixing zone. The energy amplification for $R_c = 0$ is more than that of $R_c = 0.5$ at a later time only. However, at an early time, the energy amplification is less for $R_c = 0$, and hence the system is less destabilized than $R_c = 0.5$. It shows the significance of the location where the unfavorable viscosity contrast occurs and instability appears. Here, the upstream mixing zone stabilizes the system at early

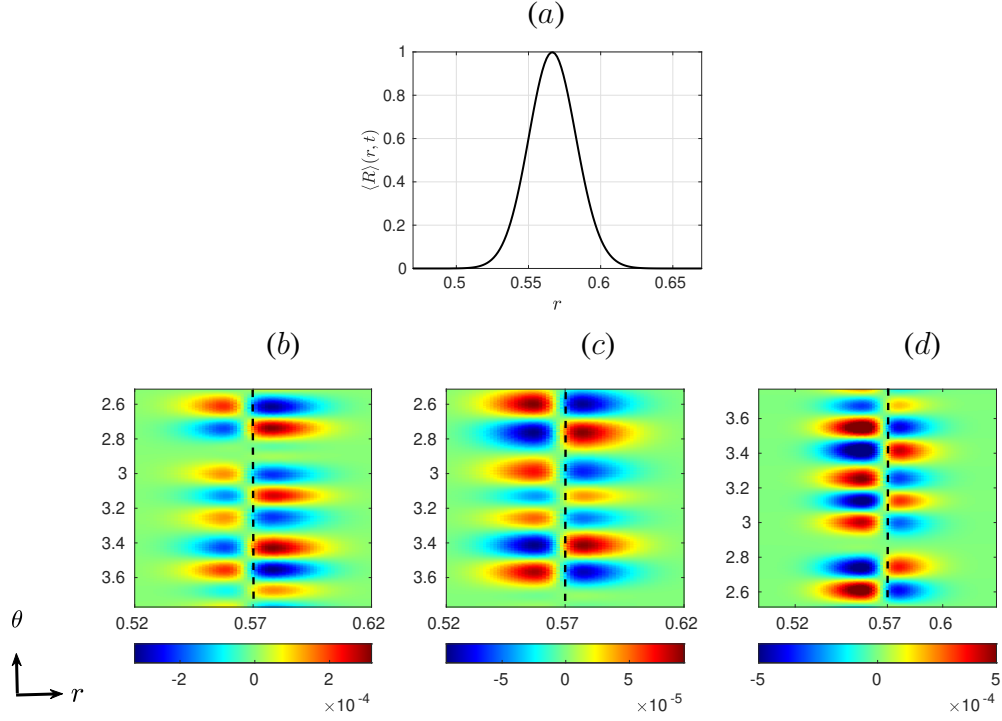


FIGURE 3.4: (a) Averaged reaction rate profile, $\langle R \rangle(r, t) = \frac{1}{2\pi} \int_{r_0}^R R(r, \theta, t) d\theta$ and $R = DaA_0B_0$ for base state for $Da = 100$. Density plot for perturbed concentration of C, c' for $Da = 100, R_b = 0.5$, (b) $R_c = -0.5$, (c) $R_c = 0.5$ and (d) $R_c = 1.5$ at final time $t = 1$ in polar coordinates. Here the black-dashed line denotes the position where the reaction rate is maximum as shown in (a).

times. While the unstable, downstream mixing zone will be carried into effect late and the system destabilizes more when instability appears in the upstream mixing zone. Thus, despite the same viscosity contrast in their unstable zone for $R_c = 0, 0.5, 1$ and $R_b = 0.5$ the system may attribute stability transition at a different time by varying unfavorable viscosity contrast locations.

Further, when $R_c = 1.5$ and $R_c = -0.5$, the viscosity profile becomes non-monotonic, resulting in unfavorable viscosity contrasts at the trailing and downstream mixing zones, respectively. For $R_c = 1.5$ ($R_c = -0.5$), the downstream (upstream) mixing zone stabilizes and instability is expected to develop at the upstream (downstream) mixing zone. To illustrate this, we plot the perturbation profile for c' in polar coordinates at $t = 1$ for both $R_c = -0.5$ and $R_c = 1.5$ in figure 3.4(b) and 3.4(d), respectively. For $R_c = 0.5$, the viscosity profile is monotonic, and hence, the perturbation profiles are distributed symmetrically across both mixing zones, as depicted in figure 3.4(a). In contrast, the presence of localized unstable zones leads to a more concentrated distribution of perturbation at the upstream (downstream) mixing zone when

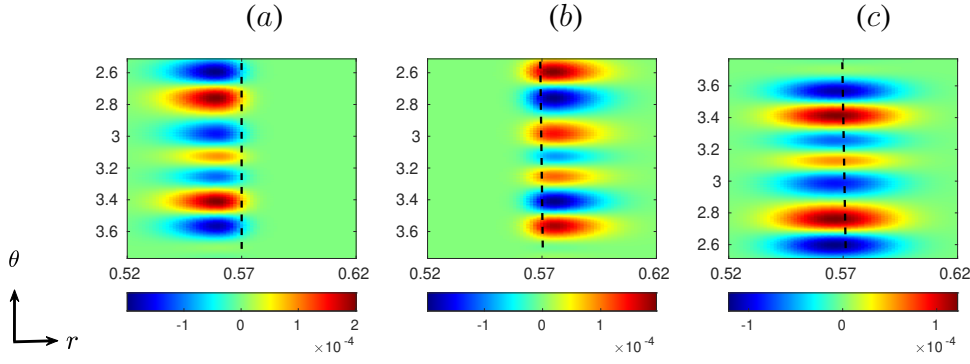


FIGURE 3.5: Density plot for perturbed concentration (a) a' , (b) b' and (c) z' for $Da = 100$, $R_b = 0.5$ and $R_c = 0.5$ at final time $t = 1$ in polar coordinates.

$R_c = 1.5$ ($R_c = -0.5$). Moreover, we plot perturbation profiles for a' , b' , and z' in figure 3.5. Given that the concentrations of base state reactants A and B are localized in the downstream and upstream mixing zones, respectively. In contrast, the perturbed z' remains unlocalized in any mixing zone, resembling the base state profile. Additionally, we observe a quadruple structure for the perturbed concentration c' in figure 3.4, influenced by the perturbed concentrations of reactants b' and a' , as described in equation 3.5.

In the energy amplification plots in figure 3.3(b), $\ln(G(t))$ increases more for $R_c = 1.5$ than $R_c = -0.5$ depicting more amplified perturbations for $R_c = 1.5$ despite the same viscosity contrast at respective unstable zone. It can be concluded that the perturbations amplify more with enhanced energy amplification $\ln(G(t))$ with a higher growth rate of perturbations for an increased viscosity contrast, $|R_b - R_c|$ for any fixed R_b . This aligns with both the findings from the existing linear stability analysis [35] and nonlinear simulations [94, 114] qualitatively. The nonlinear simulations indicate that as the viscosity ratio increases, the onset time of instability decreases which leads to rigorous viscous fingering patterns [94, 114, 113]. In addition, the mixing phenomena are enhanced [114].

Further, it can be seen that for each pair $|R_c - R_b|$, despite the identical viscosity contrasts, the system exhibits a greater energy amplification for the case $R_c - R_b > 0$ than the corresponding case, $R_c - R_b < 0$ as shown in figure 3.3(a). This raises the question of why the perturbations amplify more when the unstable zone is situated at the upstream mixing zone in contrast to the downstream mixing zone despite the viscosity contrast being the same ($|R_c - R_b|$)? The velocity profile holds the responsibility for this property of radial flow. The velocity magnitude decreases with the radial distance, which provides more convection to the upstream mixing zone than the

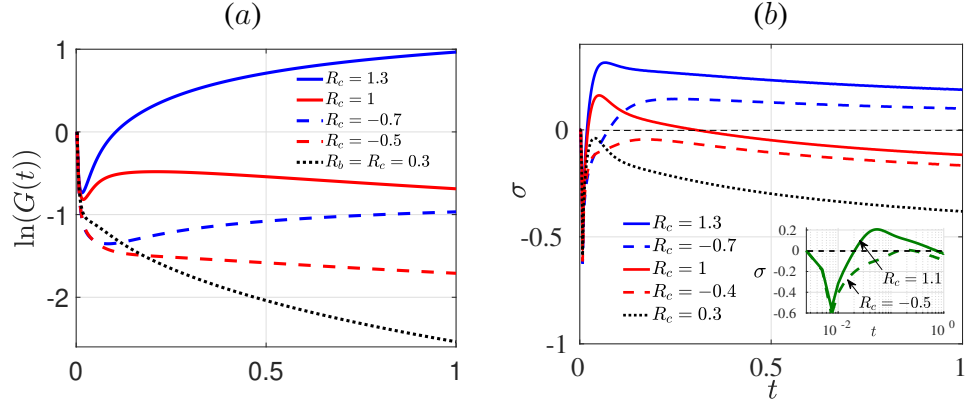


FIGURE 3.6: (a) Log energy amplification and (b) growth rate with time for $Da = 100$, $R_b = 0.3$ and various R_c showing unstable displacement. Inset: Growth rate for $R_c = 1.1, -0.5$ showing an unstable and stable displacement respectively despite the same viscosity contrast $|R_b - R_c|$.

downstream mixing zone [94, 113]. Moreover, it hints at the asymmetry in the (R_b, R_c) phase plane along the non-reactive region, $R_c = R_b$. We explore the asymmetry in the (R_b, R_c) phase plane by taking corresponding stable non-reactive situations and finding the corresponding R_c parameters that destabilize the flow. In the inset of figure 3.3(b), the flow is shown stable for $R_b = 0.3$. If the reaction generates a product with enough high or less viscosity that makes the viscosity profile non-monotonic and one of the zones becomes viscously unstable, the flow may become unstable. We will next investigate these situations.

In figure 3.6(a), the flow is shown stable for some range of R_c , including $R_c = 0.3$ and on further increment of viscosity ratio, the system becomes unstable. For the viscosity contrast $|R_c - R_b| = 1$ ($R_c = 1.3, -0.7$), the flow is unstable as $\ln(G(t))$ increases with time after attaining a minimum, while the flow is stable for $R_c = -0.4$. It is interesting to note that when $R_c = 1$, the system behaves inconsistently. Following a minimum, $\ln(G(t))$ rises at first, then starts to fall as the energy amplification increases to saturation. For better visualization, we compute the growth rate as in Tan and Homsy [102]:

$$\sigma = \frac{t}{2G} \frac{dG}{dt}.$$

Evidently, the growth rate of perturbations is negative for $R_c = 1$ at later times after onset, there is a decay in perturbation growth as shown in figure 3.6(b). The positive growth rate indicates that the perturbations grow after onset time. However, the unfavorable viscosity contrast at the upstream mixing zone is not enough to sustain the growth of perturbations for a longer time

and it starts to decrease again. A similar transition in stability is observed in literature [37] for rectilinear flow. There, the secondary instability appears at late times after the first minima in $\ln(G(t))$. However, we do not observe the secondary instability for radial displacements. The reason is the provided uniform flow that feeds convection to flow for the entire time uniformly for rectilinear flow. However, in our case, the flow velocity reduces with radial distance and at the unstable zone with time. As a result of this, once the flow is stabilized, convection is not able to induce instability again. Hence, the flow is considered stable for $R_c = 1$. In conclusion, we have obtained a stable zone for a range of R_c when the corresponding non-reactive displacement is stable. In addition, we obtain such values of R_c where the flow is unstable when $R_c - R_b > 0$ ($R_c = 1.1$) while stable for the corresponding case $R_c - R_b < 0$ ($R_c = -0.5$) showing asymmetry in (R_b, R_c) phase plane as shown in figure 3.10. We discuss this in detail in the next subsection §3.4. The growth rate of perturbations is negative for $R_c = -0.5$, while the system shows a positive growth rate after onset in perturbation evolution for $R_c = 1.1$. Now, the question arises of how changing the reaction rate, Da , influences the stability of the reactive system, regardless of whether the system is initially stable or unstable.

3.3.3.2 Effect of Da

When reactants are iso-viscous, $R_b = 0$, non-linear simulations have shown that the onset of instability gets delayed and the critical viscosity ratio for instability is exceeded with lowering Da [94]. Here, we explore the effect of Da when $R_b \neq 0$. From the comparison of the figure 3.3 and figure 3.7(a), it can be observed that the $\ln(G(t))$ is less for $Da = 10$ after onset time. It happens as a result of the reduced amount of product decreasing the viscosity and thus the viscosity gradient, resulting in slower growth of perturbations. Furthermore, if we compare energy amplification for $R_b = 0.3$, $Da = 100, 10$ and various R_c as in the figures 3.6 and 3.7(b), the stable range of R_c increases for decreased Da . Flow is unstable for both the parameters $R_c = 1.3, -0.7$ when $Da = 100$, but for $Da = 10$, these parameters belong in the stable range of R_c for $R_b = 0.3$.

We have now covered the cases when the viscosity profile is modified due to the formed product having viscosity contrast with reactants. However, there is another case when product viscosity is identical to displacing fluid reactant B i.e. $R_b = R_c$ regardless of Da , the viscosity profile remains the same as the corresponding non-reactive situation, $(R_b, Da = 0)$ [69]. For such cases,

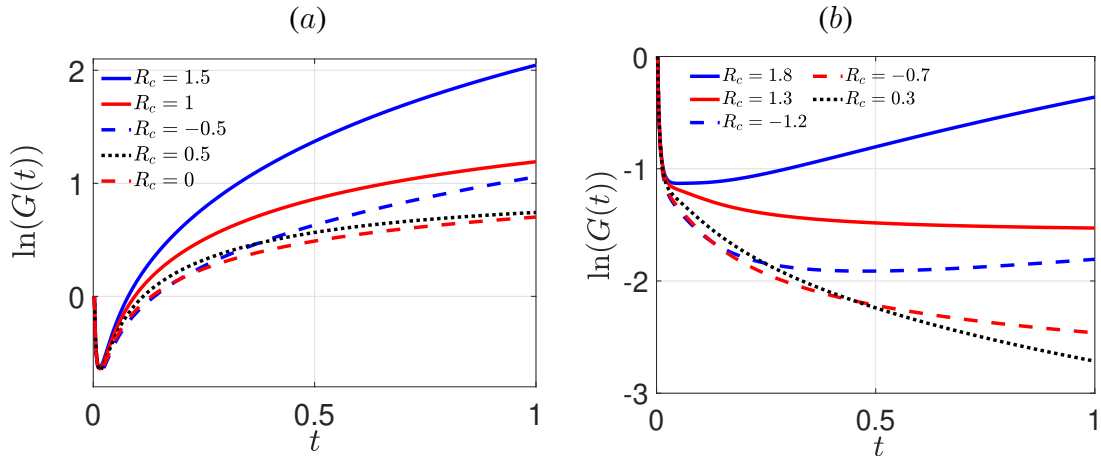


FIGURE 3.7: Log energy amplification with time for $Da = 10$, (a) $R_c = 0.5$, (b) $R_c = 0.3$ and various R_c showing unstable displacement.

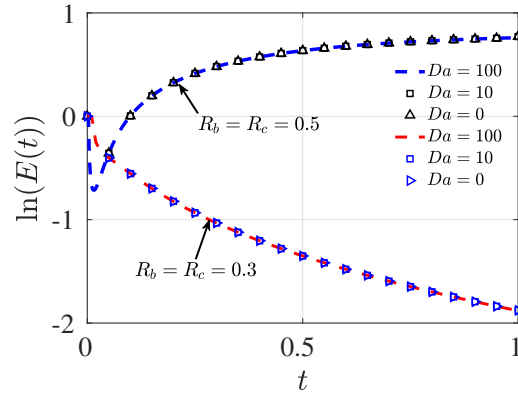


FIGURE 3.8: Log energy amplification with time for $R_b = R_c = 0.5$, 0.3 and various Da . Here all the curves for different Da and fixed viscosity contrast, are merged.

we claim that no change in the flow stability occurs when $R_b = R_c$ provided the flow is stable with or without the reaction, for instance, when $R_b = 0.3$. No change in perturbation growth or energy amplification should be observed when the system is already unstable for corresponding non-reactive situations $R_b = 0.5$ for changing Da . Instead of reactant A , we show energy amplification for dye concentration. Since dye concentration follows the convection-diffusion equation as followed by A when $Da = 0$, considering z allows us to examine the stability of the parameter $R_b = R_c$ for varied Da ranging from $Da = 0$ to $Da = 100$. From figure 3.8, it can be concluded that the stability is unaffected by a chemical reaction when $R_b = R_c$ as energy amplification regardless of whether the system is stable or unstable before the reaction.

3.4 Non-linear simulations

To support the fact that the results of LSA are not a consequence of linearised equations, we perform non-linear simulations for viscous fingering instability on the system of equations given in equation (3.1). To solve the coupled non-linear system of partial differential equations, we utilize a highly efficient pseudospectral method hybridized with the compact finite difference method. We decompose the velocity into two parts with rotational velocity (\mathbf{u}_{rot}) and potential velocity, (\mathbf{u}_{pot}) that defines the unperturbed flow as given in equation (3.3b). In addition, we define the rotational component to capture the instability by introducing the stream function as:

$$\mathbf{u} = \mathbf{u}_{pot} + \mathbf{u}_{rot}, \quad \mathbf{u}_{rot} = \left(\frac{\partial \psi}{\partial y}, -\frac{\partial \psi}{\partial x} \right), \quad (3.9a)$$

$$\nabla^2 \psi = -\omega, \quad \omega = R_c \left(v \frac{\partial c}{\partial x} - u \frac{\partial c}{\partial y} \right) + R_b \left(v \frac{\partial b}{\partial x} - u \frac{\partial b}{\partial y} \right). \quad (3.9b)$$

We solve Poisson equations (3.9b) by applying Fourier sine expansion to solve x - derivative and discretise y - derivative with the compact finite difference of sixth order. Further, the initial value problem in equations (3.1c)-(3.1f) is solved by the third-order Runge -Kutta method with adaptive time steps satisfying the Courant-Friedrichs-Lewy (CFL) condition. The remaining details are explained in Sharma et al. [94], Verma et al. [113]. We also compute the order of convergence for the numerical method in chapter 4, section 4.3.1 and convergence study for spatial discretization in appendix A.

To track the instability, we plot the dye concentration profile for $R_b = 0.3, 1, Da = 100, Pe = 3000$ and for various R_c at the final time $t = 1$ in figure 3.9. It is evident that the flow is unstable for $R_b = 1$ irrespective of R_c . On the contrary, the flow is stable for $R_b = 0.3$ and we obtain a range of R_c where a transition can be observed in flow stability. The flow remains stable for $R_c = 0, 1$. While the interface is deformed in the dye concentration profile due to the non-monotonic viscosity profile for $R_c = -2, 3$ that enhances the viscosity gradient in the reaction zone and provides a sufficient force to induce the instability. Furthermore, in figure 3.9, it can be observed that, despite an unfavorable viscosity, there is a stable zone at the upstream (downstream) mixing zone for $R_c = 1$ ($R_c = 0$), $R_b = 0.3$, whereas it becomes unstable when $R_c = 3$ ($R_c = -2$). Hence, we determine critical product viscosity, R_c for each R_b to trigger the instability if the flow is initially stable for corresponding R_b . This supports the

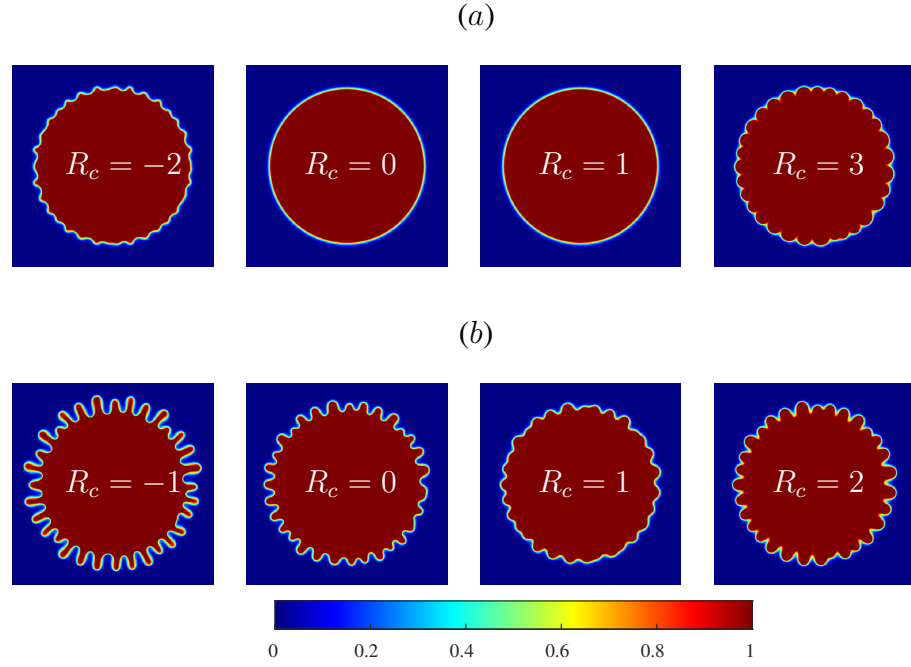


FIGURE 3.9: Dye concentration profile for $(Da, Pe) = (100, 3000)$, (a) $R_b = 0.3$ and (b) $R_b = 1$ and various R_c at final time $t = 1$.

conclusions drawn by LSA in Figure 3.3(b), indicating that an unstable displacement remains unstable in reactive flow if the corresponding non-reactive system is unstable. Furthermore, by comparing figures 3.10 (Inset figures) and 3.4, we observe that instability develops more at the upstream mixing and downstream mixing zones when $R_c > R_b$ and $R_c < R_b$, respectively. When $R_c = R_b$, the instability is not localized in any zone. Additionally, a comparison between figures 3.6(a) and 3.9(b) depicts a stable range of R_c in the (R_b, R_c) phase plane for a constant R_b in the corresponding stable non-reactive system.

The viscosity gradient at the upstream and downstream mixing zone is decided by $R_c/2$ and $R_b - R_c/2$, respectively. The instability is anticipated to occur at the upstream mixing zone if $R_c > 0$. Thus, we determine the critical viscosity ratio at the downstream mixing zone so that the diffusion can weaken the responsible forces due to convection in the upstream mixing zone. In another way, we find a critical R_b that can stabilize the flow. Similarly, if $R_c < 0$, then the flow can be destabilized for increasing viscosity gradient, $R_b - R_c/2 > 0$ at the downstream mixing zone. Hence, it will be convenient to find a critical R_b for a given R_c for the purpose of the computational study. To determine instability, we measure the deformation of the interface by interfacial length in the dye concentration [67, 94]. It is calculated by $I(t) = \int_{\Omega} |\nabla z| d\Omega$. For stable displacement, interfacial length follows the relation $I_0(t) = 2\pi\sqrt{r_0^2 + t/\pi}$ [93]. Evidently,

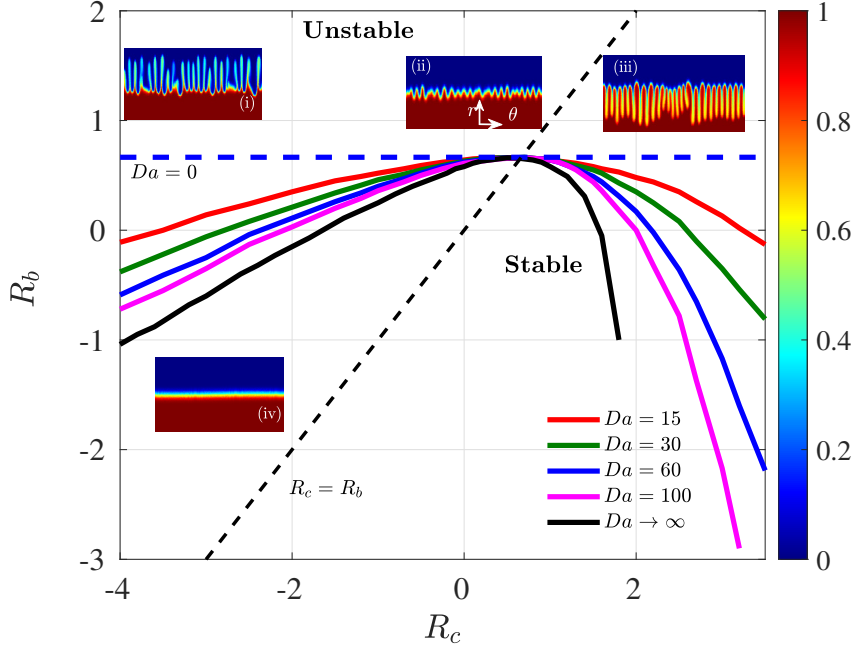


FIGURE 3.10: The (R_b, R_c) phase plane for $Pe = 3000$, various Da along with $Da \rightarrow \infty$. Dye concentration profile for $R_b = 1$, (i) $R_c = -3$, (ii) $R_c = 1$, (iii) $R_c = 5$ showing unstable displacement and (iv) $R_b = R_c = 0$ showing stable displacement in polar coordinates. The viscosity profile is non-monotonic for $R_c = -3$, and 5 with the decreased and increased product viscosity that leads to the localized fingering pattern in the upstream mixing and downstream mixing zone, respectively. While the viscosity profile remains monotonic for $R_b = R_c = 1$ and the resultant fingering patterns are not localized unlike the cases $R_b = 5, -3$.

for a deformed interface the interfacial length increases and if interfacial length, $I(t)$ coincides with $I_0(t)$ for the entire time domain, that parameter can be considered as stable displacement. We define the flow as unstable when the relative difference in interfacial length is greater than zero. $\Delta I = (I - I_0)/I_0 > 0$.

A phase plane (R_b, R_c) is presented in figure 3.10 where the solid curves show critical viscosity ratio (R_b, R_c) for instability for each Da and the region below the curve is stable and above the curve is the unstable region. It can be observed that if reactants have favorable viscosity contrast, *i.e.* $R_b < 0.66$, then two critical R_c can be determined that destabilize the flow for a given reaction rate. It happens when a chemical reaction introduces a non-monotonic viscosity profile and persuades convection and diffusion to compete, as suggested by LSA results. We obtain a range of R_c when $R_b < 0.66$ corresponds to the stable flow. This range contracts for increasing R_b and vanishes when $R_b = R_c = 0.66$. The viscosity contrast between reactants, $R_b = 0.66$, is the maximum R_b for which flow is stable before the reaction and the reaction may

alter the stability. Moreover, if reactants have viscosity contrast, $R_b > 0.66$ and the stability will not be changed by the reaction. It exhibits the limitations of the influence of reaction on the stability of the system. It is evident in figure 3.10 that the region around $R_c = 0.66$ is stable for all values of Da . This is the Da independent critical regime that we have reported for radial VF.

The value of viscosity ratio $(R_b, R_c) = (0.66, 0.66)$ is of our special interest. For $(R_b, R_c) = (0.66, 0.66)$, the viscosity profile is monotonic and identical to its inherent viscosity profile in corresponding non-reactive situations. Now, we claim that the viscosity ratio when $R_b = 0.66$ is also the critical viscosity ratio for the non-reactive fluids. For non-reactive fluids, Sharma et al. [93] have established a scaling relation between Péclet number Pe and critical log-mobility ratio R_b numerically

$$R_b = \alpha(r_0)Pe^{-\beta}, \quad \alpha = 30(1 + 10r_0). \quad (3.10)$$

Here β lies under confidence bounds $(0.52, 0.59)$ and critical parameters (R_b, Pe) lies on the boundary that is given by $R_b = \alpha(r_0)Pe^{-0.55}$. Since the above relation (3.10) is determined numerically and has theoretical and experimental support. It provides a fair opportunity to compare reactive displacement with the corresponding non-reactive displacement in the context of stability. In all the simulations, we have considered $Pe = 3000$ and $r_0 = 0.075$, if we put the same value of Pe and r_0 in equation (3.10), we obtain the critical $R_b = 0.642$. In addition, if we find the range for this critical viscosity ratio in 95 % confidence bound, we obtain $R_b \in (0.466, 0.817)$. The obtained critical viscosity R_b for the reactive case lies in the range $R_b \in (0.466, 0.817)$ and is almost the same as the calculated viscosity ratio, $R_b = 0.642$ for the non-reactive displacement.

Though the viscosity profile is modified only when $R_b \neq R_c$, thus the effect of product viscosity R_c on stability can be compared along the line $R_b = R_c$ whether the reaction increases or decreases the viscosity of the system. The specific value $(R_b, R_c) = (0.66, 0.66)$ distinguishes the stability behavior of reactive and non-reactive displacement. Furthermore, during the LSA analysis, we noticed an asymmetry in the (R_b, R_c) phase plane along the line $R_c = R_b$. Despite having the same viscosity contrast $(|R_c - R_b|)$, perturbations exhibit a higher growth rate when $R_c > R_b$ compared to the opposite case, $R_c < R_b$ as in figure 3.3(b) and 3.7(a). The critical viscosity contrast is greater when the reaction decreases viscosity, *i.e.*, $R_c < R_b$, than in the opposite case, $R_c > R_b$, if a system is stable for the non-equivalent situation as shown in figures

3.6 and 3.7(b). Similarly, in the (R_b, R_c) phase plane obtained from nonlinear simulations, we observe asymmetry along the line $R_c = R_b$. The critical R_b decreases more significantly when $R_c > 0.66$ compared to when $R_c < 0.66$. To visualize more about this asymmetry, we have plotted a phase plane between $R_c/2$ and $R_b - R_c/2$ that shows viscosity contrast at upstream and downstream mixing zone in figure 3.11(a). It can be observed that if the upstream mixing zone is stable, the critical viscosity contrast for instability, $R_b - R_c/2$ is more than $R_c/2$ if the downstream mixing zone is stable. The asymmetry is a consequence of the spatially dependent base state velocity profile. When $R_c < 0.66$, the instability appears at the downstream mixing zone due to steeper viscosity contrast while the upstream mixing zone stabilizes the flow. On the contrary, when $R_c > 0.66$, the instability appears at the upstream mixing zone for the same viscosity contrast at the unstable zone. If we compare both R_c values for the same R_b maintaining the viscosity gradient $|R_c - R_b|$, the driving force provided by convection is more efficient at the upstream mixing than at the downstream mixing zone. Consequently, the critical viscosity contrast to trigger instability at the upstream mixing zone $R_c/2$ is less than the critical viscosity ratio, $R_b - R_c/2$, to trigger the instability at the downstream mixing zone. Similar asymmetric behavior is observed in [94]. A higher viscosity ratio is required for instability when the reaction produces a less viscous product for $R_b = 0$ compared to when the product is highly viscous.

3.4.1 Effect of Da and Pe ($Da \rightarrow \infty$)

It is reported that the stable region exists for all moderate ranges of Da , and the width of the interval of stable R_c decreases with Da when $R_b = 0$ [94]. Interestingly, the stable region even exists for $Da \rightarrow \infty$ when $R_b = 0$ [113]. When we increase Da , more product is formed that enhances the viscosity of the system as in equation (3.2), leading to an enhanced viscosity contrast and a higher growth rate of perturbations in the system as predicted by LSA and illustrated in figure 3.3(b), 3.6 and 3.7. Hence, the critical viscosity ratio decreases for higher Da as shown in figures 3.6, 3.7(b) and 3.10. However, the existence of the critical viscosity contrast is shown only for the particular case, $R_b = 0$. It will be intriguing to examine whether that critical viscosity occurs or identify the range of R_c that corresponds to stable displacements when $R_b \neq 0$. To investigate the same, we have performed simulations for a wide range of Da , including the limiting case $Da \rightarrow \infty$.

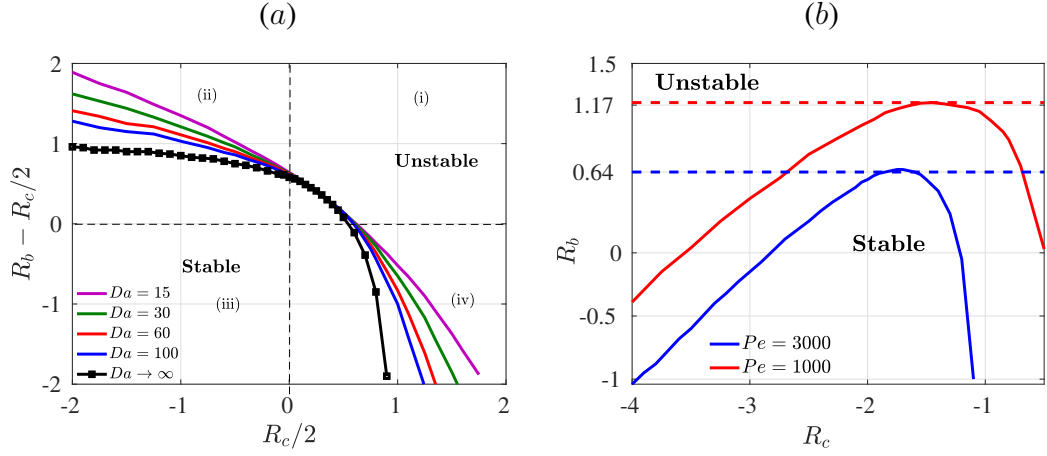


FIGURE 3.11: (a) Phase plane between the viscosity ratio at upstream mixing and downstream mixing zone, $R_c/2$ and $R_b - R_c/2$ for $Pe = 3000$ and various Da . (b) (R_b, R_c) phase plane for $Pe = 3000, 1000$ for $Da \rightarrow \infty$. Here below the curve is a stable region, and above the curve is an unstable region. Here the dashed line corresponds to the non-reactive case $Da = 0$ for $Pe = 3000$ (blue) and $Pe = 1000$ (red).

For an instantaneous reaction, $Da \rightarrow \infty$, the reaction front occurs in an infinitesimally small region. This replicates an ideal situation where reactants are fully consumed at the reaction front as soon as reactants meet *i.e.* $a \rightarrow 0, b \rightarrow 0$ at the reaction front. The concept of upstream mixing and the downstream mixing zone is also based on this ideal situation $Da \rightarrow \infty$. The upstream mixing zone is only occupied by fluid A and C and the downstream mixing zone is occupied by fluid B and C . In order to perform simulations for $Da \rightarrow \infty$, we rearrange our system of governing equations as in [113, 69, 66] as follows:

$$\frac{\partial h}{\partial t} + \mathbf{u} \cdot \nabla h = \frac{1}{Pe} \nabla^2 h, \quad (3.11a)$$

$$(a, b, c) = \begin{cases} (0, 1 - 2h, h), & h < 0.5, \\ (-1 + 2h, 0, 1 - h), & h \geq 0.5 \end{cases}. \quad (3.11b)$$

We perform numerical simulations and the numerical method is explained in the next chapter §4. In figure 3.10, we have plotted the critical (R_b, R_c) curves for various Da . The stable zone in (R_b, R_c) phase plane contracts for increasing Da but does not vanish even when $Da \rightarrow \infty$. It can be verified from the recent article [53] for the asymptotic limit of Pe and Da . For $R_b = 0$, it is reported that the minimum viscosity contrast to induce the instability is more *i.e.* $|R_c| > 0$ if the reaction generates a less viscous product ($R_c < 0$) than a high viscous product ($R_c > 0$).

Further, the stable region in the $Da - R_c$ phase plane along the line $R_c = 0$ becomes less symmetric with Da [94]. We observe the same for the case when $R_b \neq 0$. The stable region in the (R_b, R_c) phase plane becomes asymmetric for increasing Da around the line $R_c = R_b$.

In addition, if we consider $Da = 0$, the stable region is obtained as $R_b < 0.64$, and the remaining region in the (R_b, R_c) phase plane is an unstable zone. Further, the viscosity profile is monotonic in the neighborhood of $R_b = R_c$, and it is identical for each Da . Thus, the VF dynamics remain unchanged, and for this particular viscosity, all (R_c, R_b) curves showing the critical viscosity contrast, are merged for various Da in the neighborhood of $R_b = R_c$. This can be confirmed by both, LSA and NLS as shown in figure 3.8 and 3.10, respectively. Thus, the reaction affects the stability of the flow, but the inherent non-reactive system equally contributes to the instability. There exists a region in the (R_b, R_c) phase plane that is preserved and unaffected by the reaction. This illustrates that the reaction is able to influence the stability of the system and may destabilize the initially stable system, but there is some extent.

Further, it can be observed that if we increase the value of r_0 , it leads to weaker convection even at the initial time [93]. Consequently, the critical viscosity contrast required to trigger instability also increases for larger r_0 as stated in the equation (3.10), and this holds true for reactive fluids as well. In the phase plane (R_b, R_c) illustrated in Figure 3.10, the maximum critical value of R_b required to induce instability increases with the increment of r_0 , following the relationship (3.10). Below this maximum value of R_b , the stable range of R_c expands with an increase in r_0 for each R_b .

At last, we check the effect of Pe on the stability of the system for given other parameters (Da, R_b, R_c) . The Pe number definition suggests a tuning between the flow rate and diffusion coefficient. In another way, it decides the competition between forces due to convection and diffusion and flow gets stabilized for decrements in Pe as diffusion works as stabilizing factor. It is already reported that the stable region in the R_c - Da plane widens for decreasing Pe . However, the qualitative behavior shown by the critical R_c - Da curves remains preserved for varying Pe [94]. To understand the effect of Pe on the VF dynamics when $R_b \neq 0$, we have fixed Da by $Da \rightarrow \infty$ and performed simulations for $Pe = 3000, 1000$. For $Pe = 1000$, the stable zone widens, and critical (R_b, R_c) increases to trigger the instability as in figure 3.11(b). Also, we can examine the critical viscosity ratio obtained in the case $R_b = R_c$ for that VF dynamics gets

unaffected by chemical reaction for $Pe = 1000$. The critical viscosity ratio for non-reactive displacements is found around $R_b = R_c = 1.17$ for $Pe = 1000$, is the same value as computed from the equation (3.10) for $Pe = 1000$ and r_0 .

3.5 Conclusion

Reactive flows in a porous medium are encountered in several transport phenomena that affect the productivity of the process, as the chemical reaction can alter the physical properties at the fluid-fluid interface. The presented problem is motivated as the generated product modifies the viscosity profile that affects the overall stability of the system. In this chapter, we address the stability of a reactive system $A + B \rightarrow C$ in a porous medium subjected to VF instability exploring a range of (R_b, R_c) through LSA. We discuss how the product viscosity of the inherent system influences the temporal evolution of the perturbations.

The LSA predicts that the modified viscosity contrast *i.e.* $R_c \neq R_b$ stimulates the growth rate of perturbations. This leads to an earlier onset of instability and a higher growth rate of perturbations if the flow is already unstable without the reaction. These results agree with the experimental studies [71, 70] as the reaction enhances the instability for radial flow. On the other hand, if the corresponding non-reactive displacement is stable, such chemical reactions can be categorized into two parts based on product viscosity, R_c . For a given reaction rate, Da , we can find a range of reaction types, R_c including $R_c = R_b$ which correspond to the stable flow. In such reactive displacement, the altered viscosity profile is not enough to trigger instability. The system becomes unstable for the remaining reaction types R_c . Another conclusion that can be drawn from the LSA is that the system exhibits an early onset time and more amplified perturbations when induced by a high viscous product generation rather than a less viscous product. Moreover, such reactive displacements show a higher growth rate of perturbations if we increase Da . While the stable range of R_c contracts if the corresponding non-reactive displacement is stable. Also, some reactions exist where product viscosity is the same as the reactant, B , $R_c = R_b$, and thus the stability of the system remains unaltered after the reaction regardless of Da .

Further, we perform non-linear simulations to determine the critical viscosity ratio (R_b, R_c) exhibiting instability in reactive flow for a given Da and Pe . We provide sufficient data to

determine the stability of the reactive flow. We present a (R_b, R_c) phase plane separated by critical viscosity ratio for instability into the stable and unstable regions for the entire range of Da and various Pe explored. The importance of each parameter in determining the stability of the system is explained by the phase plane. The stable region in the (R_b, R_c) phase plane reduces for increasing Da and Pe but never completely disappears.

Chapter 4

Computational analysis of radial viscous fingering induced by an infinitely fast chemical reaction

4.1 Introduction

In this chapter¹, we focus on the investigation of the non-linear interactions between infinitely fast reactions and VF dynamics. Various experimental studies involve fluids undergoing neutralization reactions which are an example of instantaneous reaction as the reaction rate is very large for such reactions. [72, 74, 71]. Nagatsu et al. [71] experimentally showed the effect of an instantaneous chemical reaction on viscous fingering by considering the radial displacement of the reactive as well as non-reactive fluids. They observed widening of the fingers for the reactive case when viscosity is increased by the chemical reaction, while the shielding effect is more than the non-reactive case when the chemical reaction decreases the viscosity. In another study, Nagatsu et al. [70] explored the effect of the reaction rate on miscible VF involving radial displacement of the reactive fluids, in terms of a non-dimensional parameter Damköhler number Da defined as the ratio of the convective time scale to the reactive time scale. They reported the dynamics for moderate Da to be different than those for a sufficiently high Da [71] signifying a dependence of the fingering dynamics on the reaction rate.

Further, the effect of an infinite Da on the VF dynamics is explored numerically by Nagatsu and De Wit [69] where the chemical reaction modifies the viscosity in the system undergoing rectilinear displacement. But due to the difference in the displacement used in the simulations as well as in the experiments opposite trends in experimental finger width [71] are obtained. Recently Sharma et al. [94] have discussed VF induced by chemical reactions by considering reactants having same viscosity but generating a more and less viscous product for radial displacement. They explore the VF dynamics for a range of finite Da and obtain qualitative agreement with experiments [78, 83]. Further, for a given Da , the existence of critical viscosity contrast for the occurrence of VF is reported. However, the viscous fingering induced solely

¹This chapter is published in the *J. Fluid Mech.*.

by instantaneous chemical reactions for radial displacements is unexplored. In this work, we numerically discuss reactive fingering dynamics for the limiting case $Da \rightarrow \infty$ for reactants undergoing radial displacement. We suitably modify the governing equations to take care of $Da \rightarrow \infty$ similar to the work of Nagatsu and De Wit [69], Michioka and Komori [66]. We gain insight into the effect and the interaction of the forces due to convection, diffusion and reaction on VF in terms of the dimensionless parameters and see if the stable displacement still exists when the chemical reaction is infinitely fast. The stable displacement, if exists, implies that force due to the reaction is not sufficient to overcome the other two forces due to convection and diffusion. Thus, the triggering of the instability also depends upon the log-mobility ratio, R_c and the Péclet number, Pe which are a measure of the other two forces in the system. Hence, we determine the onset of instability in terms of these non-dimensional numbers.

The chapter is organized as follows. The governing equations are discussed in §4.2 followed by modifying the equations to deal with $Da \rightarrow \infty$ in §4.3. We discuss the results in terms of the onset of instability and finger length in §4.4, followed by the conclusion in §4.5.

4.2 Mathematical formulation

We consider two fluids A and B as reactants undergoing a second-order chemical reaction



upon contact to generate another fluid C as the product. The fluid A radially displaces fluid B in a two-dimensional homogeneous and isotropic porous medium having constant permeability $\tilde{\kappa}$. We consider the fluids to be miscible and the reactants have same viscosity $\mu_A = \mu_B = \mu_0$, while the viscosity of the product μ_C may be different than the reactants. Considering the fluids to be incompressible and neutrally buoyant, we use a system of coupled non-linear partial differential equations (PDEs) [94] to model the flow of reactive fluids in the porous medium. The system of PDEs comprises a continuity equation and Darcy's law respectively for the conservation of mass and momentum of the flow through a porous medium, coupled to three convection-diffusion-reaction equations for the mass balance of the three fluids A , B and C .

The non-dimensional governing equations are

$$\nabla \cdot \mathbf{u} = 0, \quad (4.1a)$$

$$\nabla p = -\mu(c)\mathbf{u}, \quad (4.1b)$$

$$\frac{\partial a}{\partial t} + \mathbf{u} \cdot \nabla a = \frac{1}{Pe} \nabla^2 a - Da \, ab, \quad (4.1c)$$

$$\frac{\partial b}{\partial t} + \mathbf{u} \cdot \nabla b = \frac{1}{Pe} \nabla^2 b - Da \, ab, \quad (4.1d)$$

$$\frac{\partial c}{\partial t} + \mathbf{u} \cdot \nabla c = \frac{1}{Pe} \nabla^2 c + Da \, ab, \quad (4.1e)$$

where $\mathbf{u} = (u, v)$, p, μ respectively denote the dimensionless Darcy velocity, pressure and viscosity. The non-dimensional chemical concentrations of the fluids A, B, C are a, b, c , respectively. These equations are non-dimensionalised as in chapter 2. The viscosity-concentration relation is taken here as:

$$\mu(c) = e^{R_c c}, \quad R_c = \ln \left(\frac{\mu_C}{\mu_0} \right), \quad (4.2)$$

where μ_0 and μ_C are viscosities of the reactants and product, respectively and R_c is the log-mobility ratio. Here, we encounter two more dimensionless parameters: the Damköhler number Da and the Péclet number Pe . We assume the three fluids have same diffusion coefficient D and hence only one Pe appears in all three CDR equations. The Péclet number is the ratio of the mass transfer due to convection and diffusion, while the Damköhler number being the ratio of convective time scale to reactive time scale depicts the relative importance of convection to that of reaction. As viscosity also contributes to the velocity of the fluid, we regard the log-mobility ratio as a measure of force due to convection. Thus, the three non-dimensional parameters actually provide a measure of the relative dominance of one of the three forces each due to convection, diffusion and reaction. Since $Da \rightarrow \infty$ in this study, the force due to reaction is assumingly large and the absence or presence of any instability is due to the dominance of the other two forces due to convection and diffusion which we discuss by varying R_c and Pe in §4.4.

The fluid A is contained in a circle of non-dimensional radius r_0 initially and is surrounded by the fluid B (see figure 4.1(a)). The fluid A injected continuously with flow rate per unit depth Q from the injection hole located at the origin. The fluid A radially displaces fluid B and both

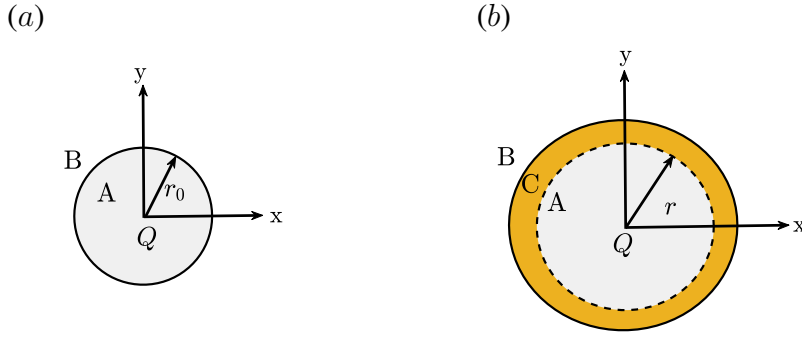


FIGURE 4.1: (a) A schematic of the problem at $t = 0$ showing reactant A contained in a circle of radius r_0 . The region outside the circle is occupied by reactant B . (b) The same schematic at $t > 0$ depicts the generation of the product C in the yellow-colored annulus region where the reactants come in contact. Here $r > r_0$.

fluids undergo a chemical reaction to produce C in the region between the reactants as shown in figure 4.1(b). Thus, the initial conditions associated with equation (4.1c)-(4.1e) are

$$(a, b, c)(x, y, t = 0) = \begin{cases} (1, 0, 0) & x^2 + y^2 \leq r_0^2 \\ (0, 1, 0), & \text{Otherwise} \end{cases}, \quad (4.3)$$

where r_0 is the radius of the circular region initial filled with fluid A . We discuss the boundary conditions in the next subsection where we describe the numerical scheme used to solve the governing system of equations.

4.3 Numerical scheme

We perform numerical computations in Cartesian coordinates by considering a square computational domain with the injection hole being at the origin of the coordinate system. For numerical computations, we choose a non-dimensional domain $\Omega = [-L/2, L/2] \times [-L/2, L/2]$. In this study, we take $L = 1.5$ and the domain is discretized into $n_x \times n_y$ grid points. (see appendix A for grid independence study). Further, $r_0 = 0.075$ throughout this study. There are a few challenges in performing a computational study of radial displacement of reactants undergoing an infinitely fast reaction. We have to deal with a singularity at the origin in the velocity field [17, 94] along with taking care of Da which approaches infinity. We discuss these two before discussing the numerical method.

As we can see that Da appears in all three convection diffusion reaction equations (4.1c)-(4.1e), hence, in order to numerically deal with infinitely fast reaction rate ($Da \rightarrow \infty$), we must wisely modify the equations. We observe that simply adding or subtracting two of the convection-diffusion-reaction equations can help eliminate Da from the equations. Hence, we add equations (4.1c) & (4.1e) and equations (4.1d) & (4.1e) to obtain following two equations:

$$\frac{\partial H_1}{\partial t} + \mathbf{u} \cdot \nabla H_1 = \frac{1}{Pe} \nabla^2 H_1, \quad (4.4a)$$

$$\frac{\partial H_2}{\partial t} + \mathbf{u} \cdot \nabla H_2 = \frac{1}{Pe} \nabla^2 H_2, \quad (4.4b)$$

where $H_1 = a + c$ and $H_2 = b + c$. It must be noted that now we have two convection-diffusion equations (4.1a), one for each $H_i, i = 1, 2$ satisfying two different initial conditions ($H_1(x, y, t = 0) = a(x, y, t = 0)$ and $H_2(x, y, t = 0) = b(x, y, t = 0)$ as $c(x, y, t = 0) = 0$), while each satisfies no flux boundary condition. Further, by using a suitable normalization [69],

$$h_i = \frac{H_i - H_{i;B_0}}{H_{i;A_0} - H_{i;B_0}}, i = 1, 2, \quad (4.5)$$

we will show that we only need to solve one convection-diffusion equation. For $i = 1, 2$, we denote normalised H_i as h_i . While $H_{i;B_0}$ is the value of H_i inside the region of displaced fluid and $H_{i;A_0}$ is the value of H_i in the region of displacing fluid, that is,

$$H_{1;B_0} = 0, \quad H_{2;B_0} = 1, \quad (4.6)$$

$$H_{1;A_0} = 1, \quad H_{2;A_0} = 0. \quad (4.7)$$

Substituting the values of $H_{i;B_0}$ and $H_{i;A_0}$ in equation (4.5), we obtain the value of $h_i, i = 1, 2$ as:

$$h_1 = a + c, \quad h_2 = 1 - (b + c). \quad (4.8)$$

It is evident that both h_1, h_2 now satisfy the following two convection-diffusion equations

$$\frac{\partial h_i}{\partial t} + \mathbf{u} \cdot \nabla h_i = \frac{1}{Pe} \nabla^2 h_i, \quad i = 1, 2, \quad (4.9)$$

associated with the same following initial condition for both the equations

$$h_i(x, y, t = 0) = \begin{cases} 1, & x^2 + y^2 \leq r_0^2 \\ 0, & \text{Otherwise} \end{cases}, \text{ for } i = 1, 2. \quad (4.10)$$

Thus, in place of solving two different equations each for $h_i, i = 1, 2$, we can denote $h_1 = h_2 = h$ and solve the following differential equation for h

$$\frac{\partial h}{\partial t} + \mathbf{u} \cdot \nabla h = \frac{1}{Pe} \nabla^2 h, \quad (4.11)$$

associated with the initial condition (4.10) with h_i replaced with h . It is not possible to find the solution of the above equation using similarity variables [93]. Thus, we solve the above equation numerically as explained ahead. The computed h value is used to find the concentration a, b, c [Nagatsu and De Wit [69] and Ref. therein] as explained below.

When we consider the chemical reaction to be infinitely fast, that is, $Da \rightarrow \infty$, the reactive time scale, $1/(\tilde{k}\tilde{a}_0)$ becomes very small such that it is negligible in comparison to the convective time scale. Introducing such small time steps in simulations is quite difficult. To avoid such circumstances, we opt conserved scalar approach to handle this infinitely fast reaction term. It is safe to use this approach as it can be utilized for infinitely fast reactions only, not for moderately fast reactions [66, 20]. To obtain a, b, c from h , we utilize the fact that the reaction occurs with an infinite reaction rate. The region where both the reactants co-exist and thus react to generate the product is termed the reaction front. But as $Da \rightarrow \infty$, the two reactants are consumed as soon as they come in contact and the concentration of both the reactants tends to zero in the reaction front [69]. (See appendix B for details.) Thus, using equation (4.8), we obtain that in the reaction front $c = h = 0.5$. The two reactants cannot co-exist outside the reaction front, that is, when $h \neq 0.5$. Thus, for $h < 0.5$, we have $a = 0$ and we get from equation (4.8) that $b = 1 - 2h, c = h$. Similarly, for $h > 0.5$ and $b = 0$, we get $a = 2h - 1, c = 1 - h$. See appendix B for details. Thus, solving only one convection diffusion equation (4.11) for h , we can obtain the reactant and the product concentration as

$$(a, b, c) = \begin{cases} (0, 1 - 2h, h), & h < 0.5, \\ (-1 + 2h, 0, 1 - h), & h \geq 0.5 \end{cases}. \quad (4.12)$$

$c = h = 0.5$. The two reactants cannot co-exist outside the reaction front, that is, when $h \neq 0.5$. Thus, for $h < 0.5$, if we assume $a = 0$, we get from equation (4.8) that $b = 1 - 2h, c = h$. It must be noted that there exist two more choices of H_1, H_2 and thus obtained h_1, h_2 are different than those used here. (See appendix B for details.). But we obtain the same equation (4.12) in each case. Thus, in order to deal with $Da \rightarrow \infty$, we actually simplified the situation by having to deal with only one convection-diffusion equation in place of three convection-diffusion-reaction equations. It is mentioned that the above method is applicable even when the initial concentration of the reactants is unequal. We define $\phi = \tilde{b}_0/\tilde{a}_0$ as the ratio of the initial concentration of the two reactants. In our study, we take $\phi = 1$ but for $\phi \neq 1$, equation (4.6)-(4.8), (4.12) will be modified to include ϕ as follows [53]:

$$(a, b, c) = \begin{cases} (0, \beta - (1 + \beta)h, h), & h < h_\xi, \\ (-\beta + (1 + \beta)h, 0, \beta(1 - h)), & h \geq h_\xi \end{cases}. \quad (4.13)$$

Here, h_ξ is the value of h at reaction front, considering $a = b = 0$, that gives $h_\xi = \frac{\phi}{1 + \phi}$. Now, we explain about resolving the singularity in the velocity field.

In the absence of any viscosity gradient, the radial flow is a potential flow with the velocity given as

$$\mathbf{u}_{pot}(x, y, t) = \left(\frac{x}{2\pi(x^2 + y^2)}, \frac{y}{2\pi(x^2 + y^2)} \right), \quad (4.14)$$

which clearly has a singularity as $(x, y) \rightarrow (0, 0)$. We get rid of this singularity by introducing an exponential modification regarded as a Gaussian source in literature [17, 94]

$$\mathbf{u}_{pot} = \left(x \frac{1 - e^{-(x^2 + y^2)/\sigma_1^2}}{2\pi(x^2 + y^2)}, y \frac{1 - e^{-(x^2 + y^2)/\sigma_1^2}}{2\pi(x^2 + y^2)} \right), \quad \sigma_1 \leq r_0, \quad (4.15)$$

where we fix $\sigma_1 = 0.075$ in all the simulations so that the exponential function introduced to deal with the singularity at the origin has no effect on the VF dynamics. We consider the fluid A inside a circle of initial radius r_0 and $\sigma_1 \leq r_0$ so that the exponential function has no effect on the VF dynamics. This is due to the fact that with an increase in r (where $r^2 = x^2 + y^2$), the exponential term will eventually decay and will have no effect on the velocity. We consider the computational domain $\Omega = [-0.75, 0.75] \times [-0.75, 0.75]$ and we have taken $r_0 = 0.075$, so that the initial circular region has covered less than 5% of the total computational domain. (See

appendix A for the effect of different σ on the dynamics.) It must be noted that \mathbf{u}_{pot} is the total velocity in the absence of any viscosity gradient but as soon as the reactants come in contact to generate a more or less viscous product than the reactants, the viscosity gradient alters the total velocity. Thus, we consider the total velocity to contain two components

$$\mathbf{u} = \mathbf{u}_{pot} + \mathbf{u}_{rot}, \quad (4.16)$$

where \mathbf{u}_{rot} is the velocity component due to the chemical reaction and must be computed at each time, while \mathbf{u}_{pot} is known at all time. To compute \mathbf{u}_{rot} , we use stream function ψ defined as $\mathbf{u}_{rot} = \left(\frac{\partial \psi}{\partial y}, -\frac{\partial \psi}{\partial x} \right)$. We take curl of Darcy's law (4.1b) to obtain stream function vorticity formulation

$$\nabla^2 \psi = -\omega, \quad (4.17a)$$

$$\omega = R_c \left(v \frac{\partial c}{\partial x} - u \frac{\partial c}{\partial y} \right). \quad (4.17b)$$

Here ω is the $\hat{\mathbf{k}}$ component of the vorticity vector. Above equation (4.17) coupled with the convection-diffusion equation (4.11) for h is solved to explore the VF dynamics after using equation (5.6b) to obtain the species concentration from h . The boundary conditions used are

$$\psi = 0, \quad (4.18)$$

$$\nabla h \cdot \hat{\mathbf{n}} = 0, \quad (4.19)$$

at $x = \pm L/2, y = \pm L/2$. Here $\hat{\mathbf{n}}$ is the unit outward normal. We perform numerical simulations by using a hybridization of compact finite difference method and the pseudo-spectral method [94]. We employ sixth-order compact finite difference method [59] along y -direction and Fourier sine expansion in x -direction to solve the Poisson equation (4.17). In order to solve the convection-diffusion equation for h , we use the method of lines. The spatial derivatives are discretized using compact finite difference of sixth order. Thus obtained semi-discretized system of ordinary differential equations is solved using the third order Runge-Kutta method. The time steps are adaptive for Runge-Kutta method and satisfy Courant-Friedrichs-Lewy (CFL) condition. More details about the numerical method can be found in [94] and the references therein.

4.3.1 Order of convergence

We discuss here the order of convergence of the numerical method. The time step dt is chosen adaptively in order to satisfy the CFL condition. So, we perform the convergence analysis for spatial discretization only. The numerical method is said to be convergent if there exist two non-zero constants C_1 and P such that $|s_N - s_0| \leq C_1 dx^P$. Here s_N, s_0 are respectively the numerical and the exact solution, P is the order of the convergence and C_1 is independent of dx , the spatial step size. In other words, a numerical method is said to be of order P if the error in numerical solution is $O(dx^P) = M_1 dx^P$ [13].

To find the order of convergence, we perform simulations for four sets of grid points $n_x = n_y$ keeping all other parameters the same. Also, we know $n_x = n_y = N + 1$, where N is the number of sub-intervals. The spatial step sizes are defined as $dx = dy = L/N$ where L is the domain length. We choose the numerical solution corresponding to the maximum value of N , that is, $N = 1024$ as the exact solution: $s_0 = s_{1024}$. The error corresponding to each N is computed as $\epsilon_N(t) = \frac{\|s_N - s_0\|}{\|s_0\|}$. Further, we consider the worst case scenario and denote the error for the solution with N sub-intervals as $E_N = \max_{0 \leq t \leq 1} \epsilon_N(t)$. We compute the order P of the numerical method as [13, 25, 43]:

$$P = \log_2 \left(\frac{E_N}{E_{2N}} \right) \quad (4.20)$$

We follow the steps below to find order:

Step 1: Compute the numerical solution s_N for each N . We take s_N, s_0 as the concentration of reactants as well as product by replacing s by a, b, c , respectively.

Step 2: The error $\epsilon_N(t) = \frac{\|s_N(x, y) - s_0(x, y)\|}{\|s_0(x, y)\|}$ for various grid points is calculated. We denote the discretised x and y domain for $N = 128, 256, 512$ as:

$$\begin{aligned} \mathbf{x} &= \{x_0(= -0.75), x_1, x_2, \dots, x_j, \dots, x_N(= 0.75)\}, \\ \mathbf{y} &= \{y_0(= -0.75), y_1, y_2, \dots, y_j, \dots, y_N(= 0.75)\}. \end{aligned}$$

Also, the discretised x and y domain for $N = 1024$ is denoted as:

$$\begin{aligned} \mathbf{X} &= \{X_0(= -0.75), X_1, X_2, \dots, X_j, \dots, X_N(= 0.75)\}, \\ \mathbf{Y} &= \{Y_0(= -0.75), Y_1, Y_2, \dots, Y_j, \dots, Y_N(= 0.75)\}. \end{aligned}$$

N	E_N^C	P	E_N^A	P	E_N^B	P
128	0.0444	1.094	0.0014	0.9489	0.0012	0.9
256	0.0208	1.5305	0.0075	1.585	0.0006427	1.5029
512	0.0072	-	0.0025	-	0.0002678	-

TABLE 4.1: Error and order for various N . Used parameters are $Pe = 2000$, $R_c = 0$. E_N^C , E_N^A and E_N^B respectively denote the error in the numerical solution of product concentration, reactant A concentration and reactant B concentration.

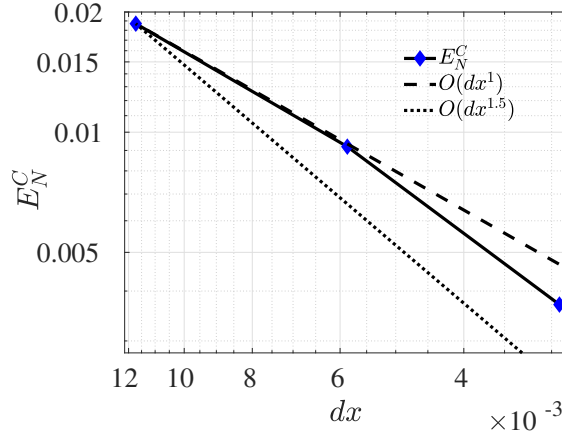


FIGURE 4.2: Error in product concentration E_N^C versus dx for $Pe = 2000$, $R_c = 0$. The dashed and dotted lines represent the reference lines with slope dx and $dx^{1.5}$, respectively.

For any N , we compute $\epsilon_N(t)$ as

$$\epsilon_N(t) = \frac{\|s_N(x = x_i, y = y_j) - s_0(x = X_{\Delta i}, y = Y_{\Delta j})\|}{\|s_0(x = X_{\Delta i}, y = Y_{\Delta j})\|},$$

where $i = \{0, 1, 2, \dots, N\}$ and $j = \{0, 1, 2, \dots, N\}$ and $\Delta = 1024/N$. For example, $\epsilon_N(t)$ for $N = 512$ is computed as:

$$\epsilon_{512}(t) = \frac{\|s_{512}(x = x_i, y = y_j) - s_0(x = X_{2i}, y = Y_{2j})\|}{\|s_0(x = X_{2i}, y = Y_{2j})\|},$$

for $i = \{0, 1, 2, \dots, 512\}$ and $j = \{0, 1, 2, \dots, 512\}$. Here we present results using 2-norm. However, it is verified that results are independent of the norm.

Step 3: Find the error as $E_N = \max_{0 \leq t \leq 1} \epsilon_N(t)$.

Step 4: Compute order of convergence of the numerical method.

We present the error and the order in table 4.1. It is evident that with an increase in N , the error reduces significantly. We plot the error in the numerical solution of product concentration E_N^C as a function of dx in figure 4.2. Also, reference lines with slope dx , $dx^{1.5}$ are plotted. It

is evident that the order of convergence of the method lies between 1 and 1.5. There exist many studies [25, 60, 43, 49] where the order of convergence of the method is lower than the order of discretization of the derivatives. In our work also, spatial discretization is performed using sixth-order compact finite difference at the internal grid points, while the boundary points are discretized using third and fourth-order compact finite difference. But since we have a coupled system of non-linear and fully coupled partial differential equations, we believe that order between 1 and 1.5 is adequate as evident from small error in table 4.1.

4.4 Results and discussion

VF induced by chemical reaction is discussed by Sharma et al. [94] and it is observed that for a given finite reaction rate (Da) and Pe , there always exists a range of R_c for which only a stable displacement is observed. Motivated by this, we ask what happens if $Da \rightarrow \infty$, that is, the chemical reaction is instantaneous. For $Da \rightarrow \infty$, the reaction rate and hence the force due to reaction is strong enough to trigger any instability but how the interplay of this force with forces due to convection and diffusion affect the overall VF dynamics is worth examining.

We consider reactants to have no viscosity contrast and they undergo an infinitely fast chemical reaction upon contact, generating a product having same or different viscosity. When all the species have same viscosity, the product is generated in a ring between the reactants A and B (see figure 4.1). Thus, the obtained region between A and C is regarded as the upstream mixing zone and that between B and C is regarded as the downstream mixing zone throughout this study independent of the displacement being stable or unstable. The product with different viscosity is of interest to us as the viscosity contrast results in the fingering instability due to the viscosity profile being a non-monotonic function of space. If the product is more viscous than the reactants, the viscosity profile experiences a maximum and thus the upstream mixing zone witnesses instability. On the other hand, for a less viscous product, a minimum is obtained in the viscosity profile, thereby making downstream mixing zone an unstable one where a less viscous fluid displaces a more viscous one. We explore various features of VF due to a chemical reaction with an infinitely fast reaction rate between the reactants undergoing radial displacement.

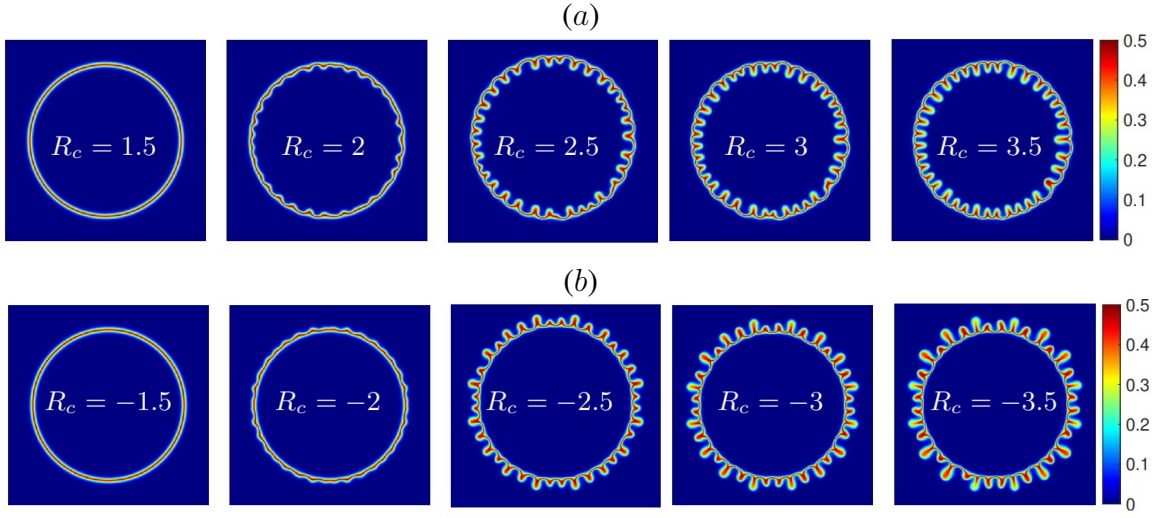


FIGURE 4.3: Density plots of product C concentration at final time $t = 1$ for $Pe = 3000$ and (a) $R_c > 0$ (in first row) (b) $R_c < 0$ (in second row). *Flower* like instability for $R_c \geq 2$ and *crown* like instability for $R_c \leq -2$ is evident.

4.4.1 Effect of different reactants on the VF dynamics

The outcome of a chemical reaction depends on the type of reactants considered. Hence, in this section, we discuss the VF dynamics by considering the reactants having different viscosity contrast and diffusion coefficients. Numerically, R_c and Pe are the two parameters describing these properties. For a fixed R_c , a higher Pe represents the reactants having a small diffusion coefficient and hence rigorous fingering instability is anticipated. Further, by the definition of R_c in equation (4.2), it is clear that $R_c > 0$ corresponds to a more viscous product while a less viscous product is generated for $R_c < 0$. We discuss the effect of these two parameters in order to understand the VF dynamics for a range of reactants undergoing infinitely fast chemical reactions.

4.4.1.1 Varying the viscosity of the reactants

As discussed, $R_c > 0$ corresponds to a more viscous product and hence the upstream mixing zone is unstable to instability. In figure 4.3(a), product C concentration for various $R_c > 0$ is plotted (see appendix D for components of velocity). We observe fingers towards the source (origin), in the form of a *flower* and the downstream mixing zone acts as a barrier to the instability preventing the fingers from penetrating further. Similarly, for $R_c < 0$, the fingers are observed at the downstream mixing zone away from the source and appear as a *crown* (see figure 4.3(b)). Further, with an increase in $|R_c|$, the fingering instability becomes more rigorous. These are in

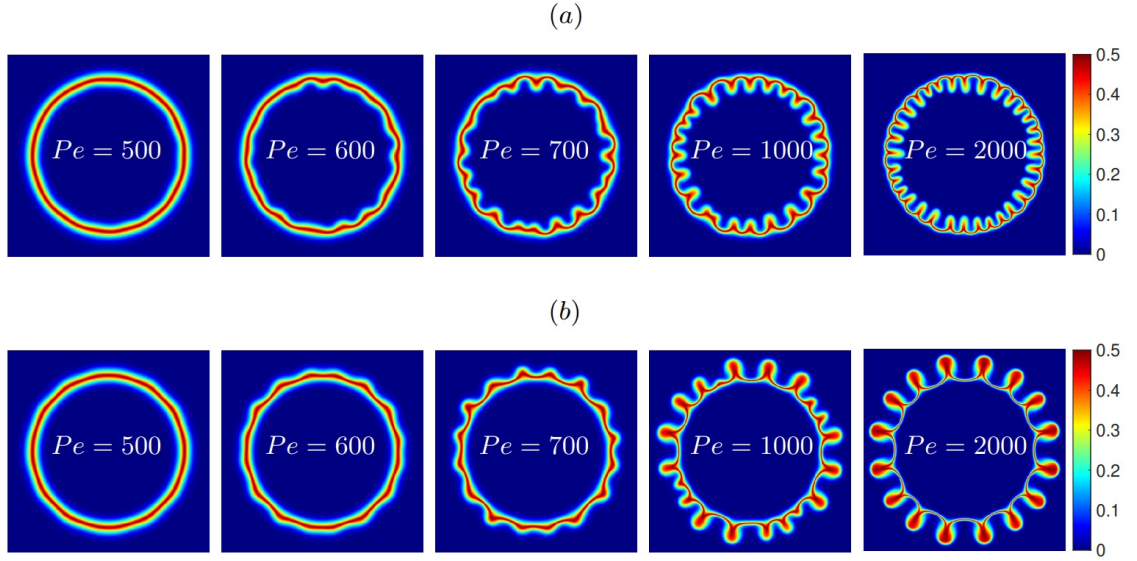


FIGURE 4.4: Density plots of product C concentration for various Pe and (a) $R_c = 5$ (in first row), (b) $R_c = -5$ (in second row) at final time $t = 1$.

agreement with the existing numerical [94] and experimental [71, 78] studies involving finite Da . Thus, these salient features of VF dynamics are independent of the reaction rate. The length of the fingers appears to depend on R_c and we shall discuss this in detail in §4.4.2.3. Also, no deformations are observed for the displacement corresponding $|R_c| = 1.5$ signifying completely stable displacement. Thus, despite, an infinite Da , stable displacement is evident for some $|R_c|$ and fixed Pe .

4.4.1.2 Effect of Péclet number

Fixing R_c , we vary the Péclet number to explore the effect of diffusion on the fingering dynamics. We plot the density plots of the product concentration at non-dimensional final time $t = 1$ for $R_c = 5$ in figure 4.4(a) and $R_c = -5$ in figure 4.4(b). As the Da is infinite, sufficient product is formed as soon as the reactants come in contact and hence rigorous instability is anticipated as convection is strong near the source. Indeed, with an increase in Pe , fingering instability is evident, however, stable displacement is observed for the smallest $Pe (= 500)$ shown. Thus, despite the reaction rate being infinite and a high viscosity contrast ($|R_c| = 5$ here), the diffusion is strong enough to prevent instability. Thus, for a given viscosity contrast between the reactants, stable displacement is observed which is in agreement with the existing recent studies [94, 93] that reported an unfavorable viscosity contrast being insufficient to induce the instability when fluids undergo radial displacement. To the best of the author's knowledge, no stable displacement

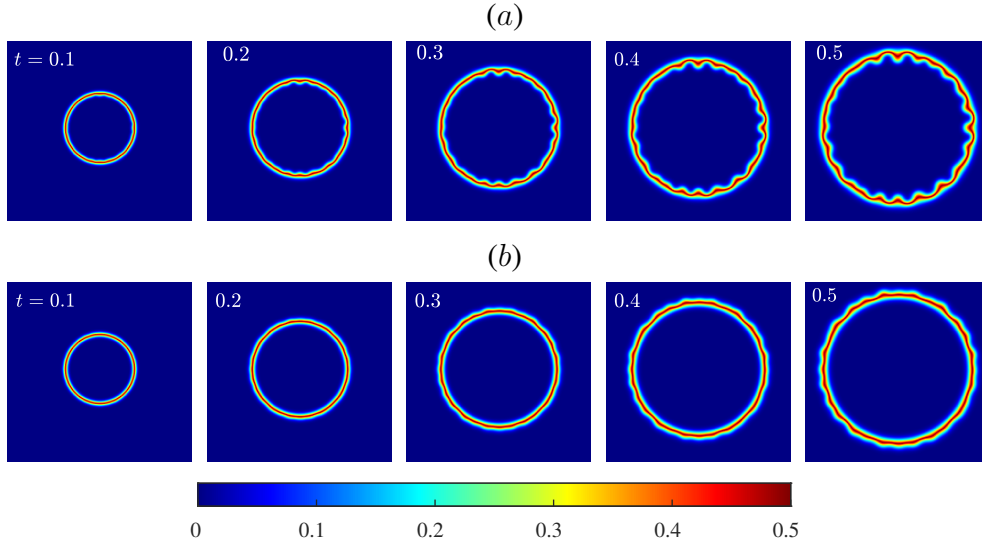


FIGURE 4.5: Temporal evolution of concentration of product for (a) $R_c = 4$ (in first row) and (b) $R_c = -4$ (in second row) for $Pe = 1000$. The instability appears at $t \approx 0.2$ for $R_c = 4$ while at $t \approx 0.3$ for $R_c = -4$.

is reported when the reactants displace each other rectilinearly [69]. Thus, three processes due to convection, diffusion and reaction interplay and affect the overall dynamics and it can be concluded that a stable region including a range of R_c for a fixed Pe and Da for which no VF is observed [94] never vanishes. We gain more insight into this by finding the onset time of instability in the next subsection.

4.4.2 Unstable displacements

We have shown in the previous section that a stable displacement exists despite an infinite Damköhler number but here we explore the unstable displacements. We start by understanding how the onset time varies with varying viscosity contrast and the Péclet number and then gain insight into the overall VF dynamics.

4.4.2.1 Onset of instability

The time when the fingers start to appear is referred to as the onset time of instability t_{on} . The density plots of product concentration for $|R_c| = 4$ and $Pe = 1000$ are shown in figure 4.5. It is evident from figure 4.5(a) that the fingering appears early for $R_c = 4$ in comparison to $R_c = -4$ in figure 4.5(b). This is due to the upstream mixing zone where the radial velocity is higher (than at the downstream mixing zone), is unstable for $R_c > 0$. We quantify the onset time with the

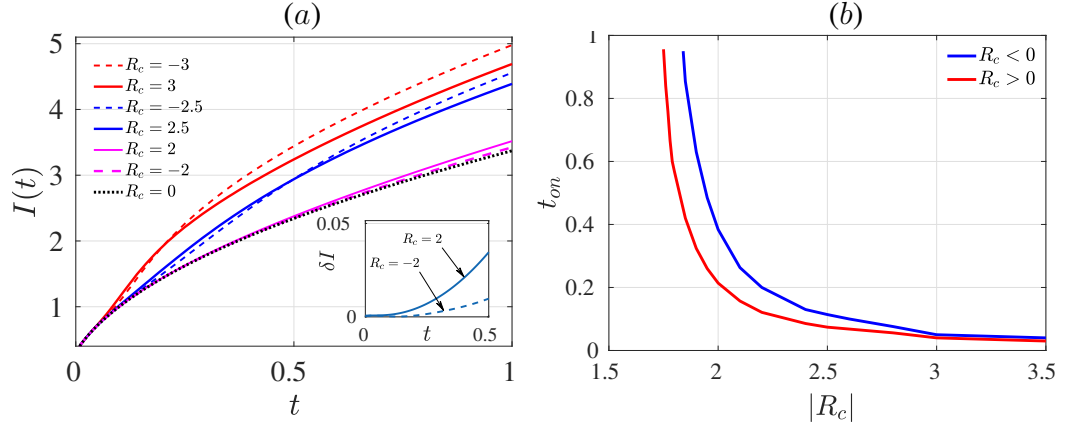


FIGURE 4.6: (a) Temporal evolution of the interfacial length for various R_c and $Pe = 3000$. Clearly, the onset of instability is early for $R_c > 0$. Inset: δI versus t for $|R_c| = 2$ showing the delayed onset for $R_c = -2$. (b) The onset time versus $|R_c|$ showing a delayed onset for $R_c < 0$.

help of the interfacial length defined as [94]

$$I(t) = \int_{x_1}^{x_2} \int_{y_1}^{y_2} \sqrt{\left(\frac{\partial c}{\partial x}\right)^2 + \left(\frac{\partial c}{\partial y}\right)^2} dy dx. \quad (4.21)$$

The product has the same viscosity as the reactants for $R_c = 0$ and hence a stable displacement is observed. We denote the interfacial length corresponding to $R_c = 0$ as I_0 and use the same as the reference for stable displacement. If the interfacial length for any $R_c \neq 0$ coincides with I_0 for some time, we regard the displacement as stable up to that time and denote the time when the two interfacial length curves start to deviate as t_{on} . We plot the interfacial length as a function of time for various R_c and $Pe = 3000$ in figure 4.6(a). Clearly, for some $|R_c|$, $I(t)$ for $R_c < 0$ deviates from $I_0(t)$ at a later time in comparison to the deviation for $R_c > 0$, indicating an early onset for $R_c > 0$. This is in contradiction to the delayed onset for $R_c > 0$ reported in the rectilinear geometry [35]. This can be attributed to the key difference between the rectilinear and the radial displacement which arises due to their respective velocity profiles. In rectilinear displacement, the velocity profile is uniform [101] which results in delayed onset for $R_c > 0$ as instability appears in a direction opposite to the flow. But in radial geometry, the velocity is spatially varying; the radial component of velocity being, $u_r = 1/2\pi r$ [102]. This velocity feeds instability with higher convective velocity when the product is more viscous and instability appears at upstream mixing zone resulting in early instability for $R_c > 0$. Further, it is observed that with an increase in $|R_c|$, the deviation occurs at the same time (see figure 4.6(a)) as sufficient product to trigger the instability is generated early. This is in agreement with the

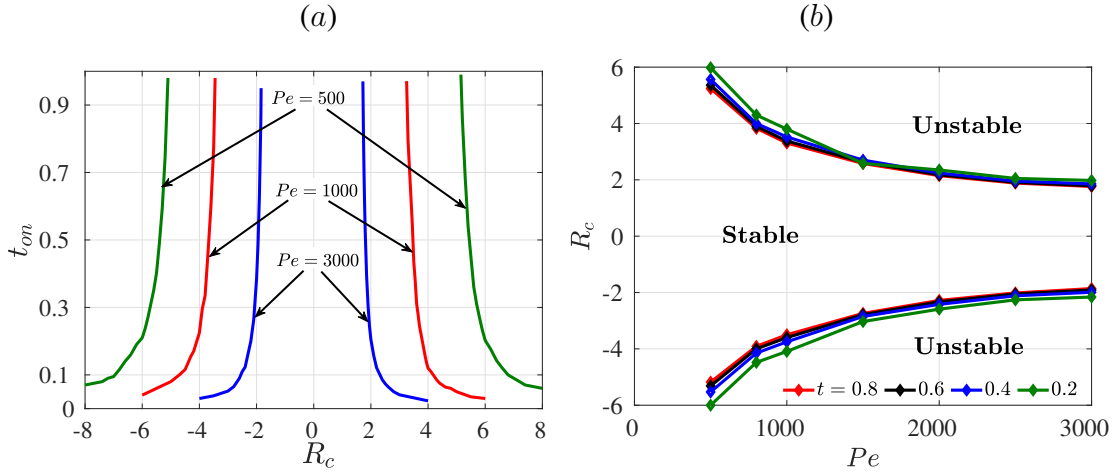


FIGURE 4.7: (a) Onset time t_{on} versus R_c for $Pe = 3000, 1000, 500$ showing a delayed onset for smaller Pe . (b) Plot for R_c versus Pe for a given time t .

instability generated by a chemical reaction with finite Da [94]. Of course, for a fixed Pe and R_c , the onset is early with an increase in Da but the force due to convection is the ultimate force out of the three forces due to convection, diffusion and reaction in action, deciding onset in this case.

For a fixed Pe , we calculate the absolute difference $\delta I(t) = |I(t) - I_0(t)|$ in the interfacial length of $R_c \neq 0$ and $R_c = 0$ and define the onset time of instability as

$$t_{on} = \min\{t > 0 : \delta I > tol\}, \quad (4.22)$$

here we have used tol to be $O(10^{-3})$. We plot t_{on} versus $|R_c|$ for $Pe = 3000$ in figure 4.6(b). Clearly, the onset is early for a larger viscosity contrast. It is evident that the displacement is more stable for $R_c < 0$ as t_{on} is more than that for the corresponding $R_c > 0$. Further, with an increase in $|R_c|$, the two curves approach each other indicating the onset time becomes independent of the sign of R_c which is a feature of radial displacement [94]. Also, no t_{on} is obtained for various $|R_c|$, for instance, $|R_c| = 1.5$. This is because a stable displacement is observed for such viscosity contrast indicating that the force due to reaction is not sufficient to trigger the instability. We conclude that for any time $t < t_{on}$, stable displacement is observed, while the VF instability is visible for $t \geq t_{on}$. Thus, the onset time can be used to divide the $t - R_c$ phase space into two zones with the region below the curve being the stable one and the region above the curve being unstable zone. Hence, this $t - R_c$ phase space provides information about the completely stable displacements and the time when instability is observed for the first

time if the displacement is unstable.

We determine the onset time of instability for various $|R_c|$ by varying Pe . The onset time t_{on} versus $|R_c|$ for various Pe is shown in the figure 4.7(a). It is evident that for each Pe , the onset time follows the same trend as explained for $Pe = 3000$. However, the stable zone in the $t - R_c$ phase space increases with a decrease in Pe . Interestingly, the onset time or equivalently, the curves marking the boundary between stable and unstable region of $t - R_c$ phase space can be made independent of Pe (see figure 4.9) using a rescaling which we obtain as explained below.

4.4.2.2 Dependence of t_{on} on R_c and Pe

Since the width of the stable region is different for each Pe , thus for each time, we find a relationship between the Péclet number and R_c . We explain below the procedure used to find a relation between $R_c > 0$ and Pe . A similar procedure is used for $R_c < 0$ and Pe . We fix a time t and for a range of Pe , choose the $R_c > 0$ values lying on the boundary between the stable and unstable zone of the $t - R_c$ phase space. Thus obtained (Pe, R_c) pairs are plotted for each t as shown in figure 4.7(b). It is evident that for a fixed Pe , there exists a range of R_c for which stable displacement is observed at the given time t , indicating a continuous competition between the forces due to convection and diffusion. In fact, we find a stable zone sandwiched between two unstable zones for each time. Further, a loglog plot is given in figure 4.8. Interestingly, the curves thus obtained follow a similar trend for each time t and using the *cftool* of MATLAB [1], we obtain a power law between R_c^+ and Pe as

$$R_c^+ = 260Pe^{-0.64}, \quad (4.23)$$

where R_c^+ corresponds to the positive log-mobility ratio for which stable displacement is observed for all time and fixed Pe . Similarly, the power law obtained for the negative log-mobility ratio up to which flow is stable, R_c^- and Pe is

$$R_c^- = -160Pe^{-0.58}. \quad (4.24)$$

It is clear that the onset time will exist only when $|R_c| > |R_c^\pm|$.

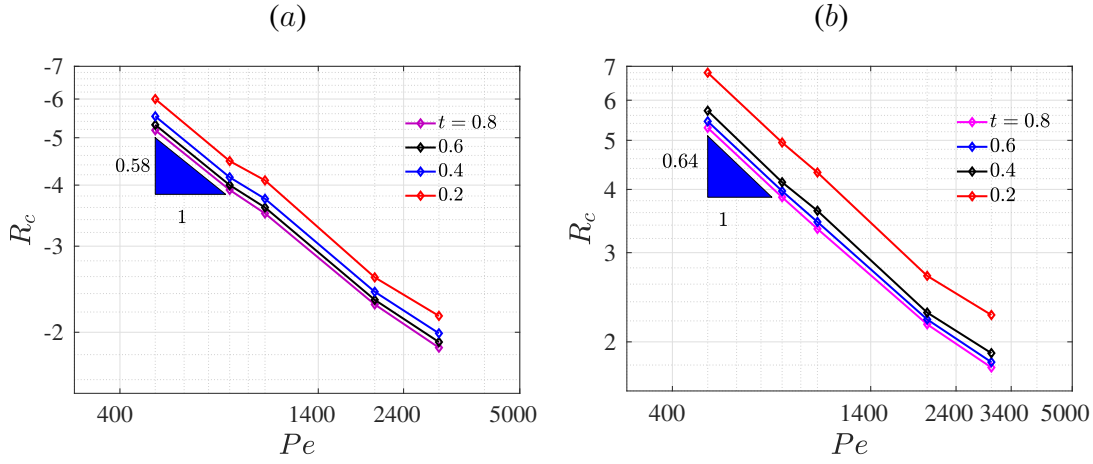


FIGURE 4.8: Log-log plot of R_c versus Pe at various time t . These curves can be well fitted using the power law $R_c^- = -160Pe^{-0.58}$ for $R_c < 0$ in (a) and $R_c^+ = 260Pe^{-0.64}$ for $R_c > 0$ in (b).

Now, to obtain the dependence of the onset time on R_c and Pe , we utilize the relation between R_c^\pm and Pe . We assume a fitting for t_{on} as

$$t_{on} \propto (|R_c|Pe^{\beta_1} - \beta_2)^{\beta_3}, \quad (4.25)$$

where the sign of R_c decides the constant of proportionality and $\beta_i, i = 1, 2, 3$. The constants β_1, β_2 are obtained using equation (4.23), (4.24) and the fact that t_{on} does not exist for completely stable displacement. Consequently, for any R_c corresponding completely stable displacement, t_{on} is not defined thus, we can take

$$\beta_1 = 0.64, \quad \beta_2 = 260 \text{ for } R_c > 0, \quad (4.26)$$

$$\beta_1 = 0.58, \quad \beta_2 = 160 \text{ for } R_c < 0, \quad (4.27)$$

and β_3 must be negative. We obtain the constant of proportionality and β_3 using *cftool* of MATLAB [1] and the onset time of instability for any $|R_c|$ and Pe can be obtained as

$$t_{on} = 31.1(Pe^{0.64}R_c - 260)^{-1.22}, \quad R_c > 0, \quad (4.28a)$$

$$t_{on} = 437(Pe^{0.58}|R_c| - 160)^{-1.85}, \quad R_c < 0. \quad (4.28b)$$

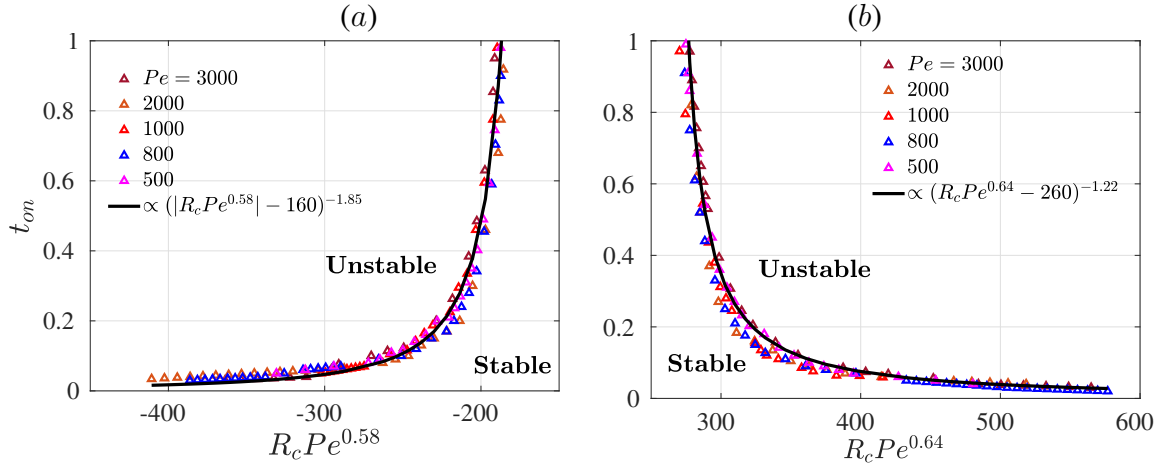


FIGURE 4.9: Onset time curves for various Pe , merged into a single curve for (a) $R_c < 0$ and (b) $R_c > 0$.

We plot t_{on} versus $R_c Pe^{\beta_1}$ for $R_c < 0$ in figure 4.9(a) and $R_c > 0$ in figure 4.9(b). The onset time appears independent of Pe as all the points fall together around a single black curve which represents the onset time calculated in equations (4.28). In other words, the boundary between the stable and the unstable zone is found to follow the power law defined above in equations (4.28). We obtain one boundary between stable and unstable regions independent of Pe . This relation can be used to find whether a displacement corresponding to any $|R_c|$, and Pe is completely stable or not. If t_{on} is not defined which may happen when the quantity within the bracket in equation (4.28) is negative or zero, then the displacement is completely stable while a finite value of t_{on} corresponds to the onset time for instability for the given $|R_c|$ and Pe .

4.4.2.3 Finger length

After the onset of fingering instability, different dynamics are observed depending on Pe and the sign of R_c . In this section, we discuss these dynamics, focusing basically on the length of the fingers. Sharma et al. [94] observed that for a fixed finite Da , the length of the fingers for $R_c > 0$ is greater than that for corresponding $R_c < 0$ but the two finger lengths approach each other with an increase in Da . However, for infinite Da , we observe that the length of the fingers depend upon R_c and Pe and a transition is observed which we discuss and quantify below.

For better visualization and comparison of the length of the fingers, we make the transformation from the (x, y) coordinates to (r, θ) coordinates as in [94]. The density plots of the product concentration are shown in figure 4.10 for $Pe = 1000$ and various R_c . It must be noted that the

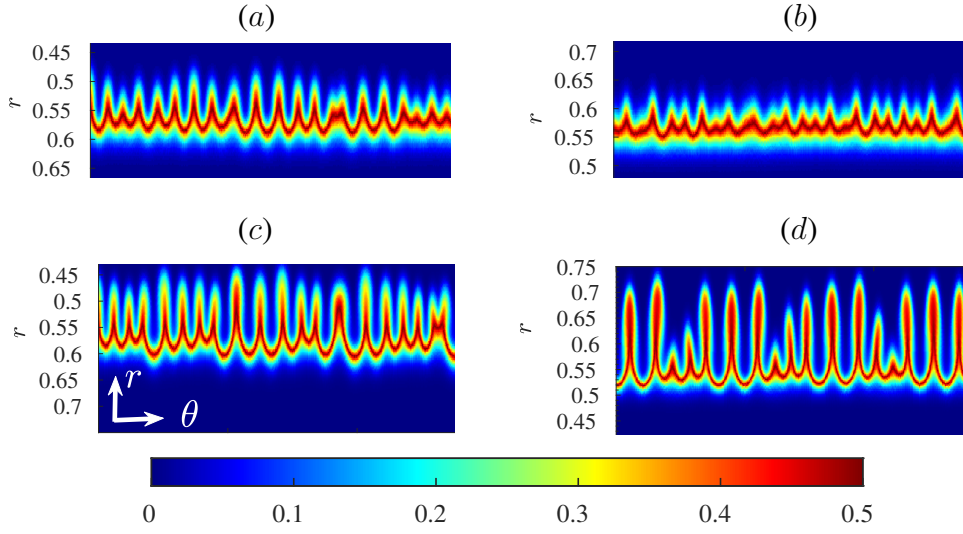


FIGURE 4.10: Density plots of product concentration in the (r, θ) coordinates for $Pe = 1000$ and (a) $R_c = 4$, (b) $R_c = -4$, (c) $R_c = 5.5$ and (d) $R_c = -5.5$ at final time $t = 1$. For $R_c < 0$, the vertical axis is reversed for a better comparison of the finger length.

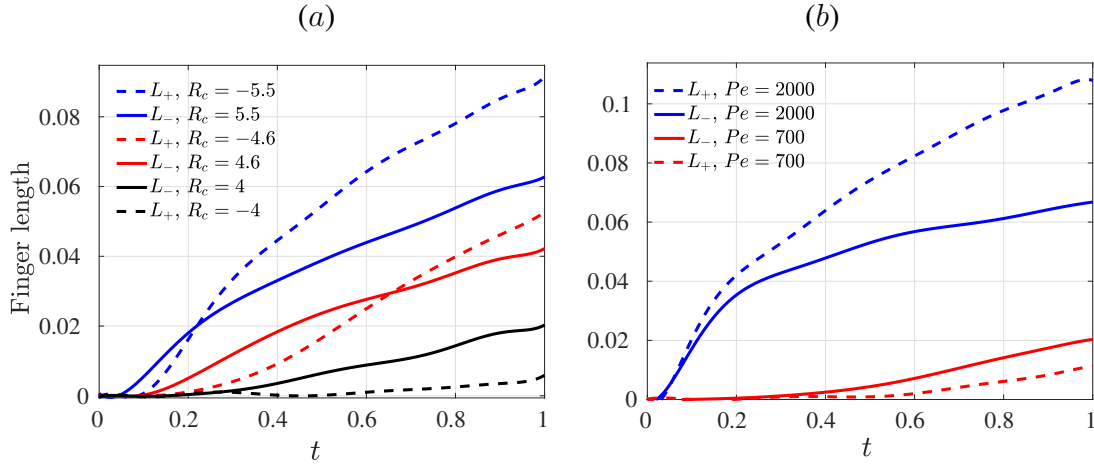


FIGURE 4.11: (a) Temporal evolution of L_- and L_+ for $Pe = 1000$ and various R_c . (b) Length of inward and outward fingers for $R_c = 5, -5$ and $Pe = 2000, 700$. Here solid lines are for $R_c = 5$ and dashed lines are for $R_c = -5$. Clearly, transition in VF dynamics also occurs for a given viscosity ratio and varying Pe .

fingers for $R_c < 0$ appear at the downstream mixing zone but we have reversed the vertical axis (r -axis) in figure 4.10(b, d) so that the fingers face in one direction for both positive and negative R_c and ease the visual comparison. Evidently, the length of the fingers is larger for $R_c = 4$ than for $R_c = -4$ (as evident from comparison of figure 4.10(a,b)). However, if we compare the length for $|R_c| = 5.5$ in figure 4.10(c,d), the trend seems to be opposite with the fingers being visibly longer for $R_c = -5.5$ than for $R_c = 5.5$.

In order to quantify the length of the fingers, we average the product concentration $c(\theta, r, t)$ along the θ direction to obtain the averaged product concentration $\langle c(r) \rangle(t)$ as [94]

$$\langle c(r) \rangle(t) = \frac{1}{2\pi} \int_0^{2\pi} c(\theta, r, t) d\theta. \quad (4.29)$$

The first and the last r values for which $\langle c(r) \rangle(t) > 0.005$ for $R_c = 0$ are termed as $r_{0,in}$ and $r_{0,out}$ [94]. Similarly, r_{in} and r_{out} are the points defined for $R_c \neq 0$. The distance between $r_{0,out}$ and r_{out} denoted as L_+ corresponds to the length of the fingers at the downstream mixing zone. We refer to such fingers as outward fingers as these fingers appear away from the source. From the discussion so far, it is evident that the outward fingers are more prominent for $R_c < 0$. Similarly the fingers at the upstream mixing zone are referred to as the inward fingers with their length being denoted L_- and being the distance between $r_{0,in}$ and r_{in} . Mathematically, we can write [94]

$$L_- = r_{0,in} - r_{in}, \quad L_+ = r_{out} - r_{0,out}. \quad (4.30)$$

We plot the length of the fingers for a fixed $Pe = 1000$ and various R_c in figure 4.11(a). Clearly, at all times, L_- for $R_c = 4$ is larger than L_+ for $R_c = -4$ which supports the observations of figure 4.10 and is a contradiction to the result in rectilinear geometry [67] where fingers are longer when the sample is less viscous. Further, with an increase in the magnitude of R_c , we observe a transition in the finger length with time. Initially, inward fingers are longer for $R_c = 4.6$ than outward fingers for $R_c = -4.6$. After some time, the outward fingers for $R_c = -4.6$ grow more than the inward fingers for $R_c = 4.6$. Ultimately, we observe a complete shift in the length of the fingers, the outward fingers are longer for $R_c = -5.5$ than the inward fingers for $R_c = 5.5$ at all times except some initial time, as evident by a comparison of L_+ for $R_c = -5.5$ with L_- for $R_c = 5.5$. It is verified that L_+ for $R_c < 0$ is longer than L_- for $R_c > 0$ on increasing $|R_c|$ further. Thus, fixing Pe , we observe that a transition in the length of the fingers is observed with an increase in R_c . Further, we see what happens if we vary Pe for a fixed R_c by plotting the finger length as a function of time in figure 4.11(b). It is evident that the trend in the relation between L_+ and L_- reverses with an increase in Pe . Thus, we observe a unique dependence on the length of the fingers on the governing parameters which is not observed for finite Da and appears to be a feature of an infinitely fast reaction rate. But what is responsible for this kind of dependence? To answer this question, we look back into the onset of instability and the spatially dependent velocity.

As discussed in §4.4.2.1, the onset time of instability is early for $R_c > 0$ than for corresponding $R_c < 0$ but the onset time becomes independent of the sign of R_c with an increase in the viscosity contrast. This is due to the spatially varying velocity and is the reason behind the dependence of the length of fingers on R_c . As t_{on} is early for $R_c = 4$, so fingers start to grow at the upstream mixing zone earlier and with faster convection velocity in comparison to the outward fingers for $R_c = -4$ which appear late and with lesser convection velocity. This results in larger L_- for $R_c = 4$ than L_+ for $R_c = -4$. As $|R_c|$ increases the difference between t_{on} decreases and so does the finger length. Ultimately when t_{on} is independent of the sign of R_c , the fingers appearing at the downstream mixing zone are longer than the inward fingers as the outward fingers grow radially outward in the direction of the flow which results in L_+ for $R_c < 0$ to be more than the L_- for the corresponding $R_c > 0$.

4.5 Conclusion

The viscous fingering dynamics induced by an infinitely fast chemical reaction between reactants having same viscosity and undergoing radial displacement is discussed. The numerical complexity arises due to a non-dimensional number $Da \rightarrow \infty$ for such chemical reactions. Thus, for the mathematical modeling of such reactions, the governing equations must be dealt properly to achieve numerical convergence. We present the governing equations comprising a system of three coupled convection-diffusion-reaction equations each containing Da . However, it is shown that using suitable transformation, the dynamics can be understood using only one convection-diffusion equation, coupled to the equations of fluid flow. The resulting system of equations is solved numerically using a hybrid numerical scheme based on compact finite difference and the pseudo-spectral method. The solution of the equations is utilized to extract the knowledge about the concentration of the reactants as well as products, which is used to see the relative effect of the forces due to convection, diffusion and reaction. We assume the reactants having same viscosity and instability appear only when the product has a different viscosity than the reactants. A more viscous product results in *flower* like instability, while *crown* like instability is observed when the product is less viscous than the reactants.

For $Da \rightarrow \infty$, the chemical reaction results in a sufficient amount of product as soon as reactants come into contact and the displacement is expected to become unstable as soon as the product is

generated. On the contrary, we observe stable displacement even for such high Da . Thus, an interplay of the forces due to convection, diffusion and reaction affects the overall dynamics. For $Da \rightarrow \infty$, although the force due to reaction is high but the triggering of the instability also depends upon other two non-dimensional parameters Pe, R_c which are a measure of other two forces due to convection and diffusion. We quantify this by measuring the onset time of instability, t_{on} , which is the minimum time when the instability appears. Using density plots of the product concentration and quantification based on the interfacial length, it is shown that the onset time of instability is a function of both Pe and R_c . For a fixed Pe , the onset is found to be delayed for $R_c < 0$ which is in contrast to the results reported for rectilinear displacement [35]. However, the onset time becomes comparable for $|R_c|$ with an increase in the viscosity contrast between the reactants and the product, and this is found to affect the fingering dynamics at a later time when finger length is found to depend on the sign of R_c . On the other hand, the onset time increases with a decrease in Pe for a fixed R_c , as the stabilizing force due to diffusion is strong for smaller Pe . Using a proper fitting, we make the onset time independent of Pe and it is observed that t_{on} curves for various Pe merge into a single curve. The onset time divides the entire time into two parts, one corresponding stable displacement when $t < t_{on}$, and unstable displacement is observed for the remaining time $t \geq t_{on}$. Thus, the onset time of instability divides the $t - R_c$ phase space into three zones with a stable zone sandwiched between two unstable zones. There exist reactions for which no finite t_{on} is observed, a stable displacement at all times is observed for such reactions, which is never observed for rectilinear displacement.

Further, we analyze the evolution of the fingering patterns at later times. For $R_c < 0$, the outward fingers appear while inward fingers are observed for $R_c > 0$. It is reported that the inward fingers for $R_c > 0$ are longer than outward fingers for $R_c < 0$, which is in contrast to that observed for rectilinear displacement [67]. This is due to larger convection at the unstable front and early onset time for $R_c > 0$. However, with an increase in $|R_c|$, the inward finger length for $R_c > 0$ and the outward finger length for $R_c < 0$ approach each other and we observe a transition in the finger length. There exists a $|R_c|$ for fixed Pe after which the outward finger length for $R_c < 0$ becomes larger than the inward fingers for $R_c > 0$. This transition appears to be due to infinite Da as no such transition is reported for finite Da [94]. A similar transition in VF dynamics is obtained for varying Pe and a given viscosity ratio.

Our results help us to understand the non-linear interaction between chemical reactions and VF

dynamics. The study finds application in controlling VF using chemical reactions, for increasing mixing in micro-fluidic devices and point-of-care devices.

Chapter 5

Non-modal linear stability analysis of reactive viscous fingering for rectilinear flow for infinitely fast reactions

5.1 Introduction

In the preceding three chapters, we have focused on the reactive displacements undergoing radial flow geometry. However, the initial exploration of numerical modeling for studying reactive viscous fingering (VF) was introduced in the context of rectilinear flow geometry by Gérard and De Wit [31]. They have performed numerical simulations and focused on a specific case characterized by $R_b = 0$ and $R_c > 0$. Subsequently, Hejazi and Azaiez [34] investigates the remaining dynamics of VF influenced by chemical reactions by examining the impact of viscosity modification expressed as $\mu = e^{R_b b + R_c c}$. Due to the difference in the basic velocity profile, the flow properties vary in different flow geometries. For rectilinear flow, the velocity profile is uniform, feeding the convection to the interface for the entire time domain, and does not attribute any critical viscosity contrast, a distinction from radial flow. On the contrary, the velocity profile decreases with radial distance for radial flow geometry, attributed to the existence of critical parameters to trigger the instability. In addition, Brau and De Wit [10] has obtained in their study that chemical reaction generates less amount of product in rectilinear flow geometry than the radial flow geometry. Evidently, it affects the reactive VF also. In this chapter¹, we study how the geometry affects the stability of reactive flow.

To understand the reactive displacement in the linear regime, Hejazi et al. [35] conducted a modal analysis using the Quasi-Steady-State Approximation (QSSA) approach. The QSSA approach assumes that the base state changes at a slower rate compared to the perturbations. Thus, the base state is considered to be steady by freezing times and QSSA solely focuses on the temporal progression of disturbances, resulting in the neglect of any rate of change in the base state. However, the reactive system may exhibit transient growth due to the negligence of an unsteady base state, which can not be captured by QSSA. Further, it is shown that QSSA is unable to

¹This chapter is submitted for publication.

anticipate the onset of instability for non-reactive fluids. Previous studies by Tan and Homsy [101] and Hota et al. [39] have shown that QSSA is unable to accurately represent the initial diffusive dynamics in non-reactive fluids. To investigate the transient growth, it is necessary to employ a non-modal linear stability analysis (NMA) [86, 39]. In addition, the reactive flow may exhibit a non-monotonic viscosity profile. The presence of both unstable and stable regions serves as to the significance and complexity of these viscosity profiles. Hota and Mishra [37] conducted NMA on non-monotonic viscosity profiles for non-reactive displacements. It is demonstrated that the underlying physical mechanism is impacted by both the viscosity contrast at the endpoints and the maximum viscosity caused by the non-monotonic viscosity profile. Further, the perturbation contours are formed in quadruple structures. However, the QSSA analysis falls short of capturing these findings.

In this chapter, we focus on the reactive flow with infinitely fast reactions only. Although a majority of experiments are conducted with infinitely fast reactive flow [71, 83], theoretical attention is not given much to such reactive flow [53, 35]. To the best of our knowledge, no literature performs non-modal analysis for reactive systems for rectilinear flow that deals with infinitely fast reactions. In the present study, we compute the onset time of instability and optimal initial condition, which corresponds to the maximum growth rate, and corresponding temporal evolution to determine the transient behavior of a reactive system. Furthermore, agreement with existing numerical results is demonstrated, and a comparison is made between our findings and the conclusions drawn by QSSA.

The chapter is organized as follows. In section §5.2, the mathematical formulation for reactive flow with infinitely fast reactions. Following base state and transient energy growth, the linearized perturbed equations are derived for carrying out NMA using the propagator matrix approach in section §5.3. An analytical formulation for base state concentration profiles of all three fluid species for infinitely fast reactions in the self-similar domain for rectilinear flow is provided. Along with conclusions and suggestions for future research, section §5.4 compares the QSSA results with the results of the NMA results in section §5.5.

5.2 Mathematical formulation

We consider the uniform displacement of two reactive fluids, named A and B , that undergo a second-order chemical reaction $A + B \rightarrow C$ and generate C in a homogeneous porous medium having constant permeability, $\tilde{\kappa}$ as represented in figure 5.1. All the fluid species are considered to be miscible, incompressible, Newtonian, neutrally buoyant, and have the same diffusion coefficient, \tilde{D} .

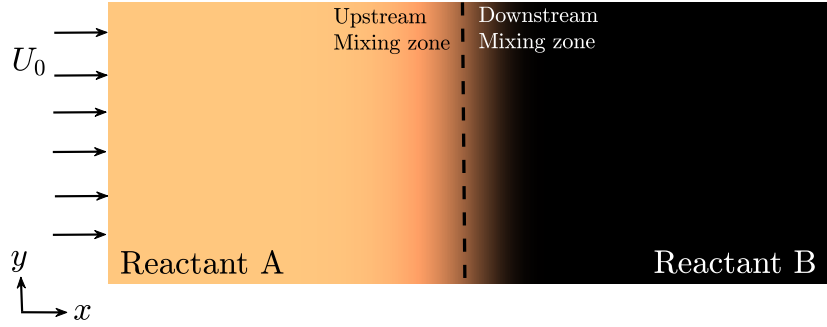


FIGURE 5.1 : Schematic of the two-dimensional rectilinear reactive flow $A + B \rightarrow C$. The dashed lines illustrate the initial position of the interface and \tilde{U}_0 is the velocity at which the reactant A has been injected. Here, brown and black colored regions are occupied with reactants A and B . The reaction zone is occupied by all three fluids.

The above-mentioned flow can be formulated mathematically as [35, 31]:

$$\tilde{\nabla} \cdot \tilde{\mathbf{u}} = 0, \quad (5.1a)$$

$$\tilde{\nabla} \tilde{p} = -\frac{\tilde{\mu}}{\tilde{\kappa}} \tilde{\mathbf{u}}, \quad (5.1b)$$

$$\frac{\partial \tilde{a}}{\partial \tilde{t}} + \tilde{\mathbf{u}} \cdot \tilde{\nabla} \tilde{a} = \tilde{D} \tilde{\nabla}^2 \tilde{a} - \tilde{k} \tilde{a} \tilde{b}, \quad (5.1c)$$

$$\frac{\partial \tilde{b}}{\partial \tilde{t}} + \tilde{\mathbf{u}} \cdot \tilde{\nabla} \tilde{b} = \tilde{D} \tilde{\nabla}^2 \tilde{b} - \tilde{k} \tilde{a} \tilde{b}, \quad (5.1d)$$

$$\frac{\partial \tilde{c}}{\partial \tilde{t}} + \tilde{\mathbf{u}} \cdot \tilde{\nabla} \tilde{c} = \tilde{D} \tilde{\nabla}^2 \tilde{c} + \tilde{k} \tilde{a} \tilde{b}. \quad (5.1e)$$

Here equation (5.1a) is the continuity equation for mass conservation, equation (5.1b) is Darcy's law for momentum conservation, equation (5.1c)-(5.1e) are convection-diffusion-reaction (CDR) equations for averaged mass volume conservation for fluid A , B , and C . Further, $\tilde{\mathbf{u}} = (\tilde{u}, \tilde{v})$, \tilde{p} , and $(\tilde{a}, \tilde{b}, \tilde{c})$ denotes velocity, pressure, and fluid concentrations of A , B , and C , respectively.

Since we aim to study the VF dynamics in the reaction zone only and the fluid (reactant A) is injected with a uniform velocity \tilde{U}_0 , we have switched to a moving reference frame by considering $\hat{x} = \tilde{x} - \tilde{U}_0 \tilde{t}$ and $\hat{\mathbf{u}} = (\tilde{u} - \tilde{U}_0, \tilde{v})$. Further, we non-dimensionalize the equations (5.1). The characteristic scales that are used to non-dimensionalized are as follows [31, 35]:

$$\mathbf{x} = \frac{\tilde{\mathbf{x}}}{\tilde{D}/\tilde{U}_0}, \quad \mathbf{u} = \frac{\tilde{\mathbf{u}}}{\tilde{U}_0}, \quad t = \frac{\tilde{t}}{\tilde{D}/\tilde{U}_0^2},$$

$$(a, b, c) = \frac{(\tilde{a}, \tilde{b}, \tilde{c})}{\tilde{a}_0}, \quad \mu = \frac{\tilde{\mu}}{\tilde{\mu}_0}, \quad p = \frac{\tilde{p}}{\tilde{D}\tilde{\mu}_0\tilde{k}},$$

where \tilde{a}_0 and $\tilde{\mu}_0$ are the initial concentration and viscosity of the reactant A , respectively. Here, the dimensional variables are denoted with a tilde, \sim , and for brevity, both tilde ($\tilde{\cdot}$) and hat ($\hat{\cdot}$) have been dropped in the non-dimensional forms. Thus, the following system of equations (5.1) in a non-dimensionalized form in moving frame of reference, can be described as:

$$\nabla \cdot \mathbf{u} = 0, \quad (5.2a)$$

$$\nabla p = -\mu(\mathbf{u} + \hat{\mathbf{i}}), \quad (5.2b)$$

$$\frac{\partial a}{\partial t} + \mathbf{u} \cdot \nabla a = \nabla^2 a - Da \, ab, \quad (5.2c)$$

$$\frac{\partial b}{\partial t} + \mathbf{u} \cdot \nabla b = \nabla^2 b - Da \, ab, \quad (5.2d)$$

$$\frac{\partial c}{\partial t} + \mathbf{u} \cdot \nabla c = \nabla^2 c + Da \, ab. \quad (5.2e)$$

Here, the Damköhler number Da represents the ratio of diffusive time scale \tilde{D}/\tilde{U}_0^2 to reactive time scale $1/\tilde{k}\tilde{a}_0$. Here \tilde{k} is the kinetic constant of the reaction. It shows how rapidly or gradually a reaction occurs. Further, to complete the system, the viscosity-concentration relation is defined as viscosity depends on fluids concentrations exponentially as follows [35] :

$$\mu = \mu(a, b, c) = e^{(R_c c + R_b b)}, \quad (5.3)$$

$$R_b = \ln \left(\frac{\mu_B}{\mu_A} \right), \quad R_c = \ln \left(\frac{\mu_C}{\mu_A} \right), \quad (5.4)$$

where, $\mu_A = \mu(a = 1, 0, 0)$, $\mu_B = \mu(0, b = 1, 0)$ and $\mu_C = \mu(0, 0, c = 1)$. The system

of equations (5.2) is supplemented with the initial condition for velocity, $\mathbf{u} = \mathbf{0}$ and fluid concentrations,

$$(a, b, c)(x, y) = (1 - \mathcal{H}(x), \mathcal{H}(x), 0) = \begin{cases} (0, 1, 0), & x > 0, \\ (1, 0, 0), & x \leq 0, \end{cases}$$

where $\mathcal{H}(x)$ is the Heavy-side function. While boundary conditions are the following [39] :

$$\mathbf{u} = \mathbf{0}, \quad \frac{\partial a}{\partial x} = \frac{\partial b}{\partial x} = \frac{\partial c}{\partial x} = 0 \quad \text{for } |x| \rightarrow \infty, \quad (5.5a)$$

$$\frac{\partial a}{\partial y} = \frac{\partial b}{\partial y} = \frac{\partial c}{\partial y} = 0, \quad \frac{\partial v}{\partial y} = 0 \quad \text{for } |y| \rightarrow \infty. \quad (5.5b)$$

In this study, we aim to do stability analysis when the reaction rate is infinitely fast, *i.e.*, $Da \rightarrow \infty$. To incorporate with $Da \rightarrow \infty$, the conserved scalar technique is utilized and the system of CDR equations is reduced into a convection-diffusion equation [66, 20]. The fluid concentrations are assigned for $Da \rightarrow \infty$ as follows [69, 113]:

$$\frac{\partial z}{\partial t} + \mathbf{u} \cdot \nabla z = \nabla^2 z, \quad (5.6a)$$

$$(a, b, c) = \begin{cases} (0, 1 - 2z, z), & z < 0.5, \\ (-1 + 2z, 0, 1 - z), & z \geq 0.5, \end{cases} \quad (5.6b)$$

where initial condition for z are $z(x, y, t = 0) = 1 - \mathcal{H}(x)$ and at boundary z follows far-field boundary condition.

5.3 Linear stability analysis

In this section, a steady base state solution is presented for a reactive system subject to infinitely fast reaction. It consists of a reaction-diffusion system with an infinitely fast reaction, and an analytical solution in the (x, t) domain is provided. It is defined by the equation (5.2) in the absence of no viscosity contrast in the system and $\mathbf{u}_b = \mathbf{0}$. In the absence of viscosity contrast, z follows the diffusion equation for x -direction whose solution can be written in terms of the

complementary error function:

$$z_b = \frac{1}{2} \operatorname{erfc} \left(\frac{x}{2\sqrt{t}} \right). \quad (5.7a)$$

Since, $z_b(x > 0) < 0.5$ and $z_b(x \leq 0) \geq 0.5$, the reactants and product concentration distribution will be as follows:

$$(A_b, B_b, C_b) = \begin{cases} (0, 1 - 2z_b, z_b) & x > 0, \\ (-1 + 2z_b, 0, 1 - z_b) & x \leq 0. \end{cases} \quad (5.7b)$$

Further, the base state is perturbed with infinitesimal perturbations with orders of magnitude of $O(10^{-3})$.

$$(a, b, c, z) = (A_b, B_b, C_b, z_b) + (a', b', c', z'), \quad (5.8a)$$

$$\mathbf{u} = \mathbf{0} + \mathbf{u}', \quad \mu = \mu_b + \mu', \quad (5.8b)$$

where prime notations are for perturbed quantities. Further, the perturbed pressure, p' , is eliminated by using the curl of the perturbed equations of Darcy's law, and the perturbed continuity equation is then used to eliminate v' . The linearized perturbed system of equations is obtained as:

$$\left[\frac{\partial^2}{\partial x^2} + \frac{\partial^2}{\partial y^2} + \left(R_b \frac{\partial B_b}{\partial x} + R_c \frac{\partial C_b}{\partial x} \right) \frac{\partial}{\partial x} \right] u' = -R_b \frac{\partial^2 b'}{\partial y^2} - R_c \frac{\partial^2 c'}{\partial y^2}, \quad (5.9a)$$

$$\frac{\partial z'}{\partial t} + \frac{\partial z_b}{\partial x} u' = \left(\frac{\partial^2}{\partial x^2} + \frac{\partial^2}{\partial y^2} \right) z', \quad (5.9b)$$

$$(a', b', c') = \begin{cases} (0, -2z', z'), & x > 0, \\ (2z', 0, -z'), & x \leq 0. \end{cases} \quad (5.9c)$$

The above set of equations is linear in terms of a function of y that allows the perturbations in the given form of Fourier mode decomposition

$$(z', a', b', c', u', \mu') = (\phi_z, \phi_a, \phi_b, \phi_c, \phi_u, \phi_\mu)(x, t) e^{iky},$$

where k is the non-dimensional wave number. The reduced set of equations are

$$L_1 \phi_u = L_2 \phi_b + L_3 \phi_c, \quad (5.10a)$$

$$\frac{\partial \phi_z}{\partial t} = L_4 \phi_z + L_5 \phi_u, \quad (5.10b)$$

where

$$\left. \begin{aligned} L_1 &= \mathcal{D}_x^2 - k^2 \mathcal{I}_x + (R_b \mathcal{D}_x B + R_c \mathcal{D}_x C) \mathcal{D}_x, & L_2 &= k^2 R_b \mathcal{I}_x, \\ L_3 &= k^2 R_c \mathcal{I}_x, & L_4 &= \mathcal{D}_x^2 - k^2 \mathcal{I}_x, & L_5 &= -\mathcal{D}_x z_b, \\ \phi_a &= 2(\mathcal{I}_x - \mathcal{H}_x) \phi_z, & \phi_b &= -2\mathcal{H}_x \phi_z, & \phi_c &= (2\mathcal{H}_x - \mathcal{I}_x) \phi_z, \end{aligned} \right\}$$

with $\mathcal{D}_x = \frac{\partial}{\partial x}$; \mathcal{I}_x and \mathcal{H}_x are Identity and Heaviside operators, respectively. The system of equations (5.10) can be re-written as:

$$\frac{\partial \phi_z}{\partial t} = \mathcal{L} \phi_z, \quad \mathcal{L} = L_4 + L_5 L_1^{-1} (2(L_3 - L_2) \mathcal{H}_x - L_3). \quad (5.11)$$

The analytical solution to equation (5.11) is unattainable, so we have to rely on the numerical method. The numerical domain is considered as $\Omega = [-L, L]$, discretized into $n + 2$ grid points. The initial condition associated with the equation (5.11) is $\phi_z(x, 0) = \alpha \text{rand}(x)$ where α is the magnitude of perturbations is of order $O(10^{-3})$ and at boundary $\phi_z(t) = 0$. Here, $\text{rand}(x)$ is a random function that considers the value between -1 and 1. It is evident that the system in the equation (5.11) is a non-autonomous system. As a result, the conventional modal analysis is not applicable to solving such a system [28]. To solve the system of equations (5.11), one method is QSSA discussed in literature [35]. We discuss QSSA based on modal analysis and the limitations of QSSA in detail in subsection §5.4.4.

5.3.1 Non-modal analysis

Following discretization, the partial differential equation (5.11), transforms into a matrix-valued differential equation. When employing non-modal analysis, there are two methods available for solving the system. The first approach involves performing initial value calculations (IVC) using random initial conditions. However, when dealing with non-reactive fluids, two significant challenges arise. The initial challenge relates to selecting a representative initial condition that corresponds to the optimal amplification of perturbations. Secondly, these perturbations should be localized at the interface. However, the perturbations take more time to localize at the interface in the IVC with random initial conditions because it is dispersed over the entire domain. Moreover, in IVC, this arbitrary initial condition may not correspond to the optimal

perturbation amplification. We address both the issues here for reactive flow and overcome by utilizing the propagator matrix method approach.

5.3.1.1 Self-similarity transformation

The base-state solution z_b , equation (5.7), is time-dependent which results in inaccurate prediction of growth of the perturbation determined by QSSA [101]. To overcome this, we consider a self-similar coordinate system, $(\xi, t) = \left(\frac{x}{\sqrt{t}}, t\right)$ which provides an implicit time-independent base state. Moreover, in the case of the non-reactive flow, it is observed that in the self-similar coordinate system, the concentration eigenfunctions are localized around both base state and dominant eigenmode $e^{-\xi^2/4}$, providing the accurate prediction of the perturbed quantities [39]. Further, the concentration eigenfunction determined from the IVC in (x, t) coordinate system converges to the dominant mode but at a later time of the onset. So it is preferable to perform calculations in the (ξ, t) domain.

Hence, the equation (5.10) can be re-cast in self-similarity transformation as:

$$\frac{\partial \phi_z}{\partial t} = M \phi_z, \quad M = M_4 + M_5 M_1^{-1} (2(M_3 - M_2) \mathcal{H}_\xi - M_3), \quad (5.12)$$

where

$$\left. \begin{aligned} M_1 &= \mathcal{D}_\xi^2 - k^2 \mathcal{J}_\xi + (R_b \mathcal{D}_\xi B_b + R_c \mathcal{D}_\xi C_b) \mathcal{D}_\xi, & M_2 &= k^2 R_b \mathcal{J}_\xi, \\ M_3 &= k^2 R_c \mathcal{J}_\xi, & M_4 &= \mathcal{D}_\xi^2 - k^2 \mathcal{J}_\xi + (\xi/2\sqrt{t}) \mathcal{D}_\xi, & M_5 &= -\mathcal{D}_\xi z_b, \\ \phi_a &= 2(\mathcal{J}_\xi - \mathcal{H}_\xi) \phi_z, & \phi_b &= -2\mathcal{H}_\xi \phi_z, & \phi_c &= (2\mathcal{H}_\xi - \mathcal{J}_\xi) \phi_z, & \mathcal{D}_\xi &= \frac{1}{\sqrt{t}} \frac{\partial}{\partial \xi}. \end{aligned} \right\}$$

The spatial derivatives are discretized using center finite difference formulas, and hence, the initial value problem described in equation (5.12) can be written in matrix form:

$$\frac{d\phi_z}{dt} = \mathcal{M} \phi_z. \quad (5.13)$$

Furthermore, a singularity is encountered within the system of equations (5.13) at the time $t = 0$. To eliminate this singularity from our system, the temporal domain is confined to the interval (t_p, t) , with t_p selected at the order of $O(10^{-3})$, as in Hota et al. [39].

5.3.1.2 Propagator matrix approach

To utilize the propagator matrix approach, we consider:

$$\phi_z = \Psi(t_p; t)X_0. \quad (5.14)$$

Here X_0 is the random initial condition and $\Psi(t_p; t)$ is the propagator matrix and satisfies the following matrix-valued differential equation

$$\frac{d}{dt}\Psi(t_p; t) = \mathcal{M}\Psi(t_p; t); \quad \Psi(t_p; t_p) = \mathcal{I}, \quad (5.15)$$

where \mathcal{I} is an identity matrix of $n \times n$.

By opting for the propagator matrix approach, we deal with a deterministic system of differential equation (5.15) with initial condition $\Psi(t_p; t_p) = \mathcal{I}$ instead of a vector differential equation system with random initial condition. The propagator operator, $\Psi(t_p; t)$, is the one that passes information from the initial perturbation time (t_p), when the perturbation is introduced to the base state, to a later time, t . The initial value problem, (5.15) is solved using the method of lines. For the same, the Runge-Kutta method of fourth order with an inbuilt MATLAB function [1], ode45, with an absolute error of order $O(10^{-5})$ is utilized. convergence study and validation of the numerical scheme are provided in §5.3.1.4, respectively.

5.3.1.3 Transient energy growth

In the non-modal stability analysis, the amplification magnitude of the perturbations is measured by normalizing with the initial perturbation magnitude at time t_p .

$$G_\phi(t) = \frac{E_\phi(t)}{E_\phi(t_p)},$$

where $E_\phi(t) = \|\phi_z(t)\| = \int_{-\infty}^{\infty} \phi_z(t)^2 dx$ and $\|\cdot\|$ is the L^2 norm. The maximum energy that a perturbation can have while taking into account all possible initial conditions is denoted by $G(t)$, which represents the optimal amplification [39],

$$G(t) = \max_{\phi_z} G_\phi.$$

The optimal amplification $G(t)$ depends on t as well as other parameters such as log mobility ratios R_b and R_c and wave number k . Further, growth rate, σ , is defined as the rate of relative change in optimal amplification [39, 106]:

$$\sigma(t) = \frac{d(\ln(G(t)))}{dt}.$$

When the growth rate, $\sigma > 0$, the system is unstable; when $\sigma < 0$, the system is stable. While the system is neutrally stable when $\sigma = 0$. The time when $G(t)$ starts to increase is called onset time,

$$t_{on} = \min_{t \geq 0}(\sigma(t) > 0).$$

In order to find optimal amplification, the singular value decomposition of the propagator matrix, $\Psi(t_p; t_f) = U M V^T$ is determined where superscript T stands for transpose of the matrix, the diagonal elements of M are the singular values, and t_f is the final time integration. The optimal amplification $G(t)$ is thus obtained from the largest singular value of the propagator matrix, $\Psi(t_p; t_f)$ while the optimal initial condition is provided by the corresponding right singular vector, V , and the evolved state for time t is provided by the left singular vector, U . Further, We consider the maximum growth rate and optimal amplification with respect to k where the range of wave number, k is determined by QSSA for which $\sigma > 0$. In the next section §5.4, we demonstrate the temporal evolution of optimal perturbation structures by plotting optimal amplification.

5.3.1.4 Convergence study and validation of numerical scheme

A convergence analysis is conducted to ensure that the numerical quantities utilized throughout this study, such as optimal amplification, remain unaffected by the coding parameters. Numerical integration is carried out in MATLAB using built-in functions such as *ode45* with an absolute error tolerance of order $O(10^{-5})$. The convergence analysis is specifically focused on spatial discretization, denoted as dx . For this purpose, simulations are performed for five sets of spatial step sizes, with dx ranging from 0.2 to 1. The numerical solution corresponding to the minimum value of dx , specifically $dx = 0.2$, is chosen as the exact solution. The error corresponding to

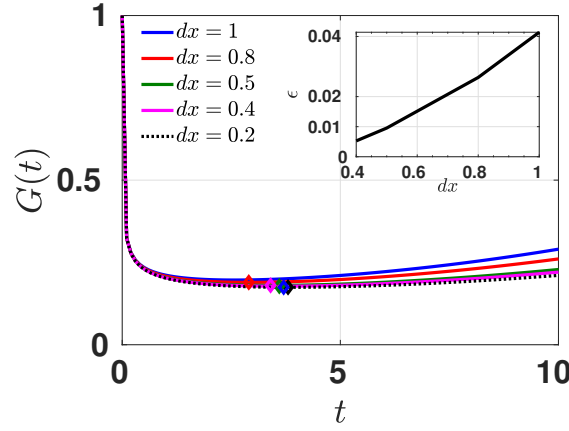


FIGURE 5.2: Optimal amplification for $R_b = 2$, $R_c = -2$, $k = 0.2$ and various dx . Here the markers denote the onset time. The onset time does not alter by taking $dx = 0.4$ in comparison to $dx = 0.2$. Inset: absolute error versus dx .

each dx is computed as follows:

$$\epsilon = \max_t \left\| \frac{G(dx) - G(dx = 0.2)}{G(dx = 0.2)} \right\|$$

The optimal amplification is plotted for $R_b = 2$, $R_c = -2$, $k = 0.2$ and various dx in figure 5.2. It is evident that the relative error decreases with decreasing dx value and reduces $\epsilon < 1\%$ by taking $dx = 0.4$. Thus, in all of our calculations, dx is fixed to 0.4 for optimal results with minimal computational time and optimal accuracy. The remaining constants, namely domain length, L , and perturbation time, t_p , are chosen as in Hota et al. [39].

TABLE 5.1: The parameters and corresponding values used in the numerical study.

Parameters	dx	L	t_p
Values	0.4	100	10^{-3}

Further, we validate our numerical scheme. To do the same, the results of Hota et al. [39] are reproduced. Equation (5.6b) allows us to deduce that z follows the convection-diffusion equation, where $z = b + c$. Furthermore, if the condition $R_b = R_c$ is considered, the viscosity profile is reduced to a monotonic viscosity profile resembling the non-reactive system with a viscosity profile $\mu = e^{R_b z}$. Consequently, the governing system of equations replicates a non-reactive system. Using this fact, a comparison is made between the optimal amplification for $R_b = R_c = 3$ and the non-reactive system for $R_b = 3$. It is expected that the optimal

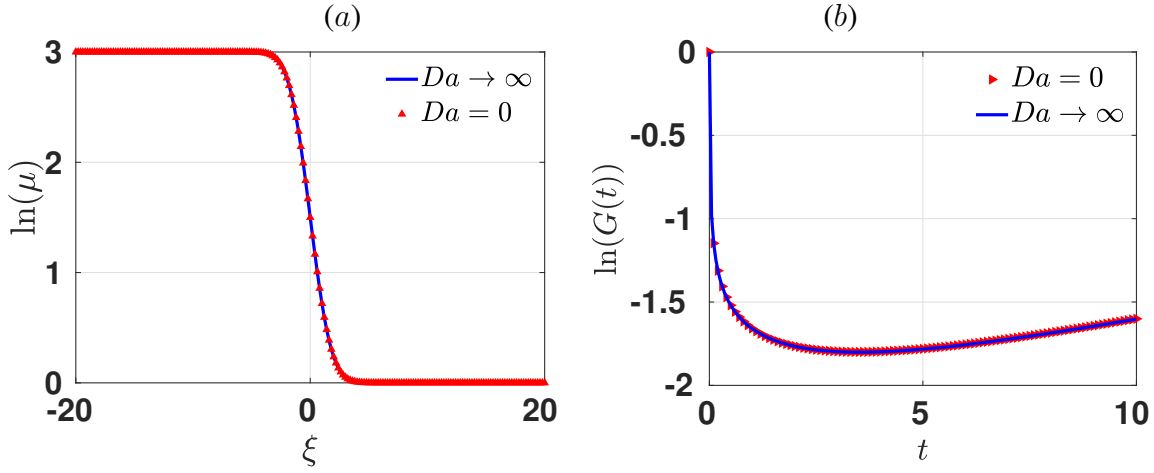


FIGURE 5.3: (a) Viscosity profile (b) optimal amplification for $R_b = 3$; $Da = 0$ and $R_b = R_c = 3$; $Da \rightarrow \infty$.

amplification curve remains the same for both $R_b = 3$; $Da = 0$ and $R_b = R_c = 3$; $Da \rightarrow \infty$. The obtained results are displayed in Figure 5.3, and that confirms the expectation.

5.4 Result and discussion

To develop a thorough comprehension of the fundamental attributes of a reactive system in the context of stability analysis, encompassing the onset time of instability and the growth rate of perturbation, the reactive system is categorized based on its viscosity profile. Further, the behavior of the system is analyzed after the product is formed, with a specific emphasis on whether the viscosity profile has a non-monotonic or monotonic trend. Since the reaction rate is infinitely fast, a mixed zone made up of reactant concentrations, $a \neq 0$, $b \neq 0$, will not exist as the product forms immediately after the reactants come into contact. Thus, the reaction zone, where C is generated and gets mixed, can be divided into two separate zones. We term them upstream and downstream mixing zone, situated at $\xi < 0$ where fluid A and C are mixed, and $\xi > 0$ where fluid B and C are mixed, respectively.

From the base state concentration distribution, it can be observed that $A_b + B_b + 2C_b = 1$ (see appendix B) and $A_b(\xi > 0) = B_b(\xi < 0) = 0$. Also, the base state concentration profile of A and B mirror image to each other about the line $\xi = 0$, *i.e.*, $A_b(\xi) = B_b(-\xi)$. Using these observations, the base state viscosity profile, $\mu_b = e^{R_b b + R_c c}$ can be re-written for an infinitely

fast reaction as below:

$$\mu_b = \begin{cases} \exp\left(\frac{R_c}{2}\right) \exp\left(-R_c \frac{A_b}{2}\right) & \xi < 0, \\ \exp\left(\frac{R_c}{2}\right) \exp\left[\left(R_b - \frac{R_c}{2}\right) \left(\frac{B_b}{2}\right)\right] & \xi \geq 0. \end{cases} \quad (5.16)$$

Equation (5.16) indicates that the nature of the viscosity profile at these two zones depends on the sign of $R_c (R_b - R_c/2)$ [35]. If $R_c (R_b - R_c/2) \geq 0$, the viscosity profile remains monotonic after the reaction. Otherwise, it becomes non-monotonic. We first discuss the flow dynamics of chemical reactions for the former case for which the viscosity profile remains monotonic.

5.4.1 VF dynamics when viscosity profile is monotonic $R_c (R_b - R_c/2) \geq 0$

To analyse the monotonic viscosity profile between the lines $R_c = 0$ and $R_c = 2R_b$, the (R_b, R_c) phase plane is shown in figure 5.4(a). It is observed that when $R_c = R_b$, the viscosity profile is also unaffected by the product viscosity. The stability analysis for this particular case allows us to compare the dynamics of the VF in the reactive system. The investigation helps in assessing the potential influence of the chemical reaction on the viscosity profile and analyzing its consequences on the stability of the flow. Moreover, upon examining the viscosity jump at the two lines $R_c = 0$ and $R_c = 2R_b$, it can be observed that the unstable region is localized at the downstream and upstream mixing zones, respectively. Therefore, it is anticipated that the system will exhibit greater instability in the scenarios where $R_c = 0$ and $R_c = 2R_b$, compared to the scenario where $R_c = R_b$, given a specific value of R_b [37].

To conduct this analysis, the parameters are chosen to keep the endpoint viscosity contrast the same by fixing R_b and vary R_c , in particular, $R_b = 2$, $R_c = 4, 2, 0$ and corresponding viscosity profiles have been depicted in the inset of figure 5.4(a). The optimal amplification, $\ln(G(t))$ illustrated in figure 5.4(b) shows that due to the dominance of diffusion, there is a decay in amplification. However, once the onset occurs, the convection starts to dominate the flow, and the $\ln(G(t))$ increases. For $R_c = 0$, the viscosity contrast becomes steeper at the downstream mixing zone than $R_c = 2, 4$, and hence, an early onset occurs. Interestingly, the onset delays despite the steeper viscosity contrast at the upstream mixing zone for $R_c = 4$ than $R_c = 2$. However, once the onset time occurs, an increment in growth rate can be observed. At later

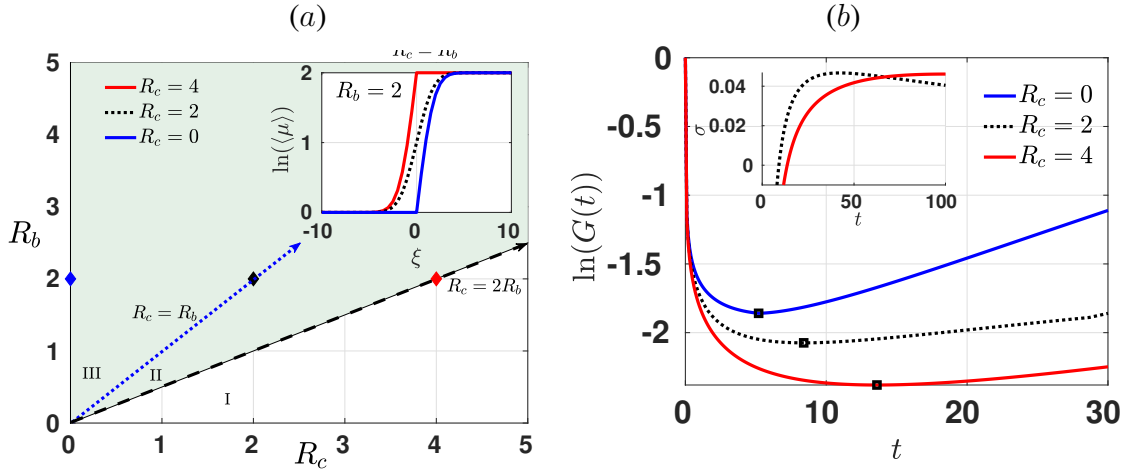


FIGURE 5.4: (a) The $R_b - R_c$ phase plane. Here in the colored region bounded between the lines $R_c = 0$ and $R_c = 2R_b$, the viscosity profile remains monotonic as shown in the Inset figure. Inset: Log-viscosity profile for $R_b = 2$ and $R_c = 4, 2, 0$. (b) Optimal amplification for $R_b = 2$, $R_c = 0, 2, 4$. Inset: Growth rate for $R_c = 4, 2$ at the later time showing that the growth of the perturbations is more for $R_c = 4$ than $R_c = 2$.

times, the perturbations have a larger growth rate, σ , for $R_c = 4$ than $R_c = 2$ showing a more unstable displacement.

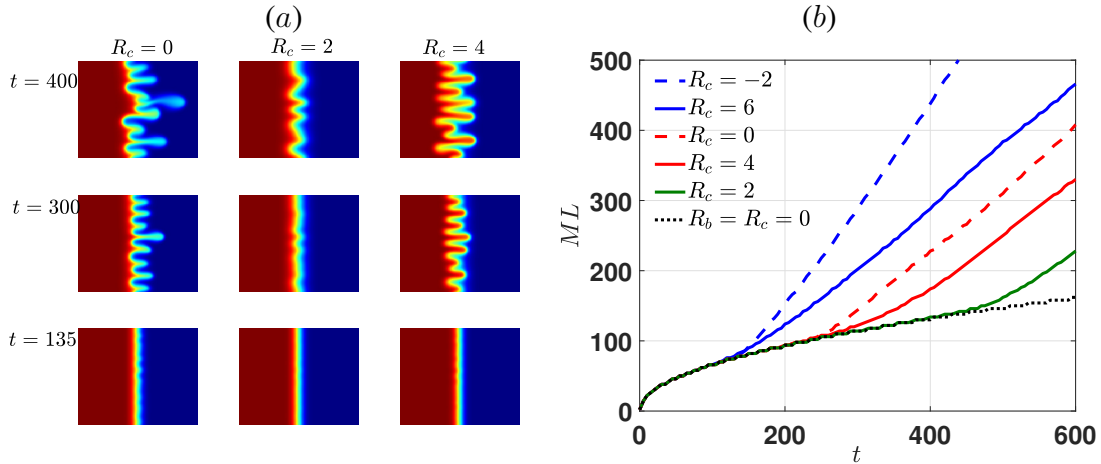


FIGURE 5.5: (a) z concentration profile for $R_b = 2$ and $R_c = 4, 2, 0$. (b) Mixing length for $R_b = 2$ and various $R_c = 0$ with the stable displacement $R_b = R_c = 0$. This figure is a reproduction of figures 6,7 and 9(a) from [69].

Moreover, we validate our results with non-linear simulation data and reproduce some results from the work of Nagatsu and De Wit [69]. Following their numerical method, the system of equations (5.6), (5.2a), (5.2b) have been solved, and the corresponding concentration profile of z and mixing length, ML , are illustrated in figure 5.5. The mixing length (ML) is calculated as the length of the region where $0.01 < \langle z(x, t) \rangle_y < 0.99$, where $\langle z(x, t) \rangle$ is the averaged z

concentration profile along y direction [69]. In the z concentration plot, the fingering pattern appears early and the mixing length is more for $R_c = 0$ than $R_c = 4, 2$. However, if the mixing length curve is compared for $R_c = 2, 4$, ML is more for $R_c = 4$ than $R_c = 2$ showing the more unstable situation for $R_c = 4$. While at the initial time, QSSA claims that chemical reactions can have a stabilizing effect when $R_c > R_b$ [35] which is consistent with NMA at early times; while at later times, the NMA results are validated through non-linear simulations. Therefore, we assert that the findings obtained using NMA are precise and align well with both the current numerical [69] and theoretical analyses [35]. Furthermore, when the early-time behavior of the non-monotonic viscosity profile is examined, a similar behavior is observed, which will be discussed in the subsequent section, namely, §5.4.2.

5.4.2 VF dynamics when viscosity profile is non-monotonic $R_c(R_b - R_c/2) < 0$

The non-monotonic viscosity profile is depicted in figure 5.6(a), zone I and IV; and figure 5.9(a), zone I and III. Such viscosity profile is particularly intriguing because it establishes a combined region of a stable and unstable zone where convection and diffusion compete. Here again, the VF dynamics re-categorize depending on the ratio of viscosity jump at stable and unstable zones. In this section, such cases are discussed depending upon whether $R_b > 0$ or $R_b < 0$.

5.4.2.1 Optimal amplification for $R_b > 0$

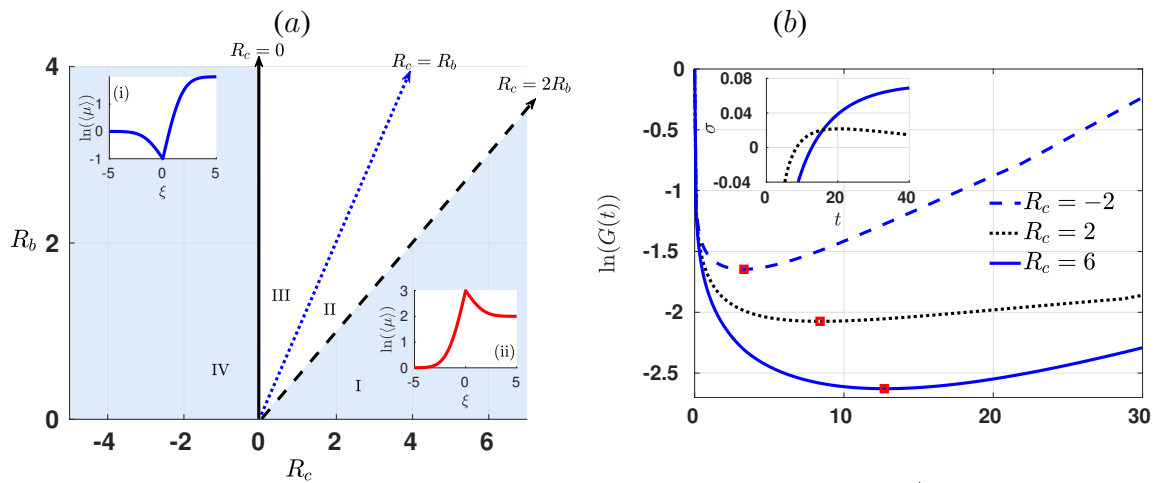


FIGURE 5.6: (a) The (R_b, R_c) phase plane for $R_b > 0$. Here in the uncolored region bounded between the lines $R_c = 0$ and $R_c = 2R_b$, the viscosity profile remains monotonic. Inset: Log-viscosity profile for $R_b = 2$, (i) $R_c = -2$, (ii) $R_c = 6$. (b) Optimal amplification for $R_b = 2$, $R_c = 6, -2, 2$. Here the squared marker denotes the onset time. Inset: Growth rate for $R_c = 6, 2$.

The viscosity profiles is illustrated for $R_c = 6, -2$ with fix $R_b = 2$ in figure 5.6(a). For these parameters, the viscosity contrast increases in the upstream (downstream) mixing zone for $R_c = 6$ ($R_c = -2$). Since the instability is supposed to develop upstream to the flow for $R_c = 6$, it results in delayed onset than the system corresponds to $R_c = 2$. However, after onset time, the growth rate of perturbations increases more than $R_c = 2$ as shown in figure 5.6(b). Further, it can be confirmed through non-linear simulation results as the mixing length due to instability is more for $R_c = 6$ than $R_c = 2$ in figure 5.5(b). On the contrary, when $R_c = -2$, the viscosity contrast increases in the downstream mixing zone while the upstream mixing zone stabilizes the flow due to a favorable viscosity contrast. The becomes more unstable than both the cases $R_c = 6, 2$ with early onset and more amplified perturbations. In such a viscosity configuration, the optimal energy of the perturbations is more amplified for a reactive system and the system becomes more unstable than the corresponding situation, $R_c = 6$ despite the same viscosity jump, $|R_b - R_c| = 4$.

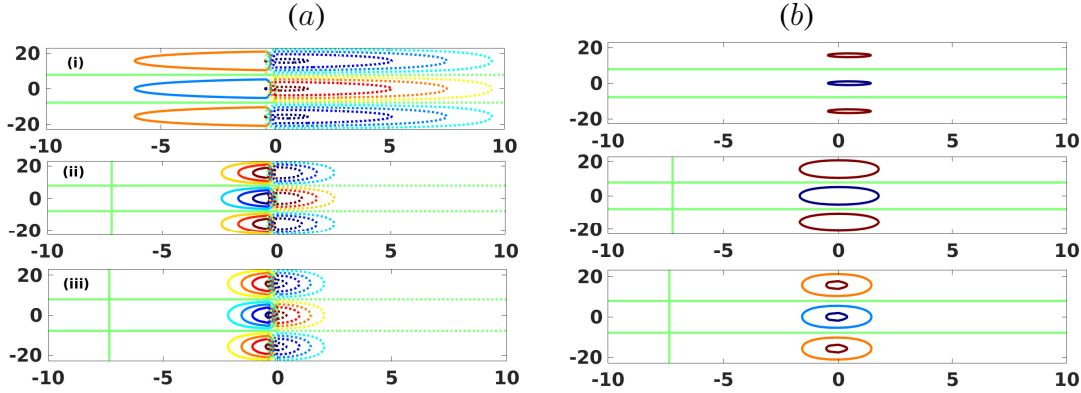


FIGURE 5.7: Perturbation contour plot for $R_b = 2$, $k = 0.2$ and $R_c = 2$, of (a) A and B and (b) C . Here the time integration intervals are (i) = $[0.001, 0.1]$, (ii) = $[0.001, 5]$ and (iii) = $[0.001, 30]$. In (a) the solid lines show the reactant A perturbation contour and dashed lines present reactant B perturbation contours.

Further, we plot the perturbation iso-contours for a' , b' and z' in figure 5.7 and explain the underlying physical mechanism. For a non-monotonic viscosity profile, it is stated that the perturbation contours are formed in a quadruple structure, while they remain in a dipole structure for a monotonic viscosity profile for a non-reactive system [39, 64]. However, it is complicated to understand the interpretation of the temporal evolution of the perturbed concentration according to the viscosity profile in the reactive system since there are four perturbed concentrations, a' , b' , c' and z' . It has been observed that dipole structures develop for z' and that the quadruple structures are always formed for the perturbed concentration of C . Since the base state reactant

A and B concentrations are localized in the upstream and downstream mixing zones respectively, the perturbation contours follow a similar profile. The perturbation contours are plotted for reactant concentration in figure 5.7. It clearly shows how perturbations respond in reference to their base state profile. Further, the perturbed concentration of C is impacted by the perturbed reactant concentration, b' and a' , as stated in equation (5.9).

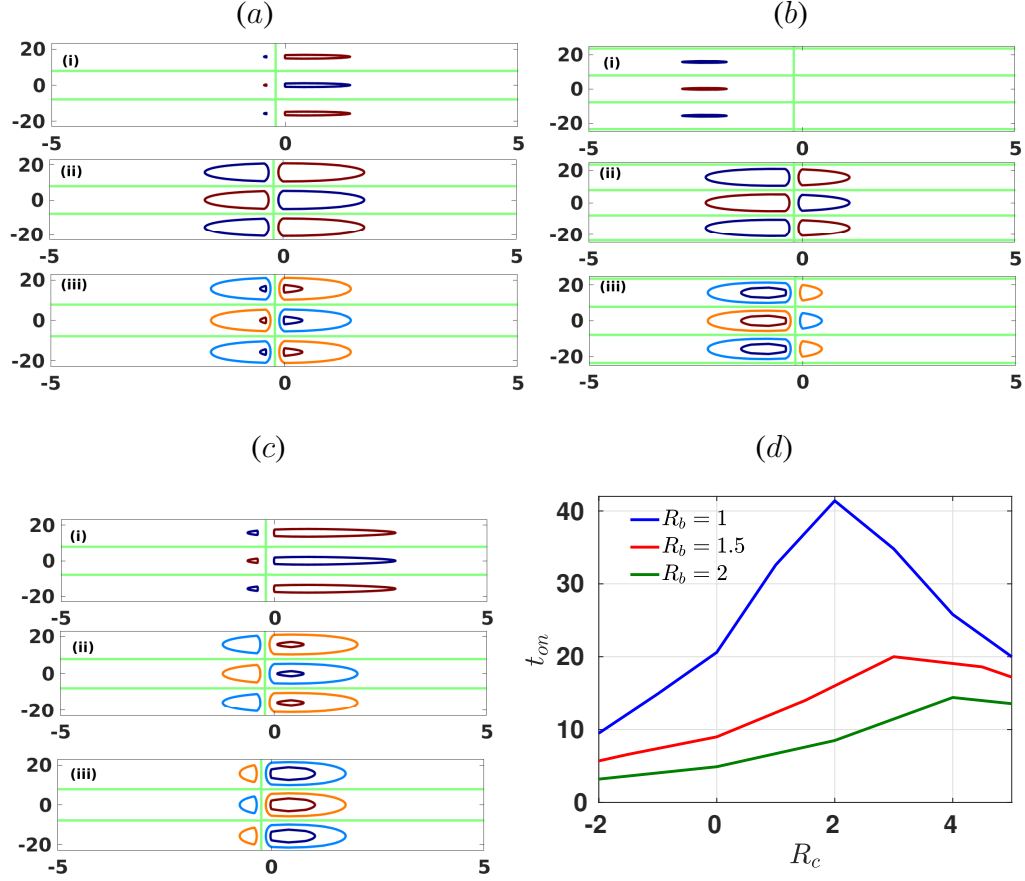


FIGURE 5.8: Perturbation contour plot for $R_b = 2$, (a) $R_c = 2$, (b) $R_c = 6$ and (c) $R_c = -2$, showing the evolution of the perturbations of product, $c = V \cos(ky)$ and $k = 0.2$. Here the time integration intervals, $[t_p, t]$ are (i) $[0.001, 0.1]$, (ii) $[0.001, 5]$ and (iii) $[0.001, 30]$. The perturbation contours are shown to span from their minimum to maximum values in five equal increments. (d) Onset time versus R_c for various R_b .

Further, we illustrate the temporal evolution of perturbations of c' for various R_c in figure 5.8. The viscosity profile is monotonically increasing for $R_c = 2$, which implies the unfavorable viscosity contrast should not be shifted at any of the zones. Consequently, the perturbation contours are almost uniformly distributed and develop with time in both regions for $R_c = 2$ as in figure 5.8(a). While the viscosity profile is modified into a non-monotonic viscosity profile with maxima for $R_c = 6$ that makes the perturbations isocontours in the downstream mixing zone,

stabilize due to diffusion. While the perturbation isocontours continue to evolve over time at the unstable upstream mixing zone shifting the perturbed concentration profile illustrated in figure 5.8(b). On the other hand, the perturbation isocontours develop more in the downstream mixing zone than the upstream mixing zone for $R_c = -2$ which is shown in figure 5.8(c). Thus, the perturbation contours demonstrate that the strength of the destabilizing contours as well as their placements are affected by R_c and have an impact on the stability of the reactive displacement.

Thus far, it has been noted that the onset experiences a delay when $R_c > R_b$ compared to the corresponding scenario where $R_c = R_b$ for a given R_b . However, it is necessary to examine whether the onset continues to be delayed for higher viscosity ratios, $R_c > R_b$ as further increment in the viscosity contrast at the upstream mixing zone. Alternatively, an early onset might be observed for higher viscosity contrast as seen in non-linear simulations at later times [69]. To analyze the same, simulations are performed for various values of R_b and R_c and check whether the VF dynamics outlined for $R_b = 2$ are qualitatively the same for other R_b values. The onset time for $R_b = 1, 1.5, 2$ and various R_c is plotted in figure 5.8(d) to determine the effect of the altered viscosity profile. We obtain there exists some reactions for which $R_c > R_b$, the onset occurs early than the corresponding non-reactive case, $R_c = R_b$. Re-analyzing the viscosity profile reveals that the least steeper viscosity contrast occurs when $R_c = R_b$ at fixed R_b . Interestingly, when $R_c = 2R_b$ as onset is delayed most for a given R_b . Even though the viscosity contrast is steeper for some values of R_c , the instability is more likely to occur at the upstream mixing zone when $R_c > R_b$ and hence, the onset is delayed [67]. We explain this through energy balance computation in section §5.4.3. In another way, it explains how, despite the steeper viscosity profile than $R_c = R_b$, the stable downstream mixing zone can dominate dynamics and delay the onset time.

5.4.2.2 Optimal amplification for $R_b < 0$

When $R_b < 0$, the reactant A is more viscous than reactant B implying the flow is stable before the reaction. The flow becomes unstable if product viscosity modifies the viscosity profile into non-monotonic when $|R_c - 2R_b| > 0$ as shown in figure 5.9(a), zone I and III. While, zone II in figure 5.9(a) between the line $R_c = 2R_b$ and $R_c = 0$, remains stable. Another important observation is that, unlike when $R_b > 0$, the viscosity contrast in stable zones is always greater than that in unstable zones for the case $R_b < 0$. It indicates that the unstable zone remains

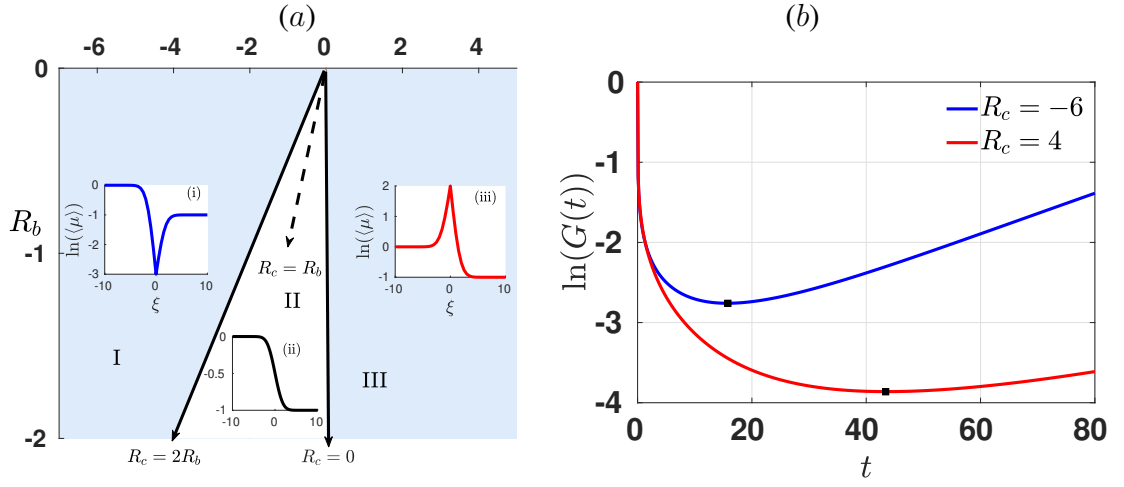


FIGURE 5.9: (a) The (R_b, R_c) phase plane for $R_b < 0$. Here the colored regions depict the non-monotonic viscosity profile. Inset: log-viscosity profile for $R_b = -1$ and (i) $R_c = -6$, (ii) $R_c = -1$, (iii) $R_c = 4$. (b) Optimal amplification for $R_b = -1$ and $R_c = 4, -6$.

weaker than the stable zone suggesting that the perturbations die at the stable zone with time as there is less dominance of the unstable zone as shown in figure 5.10. For $R_c = 4$ ($R_c = -6$), the perturbation contours are more dispersed in the unstable upstream (downstream) mixing zone and die with time in the stable zone. This emphasizes the significant impact of the endpoint viscosity contrast *i.e.* on the spatiotemporal evolution of perturbations and the underlying flow dynamics.

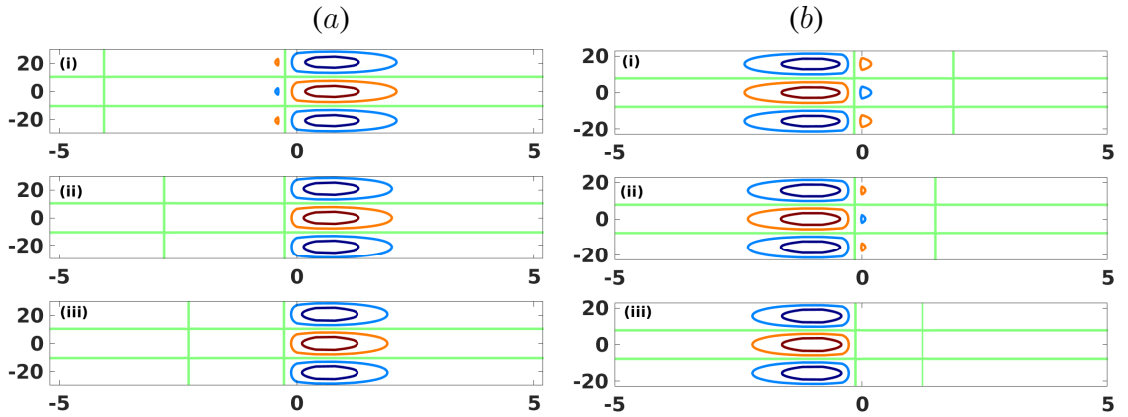


FIGURE 5.10: Perturbation contour plot for $R_b = -1$, $Da \rightarrow \infty$ and (a) $R_c = -6$, $k = 0.15$ and (b) $R_c = 4$, $k = 0.1$. Here the time integration intervals $[t_p, t]$ (i) = $[0.001, 30]$, (ii) = $[0.001, 50]$ and (iii) = $[0.001, 80]$.

Moreover, the optimal amplification is computed for $R_c = 4, -6$ retaining the same viscosity jump at both the zone, stable and unstable in figure 5.9(b). The optimal amplification, $\ln(G(t))$ is more, and early onset occurs for $R_c = -6$ than $R_c = 4$. In the next subsection, the balance

of energy attributed to various terms in linearized equations in (ξ, t) coordinates is presented, followed by a comparison with QSSA in (x, t) coordinates.

5.4.3 Computing perturbation energy balance

A more comprehensive analysis of the impact of infinitely fast reactions on perturbation stability can be achieved by examining the energy distribution of concentration perturbation eigenmodes. Upon using the QSSA in the self-similar co-ordinates (ξ, t) , i.e., $(\phi_u, \phi_z, \phi_a, \phi_b, \phi_c) =$

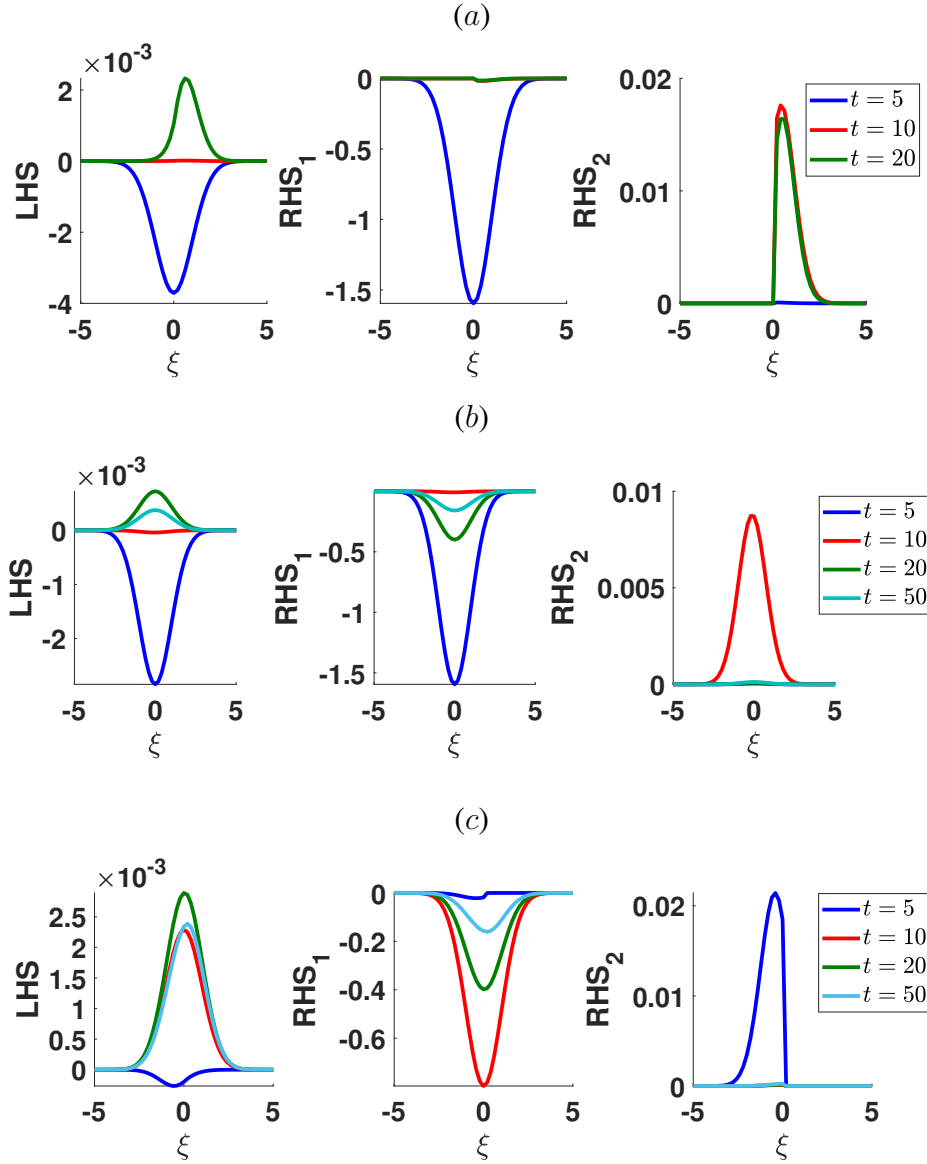


FIGURE 5.11: Energy balance for reactive fluids, $Da \rightarrow \infty$, $k = 0.2$, $R_b = 2$ obtained in (ξ, t) domain for (a) $R_c = 0$, (b) $R_c = 2$ and (c) $R_c = 4$ at different times.

$(\psi_u, \psi_z, \psi_a, \psi_b, \psi_c) e^{\sigma(t_0)t}$. Here t_0 is the freezing time and $\sigma(t_0)$ is the growth constant of the

system for a given wave number k . Equation (5.12) reduces to

$$\left(\frac{1}{t} \mathcal{D}^2 - \frac{1}{t} (R_b \mathcal{D} B_b + R_c \mathcal{D} C_b) \mathcal{D} - k^2 \right) \psi_u = k^2 (R_c \psi_c + R_b \psi_b), \quad (5.17)$$

$$\sigma(t_0) \psi_z = \left(\frac{1}{t} \mathcal{D}^2 - k^2 \right) \psi_z + \frac{\xi}{2} \mathcal{D} \psi_z - \frac{1}{\sqrt{t}} (\mathcal{D} z_b) \psi_u \quad (5.18)$$

with initial condition $(\psi_a, \psi_b, \psi_c) = \begin{cases} (0, -2\psi_z, \psi_z), & \xi > 0, \\ (2\psi_z, 0, -\psi_z), & \xi \leq 0, \end{cases}$ where $\mathcal{D} = \frac{d}{d\xi}$ and $\mathcal{D}^2 = \frac{d^2}{d\xi^2}$.

In order to get the concentration perturbation eigenmodes energy $|\psi_z|^2$, multiply the complex conjugate of ψ_z , denoted by ψ_z^* with Equation (5.17), we have

$$\sigma(t_0) \psi_z \psi_z^* = \left[\left(\frac{1}{t} \mathcal{D}^2 - k^2 \right) \psi_z \right] \psi_z^* + \frac{\xi}{2} (\mathcal{D} \psi_z) \psi_z^* - \frac{1}{\sqrt{t}} (\mathcal{D} z_b) \psi_u \psi_z^*, \quad (5.19)$$

where the term on the left-hand side, $\text{LHS} = \sigma |\psi_z|^2 = \sigma(t_0) \psi_z \psi_z^*$ expression represents the balance and the term on the right-hand side, $\text{RHS}_1 = \left[\left(\frac{1}{t} \mathcal{D}^2 - k^2 \right) \psi_z \right] \psi_z^*$ is diffusion term, and $\text{RHS}_2 = -\frac{1}{\sqrt{t}} (\mathcal{D} z_b) \psi_u \psi_z^*$ is the production of perturbed velocity and perturbed concentration by the effect of the perturbed on the base state concentration profile. Here a steady base state implies that the RHS_2 term depends on time and ψ_u only. It is observed that the eigenmodes determined from SS-QSSA are always real-valued.

The energy balance terms for $R_b = 2$ and various R_c are plotted in Figure 5.11. Initially, at time $t = 5$, when $R_c = 2$, the flow remains stable due to the negative left-hand side (LHS) term i.e., $\sigma < 0$. This stability can be attributed to the dominance of diffusion in the energy budget, as the RHS_1 exceeds RHS_2 at this point. Subsequently, after the onset time, RHS_1 experiences a significant decay. Now, the energy budget is compared for a viscosity profile with a steeper gradient, for $R_c = 0, 4$, than $R_c = 2$. In the case of $R_c = 0$ (see Figure 5.11(a)), RHS_1 decays rapidly, and RHS_2 shifts towards the downstream mixing zone, as predicted by the perturbed concentration contour plots as in Figure 5.8(c). However, the same does not happen when $R_c = 4$ as shown in Figure 5.11(c). Notably, RHS_1 decays at a slower rate compared to the $R_c = 0, 2$ case. Furthermore, it is observed that as there is a decrease in the viscosity contrast in the downstream mixing zone, RHS_1 becomes more dominant signifies diffusion, and similarly, RHS_2 , associated with convection, decays more rapidly. This justifies the delayed onset time for $R_c = 4$ compared to both $R_c = 2$ and $R_c = 0$. Moreover, it illustrates that despite the steeper

viscosity contrast occurring at the upstream mixing zone for $R_c = 4$, the flow dynamics are primarily influenced by the viscosity profile at the downstream mixing zone.

5.4.4 Comparision with QSSA

The QSSA in (x, t) coordinates assumed that the rate of change of the base state is much slower compared to the pace at which perturbations change. Here, two-time scales are considered: one related to the base state and the other to the perturbations. We freeze the base state under the same supposition and then apply modal analysis to get an eigenvalue problem. One significant drawback of this approach is that the base state undergoes rapid changes during early times. Therefore, the time-dependent stability matrix is non-normal. Therefore, the QSSA may not accurately represent the initial time dynamics. The non-normality of the stability matrix is analyzed by calculating the condition number presented in Appendix §E [37, 108].

At an initial time, QSSA predicts that the flow will be unstable when $R_c < R_b$ for increasing Da when $R_b > 0$. While the system becomes less unstable, the corresponding non-reactive situation $R_c = R_b$ will be the most unstable situation among the flow conditions $R_c \geq R_b$. On the contrary, through NMA, it is observed that there exist some reactions for which early onset occurs for $R_c > R_b$. Moreover, the growth rate increases for $R_c > R_b$ after the onset time than in the case of $R_c = R_b$ showing a more unstable displacement. Further, the flow is stable initially due to diffusion, and instability takes time when convection dominates the dynamics. Evidently, QSSA fails to capture early-time diffusion and does not anticipate the onset of instability for the reactive flow corresponding to $R_b < 0$.

5.5 Conclusion

In this theoretical study, the stability of a miscible reactive interface is addressed subject to a VF instability for a rectilinear flow in the porous medium. The perturbed system, after linearization, is determined to be a set of non-autonomous equations. To address this, Hejazi *et al.* [35], invokes QSSA and analysed the infinitely fast reactions limited to growth rate analysis at $t = 0$. The QSSA eigenmodes, however, are non-orthogonal, and there is potential for non-modal growth [86]. To the best of our knowledge, in the linear regime, a systematic stability analysis for infinitely fast reactions has not been conducted. The present study aims to address the

constraints associated with the QSSA method. To overcome the shortcomings inherent in the QSSA approach, we adopt non-modal analysis (NMA), which is based on the principles of singular value decomposition. Further, we perform NMA in a self-similar domain which provides a steady base state.

The analysis is limited to the asymptotic limit $Da \rightarrow \infty$, so the stability of the underlying reactive displacement is solely dependent on the non-dimensional parameters R_b and R_c . The destabilization of the system is enhanced when the chemical reaction yields a product with lower viscosity, denoted as $R_c < R_b$, while maintaining the same viscosity contrast $|R_c - R_b|$. While some types of reactions exist, the onset gets delayed when $R_c > R_b$ despite the steeper viscosity contrast when $R_b > 0$. Moreover, the NMA results show that the most delayed onset occurs when $R_c = 2R_b$ for each R_b despite the steeper viscosity gradient than the case $R_b = R_c$. This happens since the instability originates upstream to the flow when $R_c > R_b$ and onset gets delayed [67]. It is confirmed by analyzing the energy budget and showing the dominance of viscosity contrast at the downstream mixing zone. Further, it is demonstrated that the perturbation contours localize at the unstable front and diminish at the stable zone faster if $R_b \leq 0$ while the same can not be observed for the case when $R_b > 0$. These results all agree well with those of the non-linear simulations [69]. It concludes that for reactive displacements, the NMA approach can describe more accurately the onset time and the underlying physical mechanism of instability. Moreover, the QSSA technique is unable to capture these results due to the presence of non-normality in the stability matrix.

For the infinitely fast reaction system, the present LSA can assist in predicting early time dynamics more accurately and can be utilized to optimize the instability. In addition to the scope of this study, it is necessary to explore the impact of chemical reactions with the values (R_b, R_c) on VF dynamics. It is also important to determine whether the same chemical reaction can result in different fingering dynamics when the ratio of initial reactant concentrations is varied. Additionally, our study focuses on the continuous investigation of the consequences of a finite Damkohler number (Da) on the dynamics of fingering. A detailed analysis of this topic will be presented in the next chapter 6

Chapter 6

Non-modal linear stability analysis of reaction-induced miscible viscous fingering for rectilinear flow

6.1 General introduction

In the preceding chapter 5, our analysis primarily centered on reactive displacement that entailed reactions occurring at an infinitely rapid rate. This analysis was conducted through the utilization of non-modal linear stability analysis (NMA) employing the propagator matrix approach. However, we have not addressed reactive displacements considering finite reaction rates, denoted as Da , for rectilinear flow. For finite Da , Hejazi et al. [35] have performed a linear stability analysis (LSA) on a reactive system and approached quasi-steady state approximation (QSSA) for rectilinear displacement. They have derived the dispersion relation analytically at the initial time point, $t = 0$ and for $t > 0$, the stability analysis is studied by solving an eigenvalue problem. The viscosity profile is dependent on the concentration of reactants and product in an exponential manner. It has been observed that the flow becomes more unstable when non-monotonic viscosity profiles are present, specifically those that exhibit a minimum rather than a maximum after the reaction occurs. This phenomenon has been observed in reactive displacements involving reactants with equal viscosities. Further, they have provided contour plots illustrating the stability zones, which depict the maximum instantaneous growth rate for different reactions at various time intervals. Because the viscosity profile demonstrated non-monotonic behavior for the reactive flow, the presence of both unstable and stable zones underlines the relevance and complexity of finger pattern rheology. It is important to comprehend the implications of non-monotonicity in order to effectively manage or induce instability.

In 2018, Hota and Mishra [37] conducted a study on miscible viscous fingering (VF) with non-monotonic viscosity profiles and performed non-modal analysis for non-reactive displacements. It is demonstrated that the underlying physical mechanism is impacted by both the viscosity contrast at the endpoints and the maximum viscosity caused by the non-monotonic viscosity profile. Further, the perturbation contours are formed in quadruple structures. However, the

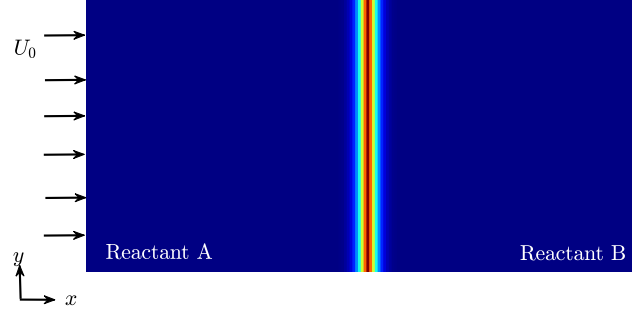
QSSA analysis falls short of capturing these findings. In this chapter, we investigate the reactive viscous fingering in a linear regime with reactions involving iso-viscous reactants and depicting a non-monotonic viscosity profile.

As described in Chapter 5, the mathematical representation of reactions that occur at an infinite rate of speed entails using a coupled equation that combines Darcy's law with the convection-diffusion equation. However, when dealing with finite values of Da , the analysis requires to incorporation of three convection-diffusion reaction (CDR) equations. Consequently, the complexity arises when conducting NMA. For instance, we have derived an analytical solution for the steady base state profile when $Da \rightarrow \infty$. However, for finite Da values, the base state profile which is determined by reaction-diffusion equations, does not possess an explicit analytic solution. Further, we have derived an analytical solution for the steady base state profile when $Da \rightarrow \infty$. Conversely, for finite Da , the base state profile is described by reaction-diffusion equations, for which an explicit analytic solution is not attainable [29, 35]. In this chapter, we will discuss the complexities mentioned above and propose a numerical method for conducting Non-Modal Analysis (NMA) on reactive displacement with finite reaction rates. In order to accomplish this objective, we employ a propagator matrix methodology in a self-similar domain.

This chapter is outlined as follows. In section §6.2, we describe the mathematical framework concerning reactive displacements characterized by finite Da within the rectilinear flow. Subsequently, in section §6.3, we derive the linearized perturbed equations following discussions on the base state and transient energy growth. Finally, our findings are discussed in section §6.4 and then, conclusions are summarized in section §6.5.

6.2 Mathematical formulation

Consider the flow in a two-dimensional homogeneous porous media as shown in figure 6.1 where the invading fluid is injected at a uniform velocity \tilde{U}_0 . The system involves two reactive fluids, namely fluid A and B that are assumed to exhibit the properties of incompressibility, Newtonian behavior, neutrality in buoyancy, and miscibility. When these two fluids come into contact, they undergo a second-order chemical reaction represented by $A + B \rightarrow C$, where C is the product after reaction.

FIGURE 6.1: Schematic of the flow of a reactive front $A + B \rightarrow C$.

The flow can be formulated mathematically as the set of partial differential equations (PDEs) including the continuity equation and Darcy's law, which together describe the conservation of mass and momentum in the flow through a porous medium. These equations are coupled with three convection-diffusion-reaction (CDR) equations that govern the mass balance for the three fluids, A , B , and C . The non-dimensionalized governing equations are as follows [31, 35]:

$$\nabla \cdot \mathbf{u} = 0, \quad (6.1a)$$

$$\nabla p = -\mu(\mathbf{u} + \mathbf{i}), \quad (6.1b)$$

$$\frac{\partial a}{\partial t} + \mathbf{u} \cdot \nabla a = \nabla^2 a - Da ab, \quad (6.1c)$$

$$\frac{\partial b}{\partial t} + \mathbf{u} \cdot \nabla b = \nabla^2 b - Da ab, \quad (6.1d)$$

$$\frac{\partial c}{\partial t} + \mathbf{u} \cdot \nabla c = \nabla^2 c + Da ab. \quad (6.1e)$$

The equations (6.1) are presented in a moving reference frame with uniform velocity, \tilde{U}_0 as in chapter 5. Here $\mathbf{u} = (u, v)$ Darcy velocity, p pressure, μ viscosity and (a, b, c) are fluid concentration of A , B , C . The equations are non-dimensionalised as chapter 5. The system of equations (6.1) supplemented with the initial condition for velocity, $\mathbf{u} = \mathbf{0}$ and fluid concentrations,

$$(a, b, c)(x, y) = \begin{cases} (0, 1, 0), & x > 0, \\ (1, 0, 0), & x \leq 0. \end{cases} \quad (6.2)$$

The reactive flow is characterized by two dimensionless parameters Damköhler number Da and log-mobility ratio R_c . The viscosity depends on the product concentration exponentially [31],

$$\mu = e^{R_c c}, \quad R_c = \ln \left(\frac{\mu(c=1)}{\mu(c=0)} \right).$$

Here we study how the chemical reaction affects the flow stability if it modifies the viscosity profile *i.e.*, $R_c \neq 0$ by performing linear stability analysis.

6.3 Linear stability analysis

To perform LSA, we introduce a base state solution for a reactive system, followed by the derivation of the linearized perturbation equations. Let us denote the base state concentrations by A_b , B_b and C_b of fluid A , B and C respectively which followed the following reaction-diffusion equations:

$$\frac{\partial A_b}{\partial t} = \frac{\partial^2 A_b}{\partial x^2} - Da A_b B_b, \quad (6.3a)$$

$$\frac{\partial B_b}{\partial t} = \frac{\partial^2 B_b}{\partial x^2} - Da A_b B_b, \quad (6.3b)$$

$$\frac{\partial C_b}{\partial t} = \frac{\partial^2 C_b}{\partial x^2} + Da A_b B_b. \quad (6.3c)$$

In the base state profile, both reactants meet via diffusion, reacting to produce C at the miscible interface. Over time, A and B are consumed by the reaction, causing a decrease in the reaction rate. Simultaneously, more and more product is formed and diffuses further as shown in figure 6.2. If we reconsider the equations (6.3) along with the initial conditions in the equation (6.2), we obtain $A_b + B_b + 2C_b = 1$ [35]. It indicates that when the reactants are entirely consumed, the maximum concentration of C can reach up to 0.5, *i.e.*, $c_{max} = 0.5$. Since an exact analytical solution for this set of base-state equations is unattainable, we solve them numerically [29, 35].

Further, we perturb the base state and the magnitude of the perturbations is of order $O(10^{-3})$. We denote the perturbed quantities with prime notations.

$$(a, b, c) = (A_b, B_b, C_b) + (a', b', c'),$$

$$\mathbf{u} = \mathbf{0} + \mathbf{u}', \quad \mu = \mu_0 + \mu', \quad p = p_0 + p'.$$

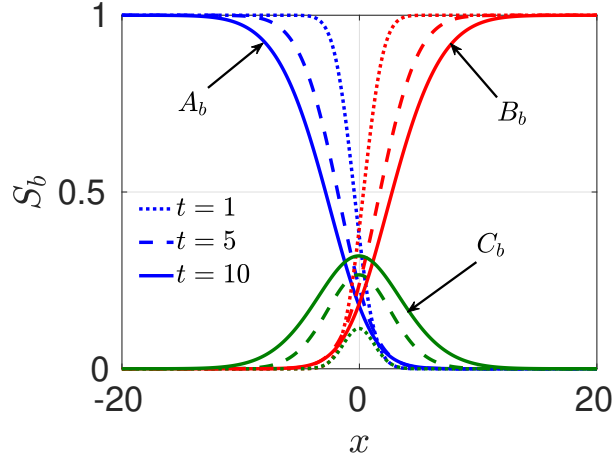


FIGURE 6.2: Base state concentration profile for A (blue lines), B (red lines) and C (green lines) at time $t = 1, 5$ and 10 represented by dotted, dashed and solid lines, respectively. Here, S_b is the dummy variable for base state concentrations.

The linearized perturbed system of equations will be,

$$\nabla \cdot \mathbf{u}' = 0, \quad (6.4a)$$

$$\nabla p' = -\mu_0 \mathbf{u}' - \mu' \mathbf{i}, \quad (6.4b)$$

$$\frac{\partial a'}{\partial t} + \mathbf{u}' \cdot \nabla A_b = \nabla^2 a' - Da(A_b b' + B_b a'), \quad (6.4c)$$

$$\frac{\partial b'}{\partial t} + \mathbf{u}' \cdot \nabla B_b = \nabla^2 b' - Da(A_b b' + B_b a'), \quad (6.4d)$$

$$\frac{\partial c'}{\partial t} + \mathbf{u}' \cdot \nabla C_b = \nabla^2 c' + Da(A_b b' + B_b a'), \quad (6.4e)$$

$$\mu' = \mu_0(R_b b' + R_c c'). \quad (6.4f)$$

Here p' can be eliminated by using the curl of the perturbed equations of Darcy's law, and the perturbed continuity equation is then used to eliminate v' . Further, the above set of equations is linear in terms of the function of y . This characteristic allows us to apply Fourier mode decomposition of the perturbations, $s' = \phi_s e^{iky}$. Here s is the dummy variable that stands for either a , b or c , and k is the wavenumber.

The reduced set of equations are,

$$\frac{\partial}{\partial t} \begin{bmatrix} \phi_a \\ \phi_b \\ \phi_c \end{bmatrix} = \begin{bmatrix} M_{11} & M_{12} & M_{13} \\ M_{21} & M_{22} & M_{23} \\ M_{31} & M_{32} & M_{33} \end{bmatrix} \begin{bmatrix} \phi_a \\ \phi_b \\ \phi_c \end{bmatrix} \quad (6.5)$$

where

$$\left. \begin{aligned} M_{11} &= \mathcal{D}_x^2 - k^2 \mathcal{I}_x - DaB_b, & M_{12} &= -DaA_b, & M_{13} &= -\mathcal{D}_x A_b \mathcal{N}, \\ M_{21} &= -DaB_b, & M_{22} &= \mathcal{D}_x^2 - k^2 \mathcal{I}_x - DaA_b, & M_{23} &= -\mathcal{D}_x B_b \mathcal{N}, \\ M_{31} &= DaB_b, & M_{32} &= DaA_b, & M_{33} &= \mathcal{D}_x^2 - k^2 \mathcal{I}_x - \mathcal{D}_x C_b \mathcal{N}, \\ \mathcal{N}_1 &= \mathcal{D}_x^2 - k^2 \mathcal{I}_x + (R_c \mathcal{D}_x C_b) \mathcal{D}_x, & \mathcal{N}_2 &= k^2 R_c \mathcal{I}_x, & \mathcal{N} &= \mathcal{N}_1^{-1} \mathcal{N}_2. \end{aligned} \right\}$$

Here, $\mathcal{D}_x = \frac{\partial}{\partial x}$; \mathcal{I}_x is Identity operators. We consider the numerical domain as $\Omega = [-L, L]$ which is discretized into $n + 2$ grid points.

In order to analyze the linearised perturbed system (6.5), the existing approaches for linear stability analysis can be classified into two categories modal analysis and non-modal analysis. In modal analysis, the differential equation system is converted into an eigenvalue problem, as perturbations are assumed to be exponentially dependent on time. Here, we study the most unstable eigenmode and predict the asymptotic behavior of the system. In the equation (6.5), the system is non-autonomous as the base state is unsteady and hence, the stability matrix M_{ij} , $i, j \in \{1, 2, 3\}$ is time dependent that prohibits to apply the traditional modal analysis. To deal with the unsteady base state, a method presented in the literature is the quasi-steady state approximation (QSSA) approach [35].

6.3.1 QSSA

In the framework of QSSA, it is assumed that the rate of change in the base state is much slower than the rate of change in perturbations, $\partial_t S_b \ll \partial_t s'$. Here S_b and s' are dummy variables to represent base state and perturbed variables. This assumption introduces two distinct time scales: the first is associated with the base state, denoted as t_0 , and the second pertains to the perturbations and is represented as t . Building upon this assumption, we freeze the base state, and subsequently, we apply modal analysis, expressed as $\phi_s = \Phi_s(x)e^{\sigma(t_0)}$. The system of

equations can then be simplified accordingly.

$$\begin{bmatrix} M_{11} & M_{12} & M_{13} \\ M_{21} & M_{22} & M_{23} \\ M_{31} & M_{32} & M_{33} \end{bmatrix} \begin{bmatrix} \phi_a \\ \phi_b \\ \phi_c \end{bmatrix} = e^{\sigma(t_0)} \begin{bmatrix} \phi_a \\ \phi_b \\ \phi_c \end{bmatrix} \quad (6.6)$$

In this context, t_0 serves as the freezing time, and $\sigma(t_0)$ represents the growth constant of the system for a given wave number k . It is important to note that in the early stages, the base state undergoes rapid changes. The QSSA anticipates that the flow remains most unstable until the product concentration reaches its peak. When $R_c = 5, 3$, the QSSA indicates a decline in the growth constant after $t = 100$, followed by flow stabilization [35] which is in contrast with non-linear simulations [31]. Evidently, the QSSA fails to accurately represent the transient time dynamics. To capture the same, we need a better approach for analysis than QSSA.

6.3.2 Non-modal analysis

Due to the linearised perturbed system being non-autonomous, we prefer using non-modal analysis [39, 86]. For the same, we employ a propagator matrix approach in the self-similar domain. In self-similar domain, we have,

$$\xi = \frac{x}{\sqrt{t}} \quad \tau = t.$$

The equation (6.5) will be transformed in self-similar domain as:

$$\frac{\partial}{\partial t} \begin{bmatrix} \phi_a \\ \phi_b \\ \phi_c \end{bmatrix} = \begin{bmatrix} L_{11} & L_{12} & L_{13} \\ L_{21} & L_{22} & L_{23} \\ L_{31} & L_{32} & L_{33} \end{bmatrix} \begin{bmatrix} \phi_a \\ \phi_b \\ \phi_c \end{bmatrix} \quad (6.7)$$

where

$$\left. \begin{aligned} L_{11} &= \mathcal{D}_\xi^2 - k^2 \mathcal{J}_\xi + (\xi/2\sqrt{t})\mathcal{D}_\xi - DaB_b, & L_{12} &= -DaA_b, & L_{13} &= -\mathcal{D}_\xi A_b \mathcal{J}, \\ L_{21} &= -DaB_b, & L_{22} &= \mathcal{D}_\xi^2 - k^2 \mathcal{J}_\xi + (\xi/2\sqrt{t})\mathcal{D}_\xi - DaA_b, & L_{23} &= -\mathcal{D}_\xi B_b \mathcal{J}, \\ L_{31} &= DaB_b, & L_{32} &= DaA_b, & L_{33} &= \mathcal{D}_x^2 - k^2 \mathcal{J}_\xi + (\xi/2\sqrt{t})\mathcal{D}_\xi - \mathcal{D}_\xi C_b \mathcal{J}, \\ \mathcal{J}_1 &= \mathcal{D}_\xi^2 - k^2 \mathcal{J}_\xi + (R_c \mathcal{D}_\xi C_b) \mathcal{D}_\xi, & \mathcal{J}_2 &= k^2 R_c \mathcal{J}_\xi, & \mathcal{J} &= \mathcal{J}_1^{-1} \mathcal{J}_2, & \mathcal{D}_\xi &= \frac{1}{\sqrt{t}} \frac{\partial}{\partial \xi}. \end{aligned} \right\}$$

Using central finite difference formulas, we discretize the spatial derivatives. The initial value problem described in equation (6.7) can be written in matrix form:

$$\frac{d\phi}{dt} = L_{ij}\phi, \quad \phi = \begin{bmatrix} \phi_a \\ \phi_b \\ \phi_c \end{bmatrix}. \quad (6.8)$$

Further, we encounter a singularity in the system of equations (6.8) at time $t = 0$. We restrict our temporal domain to (t_p, t) that will allow us to get rid of the singularity at $t = 0$ from our system, where t_p is chosen to be on order 10^{-3} [39]. To apply the propagator matrix approach, we consider,

$$\begin{bmatrix} \phi_a \\ \phi_b \\ \phi_c \end{bmatrix} = \Psi(t_p; t) \begin{bmatrix} X_a \\ X_b \\ X_c \end{bmatrix}. \quad (6.9)$$

Here $[X_a, X_b, X_c]^T$ is the random initial condition where subscript T stands for transpose of a matrix and $\Psi(t_p; t)$ is a propagator matrix. It satisfies the following matrix-valued differential equation,

$$\frac{d}{dt}\Psi(t_p; t) = L\Psi(t_p; t); \quad \Psi(t_p; t_p) = \mathcal{I}, \quad (6.10)$$

where \mathcal{I} is an identity matrix of $3n \times 3n$. By opting for the propagator matrix approach, we deal with a deterministic system of differential equation (6.10) with initial condition $\Psi(t_p; t_p) = \mathcal{I}$ instead of a vector differential equation system with random initial condition. The propagator operator, $\Psi(t_p; t)$, is the one that passes information from the initial perturbation time (t_p), when the perturbation is introduced to the base state, to time, t .

We solve the initial value problem, (6.10) using the method of lines. Further, we solve explicitly by utilizing the Runge-Kutta method of fourth order with an inbuilt MATLAB function, ode45, with an absolute error of order $O(10^{-5})$ [1]. After solving the equation (6.10), we compute the optimal amplification, $G(t)$ and growth rate, σ . The optimal amplification is obtained through the singular value decomposition of the propagator matrix, $\Psi(t_p; t_f) = U M V^T$. The largest singular value of the propagator matrix represents the optimal amplification, denoted as $G(t)$, while the corresponding right singular vector, V , provides the optimal initial condition. The

evolved state for time t is given by the left singular vector, U . In the next section §6.3.2.1, we validate our numerical method.

6.3.2.1 Validation of numerical method

To validate our numerical method, we consider $Da = 0$ and $R_b = 3$ that correspond to non-reactive flow and tried to replicate the results of non-reactive flow by generating the same viscosity profile as the non-reactive one. However, it is difficult to choose the appropriate initial condition. The obvious choice for the initial condition was for the equation (6.10), an identity matrix of $3n \times 3n$. If we reconsider the base state equations as in equation (6.3) for $Da = 0$, both A_b and B_b follow the diffusion equations, but with different initial conditions as in (6.2). Further, for non-reaction fluids, the base state concentration follows the diffusion equation adopting the same initial condition as for B_b . Hence, the base flow equations are still different for a reactive case with $Da = 0$ compared to the non-reactive fluids. Therefore, anticipating identical amplification as observed in non-reactive fluids becomes impracticable. Evidently, the initial condition did not work.

To consider the same non-reactive base state profile, we consider the base state for A and B the same, $A_b = B_b$. From figure 6.3, it can be shown that we are able to reproduce the non-reactive results as amplification curves are matched, hence we validate our numerical method. Further, it is computationally costly to solve a system of $3n \times 3n$, $3n$ times. To reduce the computation cost, we check if flow stability is affected by the initial condition for c' and a' . We observe that the stability is not affected if we consider $a'(t = 0) = c'(t = 0) = 0$ and $b'(t = 0) \neq 0$. Thus, we consider the initial condition for (6.10) as $\Psi(t_p; t_p) = \mathcal{A}$. Here, \mathcal{A} is a $3n \times 3n$ block diagonal matrix with the $n \times n$ identity matrix as the second block along the main diagonal and all other entries set to zero.

6.4 Result and discussion

Initially, the flow is stable in the absence of viscosity contrast as the viscosity of reactants are identical *i.e.*, $\mu_A = \mu_B$. If the generated product has some viscosity contrast with the reactants, a chemical reaction at time $t > 0$ changes the viscosity profile and turns into a non-monotonic viscosity profile. Owing to the presence of three fluids, the reaction zone, where the product

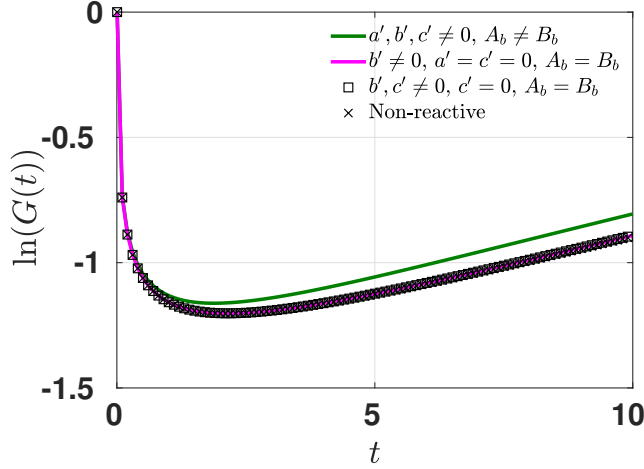


FIGURE 6.3: Log of optimal amplification, $\ln(G(t))$ for $R_b = 3$, $Da = 0$ in the reactive case. Here, the (\times) curve shows the $\ln(G(t))$ for the non-reactive case.

C is present, can be divided into two regions: the downstream mixing zone and the upstream mixing zone. The region primarily occupied by fluid A and C can be identified as the upstream mixing zones. While the downstream mixing zone is primarily occupied by fluid B and C . When the reaction produces a high viscous product *i.e.*, $R_c > 0$, the viscosity profile becomes non-monotonic with maxima and destabilizes the upstream mixing zone, while the downstream mixing zone remains viscously stable. Contrarily, the downstream mixing zone becomes unstable with increasing viscosity contrast as the less viscous product is being generated which is the case, $R_c < 0$. We plot the $\ln(G(t))$ for various values of $R_c \neq 0$ and analyze the flow stability.

6.4.1 Effect of R_c

In figure 6.4, the optimal amplification $\ln(G(t))$ is shown for various R_c and $Da = 1$. The increase (decrease) of $\ln(G(t))$ represents the relative growth (decay) of the disturbances. Moreover, the presence of extremums in this curve carries special significance: a minimum indicates the transition from a regime dominated by diffusion to one dominated by convection, which implies the onset of instability. We term the time corresponding to this minimum as the onset time of instability, denoted as t_{on} . Conversely, a maximum represents transient growth phenomena [39, 93]. This non-monotonicity in $\ln(G(t))$ curves exhibits the interplay between two forces namely, convection and diffusion.

It can be observed that there is an influence of steeper viscosity contrast and accordingly, we have an early onset for increased viscosity contrast $|R_c|$ if the reaction generates the less viscous

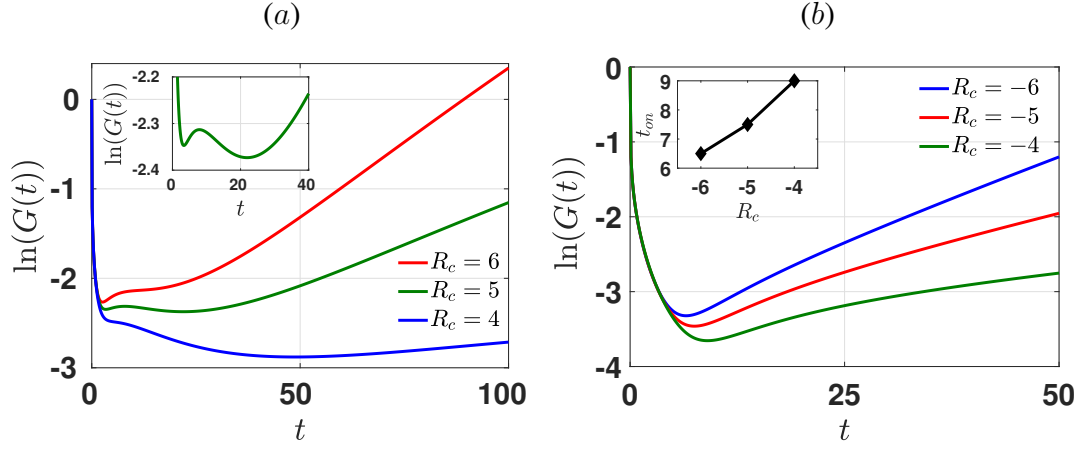


FIGURE 6.4: Logarithm of optimal amplification, $\ln(G(t))$ for $R_b = 0$, $Da = 1$ and (a) $R_c > 0$ and (b) $R_c < 0$. Here the diamond dots denote the onset time of instability.

product as shown in figure 6.4(b). While, for $R_c > 0$, the trend in $\ln(G(t))$ behaves inconsistently. Comparing the log-amplification curves for $R_c = 4$ and 6, an early onset is observed for $R_c = 6$ compared to $R_c = 4$, and after the onset time, $\ln(G(t))$ exhibits a monotonic increase with higher growth rate for $R_c = 6$. In contrast, for $R_c = 5$, the log-amplification curve displays two minima and one maxima. Following the second minima, $\ln(G(t))$ increases monotonically, and this minimum is considered the onset time for $R_c = 5$.

To understand the non-monotonic behavior of $\ln(G(t))$ before onset time for $R_c = 5$, we compute growth rate as defined in [39, 106]:

$$\sigma = \frac{1}{G} \frac{dG}{dt}. \quad (6.11)$$

We have plotted the growth rate curve for various $R_c > 0$ in figure 6.5. For $R_c = 5$, the initial increment following the first minima occurs due to the influence of unfavorable viscosity contrast at the upstream mixing zone. However, there exists a stable zone at the downstream mixing zone that impacts the flow stability and leads to the decay of perturbations. Evidently, the unfavorable viscosity contrast at the upstream mixing zone is not enough to sustain the perturbation growth. However, when diffusion weakens over time, convection becomes prominent, leading to the onset of instability. This phenomenon can be referred to as secondary instability [37]. A similar transition in stability is observed in literature [37] for the non-reactive fluids with non-monotonic viscosity-concentration relation. Interestingly, the same does not happen when $R_c = 6$ and 4. It can be explained that for $R_c = 4$, the viscosity contrast is less and not sufficient to amplify the

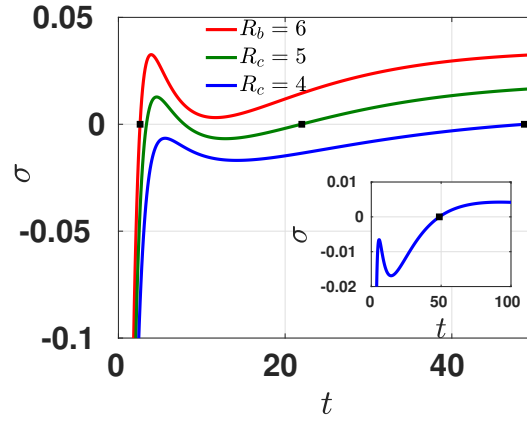


FIGURE 6.5: Growth rate, σ for $R_b = 0$, $Da = 1$ and $R_c > 0$. Here the squared dots denote the onset time of instability.

perturbations. Hence, due to the weak unstable zone, diffusion dominates the dynamics, and flow remains stable in early times. Further, the onset gets delayed until the stable zone within the downstream zone diffuses over time. Conversely, for $R_c = 6$, the higher viscosity contrast induces the onset of instability within the upstream mixing zone, sustaining perturbation growth without displaying secondary instability.

In addition, the absence of secondary instability is notable when the reaction generates a less viscous product, $R_c < 0$ despite the same viscosity contrast. When $R_c < 0$, the unstable zone is shifted at the downstream mixing zone, hence, the instability is anticipated to develop downstream to the flow. On the contrary, for $R_c > 0$, the instability will develop upstream to the flow. For non-reactive fluids, it is reported that the fingering instability is more intense when it develops downstream to the flow than the case when it develops upstream to flow for the same viscosity contrast [67]. This asymmetry in behavior persists for reactive fluids, leading to an early onset for $R_c < 0$ compared to the corresponding $R_c > 0$, despite the same viscosity jump. This suggests that if a stable zone is situated in the upstream mixing zone, then once the perturbations start to amplify at early times, it will continue to amplify over time. The presence of a stable zone does not influence the growth of the perturbations as illustrated in figure 6.4(b) for $R_c < 0$. Conversely, if the stable zone resides in the downstream mixing zone, it can impact the perturbation growth. In this situation, there might be a transient growth indicated by a maximum in the $\ln(G(t))$ curve, as evident in the instance of $R_c = 5$ depicted in figure 6.4(a). This implies that the viscosity profile has a predominant influence within the downstream mixing zone. As a consequence, an unfavorable viscosity contrast at the downstream mixing

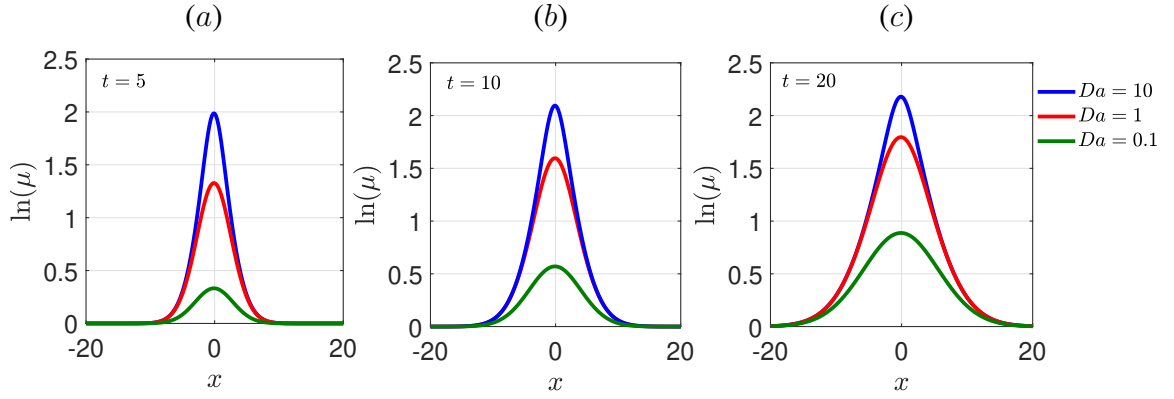


FIGURE 6.6: Viscosity profile for $R_c = 5$ and various Da at different times (a) $t = 5$, (b) $t = 10$ and $t = 20$ depicting an increased viscosity contrast with time.

zone results in early onset, and no transient growth is observed. In contrast, if the stable zone is situated at the downstream mixing zone, it influences the perturbation growth, and secondary instability may manifest for some parameters.

6.4.2 Effect of Da

The onset of instability also depends on the reaction rate, Da , for the given viscosity contrast, R_c . A larger value of Da corresponds to a slower reaction time, resulting in increased product generation. Consequently, this leads to a steeper viscosity contrast at the unstable zone, as depicted in figure 6.6. As a result, the system becomes more unstable with increasing Da , leading to an earlier onset of instability [31]. In the figure 6.7, we have plotted the log-amplification curve for $R_c = 5, -5$ and various Da . It can be observed that onset gets delayed for decreasing Da for a viscosity contrast, R_c . Further, for $Da = 1$, $R_c = 5$, we have observed a secondary instability. The question arises: does the same phenomenon occur with varying Da ? In figure 6.7(a), temporal evolution of $\ln(G(t))$ is shown for $R_c = 5$ and various Da . When we reduce Da to 0.1, the viscosity contrast reduces and is insufficient to prompt transient perturbation growth in the early times, hence the onset gets delayed. However, if we increase Da as $Da = 10$, the secondary instability can be observed with an early onset time for the case $R_c = 5$.

Further, the QSSA predicts that when the generated product concentration reaches its maximum value that is $c_{max} = 0.5$ at later times, the growth rate of perturbation does not depend anymore whether the generated product is less or high viscous ($R_c \leq 0$) [35]. Further, it predicts that the growth rate increases with time as the generated amount of product increases, but starts

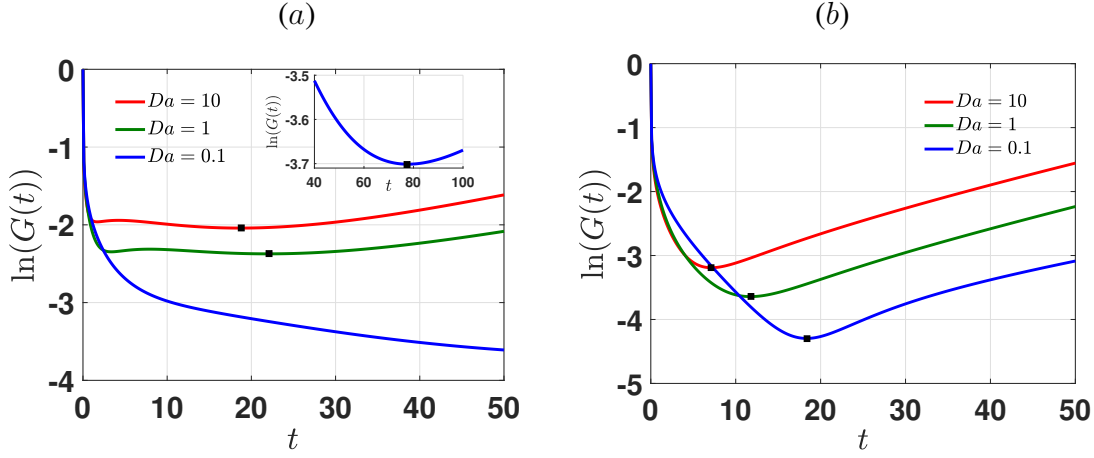


FIGURE 6.7: Logarithm of optimal amplification, $\ln(G(t))$ for $R_b = 0$, (a) $R_c = 5$ and (b) $R_c = -5$ and various Da . Here the squared dots denote the onset time of instability. Inset: $\ln(G(t))$ curve for $Da = 0.1$ at later times showing onset time.

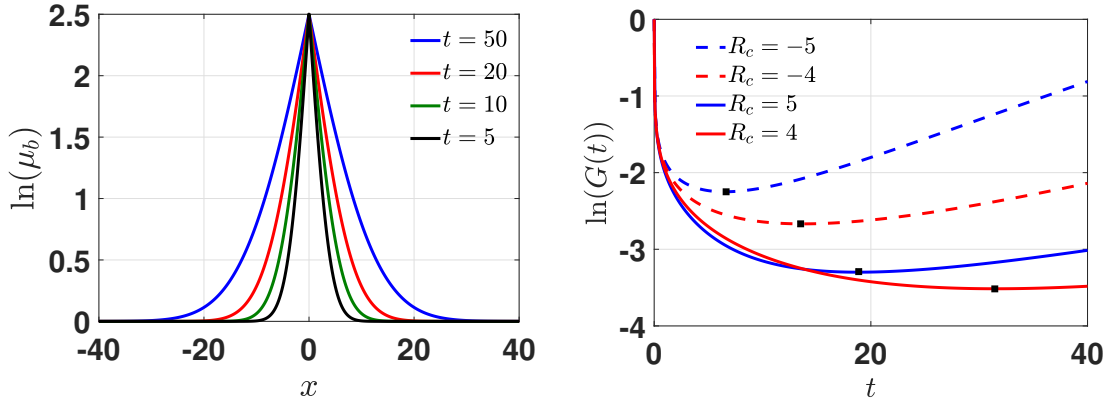


FIGURE 6.8: (a) Base viscosity profile for $R_c = 5$, $Da \rightarrow \infty$ at different times. Clearly, The viscosity gradient for infinitely fast reactions decreases with time. (b) Logarithm of optimal amplification, $\ln(G(t))$ for various R_c and $Da \rightarrow \infty$. Here the squared dots denote the onset time of instability.

to decrease once saturation occurs at $c_{max} = 0.5$. If we consider the infinitely fast reactions, the product concentration, hence the viscosity, reaches its maximum at $t > 0$ as soon as the reactants come into contact. With time, the viscosity gradient diminishes as shown in figure 6.8(a). This prompts two questions: (i) Do we observe identical onset or maximum amplification regardless of whether $R_c > 0$ or $R_c < 0$ for the same viscosity contrast? (ii) Can reactions exhibit a stabilizing effect when $Da \rightarrow \infty$ compared to reactive cases with finite reaction rates (Da) for a given viscosity contrast (R_c)?

We conduct simulations for reactive displacements involving infinitely fast reactions for various values of R_c , employing the methodology outlined in chapter 5 and plot optimal amplification,

$\ln(G(t))$ for $|R_c| = 4, 5$. It shows that the flow becomes more unstable for $R_c < 0$ than the corresponding case $R_c > 0$ with an early onset and more amplification, $\ln(G(t))$. Moreover, upon comparing the onset time for $Da \rightarrow \infty$ and finite Da in figures 6.8, 6.4, and 6.7, it is obtained that the early onset occurs for $Da \rightarrow \infty$ compared to finite Da for a given viscosity ratio, indicating a more unstable system. Hence, it can be concluded that the infinitely fast reactions demonstrate no stabilizing effect when compared to reactive displacements involving finite Da . Further, these outcomes can be validated through nonlinear simulations [69], thereby contradicting the conclusions drawn by QSSA. Evidently, the QSSA approach fails to accurately capture the dynamics at early times.

6.4.3 Effect of geometry

In this section, we compare the flow dynamics for varying the flow geometry and, hence influence of basic flow velocity on reactive VF. For radial flow, the spatially dependent velocity profile attributes the existence of critical viscosity contrast to trigger instability. While the uniform base velocity for rectilinear flow always exhibits instability if there is an unfavorable viscosity contrast. Now, the non-monotonic viscosity profile showcases an interplay between stable and unstable zones, hence between the convection and diffusion. This interplay results in a transient growth for some parameters as illustrated by a non-monotonic behavior in the $\ln(G(t))$ curve exhibiting both maxima and minima within both the flow geometries (See figures 6.4(a) and 3.6). However, in rectilinear flow, when the diffusion weakens with time, uniform base velocity feeds the convection at the interface, hence the onset of instability occurs for such parameters. While in radial flow, we do not observe the same. For radial flow, after maxima, the perturbation decays only and no secondary instability is observed. This behavior can be examined for radial flow for parameters such as $Da = 100$, $R_b = 0.3$, and $R_c = 1$ exhibiting a non-monotonic viscosity profile with maximum, as discussed in figure 3.6 from chapter 3. Therefore, the flow geometry significantly influences transient flow dynamics, in particular, when the viscosity profile is non-monotonic.

6.5 Conclusion

The chapter investigates the reactive displacement with reactions having finite reaction rates for rectilinear flow in the linear regime. We particularly focus on the reactions having iso-viscous

reactants. To study the transient growth of perturbations in reactive VF, we employ non-modal analysis. The presence of an unsteady base state introduces a significant transient response to the perturbations, a factor that has been overlooked in existing literature [35]. To address this gap, we develop a numerical method for non-modal analysis of reactive VF. In this method, we determine the dominant perturbations that undergo maximum amplification within the linear regime. For the same, we develop a numerical method, which is based on the propagator matrix approach and singular value decomposition [39, 82].

The flow stability is affected by two dimensionless parameters, R_c and Da . For $R_c \neq 0$, the reaction exhibits a non-monotonic viscosity profile showcasing an interplay of stable and unstable zones. When $R_c < 0$, instability localizes in the downstream mixing zone, leading to an earlier onset of instability compared to the corresponding $R_c > 0$ case, despite the same viscosity contrasts. Moreover, the reactive system exhibits transient perturbation growth before the onset of instability for certain R_c values, especially when the reaction generates a high viscous product. In such instances, the unfavorable viscosity contrast at the upstream mixing zone triggers perturbation growth yet fails to overcome the stable zone in the downstream mixing zone, causing the perturbation to decay. After some time, as diffusion weakens in the stable zone, the onset occurs. This phenomenon is referred to as secondary instability [37]. However, the same is not observed when $R_c < 0$, indicating a dominance of the viscosity profile in the downstream mixing zone. This behavior contrasts with the flow dynamics observed in radial flow geometry as observed in chapter 3 for considering a similar non-monotonic viscosity profile featuring a maximum. In radial flow, transient growth is also observed at early times. However, secondary instability is not observed in radial flow. Thus, the flow geometry also influences transient flow dynamics. Lastly, we examine the effect of Da on flow stability. We obtained an early onset with an increasing Da including $Da \rightarrow \infty$. This result is in contrast to QSSA predictions. However, the NMA outcomes are more consistent with the conclusions drawn from nonlinear simulations than QSSA.

Chapter 7

Summary and future work

7.1 Summary of the thesis

This thesis examines the impact of the $A + B \rightarrow C$ chemical reaction on miscible viscous fingering in a porous medium, employing linear stability analysis and numerical simulations. The instability, characterized by the formation of finger-like patterns, is observed in diverse fields including chromatographic separation and enhanced oil recovery. It occurs when a less viscous fluid displaces a more viscous one in a porous medium. Chemical reactions can alter the viscosity of fluids in porous media, impacting viscous fingering. The instability induced by chemical reactions is utilized across different scales for enhancing mixing. To understand this chemo-hydrodynamic instability, we investigate a reactive displacement involving a second-order chemical reaction, $A + B \rightarrow C$, assuming miscible, Newtonian, and neutrally buoyant fluids. We consider the viscosity profile to depend on the concentrations of the reactants and products as $\mu = \exp(R_b b + R_c c)$. This interaction is mathematically modeled using a coupled system of partial differential equations, incorporating Darcy's law and three convection-diffusion-reaction (CDR) equations. When $R_b \neq 0$ and $R_c \neq 0$, a nonlinear interaction emerges between chemical reactions and hydrodynamics. We investigate two distinct flow geometries: rectilinear and radial. In the case of radial flow, we employ non-linear simulations (NLS) to explore a wide range of reactions and flow properties. One significant finding is identifying a transient zone for radial flow depending on Da where the reaction rate exhibits temporal growth, attributed to the spatially varying flow velocity for stable displacements. Further, we compute the total amount of product following the temporal scaling as $\propto t^{f(Da)}$.

By employing both NLS and Linear Stability Analysis (LSA), we determine the stability of reactive displacements in terms of R_b and R_c , dividing the (R_b, R_c) parameter space into stable and unstable regions for each Pe and Da . The stable zone in the (R_b, R_c) phase plane contracts with increased Da and Pe but never vanishes; it persists even as $Da \rightarrow \infty$. Intriguingly, we identify a Da independent stable region in the neighborhood of $R_c = R_b$ where no transition occurs in stability despite changes in reaction rate. We explore how VF impacts reaction

properties. Our investigations reveal that enhanced mixing is achieved when a reaction generates a more viscous product ($R_c - R_b > 0$) than the equivalent case for the reactions generating a less viscous product ($R_c - R_b < 0$) for radial flow. Moreover, we observe saturation in mixing for reactive displacements characterized by higher viscosity contrasts, resulting in the formation of frozen fingers. Expanding our analysis to infinitely fast reactions, we explore the extent to which chemical reactions influence flow properties. We determine a scaling relation to compute the onset time of instability for a given viscosity ratio and Péclet number.

Furthermore, we conduct LSA for reactive displacement in rectilinear flow. We address the limitations of existing LSA approaches in the literature for rectilinear flow, such as the quasi-steady-state Approximation (QSSA) approach, and develop a numerical scheme for Non-modal Analysis (NMA) using the propagator matrix approach. We develop numerical methods for both types of reactions, those with finite and infinite reaction rates. By examining the optimal amplification and growth rate, we focus on the transient behavior of eigenmodes in response to the most unstable initial perturbations. We explore reactive displacement for the case where $R_b \neq 0$ and $Da \rightarrow \infty$. As the viscosity contrast increases, an early onset occurs and more amplified perturbations when the reaction generates a less viscous product ($R_b < R_b$) than the equivalent non-reactive scenario ($R_c = R_b$). Conversely, when $R_c > R_b$, there exist some reactive cases where onset is delayed compared to the equivalent non-reactive case ($R_c = R_b$), even with a steeper viscosity contrast. Further, we obtain that the onset time delays most when $R_c = 2R_b$ for a given R_b . However, after the onset time, we observe an accelerated growth rate of perturbations, indicating a more unstable displacement than the scenario where $R_c = R_b$. Additionally, we perform LSA for reactive displacements with $R_b = 0$ and $R_c \neq 0$ with finite Da . We observe a weak transient instability for some values of $R_c > 0$ that delays the onset time of instability. We refer to this phenomenon as secondary instability. It is noteworthy that our NMA results consistently align more closely with NLS outcomes compared to those obtained through the QSSA approach. Further, when comparing the effect of geometry, we observe transient growth for the reactive case with a non-monotonic viscosity profile with maximum. However, we do not observe the secondary instability for radial flow.

Our findings contribute to the understanding of the interaction between chemical reactions and VF dynamics. We observe a mutual influence between viscous fingering (VF) and chemical reactions. VF affects reaction characteristics, while the chemical reaction, in turn, enhances

mixing. Thus, the reactive viscous fingering can be utilized as a potent mechanism to tune enhanced mixing and location of instability in several applications such as enhanced oil recovery, frontal polymerization [79] and chemical treatment of oil-bearing formations [23], to name a few. The study has implications for various chemical-enhanced oil recovery (EOR) mechanisms aimed at reducing residual oil and increasing oil production in reservoirs. Strategies such as controlling the mobility ratio [33, 98, 118], reducing interfacial tension [89], and enhancing miscibility between displaced and displacing fluids [46] are fundamental mechanisms in EOR processes [27].

7.2 Future work

This thesis only concentrates on reactive viscous fingering with irreversible chemical reactions with symmetric flow conditions. For instance, it considers the ratio of initial concentrations of reactants to be the same, denoted as $\phi = b_0/a_0$, with $\phi = 1$. Additionally, it assumes the diffusion coefficients of fluid species (A, B, C) are equal, represented by $\delta_B = D_B/D_A$ and $\delta_C = D_C/D_B$, with $\delta_B = 1$ and $\delta_C = 1$. Furthermore, the study explores reactive fingering only for two types of flow geometries: radial and rectilinear. However, it does not investigate reactive viscous fingering for the quarter five-spot flow geometry. Based on these considerations, the future research problems are as follows:

- To conduct Non-modal analysis of reactive fingering instability under the conditions of $R_b \neq 0$ and finite Da for rectilinear flow in a porous medium.
- To explore the effect of the initial condition of miscible $A + B \rightarrow C$ reaction front for radial flow in a porous medium.
- To investigate of miscible $A + B \rightarrow C$ reaction front for radial flow in a porous medium if $\delta_B \neq 1$ and $\delta_C \neq 1$.
- To develop a numerical method to understand reactive viscous fingering in the quarter five-spot geometry.

Appendix A

Grid independence and effect of σ_1

We present here the convergence study for spatial discretization. We did not perform any temporal convergence study as the time stepping is adaptive and is obtained using the CFL condition. The existing results in the manuscript are for $N = 512$ in the x as well as y direction, where $n_x = n_y = N + 1$. We show that the results remain the same on taking double the grid points. We did not go for higher grid points as it increases the computational cost. The density plots of the product concentration are shown in figure A.1 and the interfacial length is plotted in figure A.2 for $R_c = -3.5$, $Pe = 3000$. It can be observed that the grid independence is achieved for $N = 512$.

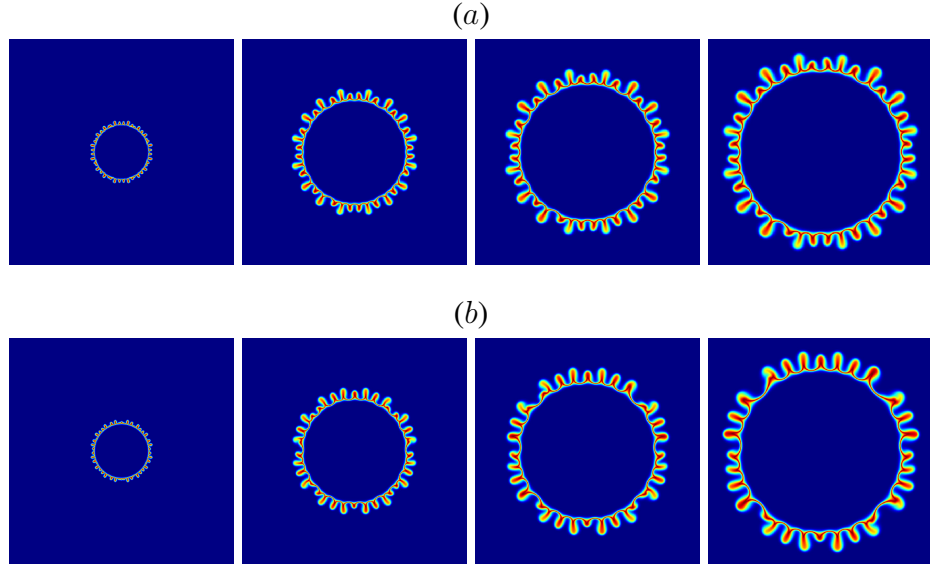


FIGURE A.1: Temporal evolution of concentration for $R_c = -3.5$, $Pe = 3000$ for (a) $N = 512$ (in first row) and (b) $N = 1024$ (in second row) at time $t = 0.1, 0.4, 0.7, 1$ (left to right).

Effect of σ on fingering dynamics: For a fixed r_0 , and $\sigma \leq r_0$, the VF dynamics are found to be identical, as shown in figure A.3. Both the fingering patterns as well as the interfacial length are the same for the different values of σ considered.

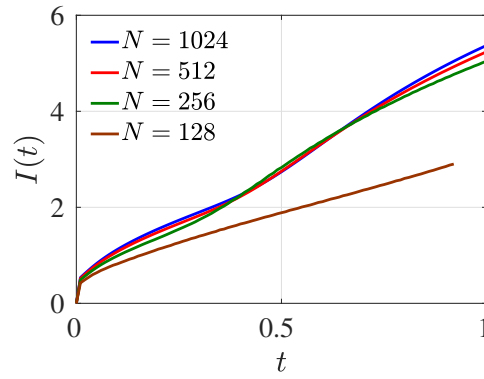


FIGURE A.2: Interfacial length for $Pe = 3000$, $R_c = -3.5$ for various grid points.

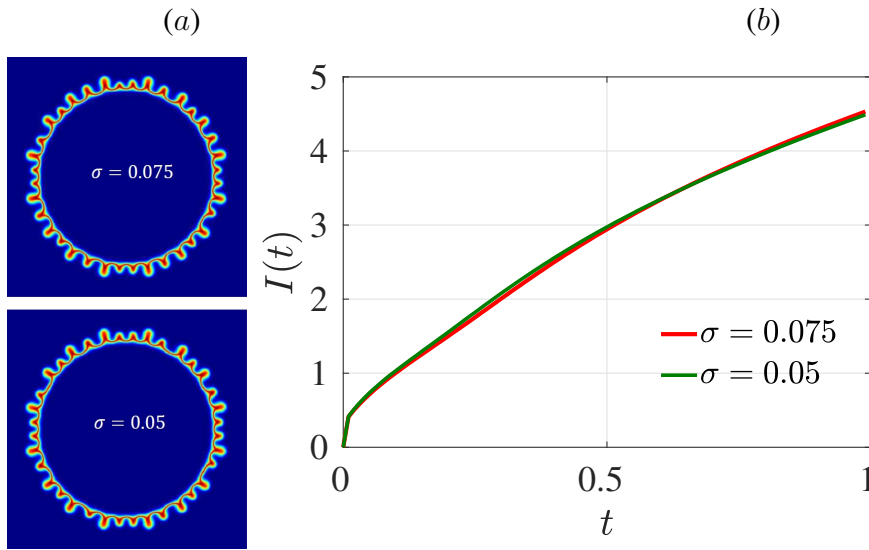


FIGURE A.3: (a) Product concentration profile at time $t = 1$ and (b) interfacial length for $Pe = 3000$, $R_c = -2.5$, $r_0 = 0.075$ and various σ . Evidently, both concentration plot and interfacial length are identical for $\sigma \leq r_0$.

Appendix B

Why $h < 0.5$ when $a = 0$?

B.1 To show $a + b + 2c = 1$

In our study, it is assumed that all fluids have the same diffusion coefficient, and the initial concentration of both reactants is identical. Under this assumption, let $z_1 = (a + b + 2c)$ follows the convection-diffusion equation with the initial condition as $z_1(\mathbf{x}, t = 0) = 1$. We have:

$$\frac{\partial z_1}{\partial t} + \mathbf{u} \cdot \nabla z_1 = D \nabla^2 z_1 \quad (\text{B.1})$$

With the condition $\mathbf{u} = 0$ at the boundary, the equation (B.1) attains only one solution as $z_1 = (a + b + 2c) = 1$ [35, 69]. For instance, we have plotted the averaged concentration profile for a , b , c , and $a + b + 2c$ for stable displacements $R_c = R_b = 0$ at different times in figure B.1 showing that $a + b + 2c = 1$. However, this is only true when the diffusion coefficient of all the fluids are same and the initial concentration for both the reactants are same.

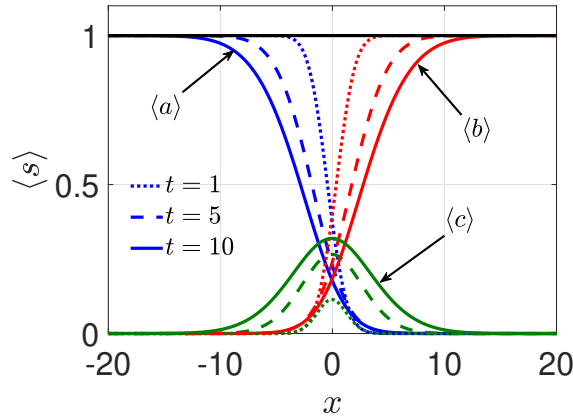


FIGURE B.1: Averaged concentration profile, $\langle a \rangle$, $\langle b \rangle$, $\langle c \rangle$ and $\langle a + b + 2c \rangle$ represented by blue, red, green and black lines, respectively, at different times. Here these curves are plotted at time $t = 1, 5$ and 10 represented by dotted, dashed, and solid lines, respectively. Here, s is the dummy variable for concentrations.

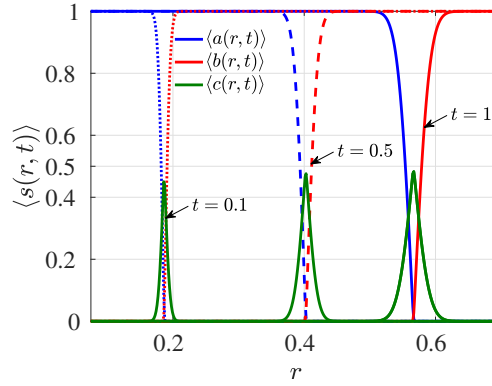


FIGURE B.2: Temporal evolution of the angular averaged concentration plots of A , B , C , for $Pe = 3000$ and $Da \rightarrow \infty$.

B.2 Why $h < 0.5$ when $a = 0$?

When the reaction rate is infinite, the reaction time tends to zero. As a result, the reactants are consumed immediately as soon as they come in contact. Thus for $t > 0$, reactants do not co-exist in the entire domain of numerical experiment, except at the reaction front. Even at the reaction front, the reaction concentration reduces and $a \rightarrow 0$, $b \rightarrow 0$ and the maximum amount of product is generated. To gain more insight into this, we compute the angular averaged concentration $\langle s(r, t) \rangle$

$$\langle s \rangle(r, t) = \frac{\int_0^{2\pi} s(r, \theta, t) d\theta}{2\pi}, \quad (\text{B.2})$$

where $s(r, \theta, t)$ is the concentration of s in polar coordinates. Please note that s is a dummy variable here. The averaged concentrations $\langle a \rangle$, $\langle b \rangle$, $\langle c \rangle$ are calculated and plotted in figure B.2 for $Da \rightarrow \infty$. The instantaneous reaction for $Da \rightarrow \infty$ results in the maximum expected amount of product at the reaction front as soon as the reactants come in contact. It is evident in figure B.2 that the product concentration does not change much with an increase in time. However, the width of the Gaussian profile followed by $\langle c(r, t) \rangle$ increases with time on account of diffusion. The reactant concentration tends to zero at the reaction front and outside it, either one of the reactants is zero, as shown in figure B.2.

To obtain a, b, c from h , we utilize the fact that the reaction occurs with an infinite reaction rate. The reaction front is the region where both the reactants co-exist and thus react to generate the product. But as $Da \rightarrow \infty$, the two reactants are consumed as soon as they come in contact and thus a, b tend to zero in the reaction front. Thus, from equation (4.8) and the fact that

$h_1 = h = h_2$, we get

$$a + c = h = 1 - (b + c). \quad (\text{B.3})$$

When $a \rightarrow 0$, from first pair, we get $h = c$. Using this and $b \rightarrow 0$ in second pair ($h = 1 - (b + c)$), we get $h = 0.5$. Hence at the reaction front, $h = c = 0.5$. The two reactants cannot co-exist outside the reaction front, that is, when $h \neq 0.5$. Thus, in the AC zone, that is occupied by injected fluid reactant A and the formed product C , we have $b = 0$. Thus, from last pair, we get $c = 1 - h$. Substituting this in the first pair, we get $a + 1 - h = h \implies h = (1 + a)/2$. In other words, we can say that $h > 0.5$ in the AC front. Similar logic holds for taking $h < 0.5$ when $a = 0$.

B.3 Different choices of H_1, H_2

In addition to the one used in the main text in §4.3, we can have two more choices of H_1 and H_2 as

$$(H_1, H_2) = \{(a - b, a + c), (a - b, b + c)\}, \quad (\text{B.4})$$

and obtain corresponding h_1, h_2 using the normalisation in equation (4.5) as

$$(h_1, h_2) = \left\{ \left(\frac{a - b + 1}{2}, a + c \right), \left(\frac{a - b + 1}{2}, 1 - (b + c) \right) \right\}. \quad (\text{B.5})$$

However, the dependence of a, b, c on h remains the same as

$$(a, b, c) = \begin{cases} (0, 1 - 2h, h) & h < 0.5, \\ (-1 + 2h, 0, 1 - h) & h \geq 0.5 \end{cases}. \quad (\text{B.6})$$

Appendix C

Pseudo-code of the numerical method

Step 1: We consider a computational domain $\Omega = [-0.75, 0.75] \times [-0.75, 0.75]$ discretised into $n_x \times n_y$ grid points. At $t = 0$, we give the initial condition for h . We consider the initial radius $r_0 = 0.075$ and utilize the axisymmetric base state solution of Tan and Homsy [102] at $t = r_0^2/2$ as an initial condition for h . For the velocity profile, we provide potential flow *i.e.* \mathbf{u}_{pot} . We assign initial fluid concentrations as $a = h = 1 - b$ and $c = 0$.

Step 2: The time is incremented by dt as $t \rightarrow t + dt$.

Step 3: The initial dt is $dt = 10^{-6}$. Then we update h value for time $t + dt$ by discretising the following convection diffusion equation as

$$\frac{\partial h}{\partial t} + \mathbf{u} \cdot \nabla h = \frac{1}{Pe} \nabla^2 h. \quad (\text{C.1})$$

We discretize space derivative using sixth-order compact finite difference and solve the resulting semi-discretized ordinary differential equation using the third-order Runge Kutta method.

Step 4: After obtaining value for h at time $t + dt$, we assign fluid concentrations a , b and c as below

$$(a, b, c) = \begin{cases} (0, 1 - 2h, h), & h < 0.5 \\ (-1 + 2h, 0, 1 - h), & h \geq 0.5 \end{cases} \quad (\text{C.2})$$

Step 5: We use the updated value of c at time $t + dt$ to find out the value ω as

$$\omega = Re \left(v \frac{\partial c}{\partial x} - u \frac{\partial c}{\partial y} \right). \quad (\text{C.3})$$

Step 6: Then we solve the Poisson equation $\nabla^2 \psi = -\omega$ by pseudo-spectral method. We employ sixth-order compact finite difference method along y -direction and Fourier Sine expansion in x -direction.

Step 7: Time is again incremented by dt , $t \rightarrow t + dt$. From this step, dt is chosen adaptively by Courant-Friedrichs-Lewy (CFL) condition.

Step 8: Step 3 to Step 6 are repeated until the final time t_f or before the fluid reaches the boundary which is specified by checking if $h > 0$ at ten grid points away from the boundary, $x = \pm 0.75, y = \pm 0.75$ in the computational domain.

Appendix D

Pressure and velocity component for radial displacement

We plot \mathbf{u}_{pot} , \mathbf{u}_{rot} and the total velocity \mathbf{u} in figure D.1. As \mathbf{u}_{pot} is independent of time and other parameters, it is shown only for one fixed time. It is evident that \mathbf{u}_{pot} decreases with an increase in the distance from the origin. Further, since \mathbf{u}_{rot} arises due to the viscosity contrast, it is non-zero only at the front where the product is generated or inside the fingers and is zero elsewhere. It decreases with time due to diffusion of the product with time. The total velocity \mathbf{u} is obtained by adding the two components of velocity and it is evident from figure D.1(c),(d) that both the components contribute in VF dynamics.

The pressure can be derived from the Darcy's Law as below:

$$\nabla p = -\mu \mathbf{u} \quad (\text{D.1a})$$

$$\Rightarrow \frac{\partial p}{\partial x} = -\mu u, \quad \frac{\partial p}{\partial y} = -\mu v \quad (\text{D.1b})$$

$$\Rightarrow p = - \int \mu u \, dx + f(y) \quad (\text{D.1c})$$

$$\text{and } -\mu v = \frac{\partial p}{\partial y} = -\frac{\partial}{\partial y} \left(\int \mu u \, dx \right) + \frac{\partial f}{\partial y} \quad (\text{D.1d})$$

By Leibnitz rule,

$$-\mu v = - \int \frac{\partial \mu}{\partial y} u - \mu \frac{\partial u}{\partial y} dx + \frac{\partial f}{\partial y} \quad (\text{D.1e})$$

$$\Rightarrow \frac{\partial f}{\partial y} = -\mu v + \int \frac{\partial \mu}{\partial y} u + \mu \frac{\partial u}{\partial y} dx \quad (\text{D.1f})$$

$$\Rightarrow f = - \int \mu v \, dy + \int \left[\int \frac{\partial \mu}{\partial y} u + \mu \frac{\partial u}{\partial y} dx \right] dy + c \quad (\text{D.1g})$$

put f into D.1c

$$\Rightarrow p = - \int \mu u \, dx - \int \mu v \, dy + \int \left[\int \frac{\partial \mu}{\partial y} u + \mu \frac{\partial u}{\partial y} dx \right] dy + c \quad (\text{D.1h})$$

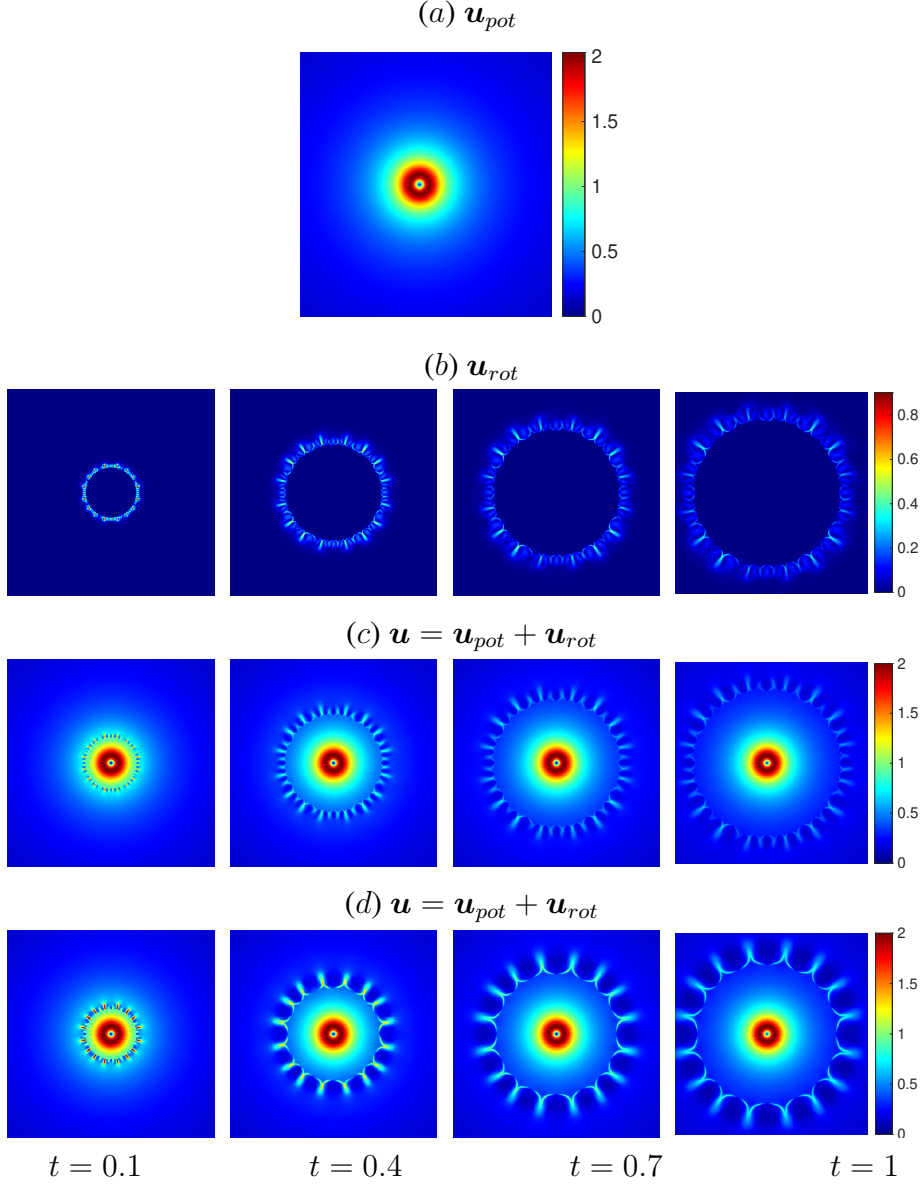


FIGURE D.1: (a) Potential component of velocity. Here only one plot is shown as it does not depend on time, Pe and R_c . Temporal evolution of (b) rotational component of velocity \mathbf{u}_{rot} and (c) total velocity \mathbf{u} for $R_c = -3.5$, $Pe = 3000$. (d) Temporal evolution of total velocity for $R_c = -5$, $Pe = 2000$.

Appendix E

Non-normality of the stability matrix

In figure E.1, the condition number of the stability matrix, $\mathcal{L}(t)$ in equation (6.5) in (x, t) domain for $R_b = 2$, $R_c = -2$ is plotted. The condition number is computed as follows in [108]:

$$\text{cond}(\mathcal{L}) = \|\mathcal{L}\|_2 \|\mathcal{L}^{-1}\|_2. \quad (\text{E.1})$$

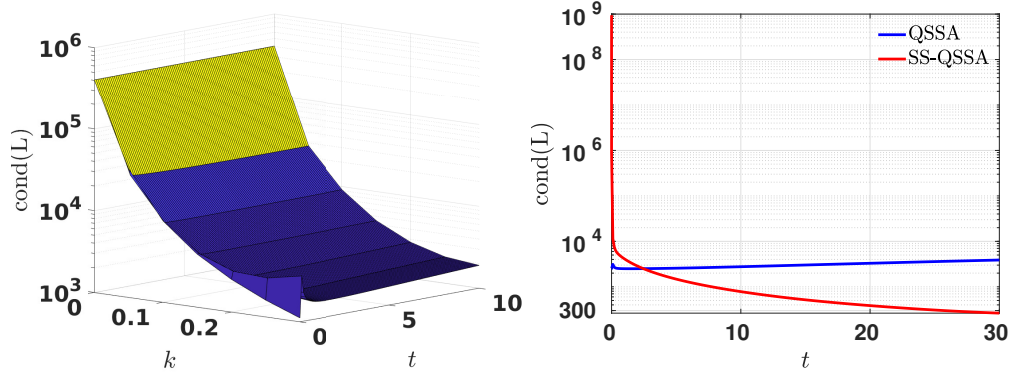


FIGURE E.1: Condition number of the stability matrix \mathcal{L} in equation (6.5) in (x, t) domain for the viscosity profile, $R_b = 2$, $R_c = -2$. (b) Condition number for the stability matrix in (x, t) and (ξ, t) domain corresponds to QSSA and SS-QSSA for $R_b = 2$, $R_c = -2$ and $k = 0.2$. For (ξ, t) domain, the stability matrix is from the equation (6.7).

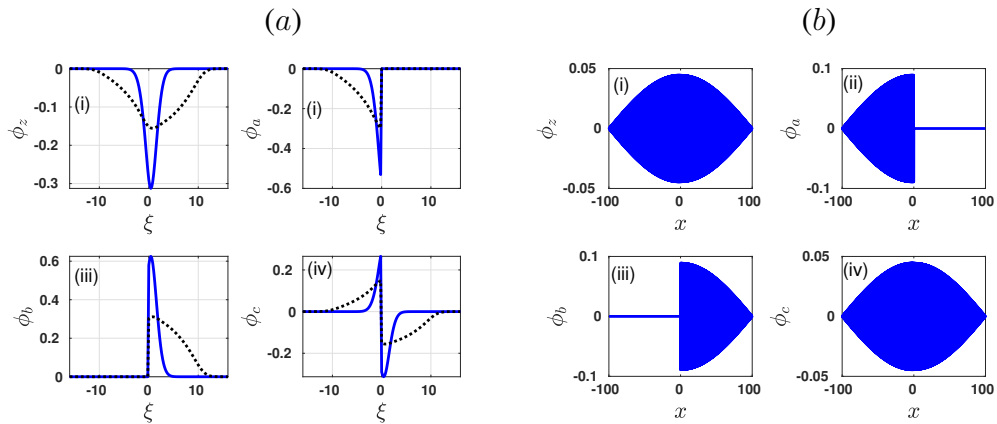


FIGURE E.2: The singular vectors and eigen functions obtained from (a) NMA and (b) QSSA, respectively, for the viscosity profile $R_b = 2$, $R_c = -2$, $k = 0.2$ for (i) ϕ_z , (ii) ϕ_a , (iii) ϕ_b and (iv) ϕ_c . Here, in figure (a), the singular vectors are plotted at $t = 10^{-3}$ (dashed lines) and $t = 10$ (solid lines).

The stability matrix, $\mathcal{L}(t)$, is highly ill-conditioned. It suggests that the eigenvalues of \mathcal{L} are very sensitive, and its eigenfunctions are non-orthogonal, implying that \mathcal{L} is highly non-normal. Due to this, significant non-modal growth in transient time can be expected, which eigenmodes cannot capture and it may be incorrect to infer instability from eigenvalues for non-normal systems [109, 38]. Moreover, the eigenvalues predict only the asymptotic behavior of a non-normal system, not the transient behavior. As a result, the transient growth of the perturbations is not captured by QSSA accurately. Moreover, we plot the condition number of the stability matrix in the (ξ, t) domain, demonstrating that even Self-similar- Quasi Steady State approximation (SS-QSSA) may not exhibit optimal transient growth due to the stability matrix's non-normality in transient time.

Further, we plot quasi-steady state eigenmodes at freezing time $t_0 > 0$ for $R_b = 2$, $R_c = -2$, and $k = 0.2$ and compare them to NMA eigenmodes in figure E.2. In contrast to the eigenfunctions in (x, t) , which occupy the entire spatial domain and appear to be global modes, the eigenmodes from NMA are concentrated around the interface, $\xi = 0$. This explains how some profiles that were determined as unstable by the QSSA analysis may end up being stable in the NMA. Moreover, the eigenmodes computed from QSSA do not predict the localized perturbation contours depending on (R_b, R_c) . Evidently, it becomes apparent that conducting the analysis in (ξ, t) coordinates is more precise than in the traditional (x, t) coordinates.

Bibliography

1. (2020). *MATLAB version 9.3.0.713579 (R2017b)*. The Mathworks, Inc., Natick, Massachusetts.
2. Atkins, P. W., De Paula, J., and Keeler, J. (2023). *Atkins' physical chemistry*. Oxford university press.
3. Banerjee, A. (2020). Rayleigh-taylor instability: a status review of experimental designs and measurement diagnostics. *Journal of Fluids Engineering*, 142(12):120801.
4. Bello, A., Ivanova, A., and Cheremisin, A. (2023). Foam eor as an optimization technique for gas eor: A comprehensive review of laboratory and field implementations. *Energies*, 16(2):972.
5. Ben, Y., Demekhin, E. A., and Chang, H.-C. (2002). A spectral theory for small-amplitude miscible fingering. *Physics of Fluids*, 14(3):999–1010.
6. Berg, S. and Ott, H. (2012). Stability of CO_2 -brine immiscible displacement. *International Journal of Greenhouse Gas Control*, 11:188–203.
7. Bhaskar, K. R., Garik, P., Turner, B. S., Bradley, J. D., Bansil, R., Stanley, H. E., and LaMont, J. T. (1992). Viscous fingering of hcl through gastric mucin. *Nature*, 360(6403):458–461.
8. Bischofberger, I., Ramachandran, R., and Nagel, S. R. (2014). Fingering versus stability in the limit of zero interfacial tension. *Nature Communications*, 5(1):1–6.
9. Boulding, J. R. (1996). *EPA environmental assessment sourcebook*. CRC Press.
10. Brau, F. and De Wit, A. (2020). Influence of rectilinear vs radial advection on the yield of $A + B \rightarrow C$ reaction fronts: A comparison. *The Journal of Chemical Physics*, 152(5):054716.

11. Brau, F., Schusztter, G., and De Wit, A. (2017). Flow control of $A + B \rightarrow C$ fronts by radial injection. *Physical Review Letters*, 118(13):134101.
12. Budroni, M., Thomas, C., and De Wit, A. (2017). Chemical control of dissolution-driven convection in partially miscible systems: nonlinear simulations and experiments. *Physical Chemistry Chemical Physics*, 19(11):7936–7946.
13. Burden, R. L., Faires, J. D., and Burden, A. M. (2015). *Numerical analysis*. Cengage learning.
14. Burrows, L. C., Haeri, F., Tapriyal, D., Shah, P. G., Crandall, D., Enick, R. M., and Goodman, A. (2023). Co₂-soluble nonionic surfactants for enhanced co₂ storage via in situ foam generation. *Energy & Fuels*, 37(16):12089–12100.
15. Casademunt, J. (2004). Viscous fingering as a paradigm of interfacial pattern formation: Recent results and new challenges. *Chaos: An Interdisciplinary Journal of Nonlinear Science*, 14(3):809–824.
16. Catchpoole, H. J., Shalliker, R. A., Dennis, G. R., and Guiochon, G. (2006). Visualising the onset of viscous fingering in chromatography columns. *Journal of Chromatography A*, 1117(2):137–145.
17. Chen, C. Y., Huang, C. W., Gadêlha, H., and Miranda, J. A. (2008). Radial viscous fingering in miscible hele-shaw flows: A numerical study. *Physical Review E*, 78(1):016306.
18. Chui, J. Y., de Anna, P., and Juanes, R. (2015). Interface evolution during radial miscible viscous fingering. *Physical Review E*, 92(4):041003.
19. Comolli, A., De Wit, A., and Brau, F. (2019). Dynamics of $A + B \rightarrow C$ reaction fronts under radial advection in three dimensions. *Physical Review E*, 100(5):052213.
20. Cook, A. W. and Riley, J. J. (1994). A subgrid model for equilibrium chemistry in turbulent flows. *Physics of Fluids*, 6(8):2868–2870.
21. Cuthiell, D., Kissel, G., Jackson, C., Frauenfeld, T., Fisher, D., and Rispler, K. (2006). Viscous fingering effects in solvent displacement of heavy oil. *Journal of Canadian Petroleum Technology*, 45(07).

22. De Wit, A. (2020). Chemo-hydrodynamic patterns and instabilities. *Annual Review of Fluid Mechanics*, 52:531–555.
23. De Wit, A. and Homsy, G. M. (1999). Viscous fingering in reaction-diffusion systems. *The Journal of Chemical Physics*, 110(17):8663–8675.
24. Dentz, M., Le Borgne, T., Englert, A., and Bijeljic, B. (2011). Mixing, spreading and reaction in heterogeneous media: A brief review. *Journal of Contaminant Hydrology*, 120:1–17.
25. Ding, H., Spelt, P. D., and Shu, C. (2007). Diffuse interface model for incompressible two-phase flows with large density ratios. *Journal of Computational Physics*, 226(2):2078–2095.
26. Engelberts, W. and Klinkenberg, L. (1951). Laboratory experiments on the displacement of oil by water from packs of granular material. In *World Petroleum Congress*, pages WPC–4138. WPC.
27. Fani, M., Pourafshary, P., Mostaghimi, P., and Mosavat, N. (2022). Application of microfluidics in chemical enhanced oil recovery: A review. *Fuel*, 315:123225.
28. Farrell, B. F. and Ioannou, P. J. (1996). Generalized stability theory. part ii: Nonautonomous operators. *Journal of Atmospheric Sciences*, 53(14):2041–2053.
29. Gálfi, L. and Rácz, Z. (1988). Properties of the reaction front in an $A + B \rightarrow C$ type reaction-diffusion process. *Physical Review A*, 38(6):3151.
30. Garg, R., Nair, S., and Bhaskarwar, A. N. (2000). Mass transfer with instantaneous chemical reaction in finite gas–liquid systems. *Chemical Engineering Journal*, 76(2):89–98.
31. Gérard, T. and De Wit, A. (2009). Miscible viscous fingering induced by a simple $A + B \rightarrow C$ chemical reaction. *Physical Review E*, 79(1):016308.
32. Govindarajan, R. and Sahu, K. C. (2014). Instabilities in viscosity-stratified flow. *Annual Review of Fluid Mechanics*, 46:331–353.
33. Green, D. W., Willhite, G. P., et al. (1998). *Enhanced oil recovery*, volume 6. Henry L. Doherty Memorial Fund of AIME, Society of Petroleum Engineers.

34. Hejazi, S. H. and Azaiez, J. (2010). Non-linear interactions of dynamic reactive interfaces in porous media. *Chemical Engineering Science*, 65(2):938–949.
35. Hejazi, S. H., Trevelyan, P. M. J., Azaiez, J., and De Wit, A. (2010). Viscous fingering of a miscible reactive $A + B \rightarrow C$ interface: a linear stability analysis. *Journal of Fluid Mechanics*, 652:501–528.
36. Hill, S. et al. (1952). Channeling in packed columns. *Chemical Engineering Science*, 1(6):247–253.
37. Hota, T. K. and Mishra, M. (2018). Non-modal stability analysis of miscible viscous fingering with non-monotonic viscosity profiles. *Journal of Fluid Mechanics*, 856:552–579.
38. Hota, T. K. and Mishra, M. (2020). Transient growth and symmetrizability in rectilinear miscible viscous fingering. *Journal of Engineering Mathematics*, 120(1):111–128.
39. Hota, T. K., Pramanik, S., and Mishra, M. (2015a). Nonmodal linear stability analysis of miscible viscous fingering in porous media. *Physical Review E*, 92(5):053007.
40. Hota, T. K., Pramanik, S., and Mishra, M. (2015b). Onset of fingering instability in a finite slice of adsorbed solute. *Physical Review E*, 92(2):023013.
41. Howison, S. (1986). Fingering in hele-shaw cells. *Journal of Fluid Mechanics*, 167:439–453.
42. Huppert, H. E. and Neufeld, J. A. (2014). The fluid mechanics of carbon dioxide sequestration. *Annual Review of Fluid Mechanics*, 46:255–272.
43. Jain, S. S., Mani, A., and Moin, P. (2020). A conservative diffuse-interface method for compressible two-phase flows. *Journal of Computational Physics*, 418:109606.
44. Jha, B., Cueto-Felgueroso, L., and Juanes, R. (2011). Fluid mixing from viscous fingering. *Physical Review Letters*, 106(19):194502.
45. Jha, B., Cueto-Felgueroso, L., and Juanes, R. (2013). Synergetic fluid mixing from viscous fingering and alternating injection. *Physical Review Letters*, 111(14):144501.
46. Jiang, J., James, S. C., and Mojarab, M. (2020). A multiphase, multicomponent reservoir-simulation framework for miscible gas and steam coinjection. *SPE Reserv. Evaluation Eng.*, 23(02):551–565.

47. Jiménez-Martínez, J., Porter, M. L., Hyman, J. D., Carey, J. W., and Viswanathan, H. S. (2016). Mixing in a three-phase system: Enhanced production of oil-wet reservoirs by CO_2 injection. *Geophysical Research Letters*, 43(1):196–205.
48. Joekar-Niasar, V. and Hassanizadeh, S. (2012). Analysis of fundamentals of two-phase flow in porous media using dynamic pore-network models: A review. *Critical Reviews in Environmental Science and Technology*, 42(18):1895–1976.
49. K, S. K., C, P., and D Veerappa Gowda, G. (2014). A finite volume method for a two-phase multicomponent polymer flooding. *Journal of Computational Physics*, 275:667–695.
50. Kessler, D. A., Koplik, J., and Levine, H. (1988). Pattern selection in fingered growth phenomena. *Advances in Physics*, 37(3):255–339.
51. Kim, M. C. and Cardoso, S. S. (2019). Diffusivity ratio effect on the onset of the buoyancy-driven instability of an $A + B \rightarrow C$ chemical reaction system in a hele-shaw cell: Numerical simulations and comparison with experiments. *Physics of Fluids*, 31(8):084101.
52. Kim, M. C. and Choi, C. K. (2011). The stability of miscible displacement in porous media: Nonmonotonic viscosity profiles. *Physics of Fluids*, 23(8).
53. Kim, M. C., Pramanik, S., Sharma, V., and Mishra, M. (2021). Unstable miscible displacements in radial flow with chemical reactions. *Journal of Fluid Mechanics*, 917.
54. Koo, Y.-E., Kopelman, R., Yen, A., and Lin, A. (1992). Experimental study of an $A+B \rightarrow C$ reaction-diffusion system in a capillary: Crossovers from reaction to diffusion-limited regimes. *MRS Online Proceedings Library (OPL)*, 290.
55. Kretz, V., Berest, P., Hulin, J., and Salin, D. (2003). An experimental study of the effects of density and viscosity contrasts on macrodispersion in porous media. *Water Resources Research*, 39(2).
56. Kull, H.-J. (1991). Theory of the rayleigh-taylor instability. *Physics Reports*, 206(5):197–325.
57. Leharne, S. (2021). Risk assessment and remediation of napl contaminated soil and groundwater. *ChemTexts*, 8(1):5.

58. Lei, T. and Luo, K. H. (2021). Pore-scale simulation of miscible viscous fingering with dissolution reaction in porous media. *Phys. Fluids*, 33(3).
59. Lele, S. K. (1992). Compact finite difference schemes with spectral-like resolution. *Journal of Computational Physics*, 103(1):16–42.
60. Liu, H.-R. and Ding, H. (2015). A diffuse-interface immersed-boundary method for two-dimensional simulation of flows with moving contact lines on curved substrates. *Journal of Computational Physics*, 294:484–502.
61. Liu, Y., Zhao, Y., Zhao, J., and Song, Y. (2011). Magnetic resonance imaging on CO_2 miscible and immiscible displacement in oil-saturated glass beads pack. *Magnetic Resonance Imaging*, 29(8):1110–1118.
62. Maharana, S. N. and Mishra, M. (2021). Reaction induced interfacial instability of miscible fluids in a channel. *Journal of Fluid Mechanics*, 925:A3.
63. Maharana, S. N. and Mishra, M. (2022). Effects of low and high viscous product on kelvin–helmholtz instability triggered by $A + B \rightarrow C$ type reaction. *Physics of Fluids*, 34(1):012104.
64. Manickam, O. and Homsy, G. M. (1993). Stability of miscible displacements in porous media with nonmonotonic viscosity profiles. *Physics of Fluids A: Fluid Dynamics*, 5(6):1356–1367.
65. Matar, O. K. and Troian, S. M. (1999). Spreading of a surfactant monolayer on a thin liquid film: Onset and evolution of digitated structures. *Chaos: An Interdisciplinary Journal of Nonlinear Science*, 9(1):141–153.
66. Michioka, T. and Komori, S. (2004). Large-eddy simulation of a turbulent reacting liquid flow. *AIChE Journal*, 50(11):2705–2720.
67. Mishra, M., Martin, M., and De Wit, A. (2008). Differences in miscible viscous fingering of finite width slices with positive or negative log-mobility ratio. *Physical Review E*, 78(6):066306.
68. Muggeridge, A., Cockin, A., Webb, K., Frampton, H., Collins, I., Moulds, T., and Salino, P. (2014). Recovery rates, enhanced oil recovery and technological limits. *Philosophical*

- Transactions of the Royal Society A: Mathematical, Physical and Engineering Sciences*, 372(2006):20120320.
69. Nagatsu, Y. and De Wit, A. (2011). Viscous fingering of a miscible reactive $A + B \rightarrow C$ interface for an infinitely fast chemical reaction: Nonlinear simulations. *Physics of Fluids*, 23(4):043103.
70. Nagatsu, Y., Kondo, Y., Kato, Y., and Tada, Y. (2009). Effects of moderate damköhler number on miscible viscous fingering involving viscosity decrease due to a chemical reaction. *Journal of Fluid Mechanics*, 625:97.
71. Nagatsu, Y., Matsuda, K., Kato, Y., and Tada, Y. (2007). Experimental study on miscible viscous fingering involving viscosity changes induced by variations in chemical species concentrations due to chemical reactions. *Journal of Fluid Mechanics*, 571:475–493.
72. Nagatsu, Y. and Ueda, T. (2001). Effects of reactant concentrations on reactive miscible viscous fingering. *AIChE Journal*, 47(8):1711–1720.
73. Nagatsu, Y. and Ueda, T. (2003). Effects of finger-growth velocity on reactive miscible viscous fingering. *American Institute of Chemical Engineers. AIChE Journal*, 49(3):789.
74. Nagatsu, Y. and Ueda, T. (2004). Analytical study of effects of finger-growth velocity on reaction characteristics of reactive miscible viscous fingering by using a convection–diffusion–reaction model. *Chemical Engineering Science*, 59(18):3817–3826.
75. Nand, S., Sharma, V., Das, S. K., Padhee, S. S., and Mishra, M. (2022). Effect of hele–shaw cell gap on radial viscous fingering. *Scientific Reports*, 12(1):18967.
76. Nicolaides, C., Jha, B., Cueto-Felgueroso, L., and Juanes, R. (2015). Impact of viscous fingering and permeability heterogeneity on fluid mixing in porous media. *Water Resources Research*, 51(4):2634–2647.
77. Pinilla, A., Asuaje, M., and Ratkovich, N. (2021). Experimental and computational advances on the study of viscous fingering: an umbrella review. *Heliyon*, 7(7).
78. Podgorski, T., Sostarecz, M. C., Zorman, S., and Belmonte, A. (2007). Fingering instabilities of a reactive micellar interface. *Physical Review E*, 76(1):016202.

79. Pojman, J. A. (2010). *Frontal polymerization*. WILEY-VCH Verlag GmbH & Co. KGaA: Weinheim.
80. Pramanik, S., Hota, T. K., and Mishra, M. (2015). Influence of viscosity contrast on buoyantly unstable miscible fluids in porous media. *Journal of Fluid Mechanics*, 780:388–406.
81. Rana, C., Pramanik, S., Martin, M., De Wit, A., and Mishra, M. (2019). Influence of langmuir adsorption and viscous fingering on transport of finite size samples in porous media. *Physical Review Fluids*, 4(10):104001.
82. Rapaka, S., Pawar, R. J., Stauffer, P. H., Zhang, D., and Chen, S. (2009). Onset of convection over a transient base-state in anisotropic and layered porous media. *Journal of Fluid Mechanics*, 641:227–244.
83. Riolfo, L. A., Nagatsu, Y., Iwata, S., Maes, R., Trevelyan, P., and De Wit, A. (2012). Experimental evidence of reaction-driven miscible viscous fingering. *Physical Review E*, 85(1):015304.
84. Sahu, K., Ding, H., Valluri, P., and Matar, O. (2009). Linear stability analysis and numerical simulation of miscible two-layer channel flow. *Physics of Fluids*, 21(4).
85. Schmid, P. and Kytömaa, H. (1994). Transient and asymptotic stability of granular shear flow. *Journal of Fluid Mechanics*, 264:255–275.
86. Schmid, P. J. (2007). Nonmodal stability theory. *Annual Review of Fluid Mechanics*, 39(1):129–162.
87. Schmid, P. J. and Henningson, D. S. (2002). On the stability of a falling liquid curtain. *Journal of Fluid Mechanics*, 463:163–171.
88. Schmid, P. J., Henningson, D. S., et al. (2001). *Stability and Transition in Shear Flows [electronic resource]*. New York, NY: Springer New York: Imprint: Springer.
89. Sedaghat, M., Mohammadzadeh, O., Kord, S., and Chatzis, I. (2016). Heavy oil recovery using asp flooding: A pore-level experimental study in fractured five-spot micromodels. *Can. J. Chem. Eng.*, 94(4):779–791.

90. Sha, X., Chen, L., Zhu, X., Wang, S., Feng, Q., and Tao, W.-Q. (2022). Pore-scale study of three-phase reactive transport processes in porous media. *Physics of Fluids*, 34(12):123318.
91. Shalliker, R. A. and Guiochon, G. (2010). Solvent viscosity mismatch between the solute plug and the mobile phase: considerations in the applications of two-dimensional hplc. *Analyst*, 135(2):222–229.
92. Sharma, V., Chen, C.-Y., and Mishra, M. (2023). A linear stability analysis of instabilities with reactive flows in porous medium. *Physics of Fluids*, 35(6). 064105.
93. Sharma, V., Nand, S., Pramanik, S., Chen, C.-Y., and Mishra, M. (2020). Control of radial miscible viscous fingering. *Journal of Fluid Mechanics*, 884:A16.
94. Sharma, V., Pramanik, S., Chen, C.-Y., and Mishra, M. (2019). A numerical study on reaction-induced radial fingering instability. *Journal of Fluid Mechanics*, 862:624–638.
95. Shen, S. (1961). Some considerations on the laminar stability of time-dependent basic flows. *Journal of the Aerospace Sciences*, 28(5):397–404.
96. Steefel, C. I., DePaolo, D. J., and Lichtner, P. C. (2005). Reactive transport modeling: An essential tool and a new research approach for the earth sciences. *Earth and Planetary Science Letters*, 240(3-4):539–558.
97. Stone, H. A., Stroock, A. D., and Ajdari, A. (2004). Engineering flows in small devices: microfluidics toward a lab-on-a-chip. *Annual Review of Fluid Mechanics*, 36:381–411.
98. Sun, Z., Wu, X., Kang, X., Lu, X., Li, Q., Jiang, W., and Zhang, J. (2019). Comparison of oil displacement mechanisms and performances between continuous and dispersed phase flooding agents. *Pet. Explor. Dev.*, 46(1):121–129.
99. Szulczewski, M. L., Cueto-Felgueroso, L., and Juanes, R. (2009). Scaling of capillary trapping in unstable two-phase flow: Application to co2 sequestration in deep saline aquifers. *Energy Procedia*, 1(1):3421–3428.
100. Taitelbaum, H., Vilensky, B., Koo, Y.-E. L., Yen, A., Lin, A., and Kopelman, R. (1994). Initially separated reaction-diffusion systems. *MRS Online Proceedings Library*, 366:451–462.

101. Tan, C. T. and Homsy, G. M. (1986). Stability of miscible displacements in porous media: Rectilinear flow. *Physics of Fluids*, 29(11):3549–3556.
102. Tan, C. T. and Homsy, G. M. (1987). Stability of miscible displacements in porous media: Radial source flow. *Physics of Fluids*, 30(5):1239–1245.
103. Tan, C. T. and Homsy, G. M. (1988). Simulation of nonlinear viscous fingering in miscible displacement. *Physics of fluids*, 31(6):1330–1338.
104. Tanveer, S. (1993). Evolution of hele-shaw interface for small surface tension. *Philosophical Transactions of the Royal Society of London. Series A: Physical and Engineering Sciences*, 343(1668):155–204.
105. Tanveer, S. (2000). Surprises in viscous fingering. *Journal of Fluid Mechanics*, 409:273–308.
106. Tilton, N., Daniel, D., and Riaz, A. (2013). The initial transient period of gravitationally unstable diffusive boundary layers developing in porous media. *Physics of Fluids*, 25(9).
107. Tran, M. and Jha, B. (2020). Coupling between transport and geomechanics affects spreading and mixing during viscous fingering in deformable aquifers. *Advances in Water Resources*, 136:103485.
108. Trefethen, L. N. and Embree, M. (2005). Spectra and pseudospectra : the behavior of nonnormal matrices and operators. Princeton University Press.
109. Trefethen, L. N., Trefethen, A. E., Reddy, S. C., and Driscoll, T. A. (1993). Hydrodynamic stability without eigenvalues. *Science*, 261(5121):578–584.
110. Trevelyan, P. and Walker, A. (2018). Asymptotic properties of radial $A + B \rightarrow C$ reaction fronts. *Physical Review E*, 98(3):032118.
111. Tsuzuki, R., Ban, T., Fujimura, M., and Nagatsu, Y. (2019). Dual role of surfactant-producing reaction in immiscible viscous fingering evolution. *Physics of Fluids*, 31(2):022102.
112. Tu, T.-Y., Shen, Y.-P., Lim, S.-H., and Wang, Y.-K. (2022). A facile method for generating a smooth and tubular vessel lumen using a viscous fingering pattern in a microfluidic device. *Frontiers in Bioengineering and Biotechnology*, 10.

113. Verma, P., Sharma, V., and Mishra, M. (2022). Radial viscous fingering induced by an infinitely fast chemical reaction. *Journal of Fluid Mechanics*, 945:A19.
114. Verma, P., Sharma, V., and Mishra, M. (2023). Understanding stable/unstable miscible $A + B \rightarrow C$ reaction front and mixing in porous medium. *Physics of Fluids*, 35:044102.
115. Videbæk, T. E. and Nagel, S. R. (2019). Diffusion-driven transition between two regimes of viscous fingering. *Physical Review Fluids*, 4(3):033902.
116. Wang, W., Zhang, C., Patmonoaji, A., Hu, Y., Matsushita, S., Suekane, T., and Nagatsu, Y. (2021). Effect of gas generation by chemical reaction on viscous fingering in a hele–shaw cell. *Physics of Fluids*, 33(9):093104.
117. Weickert, J. (1998). *Anisotropic diffusion in image processing*, volume 1. Teubner Stuttgart.
118. Weidong, L., Litao, L., Guangzhi, L., Luo, Z., Yunyun, W., and Jiang, W. (2017). Experimental study on the mechanism of enhancing oil recovery by polymer–surfactant binary flooding. *Pet. Explor. Dev.*, 44(4):636–643.
119. Witten Jr, T. A. and Sander, L. M. (1981). Diffusion-limited aggregation, a kinetic critical phenomenon. *Physical Review Letters*, 47(19):1400.

List of Publications Out of Thesis

Research paper in thesis

- **Verma, P.**, Sharma, V., Mishra M., Radial Viscous Fingering Induced by an Infinitely Fast Chemical Reaction, *J. Fluid Mech.*, 2022, 945, A19.
- **Verma, P.**, Sharma, V., Mishra M., Understanding stable/unstable miscible $A + B \rightarrow C$ reaction front and mixing in porous medium, *Phys. Fluids* 2023, 34, 4.
- **Verma, P.**, Sharma, V., Chen C.-Y., Mishra M., Damköhler Number Independent Stable Regime in Reactive Radial Viscous Fingering (Revised manuscript is submitted in *J. Fluid Mech.*).
- **Verma, P.**, Hota T. K., Mishra M., Non-modal Linear Stability Analysis of Reactive Front $A + B \rightarrow C$ for Infinitely Fast Reaction (Submitted in *Proc. R. Soc. A.*).
- **Verma, P.**, Hota T. K., Mishra M., Non-modal linear stability analysis of reaction-induced miscible viscous fingering for rectilinear displacement in linear regime (In preparation)
- **Verma, P.**, Mishra M., A computational study to understand reaction assisting fingering instability for radial flow. (In preparation).
- **Verma, P.**, Mishra M., A numerical insight into reaction inducing fingering instability when reactants have unfavorable viscosity contrast. (In preparation)

Accepted Conference Abstracts/Proceedings

- **Verma, P.**, Chen C.-Y., Mishra M., Linear Stability Analysis of Fingering Instability via Alternating Radial Flow in Porous Medium, abstract accepted at the conference, 14th Asian Computational Fluid Dynamics Conference will be held at Bengaluru, Karnataka, India on 30th October - 2nd November 2023.
- **Verma, P.**, Mishra M., Non-Linear Study of Interaction of Viscous Fingering Instability and Chemical Reaction, abstract accepted at the conference, The 10th International

Congress on Industrial and Applied Mathematics (ICIAM 2023) will be held at Tokyo, Japan from August 20-25, 2023.

- **Verma, P.**, Sharma, V., Mishra M., Saturated Mixing due to Reactive Viscous Fingering in Porous Medium, at the conference, 15th Annual International Conference on Porous Media, InterPore2023 held at Edinburgh, Scotland from 22-25 May, 2023.
- **Verma, P.**, Sharma, V., Mishra M., Effect of Computational Study of Fingering Instability due to an Instantaneous Chemical Reaction in a Porous Medium, at the conference IACM COMPUTATIONAL FLUIDS CONFERENCE (CFC) held at Cannes, France from 25-28 April 2023.
- **Verma, P.**, Sharma, V., Mishra M., Enhanced Mixing due to Reactive Viscous Fingering Instability in a Porous Medium, at the conference ‘ AGU Fall Meeting 2022 ’ held at Chicago, IL and online everywhere from 12-16 December 2022.
- **Verma, P.**, Sharma, V., Mishra M., Reaction-induced Fingering under Asymmetrical Conditions, The 19th International Conference on Flow Dynamics (ICFD2022) held at Sendai, Miyagi, from 09-11 November 2022.
- **Verma, P.**, Sharma, V., Mishra M., Fingering Dynamics in an Infinitely Fast Chemical Front in a Porous Medium, at the conference ‘ AGU Fall Meeting 2021 ’ held at New -Orleans, LA from December 13-17, 2021.
- **Verma, P.**, Sharma, V., Mishra M., Numerical Simulation of Radial Viscous Fingering Induced by an Instantaneous Chemical Reaction, held at 74th Annual Meeting of the APS Division of Fluid Dynamics, held at Phoenix Convention Center - Phoenix, Arizona, from November 21-23, 2021.
- **Verma, P.**, Sharma, V., Mishra M., A Numerical Study of Reactive Radial Viscous Fingering, The 18th International Conference on Flow Dynamics (ICFD2021) held at Sendai, Miyagi, from 27-29 October 2021.
- **Verma, P.**, Sharma, V., Mishra M., Radial Miscible Viscous Fingering Induced by an Infinitely Fast Chemical Reaction, at Solvay Workshop on ‘Nonlinear Phenomena and Complex Systems in memory of Prof. Grégoire Nicolis, 14-16 June 2021.

Oral presentations

- **Verma, P.**, Mishra M., Enhanced Mixing via Reactive Viscous Fingering in Radial Hele-Shaw Cell, at Complex Fluids Dynamics Symposium: Rheology and Instabilities in Complex Fluids, IIT Ropar from 1-2 Dec 2023. (Poster presentation)
- **Verma, P.**, Sharma, V., Mishra M., Effect of Initial Condition on Reactive Radial Viscous Fingering: A Numerical Insight, at the conference 67th Congress of the Indian Society of Theoretical and Applied Mechanics (ISTAM) held at IIT Mandi from 14-16 December 2022.
- **Verma, P.**, Sharma, V., Mishra M., A Numerical Study of a Reactive Flow for an Infinitely Fast Reaction in Porous Medium, Cynosure, 2022, Department of Mathematics, IIT Ropar. (Poster presentation)
- **Verma, P.**, Sharma, V., Mishra M., Convection-Diffusion-Reaction System with Infinite Reaction Rate, in the symposium (Online mode) on the theme "Differential Equations: Analysis, Computation and Applications" held at IIT Roorkee from December 2-3, 2021.
- **Verma, P.**, Sharma, V., Mishra M., Chemical Reaction Induced Viscous Fingering in a Radial Displacement Flow, at international conferences on Advances in Differential Equations and Numerical Analysis (ADENA) organized by Department of Mathematics, IIT Guwahati 12-15 October 2020.
- **Verma, P.**, Sharma, V., Mishra M., Effect of Chemical Reaction on Radial Miscible Viscous Fingering, Cynosure, 2019, Department of Mathematics, IIT Ropar. (Poster presentation)

CURRICULUM VITAE

Name : Priya Verma
Date of birth : July 08, 1994
Nationality : Indian
Affiliation : IIT Ropar
Email : *2017maz0006@iitrpr.ac.in*
Other Email : *priya.maths840@gmail.com*

Academic Qualifications

- PhD: Pursuing from Department of Mathematics, IIT Ropar (January 2018 onwards).
- M.Sc: Government College, University of Kota, Kota, India (2015-2017).
- B.Sc. (Mathematics): Janki Devi Bajaj Government PG Girls College, Kota India (2012-2015).

Award and Honours

- Awarded NBHM travel grant for attending the 10th International Congress on Industrial and Applied Mathematics (ICIAM 2023) will be held in Tokyo, Japan from August 20-25, 2023.
- Selected for Inbound Short-term Research Scholarship Program, at NYCU, Taiwan, from February 1, 2023 to May 15, 2023, under supervision of Prof Ching-Yao Chen.
- Awarded International Travel Support (ITS) by SERB to attend the 19th International Conference on Flow Dynamics (ICFD2022) held at Sendai, Miyagi, from 09-11 November 2022.
- Cleared Graduate Aptitude Test in Engineering (GATE), 2017.

- Awarded Junior Research Fellowship cleared by National Eligibility Test (NET) conducted by the University Grants Commission (UGC) in June 2016.

Journal Publications

- **Verma, P.**, Sharma, V., Mishra M., Radial Viscous Fingering Induced by an Infinitely Fast Chemical Reaction, *J. Fluid Mech.*, 2022, 945, A19.
- **Verma, P.**, Sharma, V., Mishra M., Understanding stable/unstable miscible $A + B \rightarrow C$ reaction front and mixing in porous medium, *Phys. Fluids* 2023, 34, 4.
- **Verma, P.**, Sharma, V., Chen C.-Y., Mishra M., Damköhler Number Independent Stable Regime in Reactive Radial Viscous Fingering (Revised manuscript is submitted in *J. Fluid Mech.*).
- **Verma, P.**, Hota T. K., Mishra M., Non-modal Linear Stability Analysis of Reactive Front $A + B \rightarrow C$ for Infinitely Fast Reaction (Submitted in *Proc. R. Soc. A.*).

Accepted Conference Abstracts/Proceedings

- **Verma, P.**, Chen C.-Y., Mishra M., Linear Stability Analysis of Fingering Instability via Alternating Radial Flow in Porous Medium, abstract accepted at the conference, 14th Asian Computational Fluid Dynamics Conference will be held at Bengaluru, Karnataka, India on 30th October - 2nd November 2023.
- **Verma, P.**, Mishra M., Non-Linear Study of Interaction of Viscous Fingering Instability and Chemical Reaction, at the conference, The 10th International Congress on Industrial and Applied Mathematics (ICIAM 2023) will be held at Tokyo, Japan from August 20-25, 2023.
- **Verma, P.**, Sharma, V., Mishra M., Saturated Mixing due to Reactive Viscous Fingering in Porous Medium, at the conference, 15th Annual International Conference on Porous Media, InterPore2023 held at Edinburgh, Scotland from 22-25 May, 2023.
- **Verma, P.**, Sharma, V., Mishra M., Effect of Computational Study of Fingering Instability due to an Instantaneous Chemical Reaction in a Porous Medium, at the conference IACM

COMPUTATIONAL FLUIDS CONFERENCE (CFC) held at Cannes, France from 25-28 April 2023.

- **Verma, P.**, Sharma, V., Mishra M., Enhanced Mixing due to Reactive Viscous Fingering Instability in a Porous Medium, at the conference ‘ AGU Fall Meeting 2022 ’ held at Chicago, IL and online everywhere from 12-16 December 2022.
- **Verma, P.**, Sharma, V., Mishra M., Reaction-induced Fingering under Asymmetrical Conditions, The 19th International Conference on Flow Dynamics (ICFD2022) held at Sendai, Miyagi, from 09-11 November 2022.
- Jangid A., **Verma, P.**, Mishra M., A Numerical Study of Linear Adsorption in Radial Miscible Flow in a Porous Matrix, The 19th International Conference on Flow Dynamics (ICFD2022) held at Sendai, Miyagi, from 09-11 November 2022.
- **Verma, P.**, Sharma, V., Mishra M., Fingering Dynamics in an Infinitely Fast Chemical Front in a Porous Medium, at the conference ‘ AGU Fall Meeting 2021 ’ held at New-Orleans, LA from December 13-17, 2021.
- **Verma, P.**, Sharma, V., Mishra M., Numerical Simulation of Radial Viscous Fingering Induced by an Instantaneous Chemical Reaction, held at 74th Annual Meeting of the APS Division of Fluid Dynamics, held at Phoenix Convention Center - Phoenix, Arizona, from November 21-23, 2021.
- **Verma, P.**, Sharma, V., Mishra M., A Numerical Study of Reactive Radial Viscous Fingering, The 18th International Conference on Flow Dynamics (ICFD2021) held at Sendai, Miyagi, from 27-29 October 2021.
- **Verma, P.**, Sharma, V., Mishra M., Radial Miscible Viscous Fingering Induced by an Infinitely Fast Chemical Reaction, at Solvay Workshop on ‘Nonlinear Phenomena and Complex Systems in memory of Prof. Grégoire Nicolis, 14-16 June 2021.

Oral/Poster Presentations

1. **Verma, P.**, Mishra M., Enhanced Mixing via Reactive Viscous Fingering in Radial Hele-Shaw Cell, at Complex Fluids Dynamics Symposium: Rheology and Instabilities in

Complex Fluids, IIT Ropar from 1-2 Dec 2023. (Poster presentation)

2. **Verma, P.**, Sharma, V., Mishra M., Effect of Initial Condition on Reactive Radial Viscous Fingering: A Numerical Insight, at the conference 67th Congress of the Indian Society of Theoretical and Applied Mechanics (ISTAM) held at IIT Mandi from 14-16 December 2022.
3. **Verma, P.**, Sharma, V., Mishra M., A Numerical Study of a Reactive Flow for an Infinitely Fast Reaction in Porous Medium, Cynosure, 2022, Department of Mathematics, IIT Ropar. (Poster presentation)
4. **Verma, P.**, Sharma, V., Mishra M., Convection-Diffusion-Reaction System with Infinite Reaction Rate, in the symposium (Online mode) on the theme "Differential Equations: Analysis, Computation and Applications" held at IIT Roorkee from December 2-3, 2021.
5. **Verma, P.**, Sharma, V., Mishra M., Chemical Reaction Induced Viscous Fingering in a Radial Displacement Flow, at international conferences on Advances in Differential Equations and Numerical Analysis (ADENA) organized by Department of Mathematics, IIT Guwahati 12-15 October 2020.
6. **Verma, P.**, Sharma, V., Mishra M., Effect of Chemical Reaction on Radial Miscible Viscous Fingering, Cynosure, 2019, Department of Mathematics, IIT Ropar. (Poster presentation)

Attended Workshop and Summer schools

- GIAN course on Interfacial Instability with Industrial Applications, Indian Institute of Technology Ropar, July 11-24, 2022.
- 2nd International Conference on Fluids under Confinement, March 14-31, 2021, IIT Kharagpur, India.
- West Asian Mathematical School (WAMS) on "Recent Developments and Applications of Partial Differential Equations, from Theory to Simulation" from August 29 to September 03, 2019, IIT Roorkee, India.

- E-Colloquium on Recent Advancements in Fluid Flow and Heat Transfer, from October 19-14, 2020, organized by the Department of Mathematics, IIT Roorkee, India.
- An Introductory Course on High-Performance Computing in Science and Engineering, February 25-March 1, 2019, IIT Kanpur, India.
- NCM IST School: PDE Theory and Computation, July 23-August 4, 2018, at IISc, India.

Teaching experience

Teaching assistant (TA), for the following courses at the Indian Institute of Technology Ropar, Rupnagar, Punjab, India.

- Differential equations (undergraduate course): August 2018 - December 2018, August 2020 - December 2020.
- Linear algebra, Integral transformations and Special functions (undergraduate course): January 2019 - May 2019, January 2020 - May 2020.
- Mathematical Mathematics (postgraduate Course): August 2019 - December 2019.
- The Computing Lab (undergraduate course): January 2021 - May 2021.
- Calculus (undergraduate course): August 2021 - December 2021.
- Introduction to Numerical Analysis (postgraduate Course), January 2022 - May 2022.

Programming/ Technical Skills

FORTTRAN, MATLAB, C language, MS Office, Latex

Known Languages

English, Hindi